SMALL, HIGH-PRESSURE RATIO COMPRESSOR -
AERODYNAMIC AND MECHANICAL DESIGN

by

Dr. C.A. Bryce
J.R. Erwin
G.L. Perrone
Dr. E.L. Nelson
Dr. R.K. Tu
A. Bosco

AIRESEARCH MANUFACTURING COMPANY OF ARIZONA

Prepared For

NATIONAL AERONAUTICS AND SPACE ADMINISTRATION

MP-13432

NOTICE

1. Report No. NASA CR-120941	2. Government Accession No.	3. Recipient's Catalog No.
4. Title and Subtitle SMALL, HIGH PRESSURE RATIO COMPRESSOR AERODYNAMIC AND MECHANICAL DESIGN		5. Report Date June 1973
		6. Performing Organization Code
7. Author(s) Dr. C. A. Bryce, J. R. Erwin, G. L. Perrone, Dr. E. L. Nelson, Dr. R. K. Tu, A. Bosco		8. Performing Organization Report No. APS-5404-R
9. Performing Organization Name and Address AiResearch Manufacturing Company of Arizona Phoenix, Arizona 85010		10. Work Unit No.
		11. Contract or Grant No.
12. Sponsoring Agency Name and Address National Aeronautics and Space Administration Washington, D.C. 20546		13. Type of Report and Period Covered Contractor Report
		14. Sponsoring Agency Code

15. Supplementary Notes

Program Monitor, Robert Y. Wong, NASA Lewis Research Center, Cleveland, Ohio

16. Abstract

The Small, High-Pressure-Ratio Compressor Program was directed toward the analysis, design, and fabrication of a centrifugal compressor providing a 6:1 pressure ratio and an airflow rate of 2.0 pounds per second.

The program consists of Preliminary design, detailed aerodynamic design, mechanical design, and mechanical acceptance tests. The preliminary design evaluated radial- and backward-curved blades, tandem bladed impellers, impeller- and diffuser-passage boundary-layer control, and vane, pipe, and multiple-stage diffusers. Based on this evaluation, a configuration was selected for detailed aerodynamic and mechanical design.

Mechanical acceptance test was performed to demonstrate that mechanical design objectives of the research package were met.

The final report is in two volumes. The first volume (NASA CR-120941) covers the preliminary design and detailed aerodynamic and mechanical design of the selected configuration and research package. The second volume (NASA CR-121193) covers the fabrication and mechanical acceptance tests.

17. Key Words (Suggested by Author(s)) Compressor/Impeller High Pressure Ratio	18. Distribution Statement Unclassified-unlimited

19. Security Classif. (of this report) Unclassified	20. Security Classif. (of this page) Unclassified	21. No. of Pages 131	22. Price* $3.00

* For sale by the National Technical Information Service, Springfield, Virginia 22151

FOREWORD

This is Volume I of the final report covering the work performed under Contract No. NAS3-14306 during the period May 1, 1970 through September 30, 1971.

TABLE OF CONTENTS

TABLE OF CONTENTS (Contd)

LIST OF TABLES

LIST OF FIGURES

LIST OF FIGURES (Contd)

LIST OF FIGURES (CONTD)

LIST OF FIGURES (CONTD)

LIST OF FIGURES (CONTD)

FINAL REPORT

SMALL, HIGH-PRESSURE-RATIO COMPRESSOR - AERODYNAMIC AND MECHANICAL DESIGN

SUMMARY

This report provides a detailed description of a 2 lb/sec flow, 6:1-pressure-ratio Compressor Program performed under Contract NAS 3-14306 with the NASA Lewis Research Center. The objective of this program was to design and fabricate a centrifugal compressor that incorporates concepts that offer the potential of high efficiency and operating range. This program consists of preliminary design, detailed aerodynamic and mechanical design, and mechanical testing. Detailed descriptions of the preliminary, aerodynamic, and mechanical designs are given in Volume I (NASA CR-120941) of the final report. Volume II of the final report (NASA CR-121193) presents the problems, modifications to the mechanical hardware, and the compressor rig test results obtained during the mechanical acceptance tests.

The preliminary design included an aerodynamic evaluation of the impeller and diffuser configurations exhibiting high-efficiency potential with an adequate operating range. Preliminary design analyses were conducted on the following configurations:

(a) Impellers

● Conventional with radial- or backward-curved blades

● Tandem-bladed with radial- or backward-curved blades

(b) Diffusers

● Conventional (vane island)

● Pipe

● Tandem/cascade

In addition, an initial screening was made of various boundary-layer control methods for adaptation to the configurations investigated.

As a result of these analyses, a tandem-bladed impeller and a cascade-vane diffuser was selected for detailed aerodynamic design.

Analysis of the inducer section applied standard axial flow rotor design practices rather than centrifugal design procedures. Final acceptability of the detailed impeller design, made up of a separate inducer and a centrifugal impeller, was determined by meanline velocity distributions and blade-loadings for several streamlines in the flow field.

Once the impeller design was fixed, an optimum diffusion split between the vaneless space region and vaned diffuser was determined. Two rows of radial cascade blades of the NACA 65 Series were used to diffuse and straighten the airflow. Additional diffusion to Mach 0.2 was accomplished in the vaneless space downstream of the cascade diffuser.

Boundary-layer calculations were made to indicate any possible unstable growth condition. Where the analysis indicated that flow separation could become a problem, provision was made to withdraw a portion of the boundary layer fluid to inhibit or eliminate this condition.

The selected compressor configuration was incorporated into a research package for delivery to the Lewis-Research Center.

INTRODUCTION

The NASA Lewis Research Center is currently engaged in the study of small, advanced concept, high-pressure-ratio centrifugal compressors. The program discussed in this report was conducted by the AiResearch Manufacturing Company of Arizona under Contract NAS 3-14306. Its intent was to design and fabricate a centrifugal compressor research package in which both the impeller and the diffuser incorporate concepts that offer the potential of high efficiency by using high diffusion and high blade loading without separation or high losses. A pressure ratio of 6:1 and a flow rate of 2 lb/sec was selected as being representative of the range of NASA interest.

To accomplish the goal of this program, radial and backward-curved impellers, boundary-layer control, tandem bladed impellers, and vane, pipe, and multiple-stage diffusers were investigated. From these, one configuration was selected for detailed design and fabrication. The research package was also designed to provide the capability to test other shroud, impeller, or diffuser configurations, and included provision for instrumentation and a shroud-diffuser assembly mounted on air bearings for torque measurement.

Volume I of the final report discusses the preliminary design which covers the optimization and selection of a configuration for detailed design; the aerodynamic design of the selected configuration; and the mechanical design of this configuration for the research package. Detailed descriptions of the procedures employed during the preliminary and detailed design as well as the results and conclusions of the program are included. In addition, AiResearch Reports AT-6091-R, Mechanical Design Analysis of NASA Advanced Compressor Test Rig (SA-9163-MR), and Air Bearing for NASA Compressor Test Rig (SA-9158-MR) have been included as Appendixes A and B, respectively.

Volume II of the Final report presents the problems, modifications to the mechanical hardware, and the compressor rig test results obtained during the mechanical acceptance tests.

PRELIMINARY DESIGN

This section consists of the evaluation of impeller and diffuser configurations that exhibit the potential for high efficiency and adequate operating range. These configurations will be compared on the basis of performance, and one impeller and diffuser configuration will be selected for detailed aerodynamic design and fabrication.

The impeller configurations considered in this section include radial and backward curved impellers with conventional blading and tandem blading. The diffuser configurations considered include single-row vane diffusers (conventional vane diffuser), multiple-row vane diffusers (cascade diffusers), and pipe diffusers. Each of these configurations will be discussed in a separate section. Also included will be initial screening of possible boundary layer control methods for adaptation to these configurations.

Conventional Impeller

An operating speed of 75,000 rpm was selected for the conventional impeller configuration based on a compromise between specific speed and inlet relative Mach number. The performance of centrifugal compressors has been correlated by AiResearch in terms of polytropic efficiency as a function of specific speed. Therefore, for a fixed-stage pressure ratio and weight flow through the compressor, specific speed becomes a function of wheel speed. Polytropic efficiency and specific speed was converted to adiabatic efficiency and wheel speed for a pressure ratio of 6:1 and a corrected weight flow of 2 lb/sec and plotted in figure 1. This curve shows that the peak efficiency occurs at a wheel speed of 90,000 rpm. However, at this wheel speed, the inlet relative Mach number in the tip region for this application is approximately 1.39 (figure 2) which is higher than is normally used in centrifugal design practice. AiResearch experience has indicated the tip Mach number should be limited to 1.2 for good compressor performance. Above this limit, the polytropic efficiency versus specific speed correlation must be corrected for inlet shock losses. Taking into account these losses, the efficiency curve (figure 1) would drop off more rapidly at higher wheel speeds as the inlet Mach exceeds 1.2. Thus, the peak efficiency that can be expected is closer to 75,000 rpm for this application.

The polytropic efficiency data used to generate figure 1 is for compressors with through-flows (W_{corr}) of approximately 7 pounds/sec or greater, nominal clearances of approximately 0.010 inches, and a Reynold's number (Re) of approximately 3×10^6. Therefore, the level of efficiency shown in figure 1 is
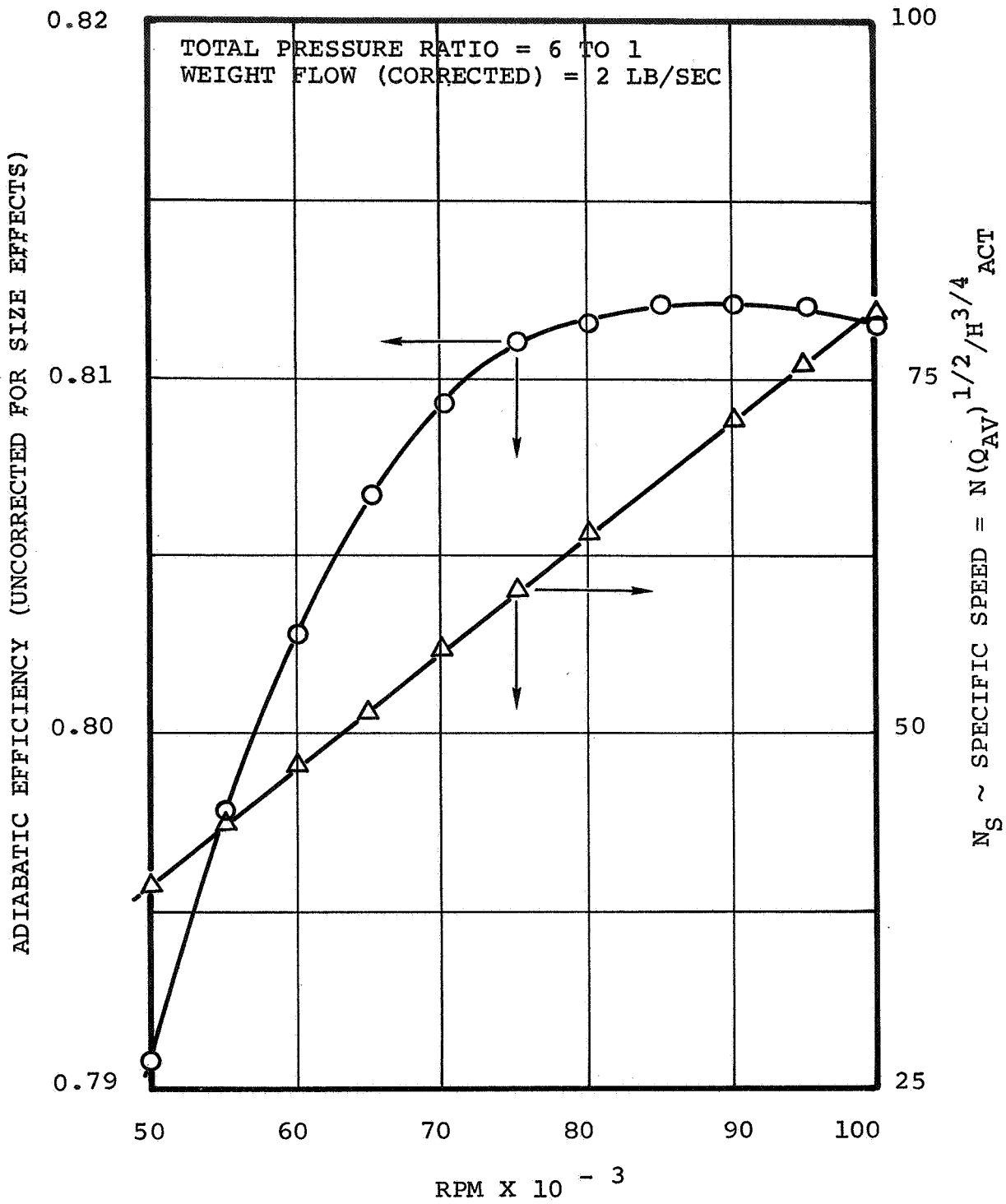
Figure 1. - Adiabatic efficiency and specific speed.

6
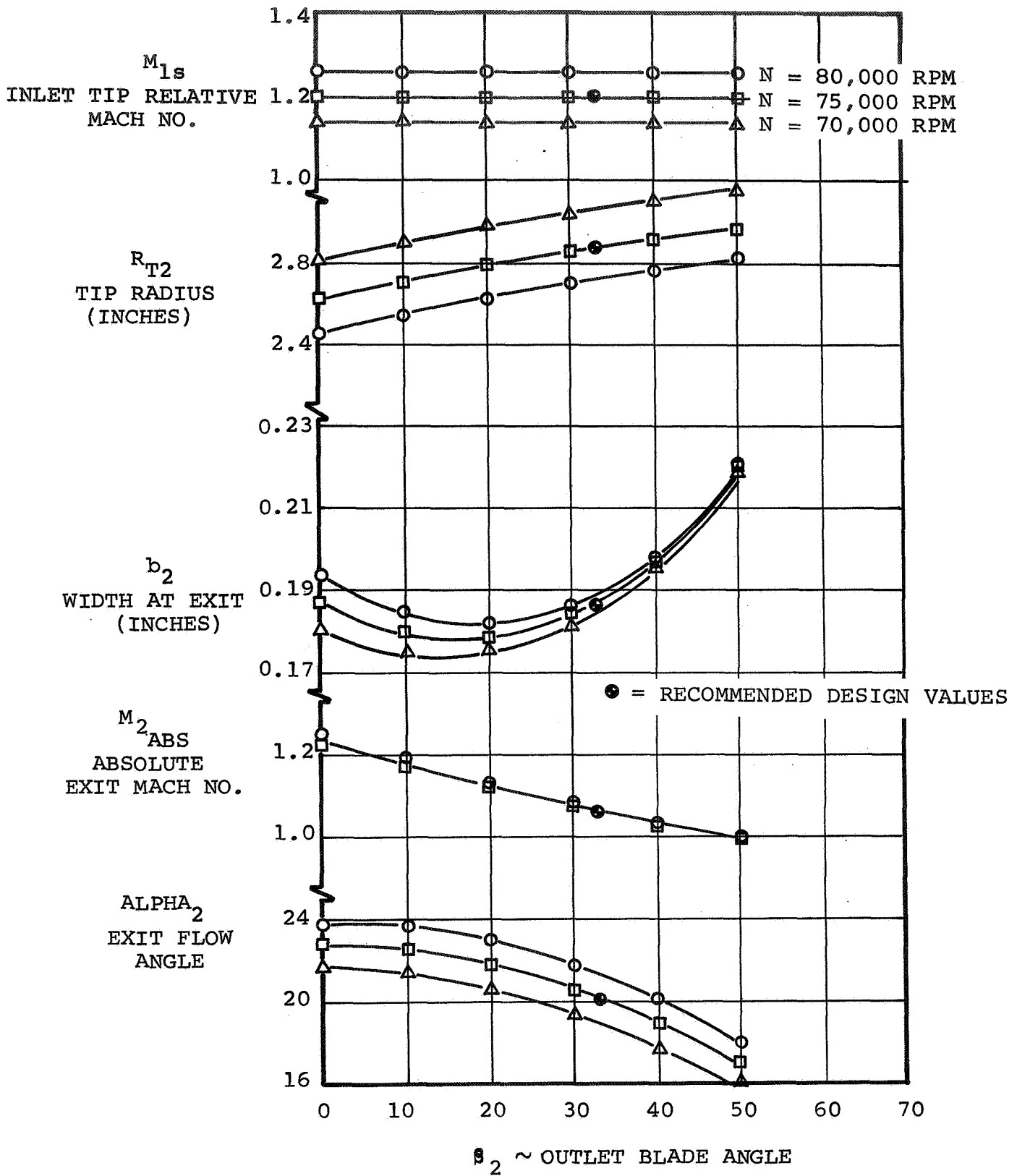
Figure 2. - Preliminary design parameters.

optimistic for this application. However the general trend of performance with wheel speed should be valid if the tip Mach does not exceed 1.2.

A hub diameter of 1.5 inches was selected for the conventional centrifugal compressor design. This is close to the minimum allowable for adequate attachment of the impeller to the shaft.

A loss optimization study with a fixed speed and hub diameter was conducted and included consideration of the following losses:

(a) Impeller friction and turbulence

(b) Impeller dump (mixing)

(c) Impeller disk friction

(d) Impeller axial clearance

(e) Vaneless diffuser

(f) Vaned diffuser

The impeller exit blade angle (backward curvature) was the primary variable parameter. The resulting loss breakdown as a function of exit angle is presented in figure 3. The peak overall efficiency point was at an exit angle of 33.0 degrees.

An approximate meridional flow path is shown in figure 4. Dimensions which were fixed at this point in the analysis are included. The estimated inlet and exit velocity triangles are shown in figure 5.

The salient features for the conventional impeller may be summarized as follows:

Corrected flow = 2 lb/sec

Speed = 75,000 rpm

Impeller total pressure ratio = 6.807

Inducer hub-tip radius ratio = 0.422

Corrected flow/unit frontal area = 29.1 lb/ft^2 sec
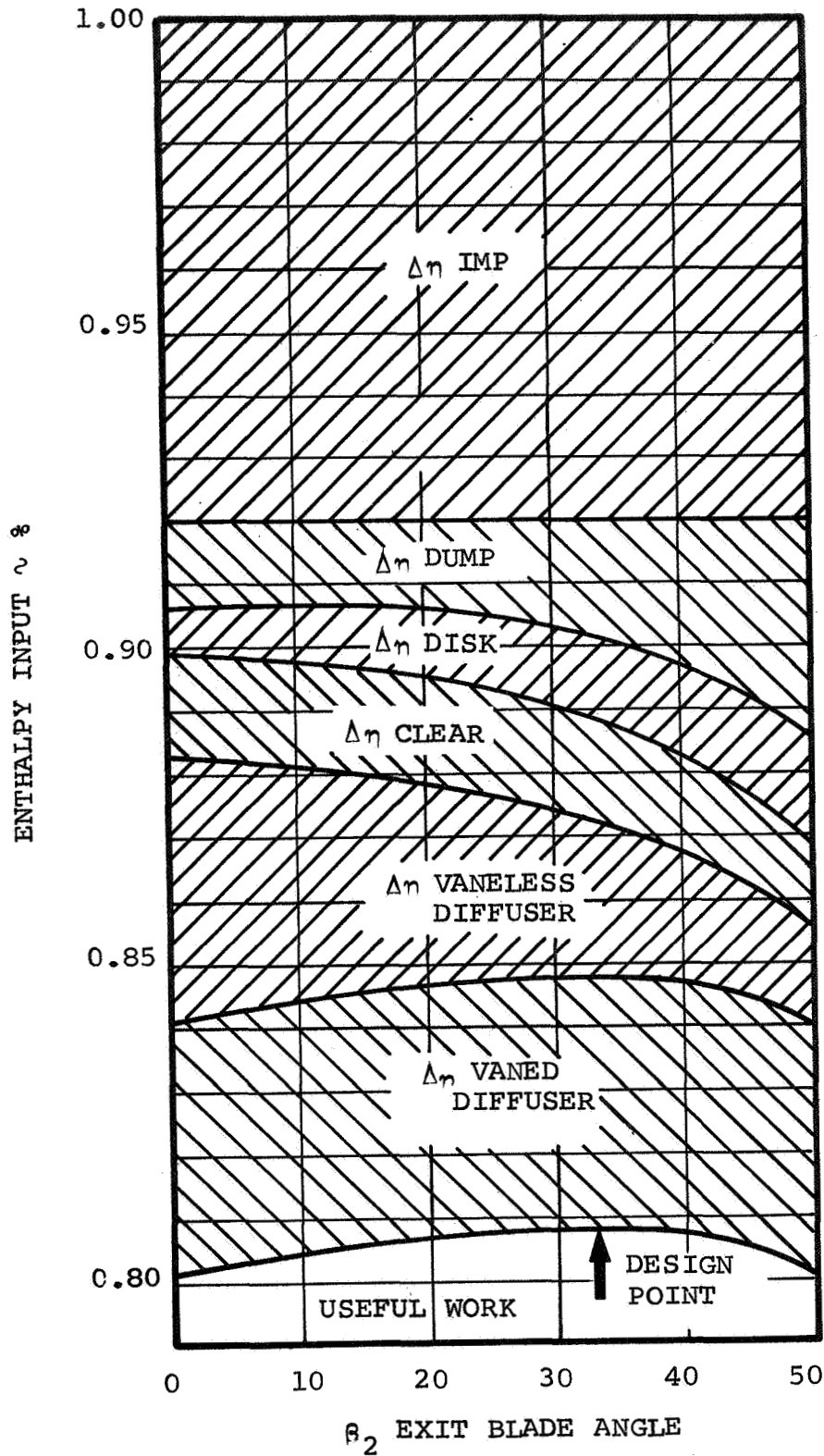
Figure 3. - Estimated input enthalphy distribution.
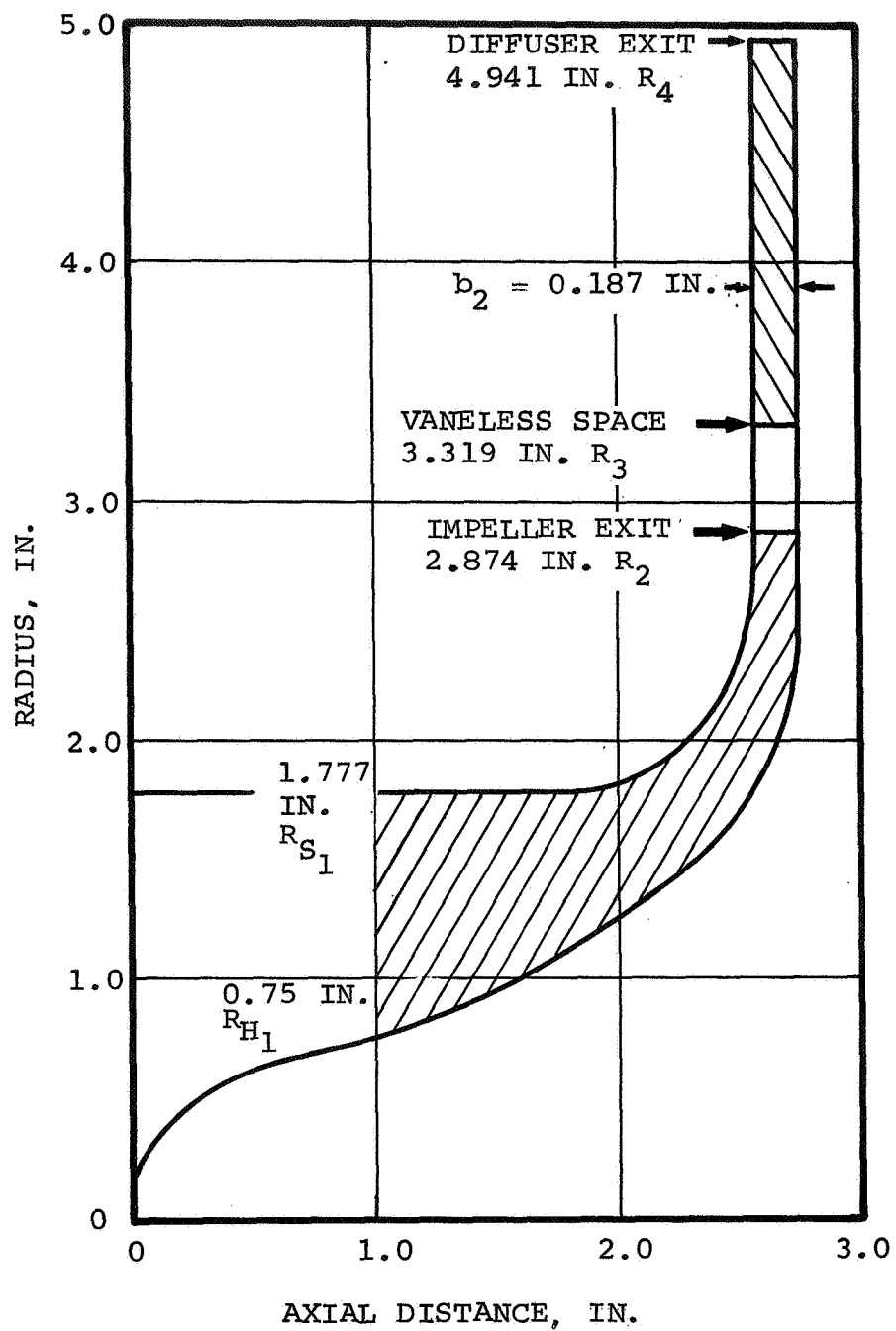
Figure 4. - Preliminary impeller dimensions

SHROUD INLET

$W_1 = 1300$
$M_1 = 1.195$

$63.4°$

$V_{M_1} = 582 = V_1$

$U = 1163$

HUB INLET

$W_1 = 687$

$45.6°$

$V_{M_1} = 481 = V_1$

$U = 491$

IMPELLER EXIT

β_2 (BLADE) = 33°

IDEAL, ZERO SLIP

$41.9°$

$V_2 = 1479$

$V_{M_2} = 580$

$W_2 = 780$

$W_{U_2} = 521$ $V_{U_2} = 1360$

$U = 1881$
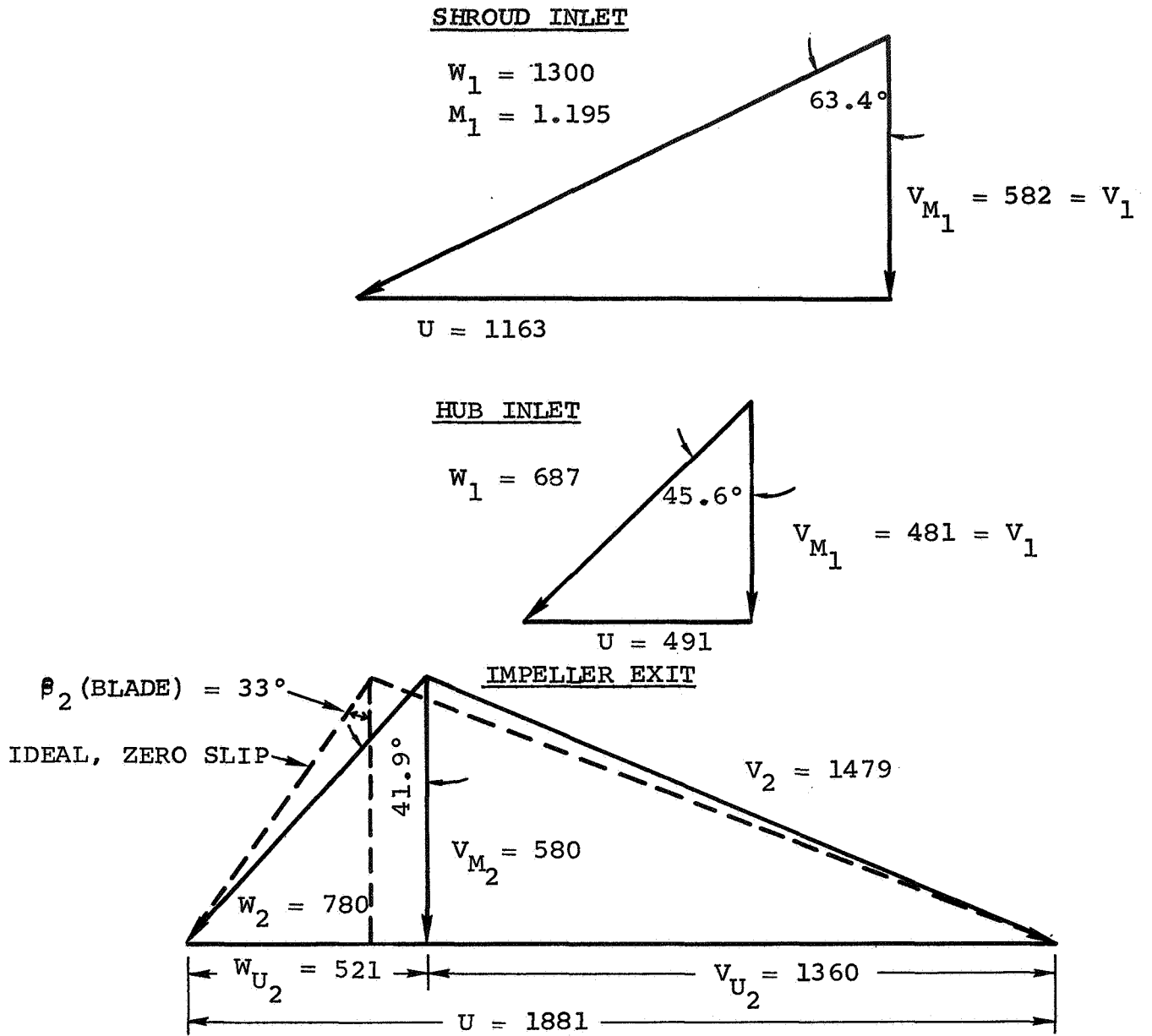
Figure 5. - Design point velocity triangles,
conventional compressor.

Corrected flow/unit annulus area = 35.4 lb/ft^2 sec

Inducer tip speed = 1162 ft/sec

Inducer tip radius = 1.7765 in.

Temperature ratio = 1.826

Adiabatic efficiency = 0.873

Tandem Bladed Impeller

The tandem impeller consists of a separate inducer followed by a centrifugal impeller. The overall design parameters for the tandem impeller were arbitrarily made identical to those of the conventional impeller listed above. The inducer design point performance was first computed and the remaining overall performance required was accomplished with the centrifugal impeller.

Inducer Design Point Performance: Inlet and outlet vector diagrams were determined with the aid of an axial flow rotor blade design computer program which provides for the solution of the radial equilibrium equation described in a rotating coordinate system. Based on previous axial flow rotor designs, the following assumptions and limitations were used to determine inducer inlet and outlet vector diagrams:

(a) Rotor efficiency was 94 percent (for large rotors)

(b) Air was not turned past the axial direction on the hub streamline

(c) Hub solidity (σ), based on the average between inlet and outlet radius of the hub streamline, was not greater than 2.1

(d) Diffuser factor (D) across the rotor was not greater than 0.5

(e) Static pressure rise coefficient (C_p) (excluding the effect of radius change) was less than 0.55

(f) Enthalpy rise across inducer equal to 71.5°F (constant from hub to tip)

The preceding conditions were satisfied by using negative curvature on the hub streamline. Final estimated inducer design-point conditions were: Total pressure ratio 1.5308, total temperature ratio 1.1377.

The inlet and outlet vector diagrams at the hub and shroud are presented in figure 6. Figures 7 through 10 indicate the variation of relative Mach number, relative air turning angle, diffusion factor, and static pressure rise coefficient across the inducer.

12

$W_1 = 1295.6$

$63.8°$

$V_M = 571.5 = V_1$

$M_1 = 1.1923$

$M = 0.526$

U = 1162.7
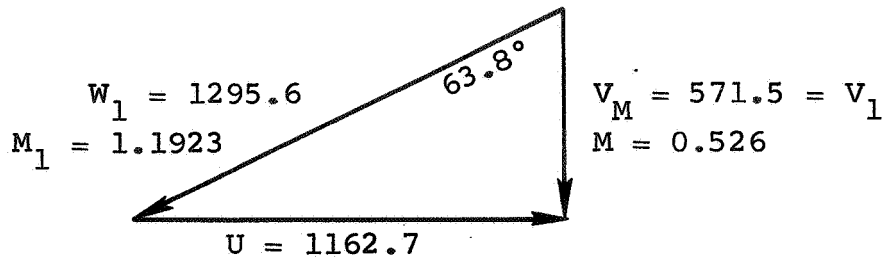
SHROUD INLET

SHROUD EXIT

$W_2 = 960.6$

$55.7°$

$34.3°$

$V_2 = 654.9$

$M_2 = 0.832$

$V_M = 541.1$

$M_2 = 0.568$

$M = 0.468$

$W_{U2} = 793.7$

$V_{U2} = 369.0$

U = 1162.7

HUB INLET

$W_1 = 699.9$

$44.5°$

$V_M = 498.9 = V_1$

$M_1 = 0.640$

$M_1 = 0.456$

U = 490.9

HUB EXIT

$7.1°$

$W_2 = 539.2$

$49.2°$

$V_2 = 819.4$

$M_2 = 0.476$

$M_2 = 0.724$

$W_{U2} = 66.7$

$V_{U2} = 620.6$

U = 687.3
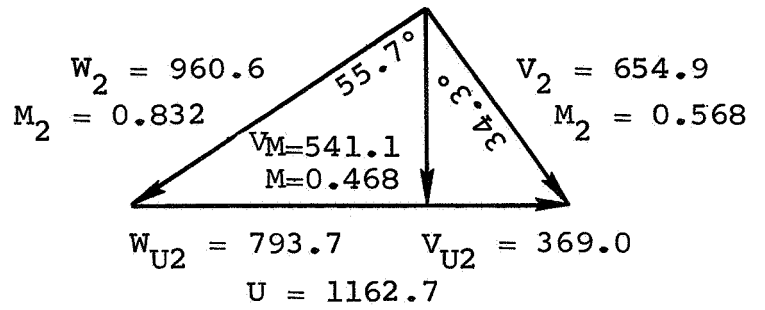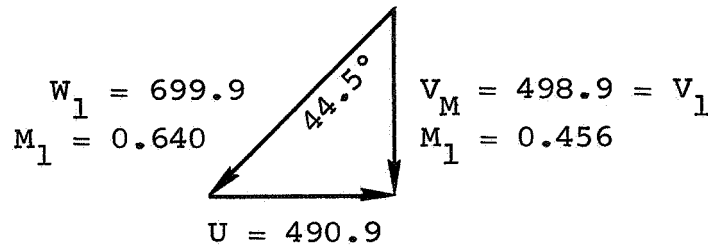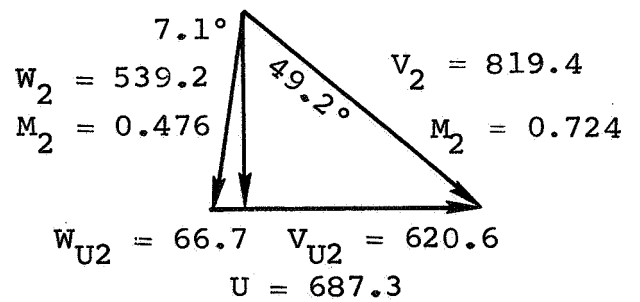
Figure 6. - Inducer vector diagrams.
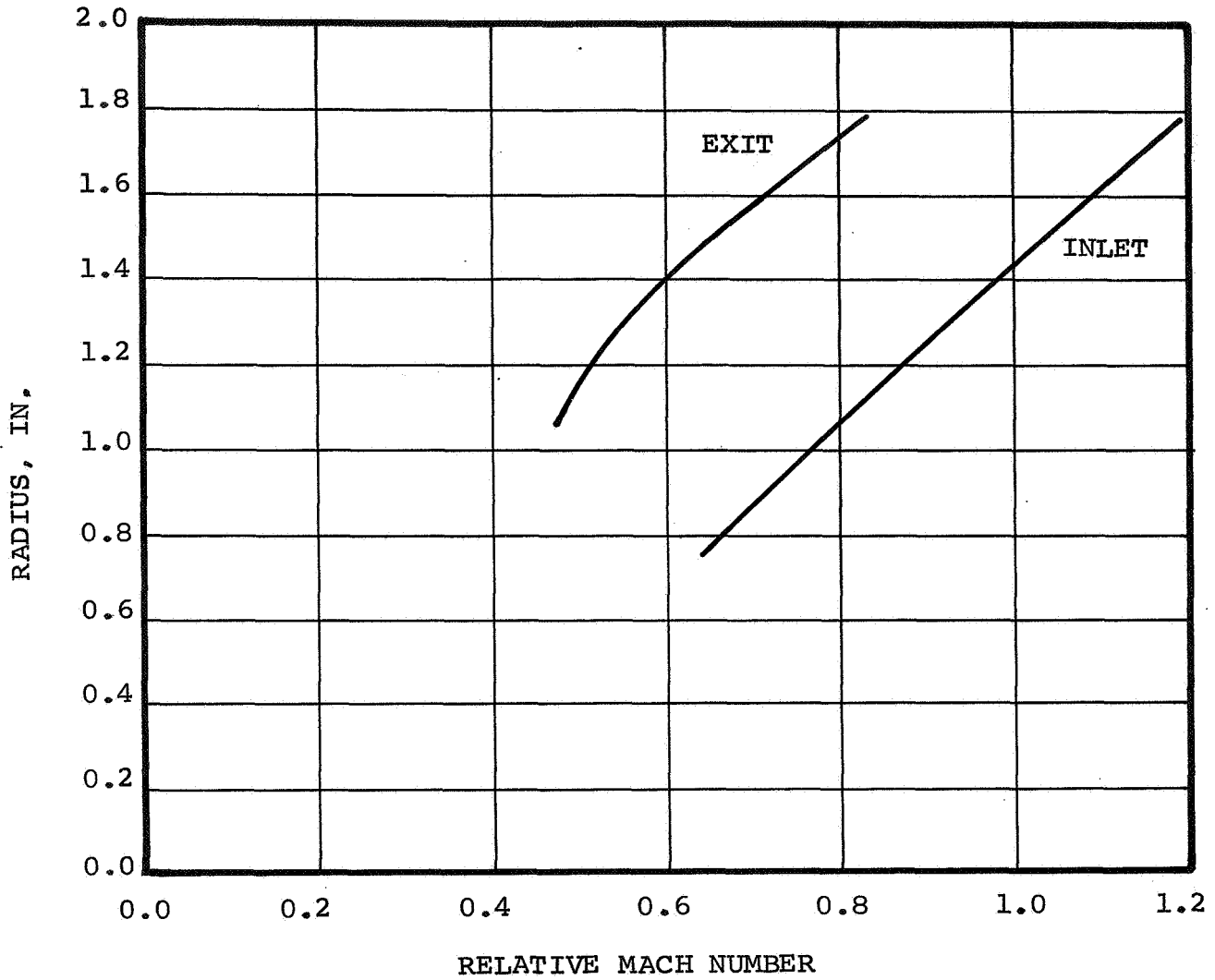
Figure 7. - Inducer relative Mach number versus radius.

14
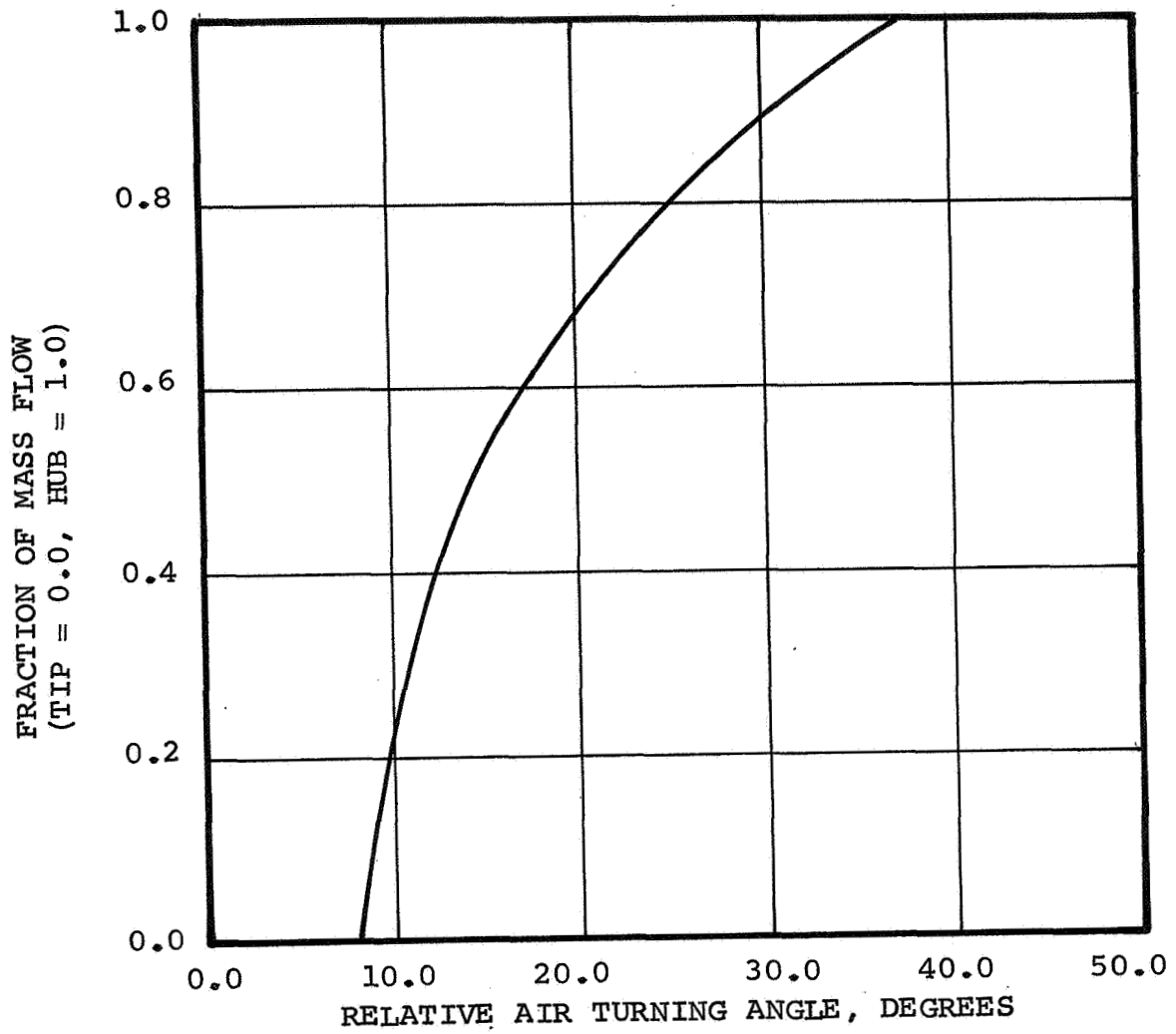
Figure 8. - Relative air turning angle versus fraction of mass flow.

DIFFUSION FACTOR, D

$$D = 1 - \frac{V_2 + \dfrac{r_2 V_{u2} - r_1 V_{u1}}{2 \bar{r} \, \sigma \, V_1}}{V_1}$$
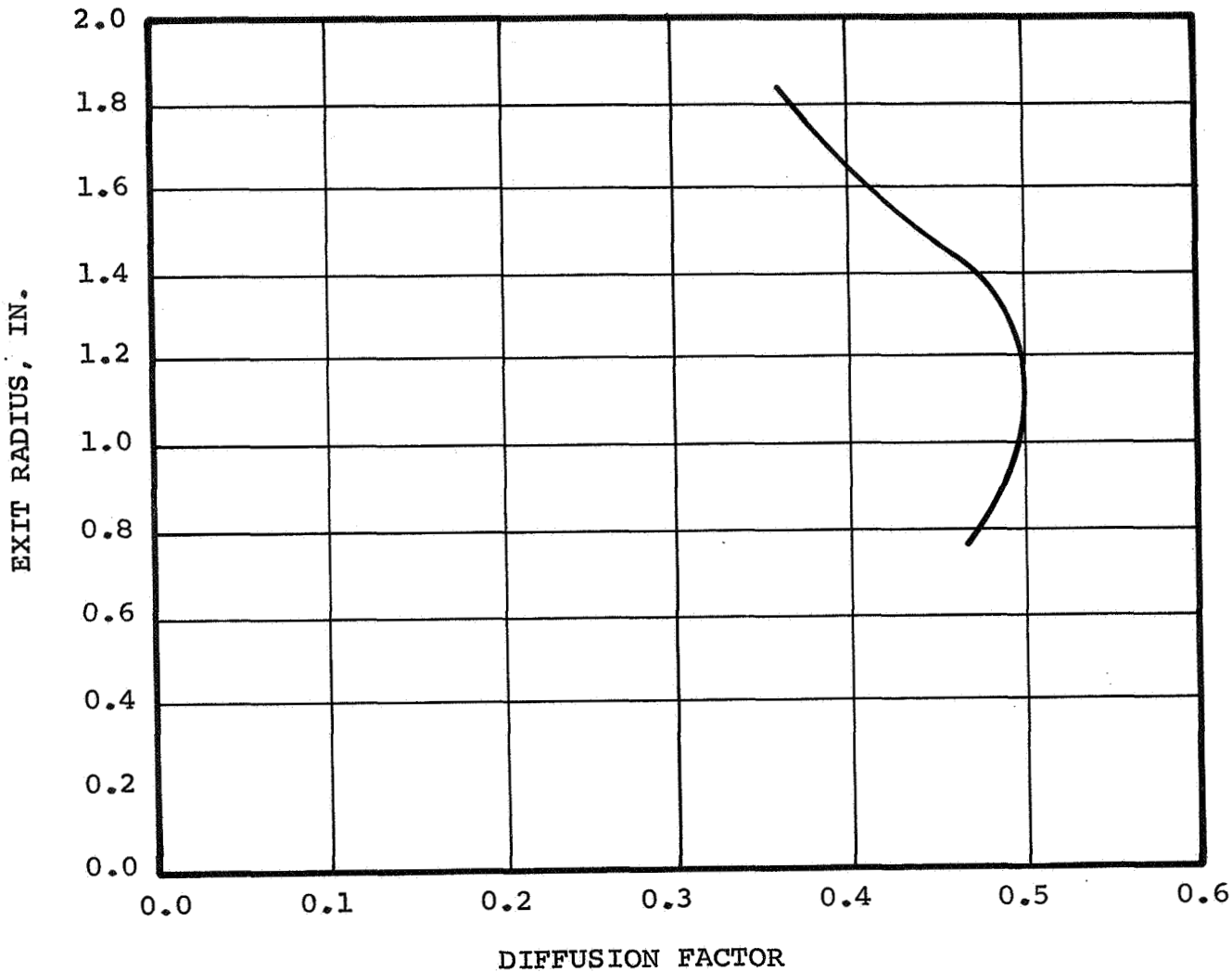
Figure 9. - Tandem inducer diffusion factor versus radius

$$(C_p)_{corr} = \frac{\bar{\rho}}{\rho_1} \frac{U_2^{\,2} - U_1^{\,2}}{V_1^{\,2}}$$
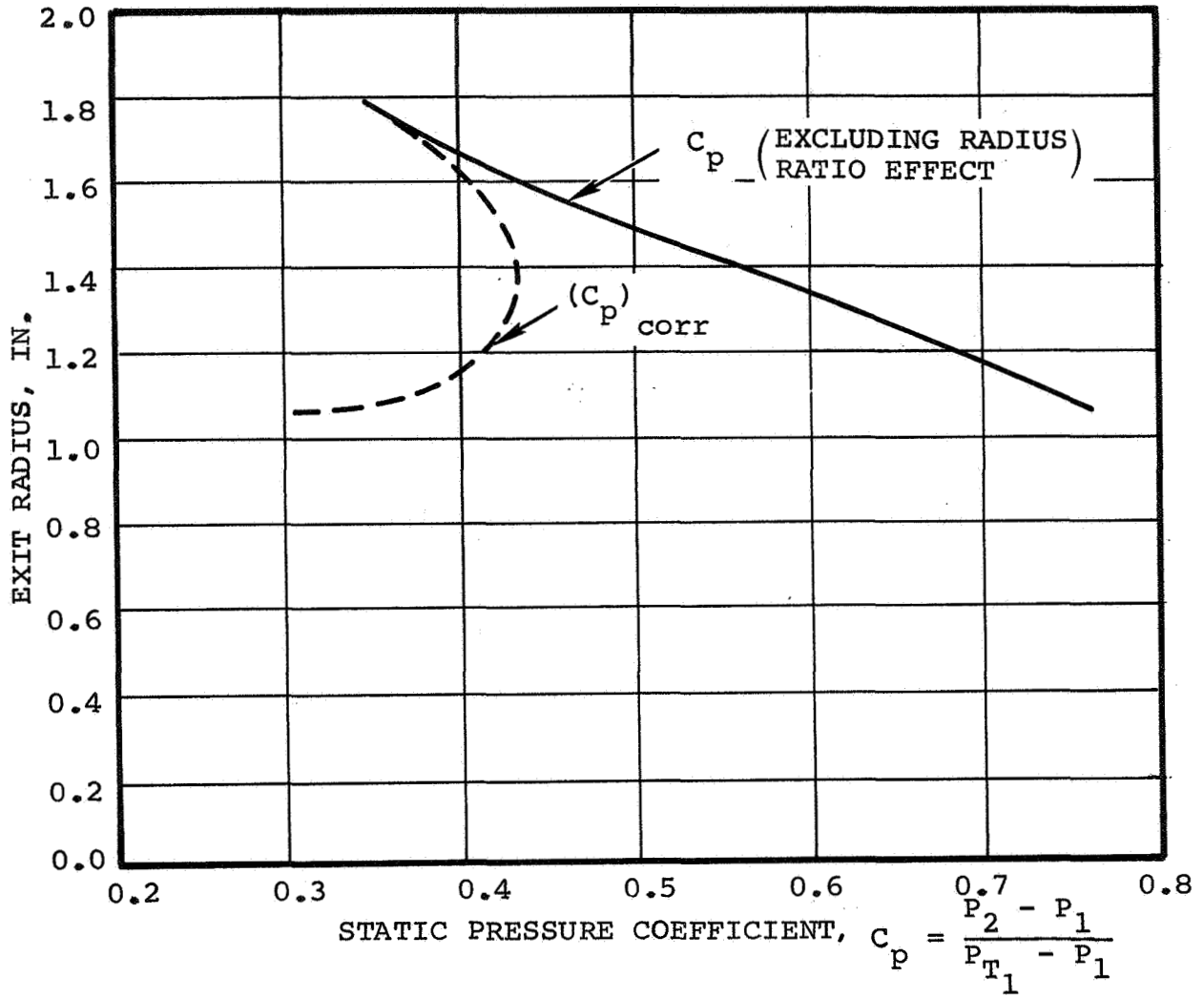
Figure 10. - Inducer static pressure coefficient versus radius.

Overall Tandem Impeller Performance: After estimated inducer performance was established, overall performance was calculated using data from an existing, conventional 6:1 compressor.
Data from this impeller indicated that an efficiency of 87.4 percent was necessary to increase the wheel total pressure ratio
from 1.531 (inducer exit condition) to the required 6.807 (impeller exit). Vector diagrams for the radial impeller are shown in
figure 11. An efficiency of 87.4 percent was used for the radial
portion of the tandem impeller, and an overall impeller total
pressure ratio of 6.807 was used to obtain a total temperature
ratio of 1.822 and an overall adiabatic efficiency of 0.8774.

Inducer Blade Shape: Having established the inducer vector
diagrams, a preliminary blade shape was designed for preliminary
stress calculations. The following assumptions, based on past
axial flow rotor design experience, were used:

(a) The suction surface incidence angle varies linearly
     along the radius from zero at the shroud to
     1 degree at the hub.

(b) The mean camber line incidence angle varies linearly
     along the radius from a 2.5-degree half-wedge angle
     at the shroud to an 8-degree half-wedge angle at the
     hub.

(c) The deviation angle is based on a modified Carter's
     rule (ref 1).

(d) Double circular arcs are used at all surfaces.

Figures 12 and 13 indicate the variation of incidence angles
and deviation angle with radius. Using these criteria, blade
shapes at the shroud, 50 percent, and hub streamlines were generated. Figures 14 through 18 present solidity, camber and stagger, maximum thickness/chord, chord, and leading edge thickness
as a function of radius. Blade shapes on a streamline (cascade)
projection are shown in figure 19. Because of the small wheel
size and stress considerations, a parametric study was made for
various aspect ratio inducers. The variation of aspect ratio
with blade number is shown in figure 20. The preliminary meridional flowpaths for aspect ratios of 0.85, 1.2, and 1.6 are shown
in figure 21. An aspect ratio of 1.6 would require 19 inducer
blades, which is satisfactory aerodynamically since 19 blades
could be used in the radial portion of the impeller. The radial
portion efficiency was estimated from a 19-bladed conventional
impeller, so no adjustment in estimated efficiency was needed for
this case, although the small chord distribution required presented a possible manufacturing problem. An aspect ratio of 1.2
would require 14 inducer blades; however, a check of the loading
diagrams for a 14-bladed radial impeller revealed excessive blade

18

INLET

$W_1^1 = 960.6$ 55.7°   34.3° $V_1^1 = 654.9$

$M_1^1 = 0.832$ $V_M = 541.1$ $M_1^1 = 0.568$ SHROUD

$M = 0.468$

$W_{U1} = 793.7$ $V_{U1} = 369.0$

$U = 1162.7$

EXIT

$W_2^1 = 780.2$ 66.2° $V_2^1 = 1500.7$

$M_2^1 = 0.578$ 39.1° $M_2^1 = 1.111$

$V_M = 605.5$

$M = 0.448$

$W_{U2} = 492.0$ $V_{U2} = 1373.0$

$U = 1865.0$

INLET

7.1° $V_1 = 819.4$

$W_1 = 539.2$ 49.2°

$M_1 = 0.476$ $M = 0.724$

$W_{U1} = 66.7$ $V_M = 535.1$

$M = 0.4725$ HUB

$V_{U1} = 620.6$

$U = 687.3$

EXIT

$W_2^1 = 780.2$ 66.2° $V_2^1 = 1500.7$

$M_2^1 = 0.578$ 39.1° $M_2^1 = 1.111$

$V_M^1 = 605.5$

$M_M = 0.448$

$W_{U2} = 492.0$ $V_{U2} = 1373.0$

$U = 1865.0$
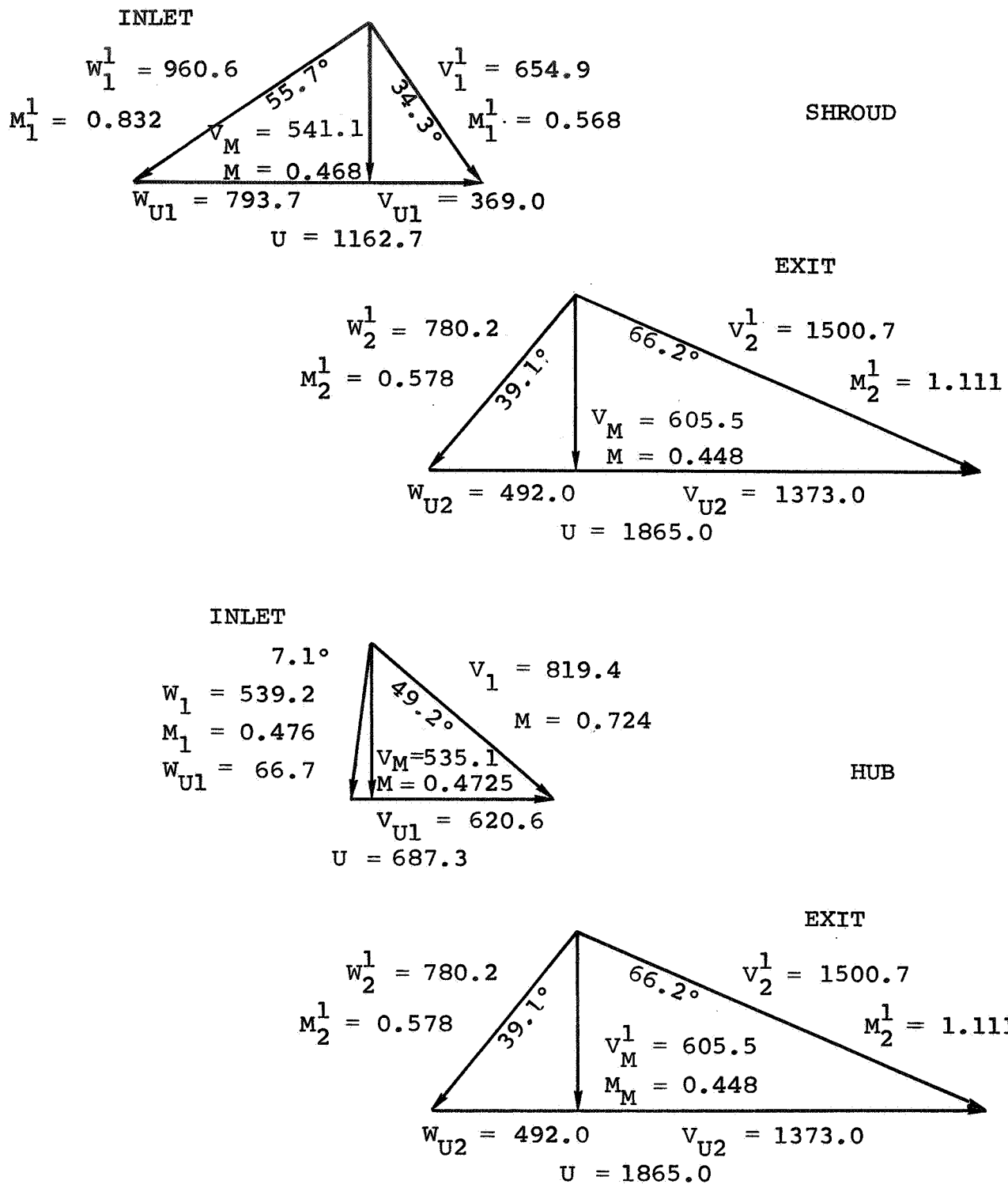
Figure 11. - Vector diagrams for centrifugal portion of tandem impeller.
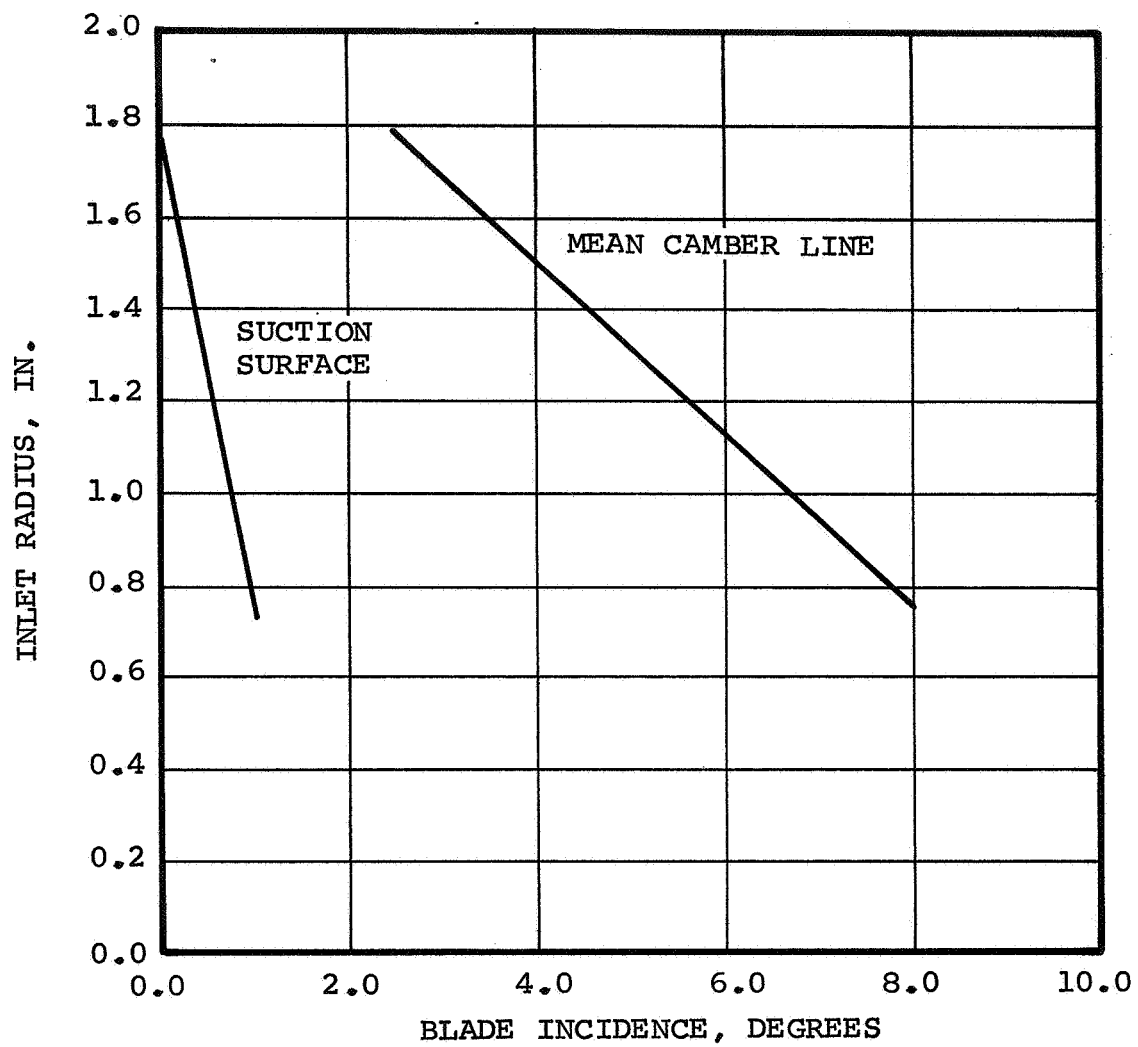
Figure 12. - Tandem inducer incidence angles versus inlet radius.
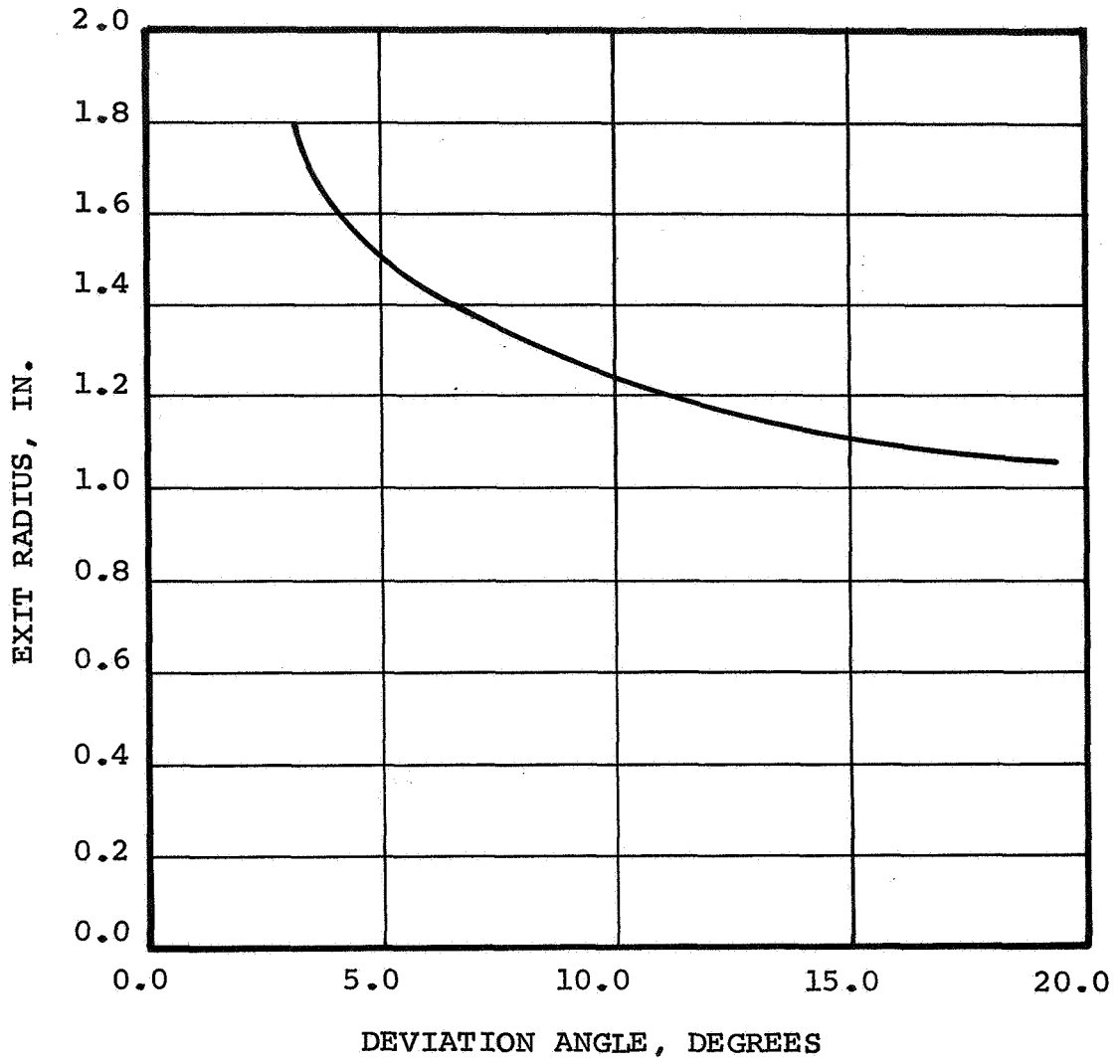
Figure 13. — Tandem inducer deviation angle versus exit radius.
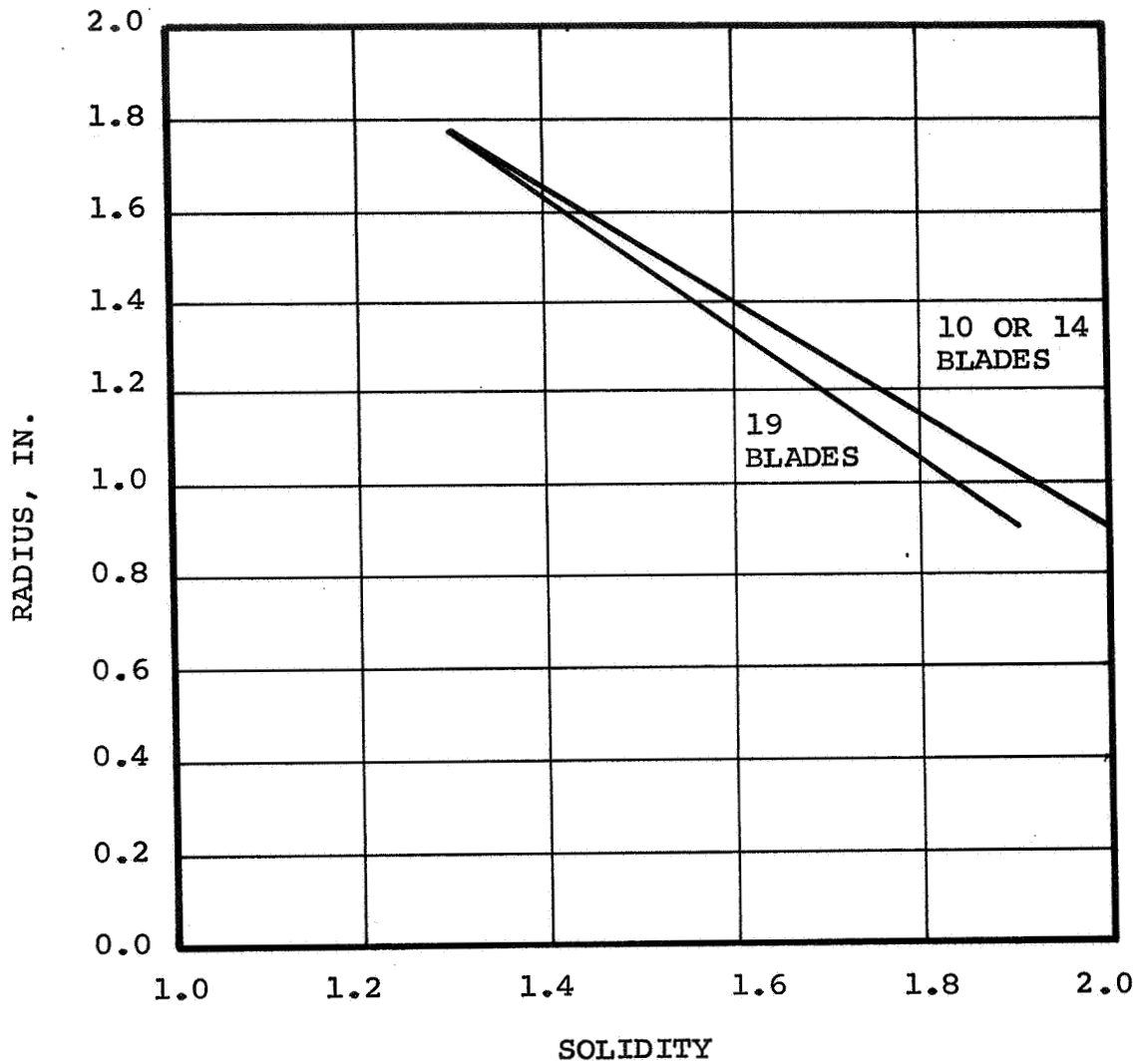
Figure 14. - Tandem inducer solidity versus radius.

22
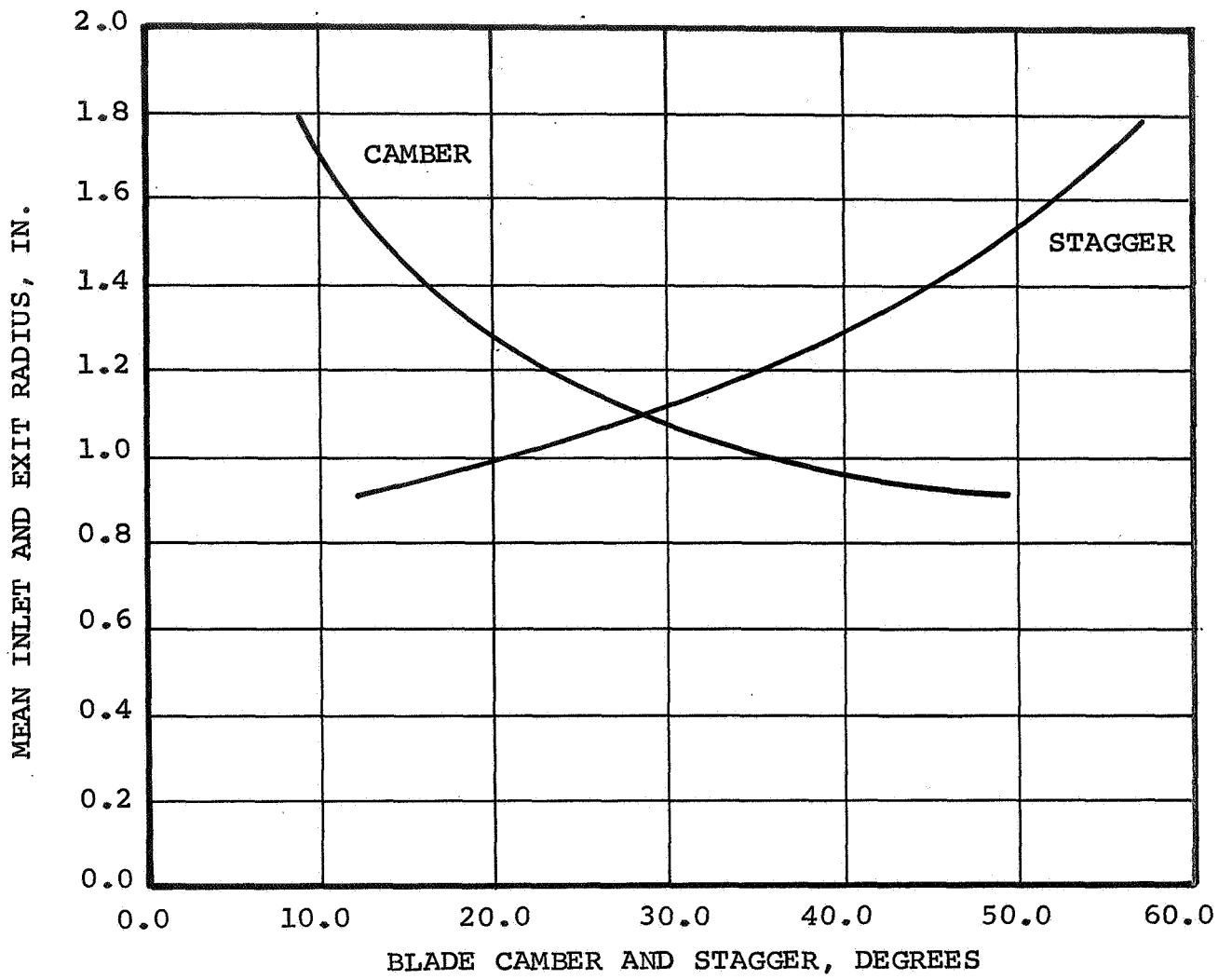
Figure 15. - Tandem inducer blade camber and stagger versus mean radius.
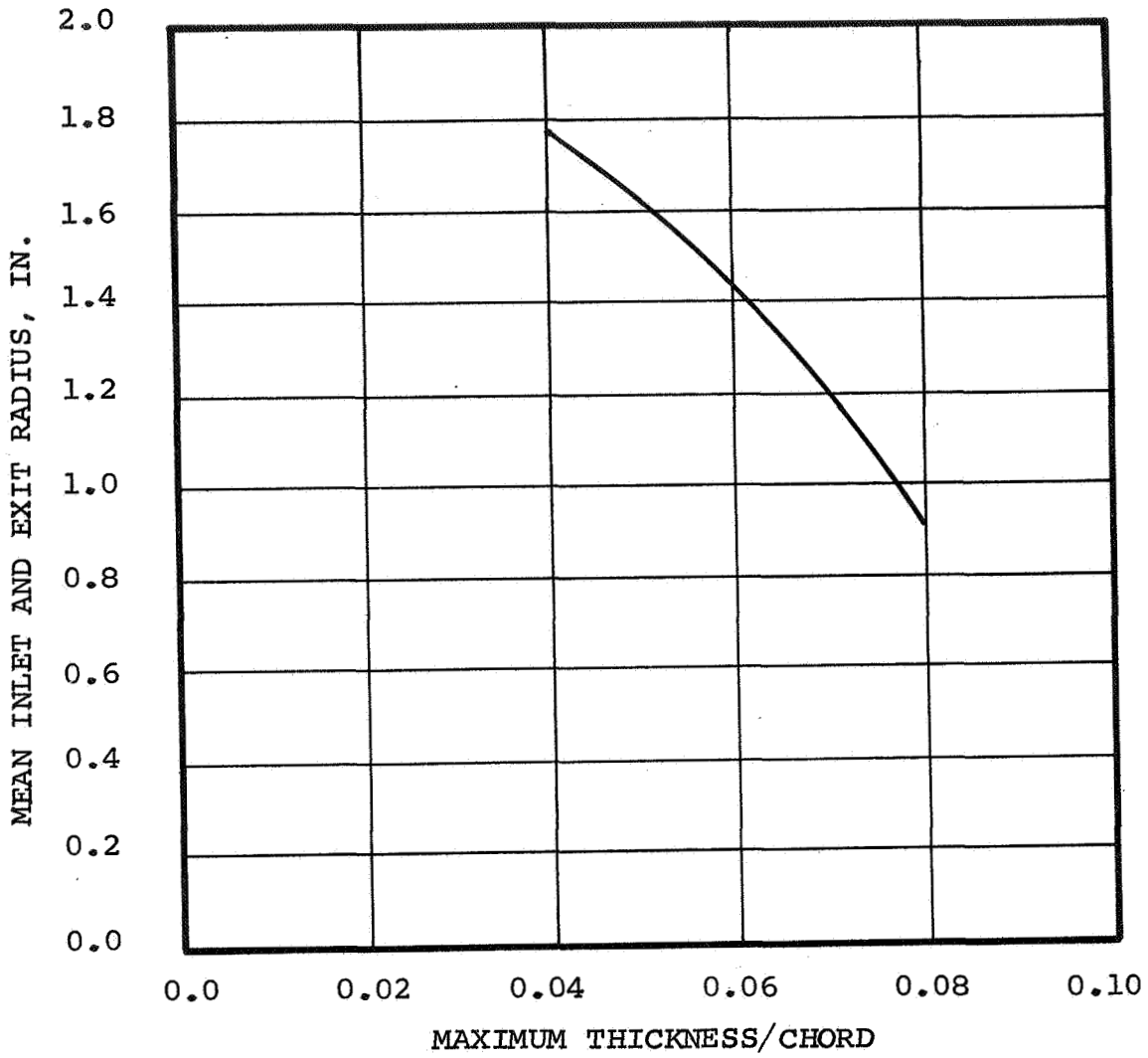
Figure 16. — Tandem inducer maximum thickness/chord versus mean radius.

24
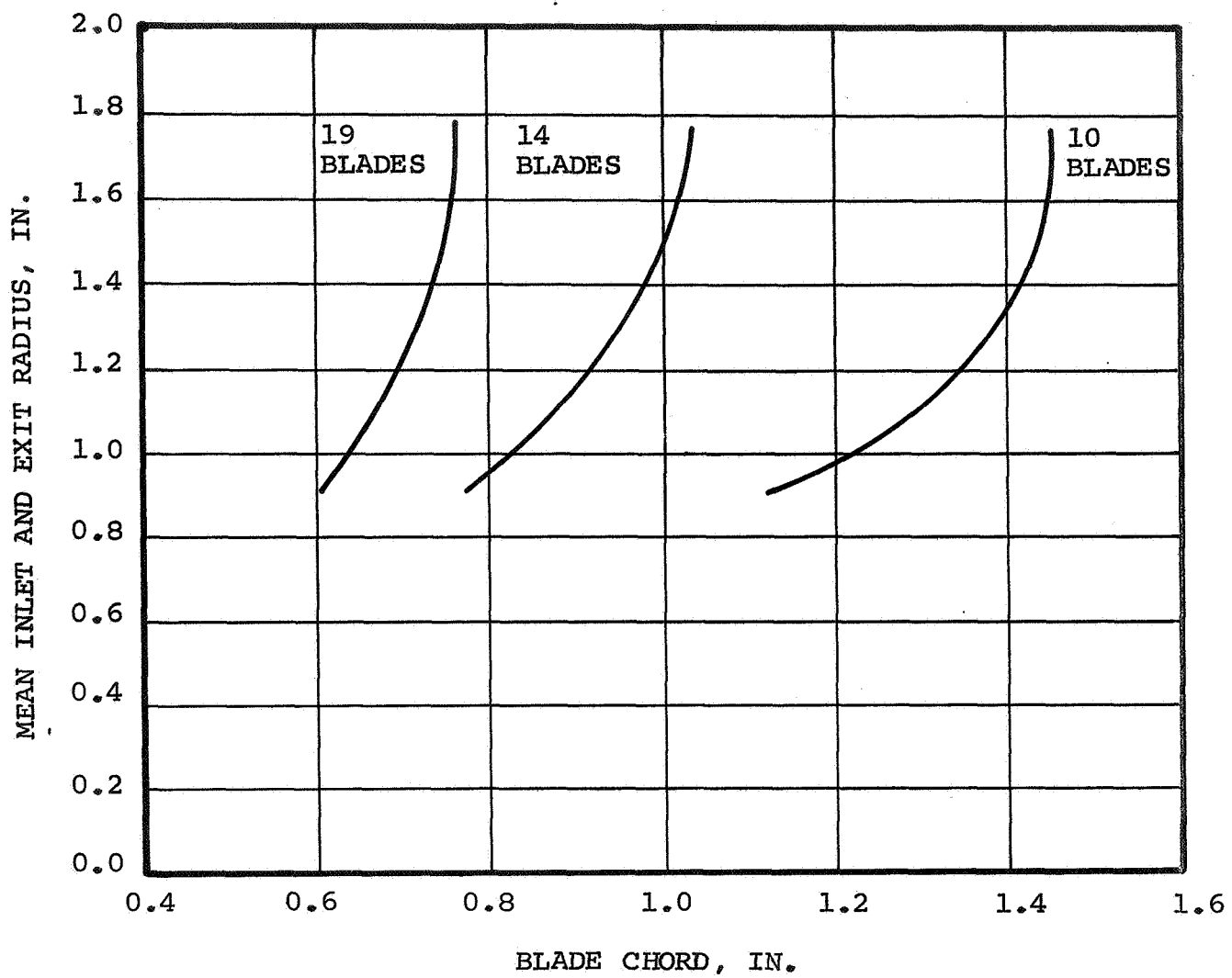
Figure 17. - Tandem inducer blade chord versus mean radius.
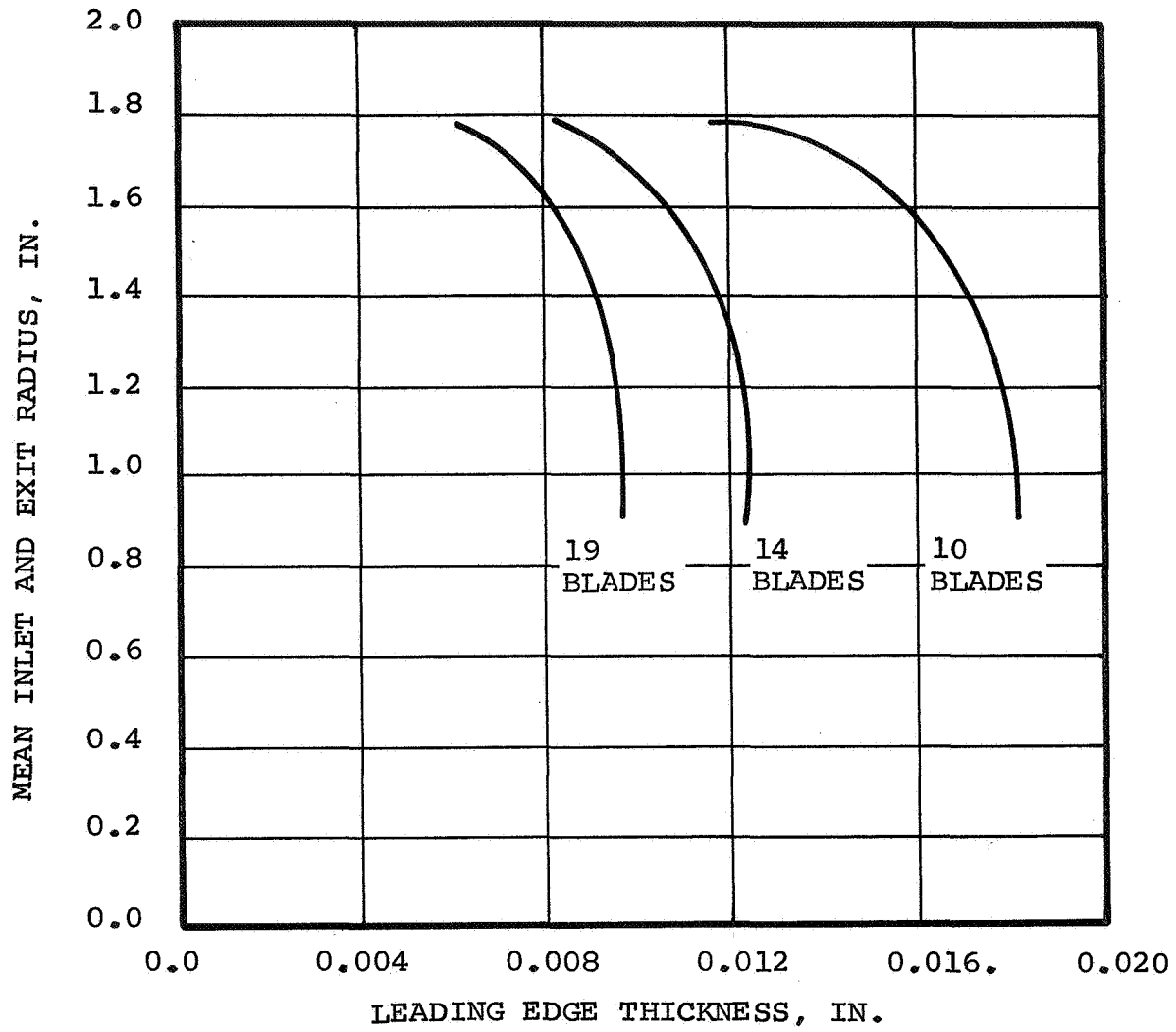
Figure 18. - Tandem inducer leading edge thickness versus mean radius.
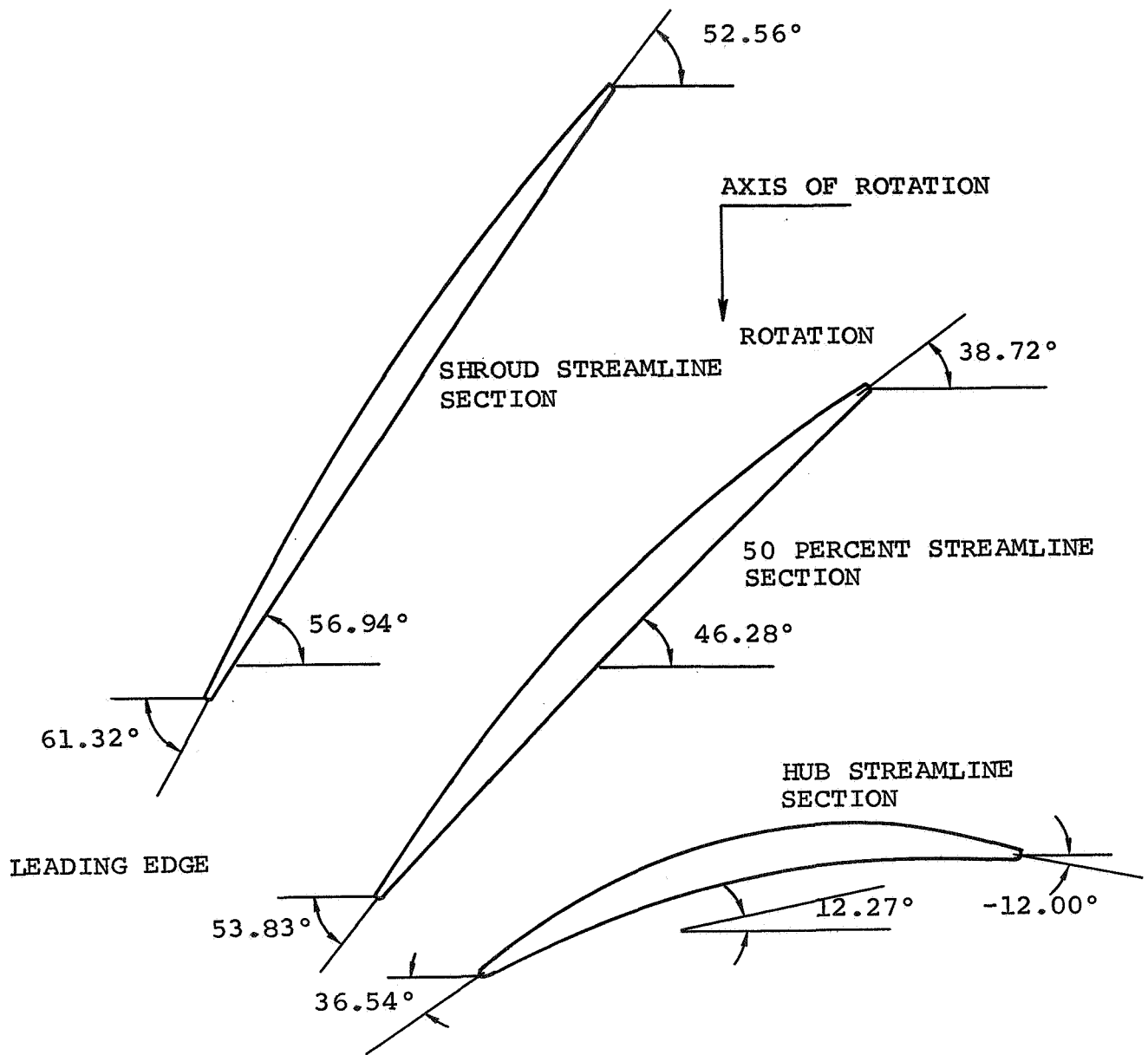
Figure 19. - Tandem inducer blade shape (cascade projection).

ASPECT RATIO = BLADE HEIGHT/BLADE CHORD
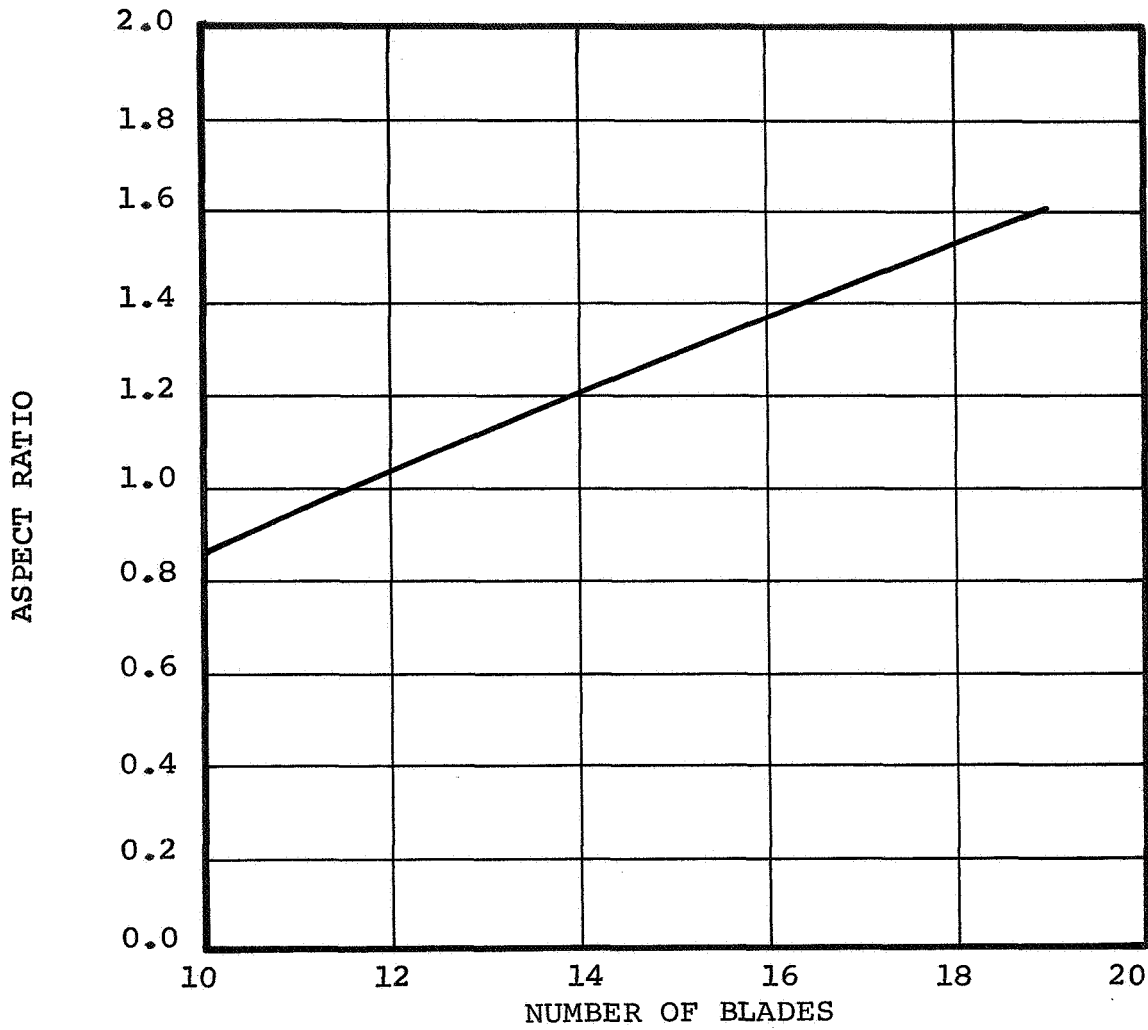
Figure 20. - Tandem inducer aspect ratio versus number of blades.
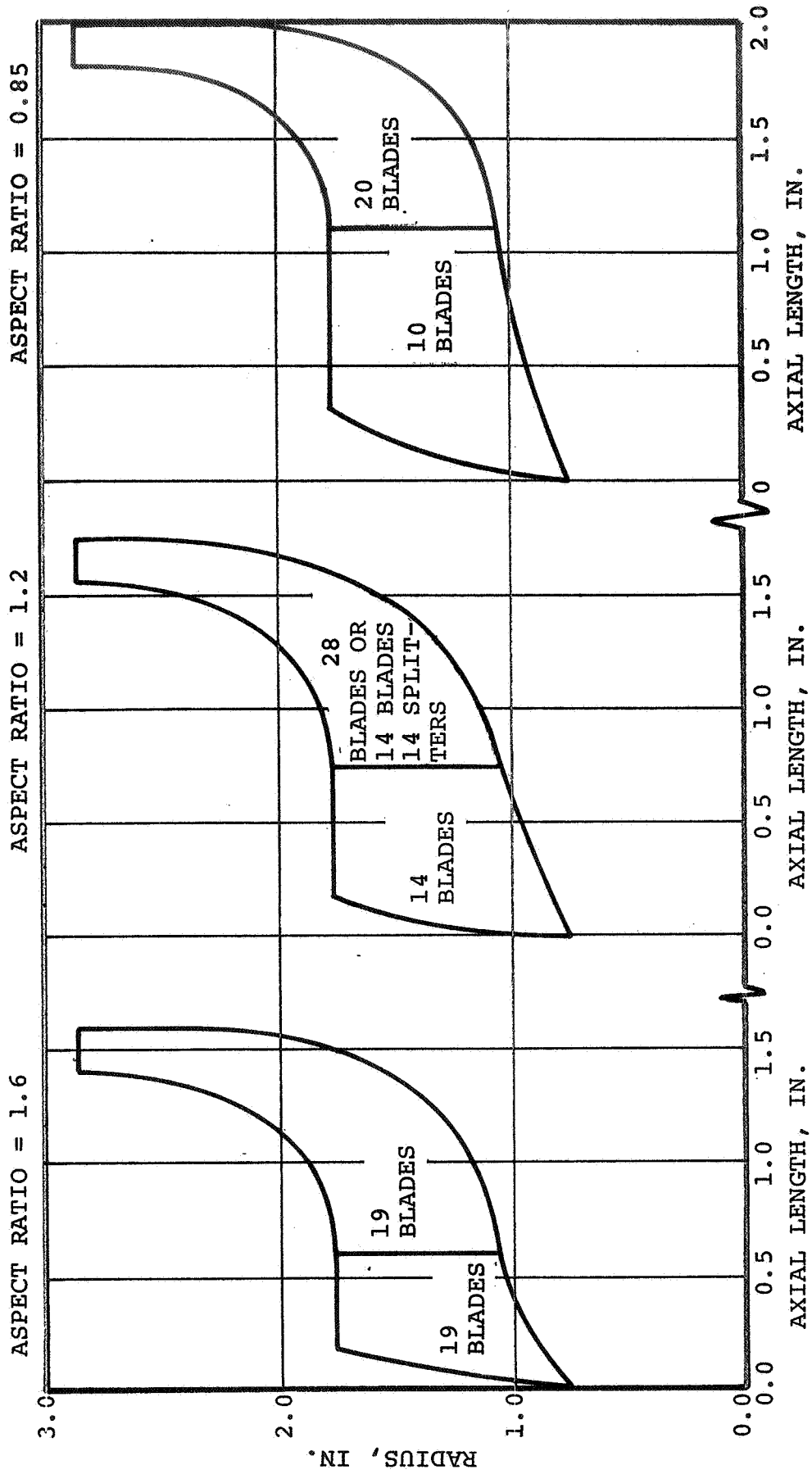
Figure 21. - Tandem bladed impeller preliminary flow path for three different aspect ratio inducers.

29

loading. When considering 28 impeller blades, it was necessary to decrease the estimated efficiency to allow for increased skin friction losses. The possibility of using 14 blades with 14 splitter vanes was also considered, but a detailed analysis would have to be made to determine its feasibility. Finally an aspect ratio of 0.85 would require only 10 inducer blades and 20 impeller vanes. However, stress considerations indicated a potential problem due to the large lean angle at the inlet to the radial impeller if the inducer blades were stacked at the center of mass. Thus, each combination considered had certain limitations.

Impeller Comparison and Selection

An overall comparison between a conventional impeller and a tandem-bladed impeller designed to meet the contract requirements for a compressor pressure ratio of 6:1 and a design weight flow of 2.0 pounds per second is presented in table I. Results of the preliminary design effort indicated that the tandem-bladed impeller offered 0.44 points higher efficiency than the conventional impeller. This difference is due to lower losses predicted for the inducer portion of the tandem impeller. A comparison of the temperature-entropy (T-S) diagrams for the two impellers is shown in figure 22. Because the efficiency of the radial portion of the tandem impeller was based on test data from a conventional impeller, the following conditions that would occur in a tandem impeller could not be assessed quantitatively:

(a) Boundary layer energization due to selective orientation of the inducer blades with respect to the blades of the centrifugal portion.

(b) The effect of a new boundary layer starting at the inlet of the radial portion

(c) The effect of inducer blade wakes at the impeller inlet

(d) The difference in wetted area between the radial portion and the conventional impeller that was used to estimate efficiency

It is believed that these factors together with utilizing a new design technique currently being applied to a transonic fan at AiResearch under NASA contract NAS3-13498, the overall tandem impeller efficiency could be one point or more better than the conventional impeller.

No quantitative assessment of the operating range of the tandem impeller could be made. The higher efficiency potential of the tandem bladed impeller resulted in its selection for

30

TABLE I. - COMPARISON OF CONVENTIONAL
AND TANDEM IMPELLERS

	Conventional	Tandem
RPM	75,000	75,000
Corrected flow, lb/sec	2.0	2.0
Total pressure ratio (to impeller exit)	6.807	6.807
Total temperature ratio	1.826	1.822
Diameter, in.	5.748	5.748
No. blades/Inducer blades	19/0	19/19
Adiabatic efficiency	0.873	0.8774
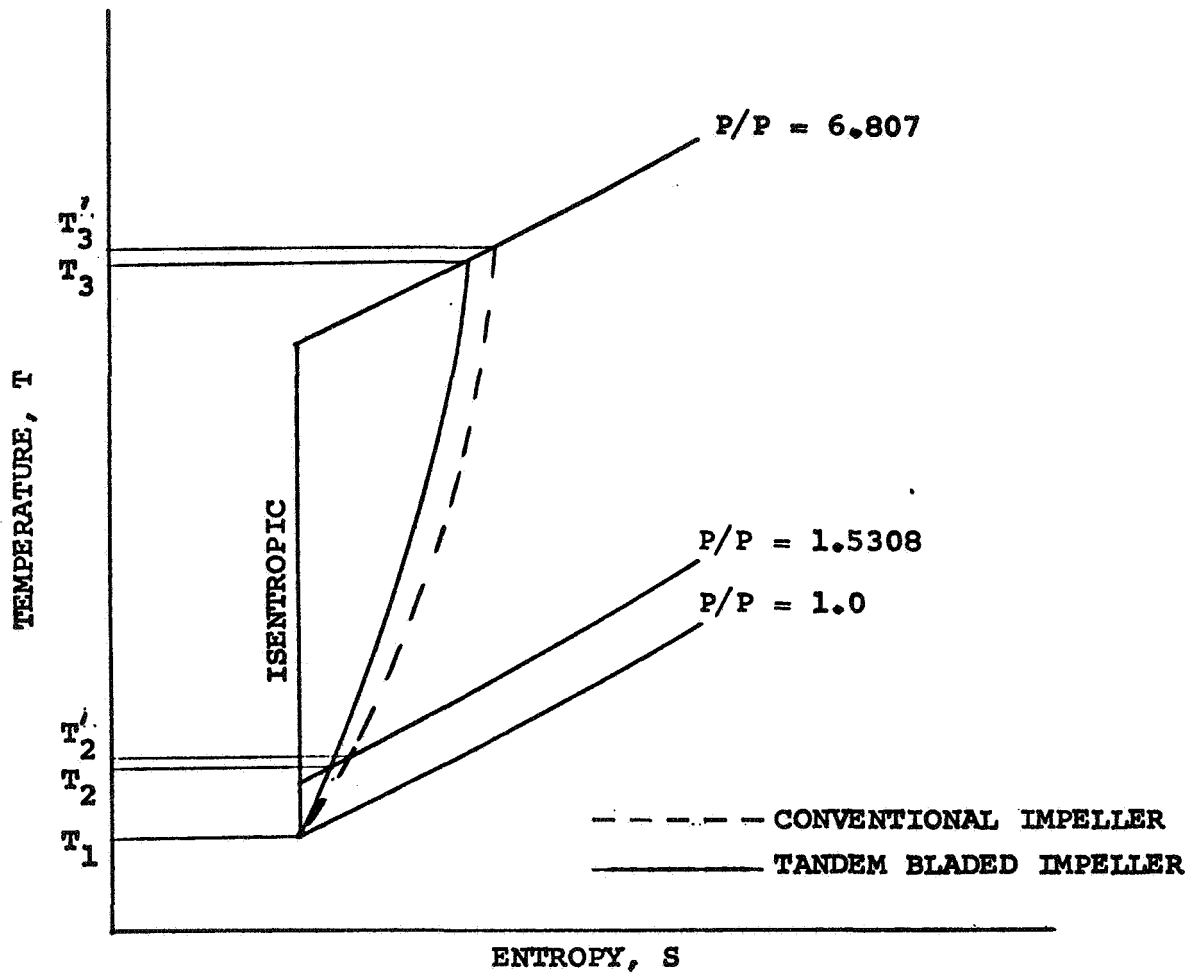
Figure 22. - T-S diagram comparing conventional and tandem bladed impeller.

detailed aerodynamic design.

As with most advanced developments, there are possible pitfalls that may have been overlooked which could have altered the conclusions. Possible problem areas for the tandem configuration included: (1) precise matching of the flow from the inducer to the inlet conditions of the impeller at design conditions, (2) the effect of flow mismatch on the range and low-speed characteristics of the tandem impeller under off-design conditions was not known, and (3) operating range may not be as great as the conventional impeller.

Diffuser Design

Several diffuser configurations were considered, and a preliminary design study was conducted to examine the performance of three candidate diffuser geometries. Essential results of these analyses are presented in the following paragraphs.

Conventional Vane Diffuser: This type of diffuser is typical of many recent AiResearch designs for centrifugal compressors. A preliminary sketch of the proposed vane configuration is presented in figure 23. The gap shown between the impeller exit and the leading edge of the vaned diffuser section is the vaneless space where some initial diffusion takes place. For this particular design, the vaneless space was sized to reduce the absolute Mach number leaving the impeller from 1.06 to 0.85 at the entrance of the vaned diffuser section. The proper inlet Mach number to the vaned section was determined from a trade-off between shock losses and viscous losses in the vaneless space.

Twenty-five vanes were selected for the configuration. This selection was made with consideration to the aspect ratio of the diffuser passage; aspect ratio for the two-dimensional diffuser passage refers to the diffuser-width over the throat-width normal to the inlet flow. Experience has shown that diffuser performance drops considerably below an aspect ratio of 0.75. With this as a limit, the selection of 25 vanes was reasonable in that more vanes only result in increasing the drag losses.

Performance of the vaned diffuser at design conditions was calculated from data obtained from Runstadler and Dean (ref. 2). A comparison of existing experimental diffuser performance from previous AiResearch centrifugal compressors with Dean's data indicated good correlation where the inlet blockage could be estimated satisfactorily. In fact, the experimental data correlation resulted in the definition of an empirical blockage factor which best fit the test results. This factor and the performance curves of Runstadler and Dean were used to determine the performance of the conventional vaned diffuser. These performance values and pertinent design parameters are summarized in figure 23.

33

NOTES:
1. VIEW IS FROM IMPELLER BACK FACE
2. NUMBER OF BLADES = 25
3. EFFECTIVE AREA RATIO = 3.03:1
4. STATIC PRESSURE RECOVERY = 0.751

$t_2 = 0.050$

$\beta_1 = 70.1°$

$t = 0.020$

$\beta_2 = 46.8°$

$R_{IMP} = 2.874$

$R_{LE} = 3.319$

$R_{TE} = 4.945$
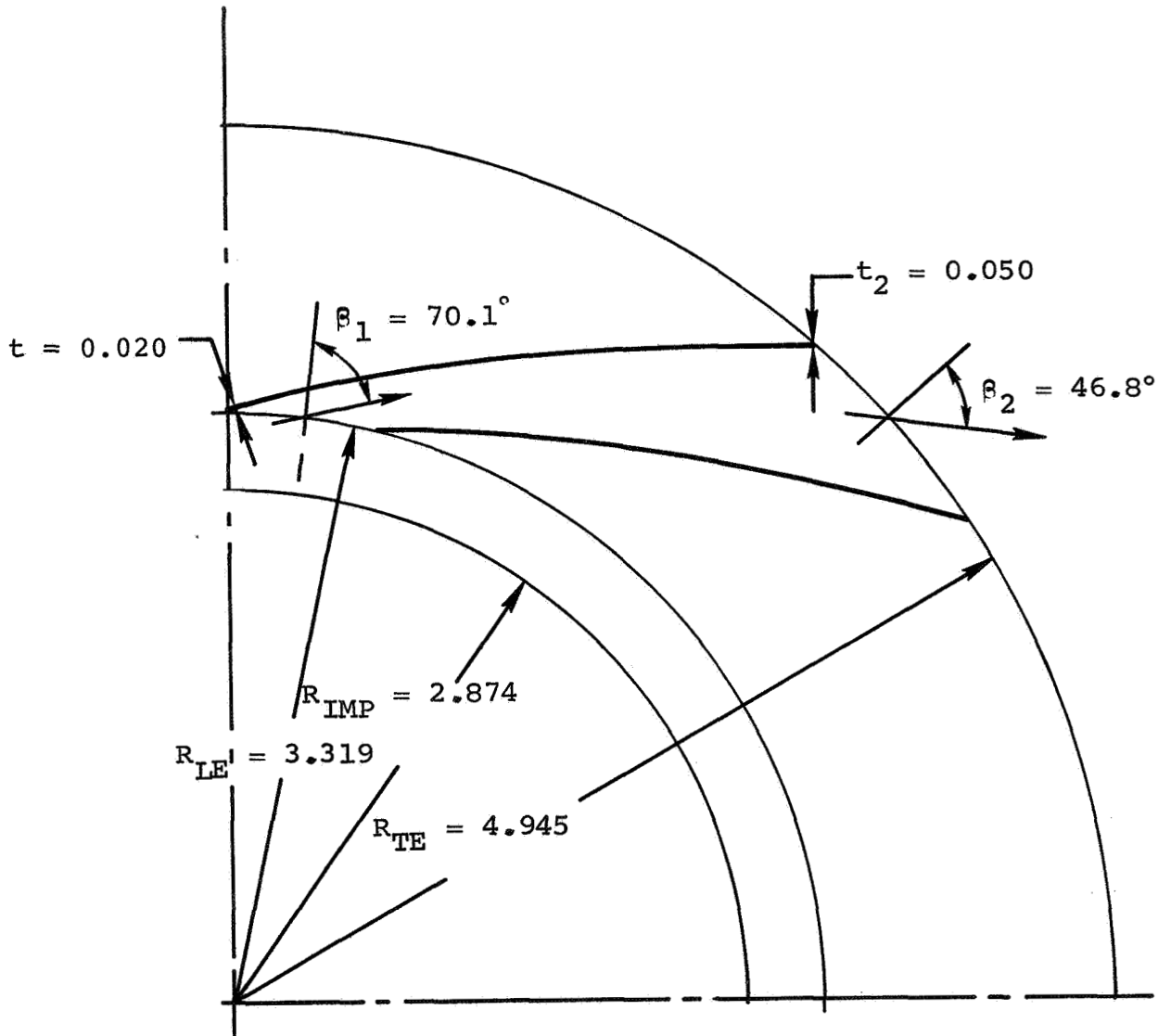
Figure 23. — Conventional diffuser design

Performance levels shown here will meet the basic requirements of the NASA Advanced Research Compressor Program.

Some boundary-layer control techniques were considered for adaptation to this diffuser configuration. One pseudo boundary-layer technique, recently evaluated experimentally at AiResearch, was the use of a slotted vane at the diffuser inlet. Slots in both sides of the vane surface along the hub and shroud walls permitted a portion of the boundary layer flow to pass from the pressure surface to the suction surface relieving the loading in the inlet region. The overall effect was that the operating range increased by 20 percent with a penalty of one point in efficiency at design conditions which, under certain circumstances, would be desirable. It was felt that boundary layer suction along one or both walls might have a similar effect with only a minor change in design performance. However, further analysis was required to assess the potential of boundary-layer control on vane-type diffusers.

Pipe Diffusers: A pipe diffuser is made up of a series of drilled passages where the flow is essentially axisymmetric. The passages are drilled on an oblique angle which, if extended, would intersect the impeller tangent at the exit radius. A sketch of the design features of a pipe diffuser is presented in figure 24. Data from references 3 and 4 were used as the basis for this design.

There were four sections in this pipe diffuser design: (1) the entrance sections that form elliptical passages in the confining ring which serve to accommodate the highly three-dimensional nature of the flow existing from the impeller, (2) a short, constant-area throat section to permit some flow stabilization before diffusion, (3) an initial diffusion section where the flow diverges at a conical angle of 3 degrees, and (4) a section where the conical angle is increased to 6 degrees and further diffusion occurs. A brief analysis showed this two-step diffusion process to be slightly more efficient than conical diffusion at a fixed angle.

A total of 45 separate pipe diffusers was required in this design as a result of the narrow width of the impeller discharge passage. With this many passages arranged circumferentially in a relatively small circle, there were some restrictions on how small to make the vaneless space. Pipe diffuser tests (refs 3 and 4) with very short vaneless space regions have demonstrated satisfactory operation under high subsonic or slightly supersonic inlet conditions. However, because of the large number of passages, the present design required a relatively large vaneless space due to physical limitations imposed by the geometry of the section. Diffuser performance was somewhat impaired by the vaneless space because of the inlet blockage that resulted from

NOTES:

1. VIEW IS FROM IMPELLER BACK FACE
2. NUMBER OF PIPES = 45
3. EFFECTIVE AREA RATIO = 1.97
4. STATIC PRESSURE RECOVERY = 0.678

INITIAL DIFFUSION, $\phi = 3°$

FINAL DIFFUSION, $\phi = 6°$

THROAT $L/d^* = 0.50$

$d^* = 0.1874$

ϕ

IMP RAD = 2.874

L.E. RAD = 3.25

T.E. RAD = 4.28
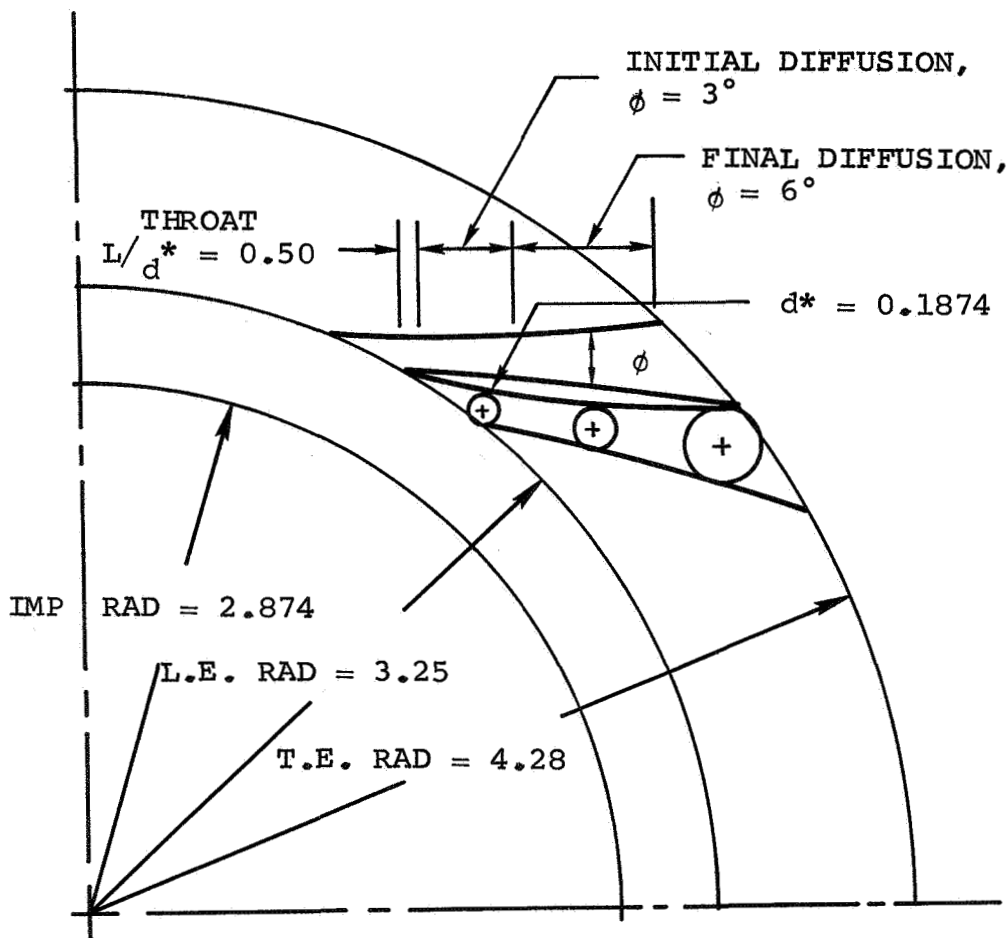
Figure 24. - Preliminary pipe diffuser design

36

the boundary layer build-up in this region. The effect of inlet blockage on conical diffuser performance is presented in figure 25. This indicated that the effective area ratio for diffusion and hence, pressure recovery, was significantly reduced as a result of inlet blockage. These calculations were obtained from the AiResearch computer program which employs Truckenbrodt's (ref 5) method (modified for compressible flow) for defining the boundary layer along the wall and the subsequent separation plane. This program has been thoroughly checked with existing experimental data from various sources, and has shown excellent agreement as to the prediction of boundary-layer separation and growth.

Computer performance for the pipe diffuser design is presented in figure 26. These calculations were made for an inlet blockage of 0.05, a reasonable value for the vaneless space provided by this design. Results indicated that the pipe diffuser would only diffuse to an exit Mach number of 0.325 before separation, thus limiting the design pressure ratio to about 5.93:1 after dumping the flow at the diffuser exit. Since the desired pressure ratio at design was 6:1, the pipe diffuser was marginal as far as making the program goal without some form of boundary-layer control to increase diffuser effectiveness. One form of boundary-layer control that could have been employed was the use of a vortex generator along the wall upstream of the diffuser inlet. The vortex motion along the wall would tend to retard boundary-layer separation to some extent, and as such should permit higher diffusion area ratios. Kenny (ref 3) stated that there was some evidence that the asymmetry of the entering flow to a pipe diffuser inherently contained some vortex motion, which could result in increased boundary-layer stability. If true, the performance estimates were somewhat conservative. However, there was no way to theoretically evaluate the effect of vortex flow on the performance of this particular design.

Cascade Vane Diffuser: The cascade diffuser design utilized two to three radial cascade blade rows to diffuse and straighten the airflow. Airfoil shapes were NACA 65-series transformed from the axial to the radial plane. Cascade diffuser tests at AiResearch have provided data on the loss and turning characteristics of the various sections. Loss trends were similar to those of the NACA two-dimensional cascade test data, but the levels had to be increased by a factor of 6.0 to 8.0 to account for aspect ratio and three-dimensional, turbulent, inlet flow-field effects. Turning characteristics generally indicated some overturning due to the three-dimensionality of the flow. Each of these effects was accounted for in the preliminary design.

The final design was comprised of a tandem configuration as shown schematically in figure 27. The first blade row utilized an NACA 65-4(A10)06 and the second row an NACA 65-8(A10)06.
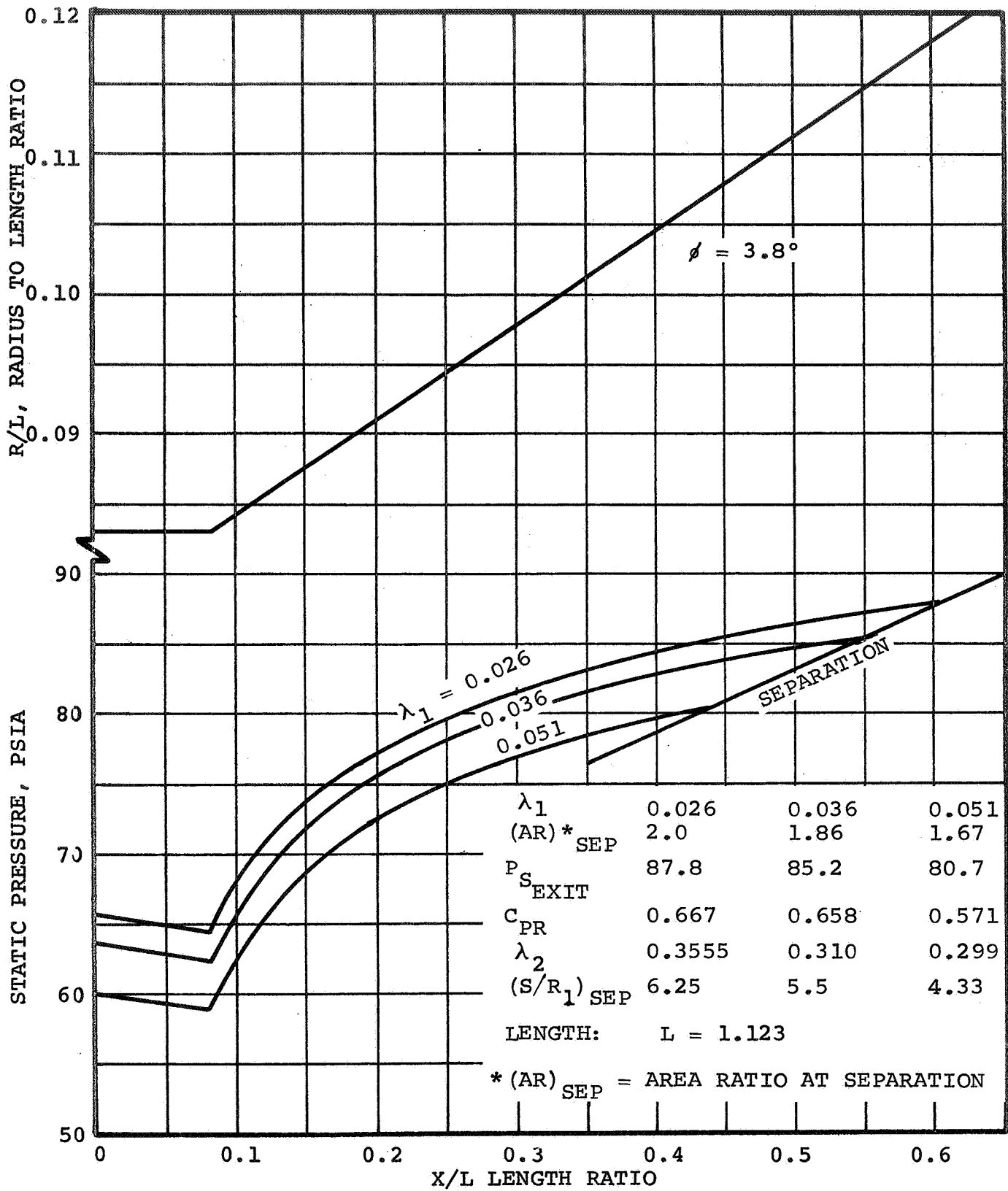
Figure 25. - Effect of inlet blockage on pipe diffuser performance

38
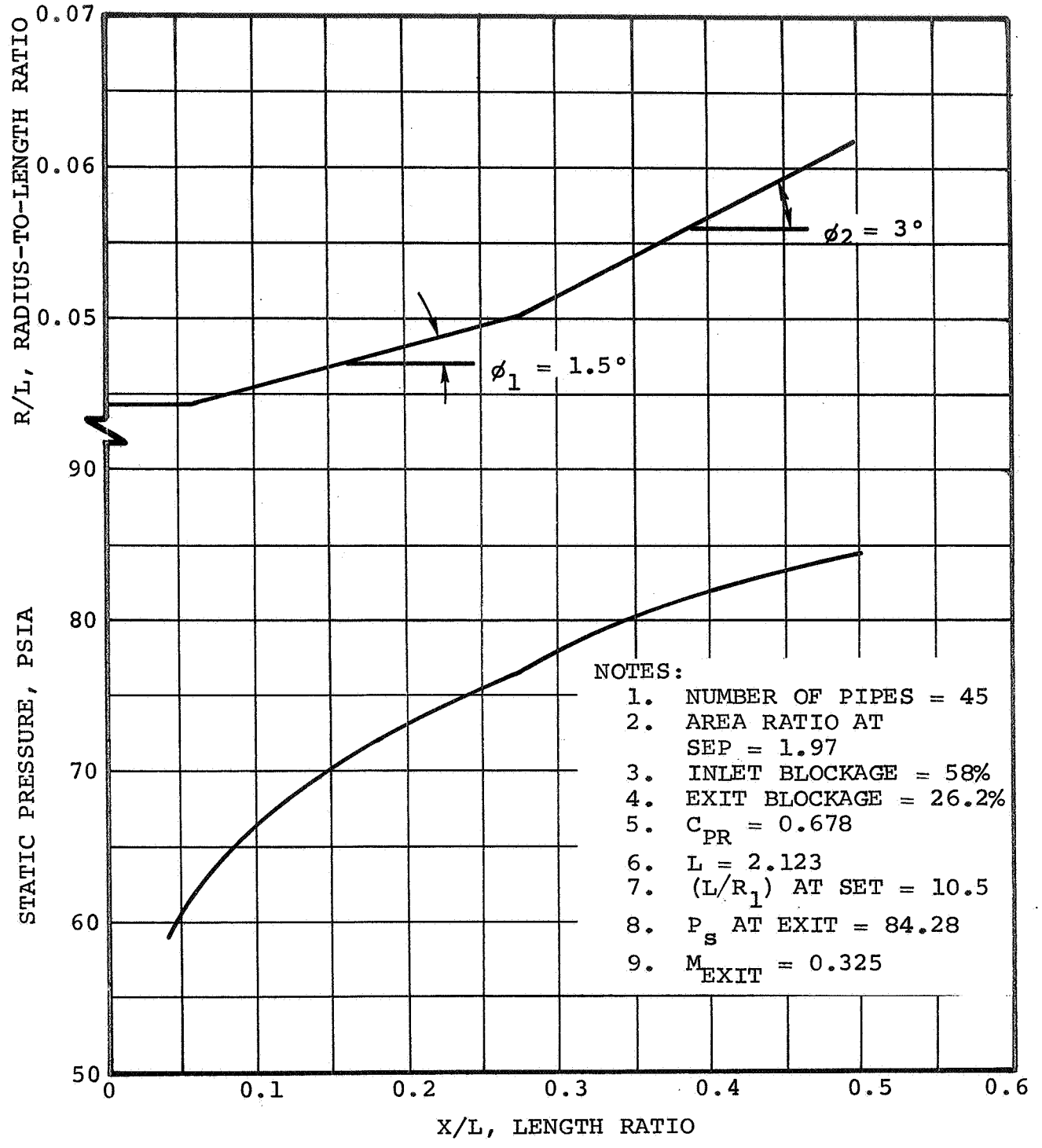
Figure 26. - Preliminary pipe diffuser design

4.483 RADIUS

3.822 RADIUS

3.449 RADIUS
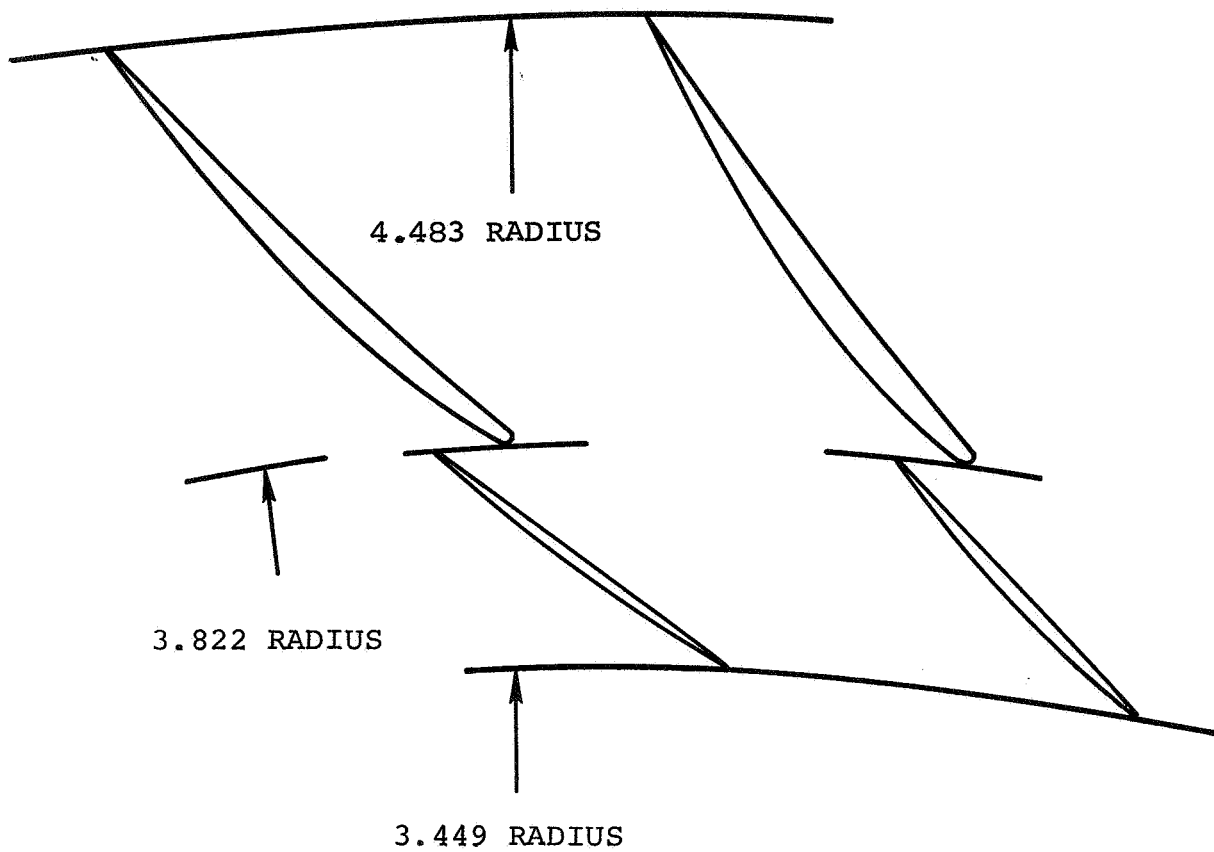
Figure 27. - Cascade diffuser vane alignment schematic

Performance characteristics for each airfoil shape and a friction
coefficient for the vaneless space preceding and following the
cascade diffuser were input data to a computer program that cal-
culated the flow conditions at various points in the radial flow
path. A meridional view of the final flow path is shown in
figure 28.

The total diffuser loss is given by

$$\Delta \eta_T = \Delta \eta_{(vaneless\ space)_1} + \Delta \eta_{cascade} + \Delta \eta_{(vaneless\ space)_2} \qquad (1)$$

Each efficiency decrement is a function of Mach number, thereby
necessitating an optimization of the vaned-diffuser leading-edge
radius ratio (R/R_T). The minimum total diffuser loss was estab-
lished at a radius ratio of 1.16.

Diffuser Comparison and Selection

A preliminary design study was conducted to examine the per-
formance of three candidate diffuser geometries. The candidate
configurations were: (1) a conventional vane diffuser, (2) a
pipe diffuser, and (3) a cascade vane diffuser. All diffusers
were assumed to have the same inlet conditions. Overall effi-
ciencies were based on diffuser exit total conditions which
resulted from geometries having an average exit Mach number of
0.2. Computed total pressures at each station were then used to
define local compressor efficiency employing the following rela-
tion:

$$\eta_c = \frac{(P_{t_2}/P_{t_1})^{\frac{\gamma-1}{\gamma}} - 1}{\Delta T_t/T_{t1}} \qquad (2)$$

where:

Subscript t = Total pressure or temperature

Subscript 1 = Compressor inlet

Subscript 2 = Local conditions

ΔT_t = Temperature differential between compressor
inlet and outlet

Overall compressor performance for the individual diffuser config-
uration is summarized in table II.

41

NOTES:
1. NUMBER OF TANDEM BLADES = 22
2. FIRST BLADE ROW IS NACA 65-4 (A10)06
3. SECOND BLADE ROW IS NACA 65-8(A10)06

STATION	RADIUS	TOTAL PRESSURE RATIO	MACH NUMBER
6	6.783	6.090	0.197
5	4.483	6.187	0.334
4	3.822	6.290	0.546
3	3.449	6.530	0.847
2	2.874	6.807	1.070

COLLECTOR

DIFFUSER ROW 2

DIFFUSER ROW 1

VANELESS SPACE

RADIAL IMPELLER
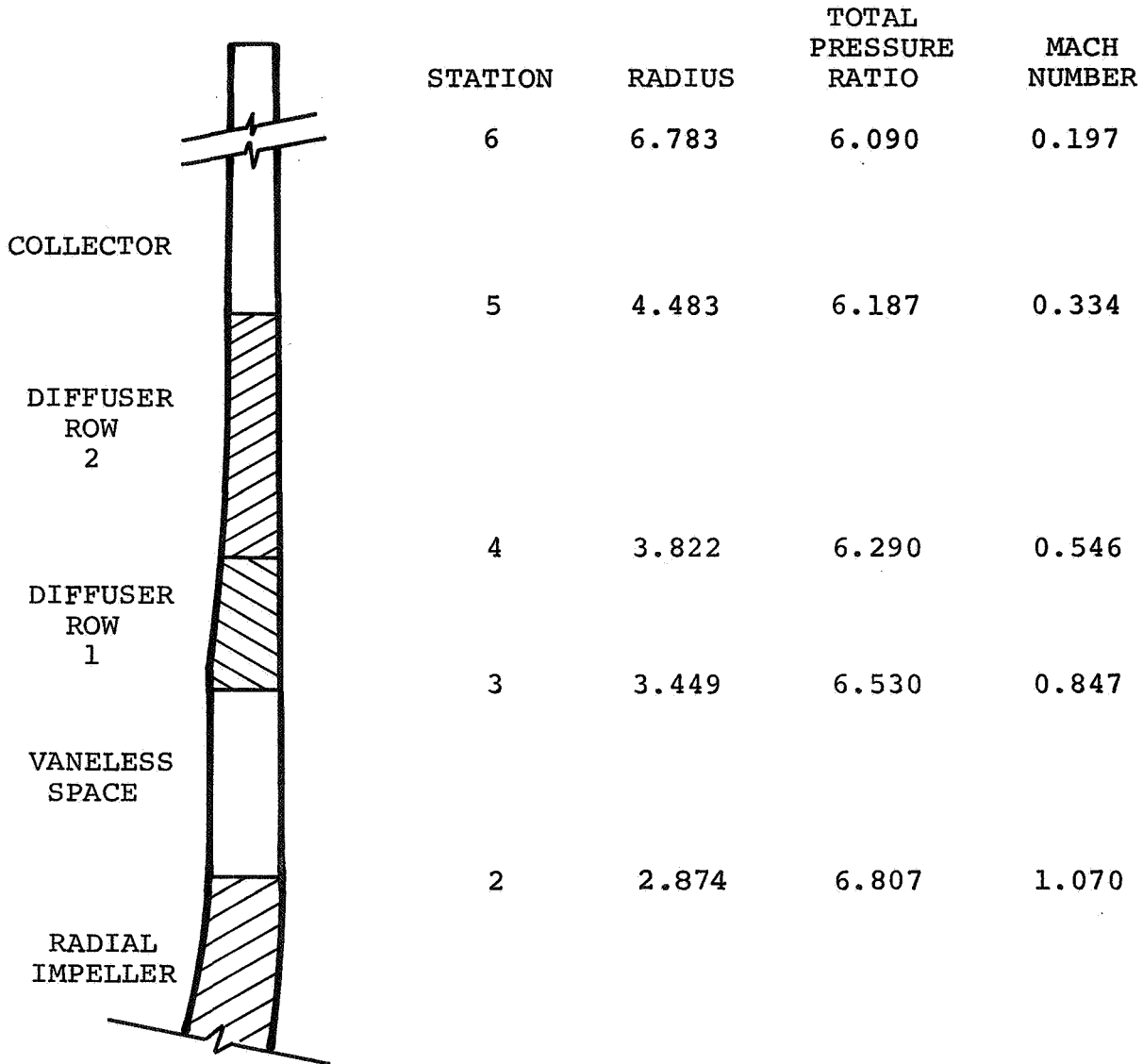
Figure 28. - Cascade tandem diffuser design

A performance trade-off between the vaneless space and vaned section diffusion indicated that an inlet Mach number of 0.85 was optimum for the conventional vane design. Vaneless space performance was obtained from a one-dimensional, compressible flow program based on the analysis of J.D. Stanitz (ref. 6) and using friction factors derived from AiResearch data. Vaned section performance was computed from a two-dimensional analysis of the boundary layer based on Truckenbrodt's analysis as modified by Scholz (ref. 7). The latter modification accounted for both compressibility and arbitrary wall temperature distribution. This computer program has demonstrated excellent agreement with existing experimental data for both internal and external flows. Calculated performance of the conventional vane diffuser (table II) was sufficient to meet the overall goals of the program (pressure ratio = 6:1 and compressor efficiency ~ 80 percent).

Pipe diffuser performance was determined by using the same computer programs employed in the analysis of the conventional vane design. However, an option for handling two-dimensional, axisymmetric flow was employed with the boundary layer program. In the case of the pipe diffuser, no attempt was made to optimize Mach number at the inlet of the pipe throat section. Previous experimental evidence by Kenny (ref. 3) indicates that the pipe diffuser operates quite effectively with a small vaneless space. Therefore, reasonable fabrication considerations were used to determine the pipe diffuser inlet location. A Mach number to the pipe diffuser inlet of 0.88 was found to allow sufficient manufacturing tolerances at the entrance section.

Several downstream section designs were then evaluated using the boundary layer program. Calculations showed that diffusing the flow to the area where separation occurs, and then dumping, resulted in the best total pressure recovery. In turn, this resulted in a downstream Mach number after dump of slightly less than Mach 0.2.

Cutting off the diffuser before the separation point increased basic diffuser performance, but the overall performance loss associated with dumping at higher exit Mach number resulted in a lower total pressure recovery. Performance values reported in table II are for the best pipe diffuser configuration investigated. The results show that the pipe diffuser would not meet the basic performance goals of the program.

Experimental evaluation of diffuser performance indicated that a tailpipe or constant-area extension at the diffuser exit would increase the overall total pressure recovery of both conical and two-dimensional diffusers. Therefore, a pipe diffuser with a constant area extension was evaluated using the boundary layer program. The constant area extension permits diffusion to a larger area ratio without flow separation. This has been observed experimentally and is predicted analytically by the

TABLE II. - DIFFUSER PERFORMANCE COMPARISON

Station	Conventional Vane			Pipe Diffuser			Cascade Vane		
	Radius	P_{T2}/P_{T1}	η	Radius	P_{T2}/P_{T1}	η	Radius	P_{T2}/P_{T2}	η
Rotor Exit	2.874	6.81	0.873	2.874	6.81	0.873	2.874	6.81	0.873
Vaneless Space	3.319	6.52	0.848	3.25	6.55	0.851	3.319	6.52	0.848
Diffuser (1)	4.95	6.01	0.801	4.23 (4.56)	6.00 (6.08)	0.800 (0.807)	3.678	6.29	0.827
(2)							4.314	6.19	0.817
Exit at M ~ 0.2	4.95	6.00	0.800	4.23 (4.56)	5.93 (6.00)	0.793 (0.800)	6.527*	6.09	0.808

*Vaneless space diffusion to M = 0.2
( )Pipe diffuser with constant area extension

44

boundary layer computer program. The configuration evaluated and the resulting static pressure profile are shown in figure 29. Calculation of the overall compressor performance downstream of dump indicated a recovery essentially equivalent to that obtained with the conventional vane design. As a result, considerations other than efficiency were necessary to determine the selection between a conventional vane or a pipe diffuser configuration.

Cascade vane diffuser performance presented on table II was computed from empirical loss and turning correlations based on experimental radial cascade data. Basic loss characteristics, associated with two-dimensional NACA 65 Series cascades, were computed from D-factors illustrated in ref. 8. These losses were then increased by empirically derived factors of 6.0 to 8.0 to account for aspect ratio and three-dimensional inlet flow field effects. An optimization of the cascade inlet Mach number indicated overall compressor performance peaks of approximately 0.85. Thus, the resulting vaneless space diffusion was identical to that obtained for the conventional vane diffuser. Both three- and two-row cascades were examined for diffusing to the required Mach 0.2 exit condition. It was found that a two-row cascade followed by an additional vaneless space resulted in slightly higher pressure recovery than a three-row cascade. The large exit radius for this design was a result of the vaneless space diffusion from Mach 0.334 to 0.2. Computed compressor performance with a cascade diffuser was 0.8 points higher than for the previous two designs. Despite the fact that cascade vane performance was computed from empirical correlations and performance for other diffusers were determined analytically, the incremental difference appeared quite realistic based on previous AiResearch experience.

Recommended Diffuser Configuration

The conventional vane diffuser was relatively easy and inexpensive to fabricate. It was possible to design them for a fairly wide operating range, although some trade-off was necessary between peak efficiency and range. Despite the degree of sophistication employed in the overall compressor design, several vane orientations were evaluated experimentally to obtain the desired overall compressor characteristics. The basic vane configuration was not changed, only the incidence angle was varied. However, application of a conventional vane diffuser in the initial compressor design served a more basic purpose. Since this was a research compressor package program, several new concepts were eventually investigated in an attempt to improve overall performance. Therefore, incorporation of a conventional vane design at that time served as a convenient foundation for comparing performance gains associated with more sophisticated systems.

The principal advantage of pipe diffusers was that they were relatively inexpensive and easy to fabricate. Based on
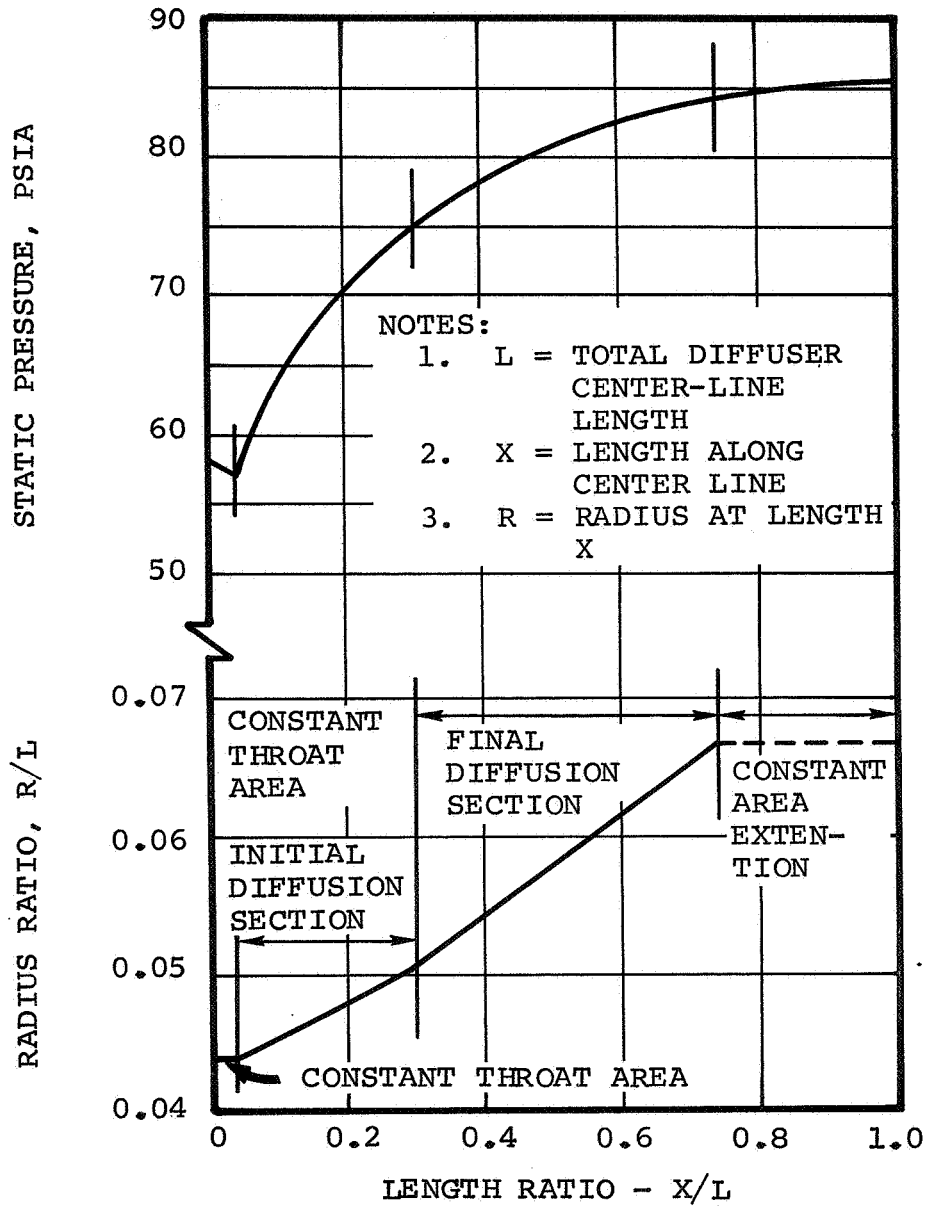
Figure 29. - Pipe diffuser pressure recovery with constant
area extension.

46

the previous performance analysis, a pipe diffuser could possibly be designed that would meet the performance goals of the program. However, the experimental results of Kenny (ref. 3) indicate a fairly limited operating range. A comparison of the operating range characteristics of conventional vane (AiResearch) and pipe (UACL) diffusers is presented in figure 30. From this figure, it is evident that for a 5:1 pressure ratio compressor, a vane diffuser can have a much wider range between choke and surge than a pipe diffuser.

The cascade diffuser appeared to offer certain performance advantages over the two preceding diffuser configurations. Previous AiResearch experience has not only shown higher peak efficiencies for cascade vane diffusers, but also a somewhat wider operating range when compared with a conventional vane configuration. However, to obtain high efficiencies, three-dimensional blade shapes are required that are expensive to fabricate. They also require extensive cut-and-try testing to arrive at the proper orientation of the individual blade rows. This means the initial design must be fabricated with rotatable blade sections. Therefore, development of a cascade vane diffuser is quite time-consuming and expensive. The current program schedule does not allow impeller mapping to determine orientation of blade rows.

The cascade vane diffuser was selected for detailed aerodynamic design based on the potential performance advantage shown in table II. This design incorporated two blade rows of fixed stagger with the incidence defined by analytical methods, but tempered by related experimental information. Caution was expressed concerning the blade settings in the initial design, based on past experience with similar diffuser configurations.

Boundary-Layer Control

While it was not possible to perform any detailed boundary layer analysis until the design of the final configuration had progressed sufficiently, the following items were contemplated during the preliminary design phase:

(a) Employing shroud suction in the impeller

(b) Withdrawing boundary layer bleed by venting to atmosphere, requiring no additional pumps

(c) Placing slots and/or porous walls at locations along the shroud. These openings would dump into a collector which would then exhaust through one or more calibrated ducts to allow measurement of boundary-layer bleed flow. If necessary, provision was to be made to ensure that no torque was produced by the exhausting boundary layer flow. The amount of
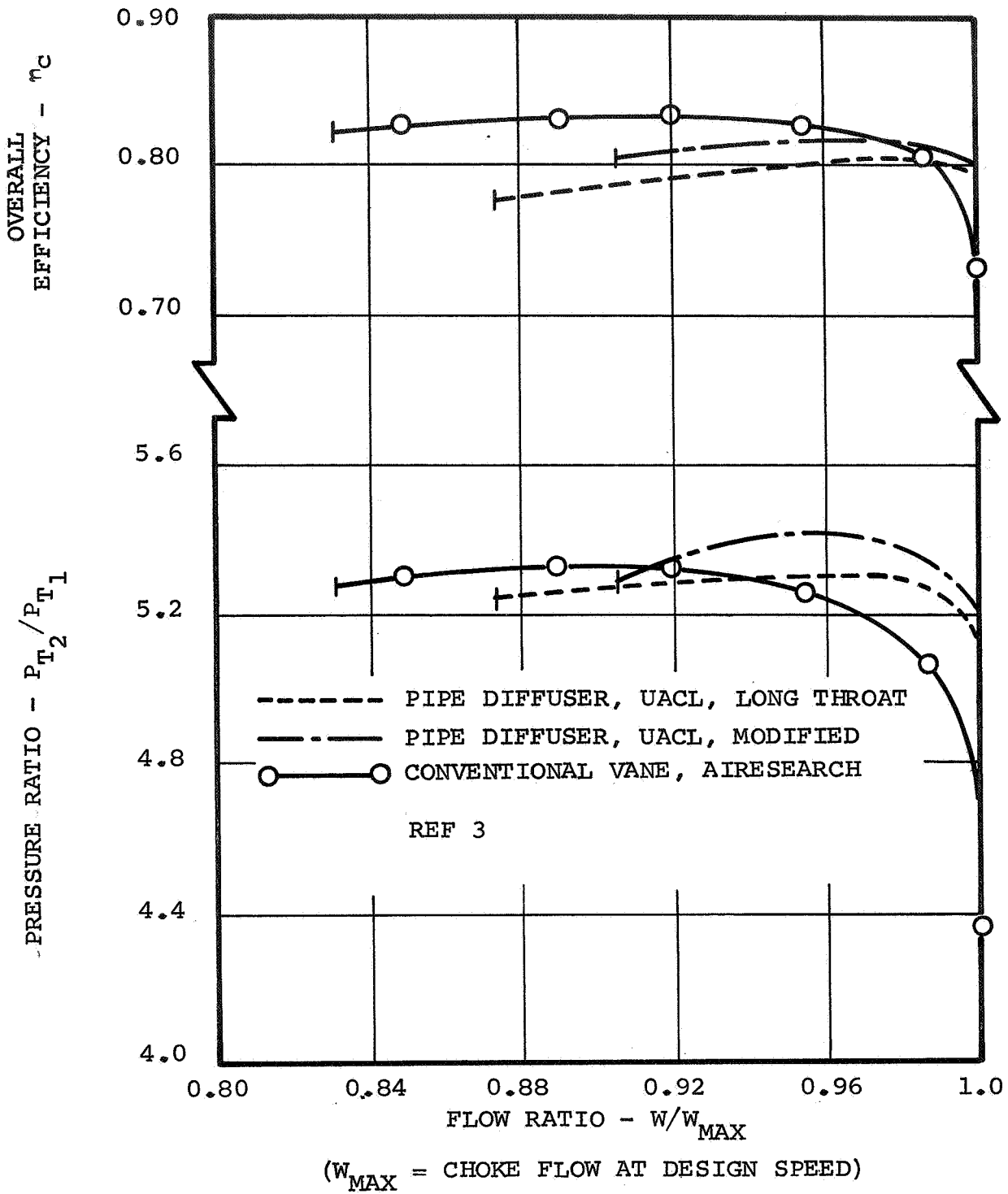
Figure 30. - Operating range characteristics of pipe
diffusers in single-stage compressors.

boundary-layer bleed could be controlled by throttles in the ducts or by changing duct size

(d)   No impeller blade boundary-layer suction was considered since the thickness of blade required would compromise the efficiency of the basic design

As the final design evolved, adjustments were made as necessary to ensure a practical, flexible unit.

DETAILED AERODYNAMIC DESIGN

This section includes the detailed aerodynamic design of the tandem impeller, cascade vane diffuser, and detailed analysis for boundary layer control. The tandem impeller and cascade vane diffuser were selected in Preliminary Design because of indicated performance potential.

The tandem impeller consists of two main parts, a separately bladed inducer followed by a centrifugal impeller section. Standard axial flow rotor design practice was employed in the design of the inducer section which differs considerably from centrifugal design procedures. Therefore, the design of each section of the tandem impeller is presented separately. Since in Preliminary Design the speed and geometry was restricted to being the same as the conventional,further optimization of the tandem impeller was made to take full advantage of using axial flow rotor design practice and to alleviate the inducer blade stress problem.

The cascade vane diffuser consists of two rows of vane diffusers and sufficient vane loss upstream and downstream the vane rows to reduce inlet Mach to about 0.85 and the outlet Mach number to 0.2.

Also a cursory evaluation of blade loading for a cut back rotor was made and presented.

Optimization of Tandem Impeller Design Point

In Preliminary Design, the tandem impeller was compared with the conventional centrifugal design under conditions where the inlet tip relative Mach number for both designs was restricted to a value of 1.2. This Mach number restriction is applicable to a conventional centrifugal configuration where the impeller blades are normally not tailored to handle strong inlet shocks. However, an axial flow rotor can be designed to operate quite effectively at higher Mach numbers by design techniques that attempt to minimize inlet shock loss. Thus, in order to take full advantage of using axial flow design practice in the inducer of the tandem impeller configuration, the limiting tip Mach number was increased to the range of 1.3 to 1.35. This limitation was imposed because above this range the shock strength can become strong enough to separate the boundary layer on the rotor suction surface in the shock-boundary interaction region. With a higher inlet Mach number limitation for the tandem impeller configuration, it is expected that the efficiency curve shown in figure 1 will peak closer to 80,000 rpm when corrected for shock losses.

In an attempt to utilize past experience in the design of the inducer, some design parameters were either scaled or taken directly from a NASA rotor built by General Electric. This rotor, designated NASA Rotor 1B (R1B) was found to operate quite satisfactorily at high inlet relative Mach numbers and to perform at high efficiency with good range characteristics (ref. 1). The inlet hub radius ratio of the inducer for this program was made the same as R1B. Thus the hub/tip ratio was increased from the 0.42 used in Preliminary Design to 0.5. This change also reduces blade lean at the inducer exit. The decreased lean in the inducer not only lowers the stress levels in the blade, but also assists in matching the inducer exit and impeller inlet blade angles.

Other information required as input to the computer program is as follows. The blade aspect ratio of R1B was not retained, since comparatively greater chord lengths were desired for manufacturing practicality and increased Reynold's number. A design aspect ratio of 1.29 was selected based on AiResearch design experience in this operating range. Chord length for this aspect ratio was 0.625 in. with only a small variation from hub to tip across the rotor. Tip solidity for R1B was approximately 1.3, which when applied to the tandem inducer design, resulted in a total of 24 blades for the inducer section. A preliminary check of the impeller inlet configuration indicated that 24 blades were also satisfactory for the centrifugal impeller. Not all the blade thicknesses of R1B could be scaled for the inducer design. The maximum thickness/chord ratio was used directly, but when scaled, the leading and trailing edge thicknesses were too small to fabricate. Therefore, the minimum blade leading and trailing edge thicknesses were set at 0.006 in., a reasonable value for fabrication purposes. The actual blade selection for the inducer section, including camber, stagger, supersonic camber ratio, and maximum thickness location, was not scaled from R1B, but resulted from a detailed analysis of the flow field within the blade passages.

Design vector diagrams for the revised operating speed and geometry of the tandem impeller configuration are shown in figure 31. Velocities reported were obtained from the simplified, one-dimensional preliminary design program used in Preliminary Design.

Inducer Design

The purpose of the inducer is to bring the air flow into the tandem impeller with a minimum overall loss. With this goal in mind, the Mach number into the centrifugal portion of the tandem impeller was limited to 0.92 so that total impeller losses would not be excessive by having a second set of shock losses. Since meridional contour has been found to have a significant effect

INDUCER INLET

SHROUD

$M_{S_R} = 1.291$

65.4°

583

1402

1275

MEAN

$M_{M_R} = 1.129$

63.3°

553

1231

1100

HUB

$M_{H_R} = 0.695$

50.3

528

828

638

IMPELLER EXIT

$\beta_{FL} = 37.2°$

$\beta_{BL} = 30°$

$M_{2_{AB}} = 1.131$

26.1°

1522

670

841

508

1367

1875
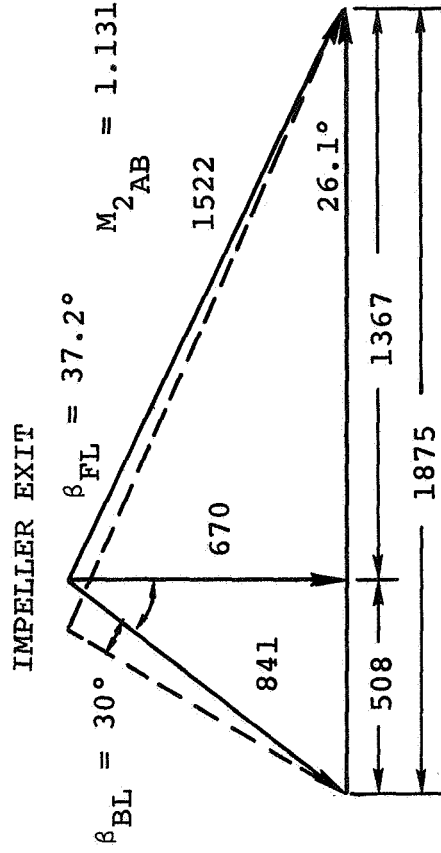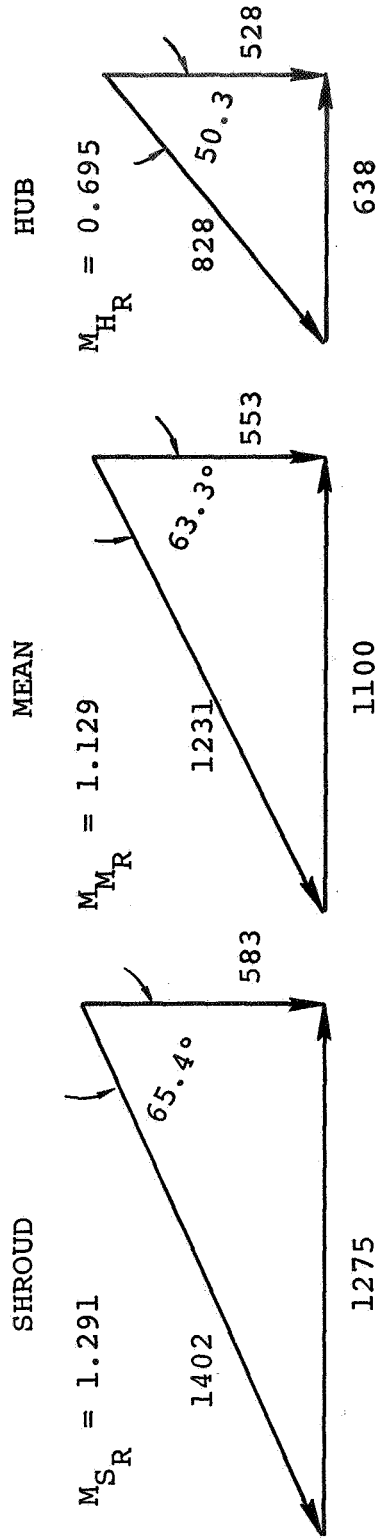
Figure 31. Tandem impeller design velocity vector diagram.

53

on the Mach number within a blade row, the design of the inducer will be divided into three sections: (1) the selection of the meridional contour which gives the highest efficiency consistent with the 0.92 limit on exit Mach number, (2) computation of inlet and outlet vector diagram, and (3) the selection of blade profiles to produce these vector diagrams.

Meridional Contour Selection: Four meridional contours typical of those considered for this application are shown in figure 32. In each case considered, the hub and shroud contour was varied. The different meridional contours analyzed are summarized in table III. Calculations were made with a computer program which assumes radial equilibrium and steady axisymmetric flow across the blade row. Both shock and blade profile are for simple airfoil sections only; thus, the absolute efficiency levels presented on table III may be in error. However, the relative values should serve as an adequate basis for comparison of the different configurations.

Results of the meridional contour analysis are presented in figure 33, where adiabatic efficiency is plotted against peak exit Mach number. Initially, three configurations were selected for evaluation. The first (figure 32a) had conical ramps on both the hub and shroud walls. This required that the centrifugal impeller shroud be split both circumferentially and axially in the region of the minimum tip diameter for assembly. This case had the highest potential performance within the exit Mach number restriction imposed earlier. However, the split shroud would have resulted in some mismatch between mating parts and subsequent aerodynamic losses due to the mismatch. It was felt the potential problems connected with this design would more than offset the possible performance gain associated with the double-conical ramp design.

The second configuration (figure 32b) had a conical ramp in the hub section and a shroud that sloped inward initially, but turned back to zero slope at the inducer exit. This configuration delivered relatively good performance, but the slope change in the tip section tended to increase the tip Mach number to prohibitive values before a favorable performance gain was demonstrated.

The third configuration shown in figure 32c had a cylindrical shroud section with a relatively steep conical ramp in the hub region. It showed a small performance gain over Case 14, but had a slightly higher exit relative Mach number in the tip region. The basic simplicity of this design, along with its relatively good performance characteristics, resulted in the selection of this meridional profile for the final tandem impeller configuration.

54
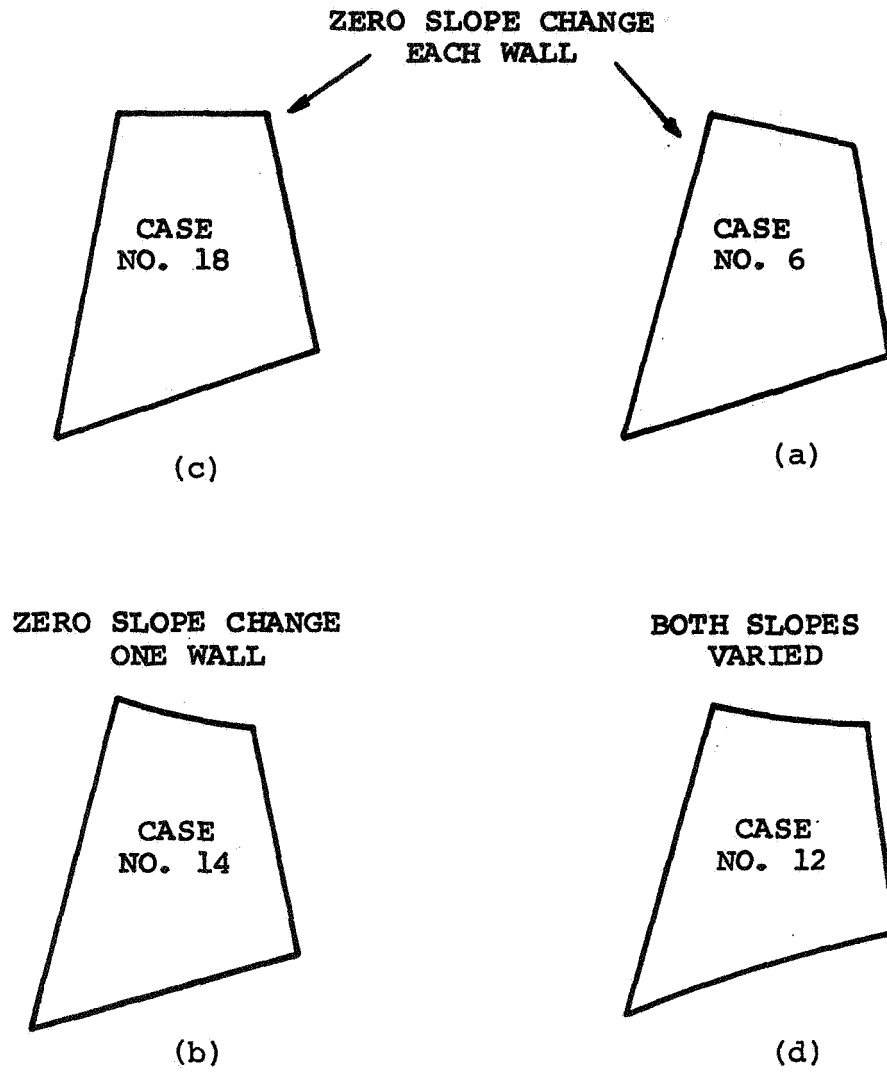
Figure 32. - Candidate inducer shapes.

TABLE III. BLADE PROFILE PERFORMANCE COMPARISON

| Case No.	M_1 Range S	M_1 Range H	Inlet Radii S	Inlet Radii H	Outlet Radii S	Outlet Radii H	Inlet Slopes, deg S	Inlet Slopes, deg H	Outlet Slopes, deg S	Outlet Slopes, deg H	Inlet Curvature S	Inlet Curvature H	Outlet Curvature S	Outlet Curvature H	M_2 Range Relative S	M_2 Range Relative H	v_{M_2}/v_{M_1} Range S	v_{M_2}/v_{M_1} Range H	N_{ad}	Remarks
1	1.317	0.762	1.825	0.9125	1.825	1.12	0.0	20.0	0.0	20.0	0.0	0.0	0.0	0.0	0.87	0.5	0.83	0.927	0.9164	
2	1.322	0.759	1.825	0.9125	1.825	1.14	0.0	21.9	0.0	21.9	0.0	0.0	0.0	0.0	0.879	0.514	0.843	0.952	0.9188	
3	1.319	0.759	1.825	0.9125	1.825	1.14	0.0	21.9	0.0	21.9	0.0	0.0	0.0	0.0	0.867	0.551	0.820	1.035	0.9178	Same as No. 2 except opened up downstream station
4	1.314	0.760	1.825	0.9125	1.825	1.14	0.0	21.9	0.0	21.9	0.0	0.0	0.0	0.0	0.889	0.514	0.818	0.987	0.9188	Same as No. 3 except design P_R = Const
5	1.311	0.760	1.825	0.9125	1.825	1.14	0.0	21.9	0.0	21.9	0.0	0.0	0.0	0.0	0.900	0.519	0.797	0.958	0.9184	Same as No. 3 except design P_R maximum at pitch; minimum at walls
6	1.307	0.743	1.825	0.9125	1.775	1.14	-8.0	21.9	-8.0	21.9	0.0	0.0	0.0	0.0	0.891	0.613	0.982	1.227	0.9295	Scaled R1B (no curvatures)
7	1.307	0.743	1.825	0.9125	1.785	1.01	-5.75	9.6	-5.75	9.6	0.0	0.0	0.0	0.0	0.842	0.451	0.876	0.945	0.9141	
8	1.291	0.755	1.825	0.9125	1.785	1.01	-5.75	9.6	-5.75	9.6	0.0	0.0	0.0	0.0	0.840	0.449	0.881	0.942	0.9142	Scaled R1B; match P_R to test data
9	1.315	0.738	1.825	0.9125	1.775	1.14	-13.5	15.0	0.0	30.0	0.0	0.0	0.416	0.25	0.988	0.497	1.182	0.976	0.9327	
10	1.316	0.732	1.825	0.9125	1.775	1.14	-13.5	15.0	0.0	30.0	0.25	0.114	0.416	0.25	0.987	0.498	1.174	0.996	0.9329	Same as No. 9 except inlet curvature added
11	1.319	0.738	1.825	0.9125	1.782	1.145	-10.0	18.0	0.0	30.0	0.0	0.0	0.416	0.25	0.975	0.499	1.132	0.977	0.9316	
12	1.325	0.740	1.825	0.9125	1.797	1.145	-7.6	18.0	0.0	30.0	0.0	0.0	0.25	0.20	0.947	0.489	1.036	0.945	0.9280	
13	1.324	0.738	1.825	0.9125	1.797	1.145	-7.6	21.6	0.0	21.6	0.0	0.0	0.25	0.0	0.923	0.531	0.975	1.051	0.9265	
14	1.323	0.746	1.825	0.9125	1.810	1.145	-5.0	21.6	0.0	21.6	0.0	0.0	0.156	0.0	0.900	0.525	0.919	1.012	0.9234	
15	1.334	0.739	1.825	0.9125	1.810	1.20	-5.0	26.2	0.0	26.2	0.0	0.0	0.156	0.0	0.957	0.577	1.007	1.093	0.9312	
16	1.322	0.740	1.825	0.9125	1.797	1.20	-5.0	26.2	-5.0	26.2	0.0	0.0	0.0	0.0	0.964	0.588	1.117	1.039	0.9351	
17	1.330	0.750	1.825	0.9125	1.825	1.20	0.0	26.2	0.0	26.2	0.0	0.0	0.0	0.0	0.934	0.565	0.945	1.030	0.9281	
18	1.323	0.757	1.825	0.9125	1.825	1.175	0.0	24.0	0.0	24.0	0.0	0.0	0.0	0.0	0.919	0.539	0.939	0.979	0.9251	
19	1.321	0.754	1.825	0.9125	1.825	1.160	0.0	23.0	0.0	23.0	0.0	0.0	0.0	0.0	0.912	0.520	0.917	0.962	0.9233	

S = Shroud
H = Hub
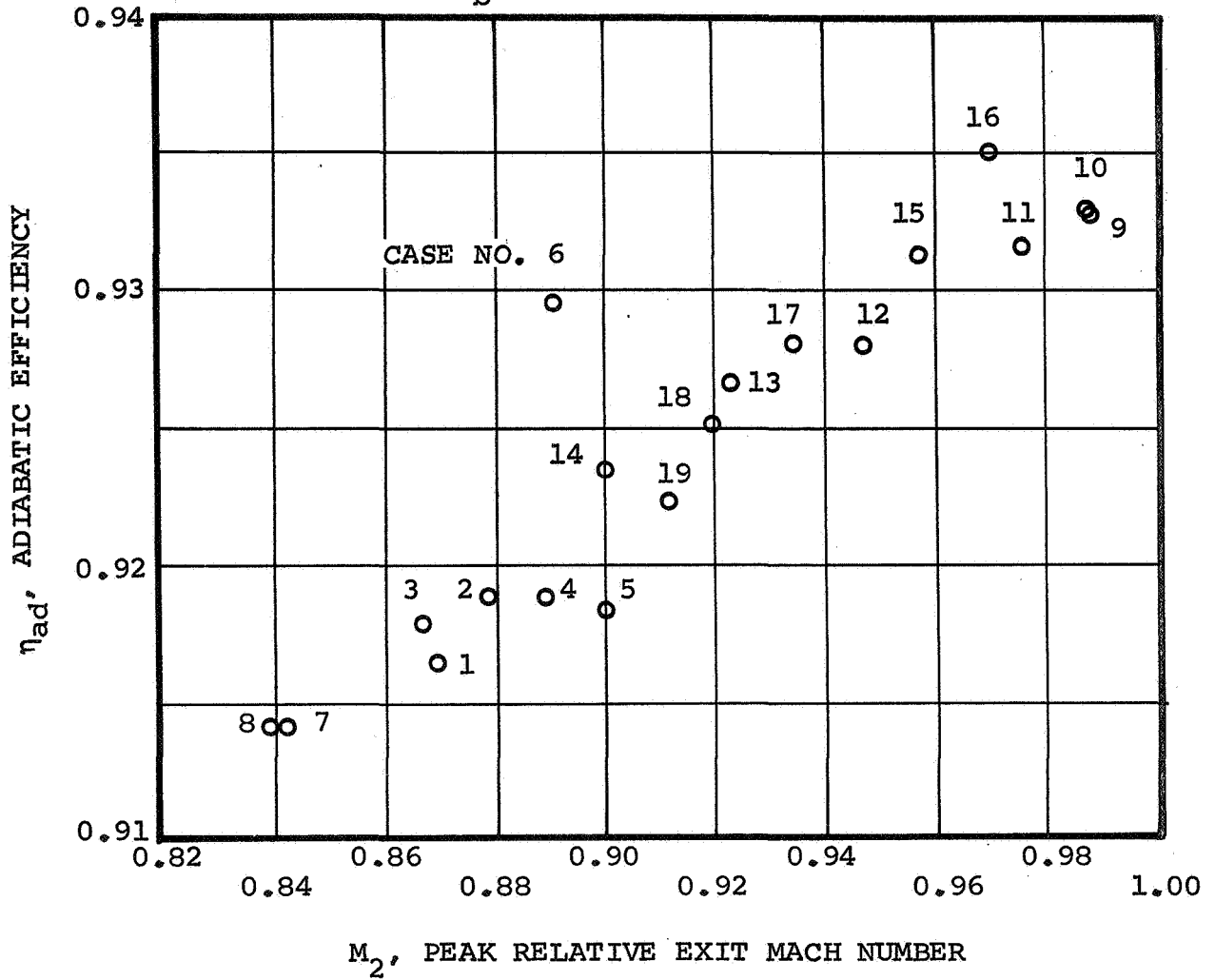
Figure 33. - Inducer rotor performance, peak relative
exit Mach number versus adiabatic efficiency.

Design of an axial flow compressor stage normally requires a certain amount of diffusion of the meridional velocity across the rotor ($V_{M2}/V_{M1} \sim 0.8$). Since the rotor is directly followed by a stator, diffusion in the rotor helps to unload the stator; the overall effect is to increase stage performance. In a conventional centrifugal compressor, it is desirable to first increase the meridional velocity over about 70 percent of the entire impeller length and then diffuse near the impeller exit for peak efficiency. The design incorporates a steeper ramp in the axial section to more closely match conventional centrifugal inducer practice. In turn, the higher meridional velocities at the inducer exit effect a lower blade profile loss, and the inducer section can operate at a higher rotor efficiency than normally encountered in standard axial compressor practice.

Two methods of inducer blade stackup were considered for this application. The first design employed the normal practice of stacking the rotor blade on the center of mass for each radial cross section of the blade. A side view for this type of blade stacking is presented as Figure 34. With a radial leading edge on the centrifugal portion of this impeller, the gap between the two sections would not be uniform. It is felt that a nonuniform gap between the inducer and impeller sections may have a deleterious effect on range and performance as a result of cross flow in the gap region. Recent axial compressor rotor-stator experience has indicated overall performance could be improved by minimizing the gap between the rotating and stationary elements. Cascade tests of tandem airfoil sections have shown higher turning efficiencies with little or no axial displacement between sections. On the basis, it was decided that an inducer rotor with a radial trailing edge projection be designed to minimize the gap between the inducer and impeller. A side view of the radial trailing edge stackup configuration is presented on Figure 35.

Inducer Design Velocity Diagrams: The next task in the design of the inducer was the definition of flow conditions in the freestream at the rotor inlet and exit stations. AiResearch Computer Program No. 6018 provided an iterative solution of the equations of motion for an axisymmetric, nonisentropic flow in an arbitrary annular flow passage. Input to this program included the desired total pressure ratio along a streamline together with the estimated loss coefficients ($\bar{\omega}$). These loss coefficients are the sum of the shock and profile losses along a specific stream-tube. Considerable profile loss data for standard 65-series blades and some double-circular-arc configurations based on low-speed cascade tests are available. However, because of high surface Mach numbers, multiple-circular-arc (MCA) sections over most of the blade height were employed. Since profile loss data for these sections had not been correlated systematically, it became necessary to employ existing test data from Rotor 1B (ref. 9) to define profile loss information for MCA blade sections.

58
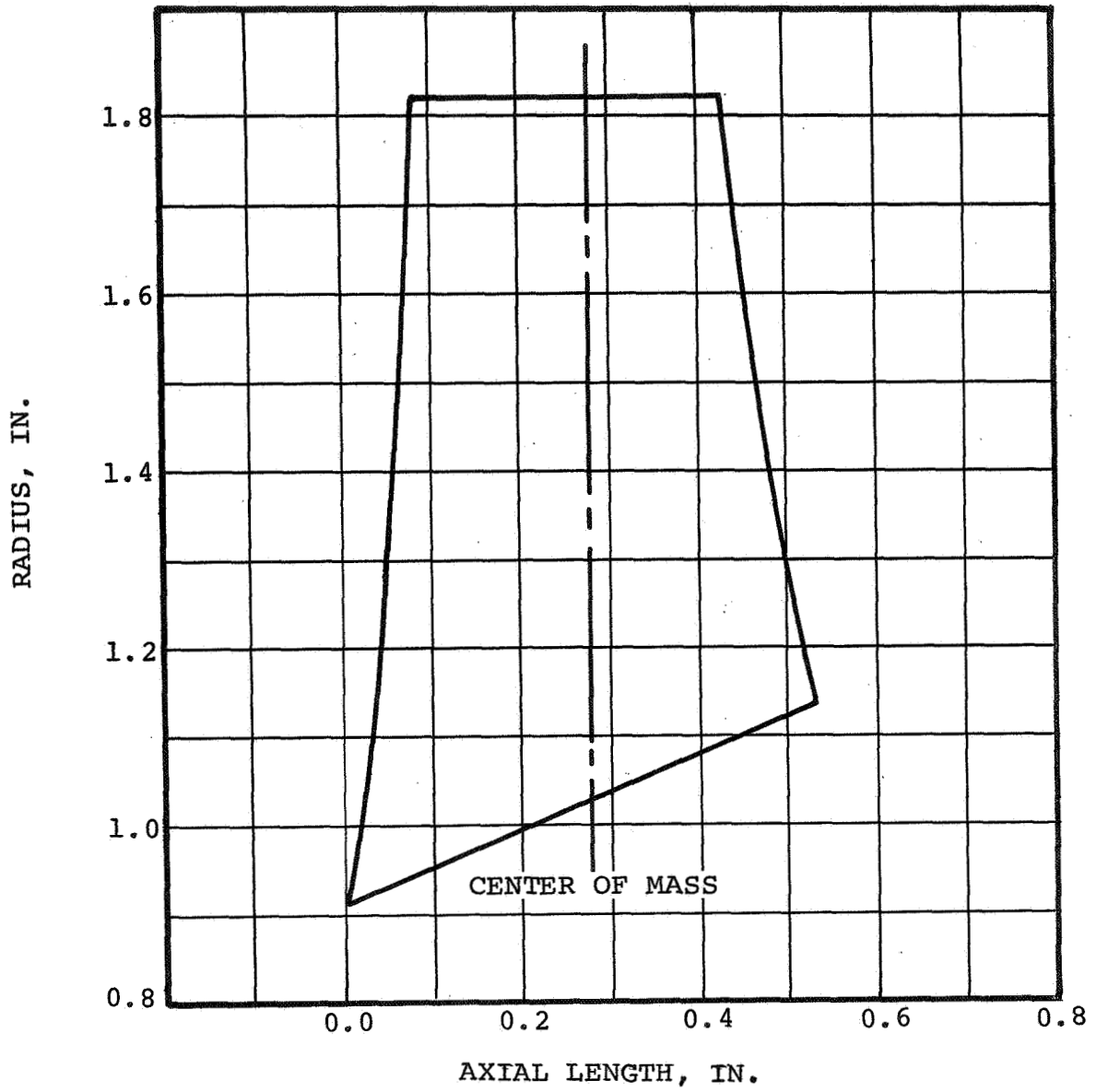
Figure 34. - Side view of inducer blade with stackup on center of mass.
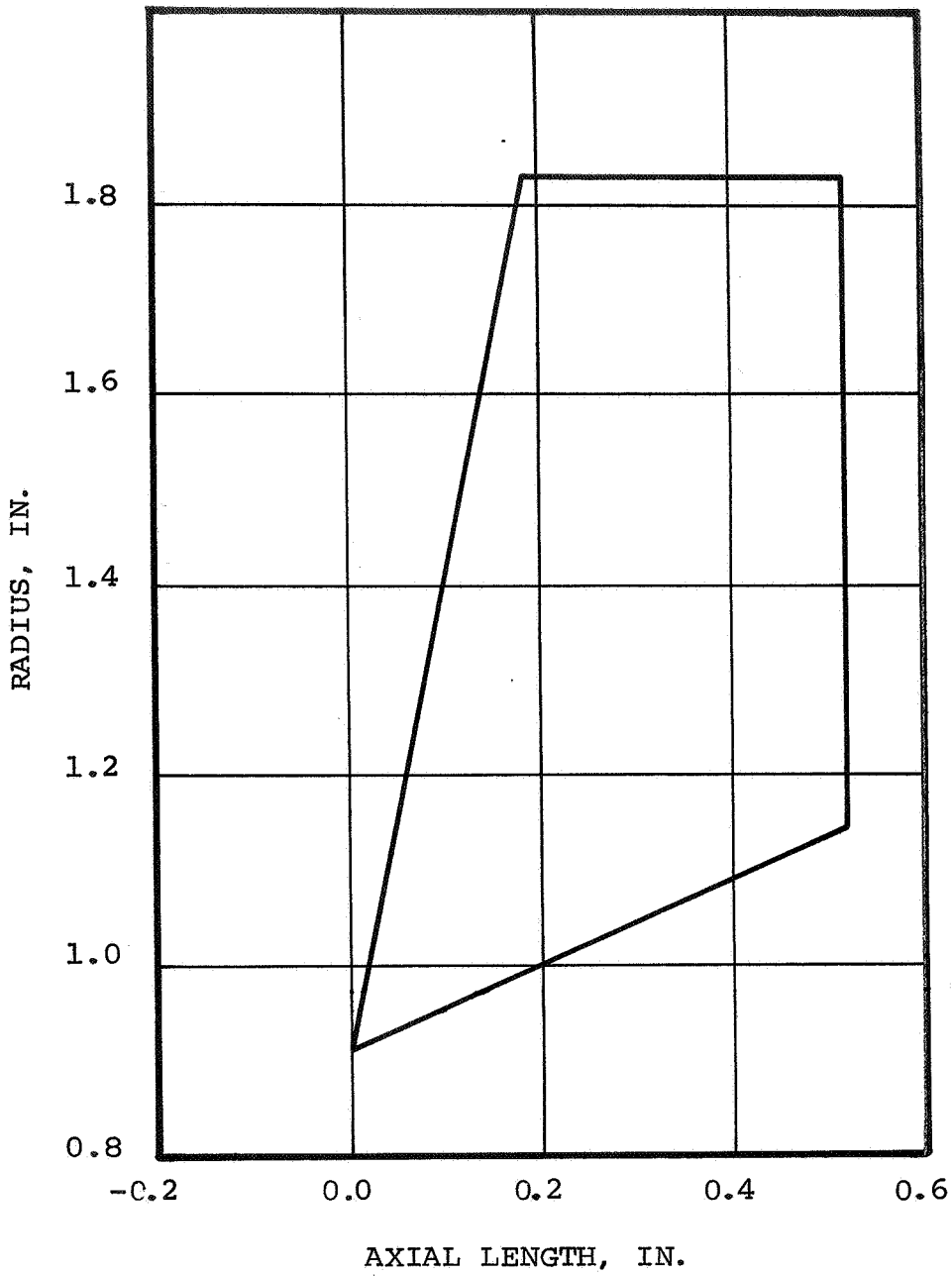
Figure 35. - Side view of inducer blade with trailing stacked up in a radial plane.

This was accomplished by taking the reported total loss coefficient data minus the loss for one normal shock at the inlet relative Mach number as representing the profile loss. The shape of the loss curve as a function of the diffusion (D) factor shown in figure 36 was established using a shape at the NASA-recommended tip loss correlation as a basis as shown in figure 36. The NASA-recommended tip loss correlation was obtained from ref. 8.

Computer solutions of the flow conditions at the rotor inlet and exit took several trials with the estimated loss coefficients recomputed for each new case. When the estimated and actual loss coefficients were matched, the flow solution was considered final. The resulting inlet and exit air angles from the across-the-blade flow solution were then used to establish the blade camber and stagger along each streamline. Vector triangles for the inducer section are presented in figure 37.

The inducer rotor was designed for zero incidence to the suction surface where the inlet relative Mach number is supersonic. Design incidence then became the difference between the inlet suction surface angle and mean camberline angle. However, the inlet air angle first had to be corrected for the effect of leading edge thickness on the flow direction just inside the blade row. The multiple-circular-arc sections employed for the supersonic portion of the blade were designed to have very little turning over the exposed portion of the inlet suction surface. This means the supersonic camber ratios were purposely set low to produce almost no camber to the point of maximum blade thickness. This reduced the effect of initial acceleration of the air along the suction surface on the shock loss inside the covered portion of the blade. Previous experience with supersonic axial blade rows was used to establish the fundamental design parameters that were applied to this design. When the corrected inlet air angle and incidence were determined, the inlet blade angle was then established. In the subsonic portion of the blade, double circular arc sections were used with the incidence angle initially selected from previous experience. However, this was subject to change during the detailed design phase to increase the area for flow if required to prevent choking. The design and final incidence angles for the inducer are presented in figure 38.

Exit blade angles for the inducer rotor were calculated from the exit angle and a deviation determined from certain blade and flow parameters. Thus, the deviation determination became a trial-and-error calculation with the blade camber and stagger computed iteratively. Deviation used here is a modified version of Carter's rule expressed as follows (ref. 1):

$$\delta^o = \frac{\beta_1 - i - \beta_{2e}}{\frac{\sqrt{\sigma}}{m} - 1} + \overline{X} \tag{3}$$

61

PROFILE LOSS, $\dfrac{\bar{\omega}\cos\beta'_2}{2\delta}$

0.05

○ ROTOR 1B TEST DATA
   90% DESIGN SPEED
   PEAK EFFICIENCY (REF. 9)
Ψ = STREAMFUNCTION

0.04

NASA MIN.
TIP LOSS
(REF. 8)

0.03

Ψ = TIP &
0.9

0.02

0.9

0.75

0.7

0.5 & HUB

0.5

0.01

0.3   0.25

0.1 (FRACTION
OF BLADE
HEIGHT)

0

0.3   0.4   0.5

D-FACTOR
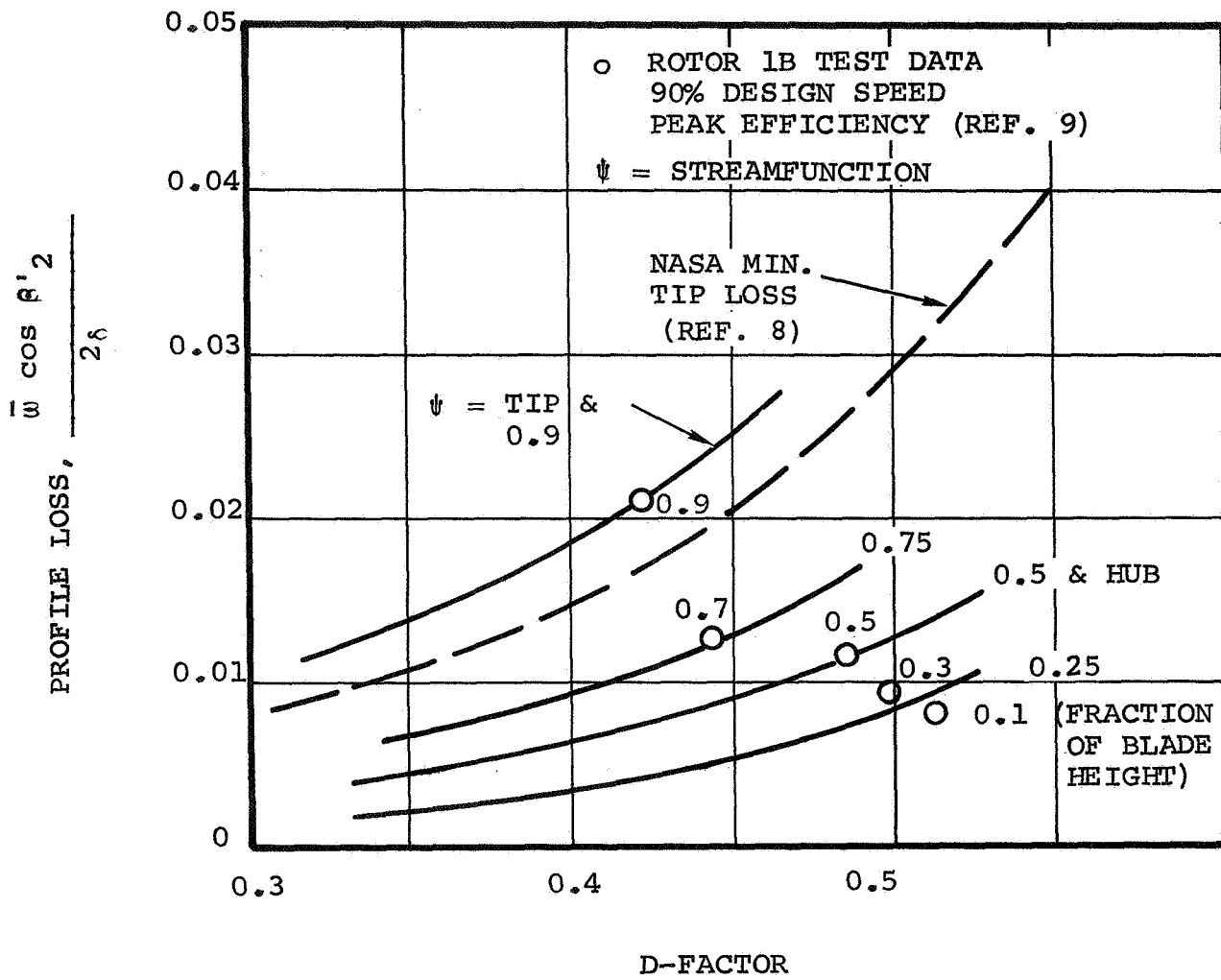
$$D = 1 - \frac{V_2}{V_1} + \frac{r_2 V_{u_2} - r_1 V_{u_1}}{2\,\bar{r}_\sigma V_1}$$

Figure 36. - Rotor element loss curves.
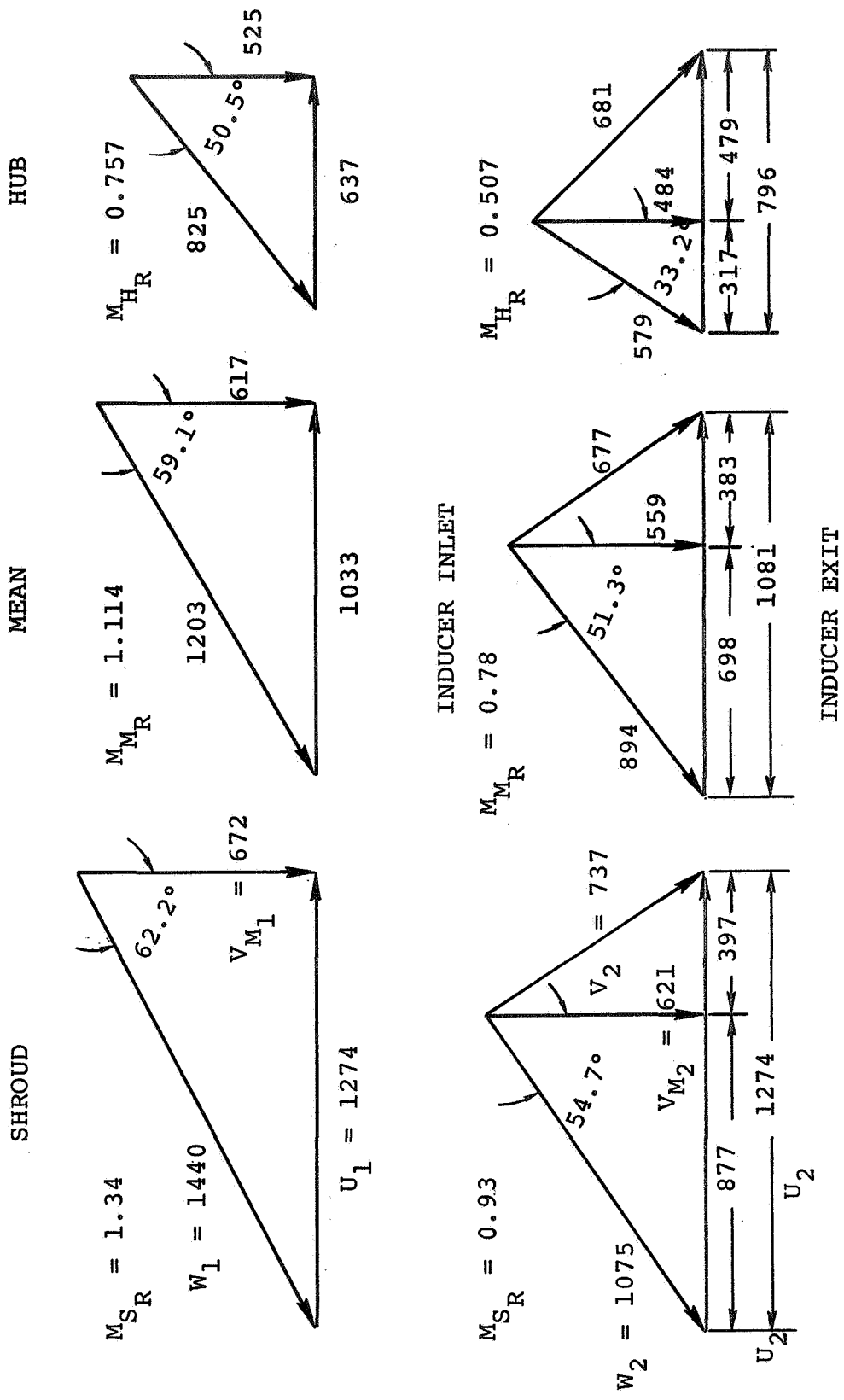
Figure 37. - Design vector triangles - inducer section (across the blade).

63
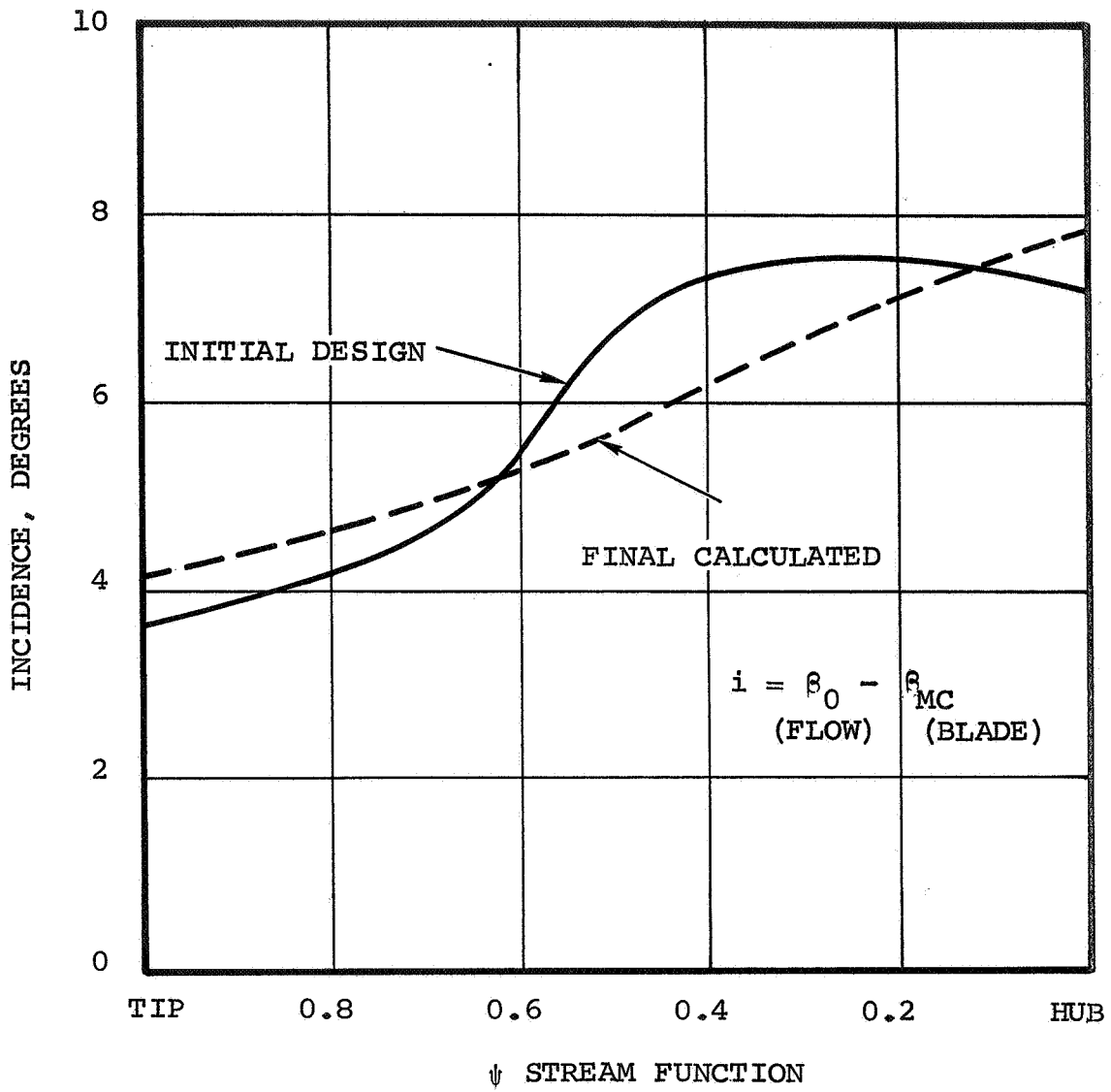
Figure 38. – Inducer incidence.

where:

β_1 = inlet air angle

i = incidence

β_{2e} = equivalent exit air angle

σ = solidity

m = deviation coefficient

$\bar{X}$ = empirical adder

Here the deviation coefficient, m, was obtained graphically from a plot of m versus blade-chord stagger with the location of the maximum camber rise as an additional variable. The equivalent exit air angle used in this expression corrected the flow to an equivalent cascade of the same absolute circulation. Calculation of equivalent and actual air angles was made in the across-the-blade computer program. With the deviation and actual air angles determined, the exit blade angle was then specified along with the blade camber and stagger. The design and final calculated deviation angles for the inducer section are presented on Figure 39.

Blade Profile Design: Two AiResearch computer programs were employed in the detailed design of the inducer blade sections. Program No. 1188 computed the basic rotor blade shapes, and stacked the sections in a desired manner. Input for this program included coordinates of the streamlines, type of blade shape, inlet air angle, incidence, chord, leading and trailing edge, and maximum blade thicknesses. In addition, the blade sections may be stacked about the center of mass or along any arbitrary radial line. Output from the program included a complete description of the blade stacking (both constant-radial and cascade sections) and a set of input cards for the second computer program. These computer cards specified the blade angles, lean, thicknesses, and streamline slopes at several specified grid points along an axial plane within the blade row. A complete flow solution through-the-blade was then obtained using AiResearch Computer Program No. 6018. This was the same program used to determine the across-the-blade solutions with several additional calculation stations added within the blade row. Since streamline data was input to the blade stacking program and new streamline data was generated by the flow solution program, both programs had to be run several times to iterate on an acceptable final solution.

The through-the-blade solution required that some method be used to specify the aerodynamic losses along each streamtube within the blade row. The overall loss for each streamtube was available from the across-the-blade flow solution. Previous experience had shown that a sinusoidal variation of axial energy

$$\delta^{O} = \beta_{2_{BL}} - \beta_{2_{FLOW}}$$
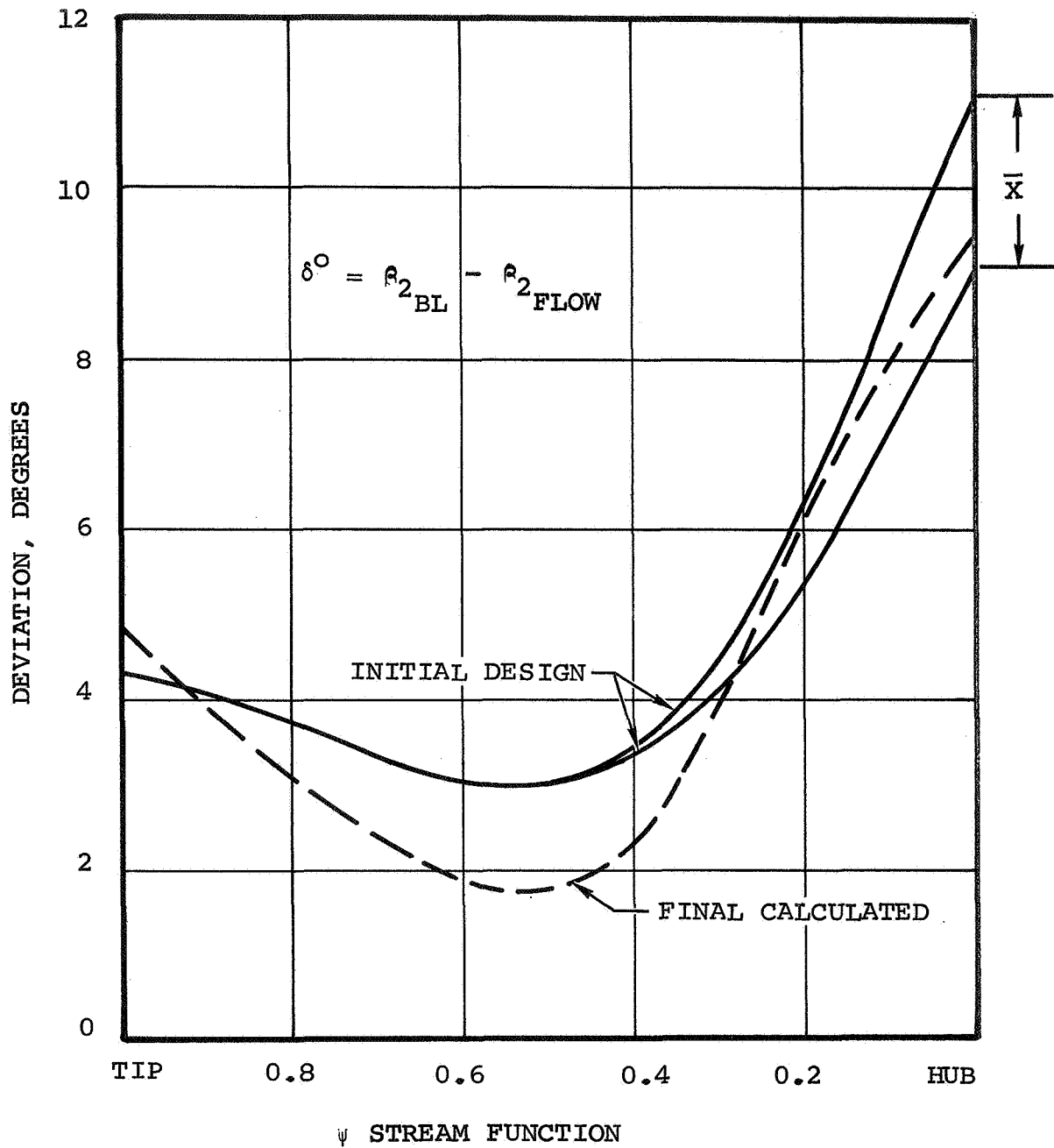
Figure 39. - Inducer deviation.

addition best represented the actual situation where shock waves crossed the flow path. Normally a shock system would be represented by a sharp discontinuity in the flow properties at the shock front. However, the flow solution obtained considered mean flow conditions at a particular axial location, and under most circumstances, the effects of the inlet shock system should be distributed across several axial stations. A linear loss distribution was assumed for the subsonic streamlines through the inducer blade. A plot of the final loss distribution is presented as Figure 40. The station numbers shown here correspond to the calculation stations indicated on Figure 41. Streamlines resulting from the through-the-blade calculation are also presented on Figure 41.

Before finalizing a design, a check had to be made to determine whether each blade element would pass the flow for which it is designed. This was accomplished by making a two-dimensional flow area comparison that considered the passage width between blades and the streamline convergence with meridional distance. Flow passage widths for each streamline were computer plotted at ten times scale and passage width variations with meridional distance measured normal to the pressure surface. Streamline convergence in the meridional direction was determined from gas property information as a part of the flow solution results. A satisfactory design was accomplished when the minimum throat area parameter had a three- to five-percent margin over the critical flow area along each streamline. Flow area results for this inducer configuration are shown plotted as individual streamline points in Figure 42. The desired margin fell above the theoretical curve for one normal shock at the inlet Mach number. The necessity for a margin came from real flow effects not considered in the simplified model which tended to require more area for flow.

Design of Centrifugal Portion of Impeller

Blade Specification: Design of the centrifugal section was a cut-and-try process wherein meridional shape and blade angles were varied to produce desirable blade loadings. For these computations, a total of fifteen calculation stations was set up within this portion of the impeller. Station locations (11 through 25) are shown on Figure 43, which also includes the other calculation stations used in the flow-field computation. Initial estimates of the blade angle distribution, meridional shape, blockage, and loss distributions were based on a previous 6:1 pressure-ratio conventional impeller design. The fact that the inducer configuration for this impeller is tandem bladed was taken into account.

Q   IS THE STREAMLINE ENTROPY FUNCTION DEFINED BY: $Q = e^{(-s/c_p)}$

Q_i IS THE INLET STREAMLINE ENTROPY FUNCTION
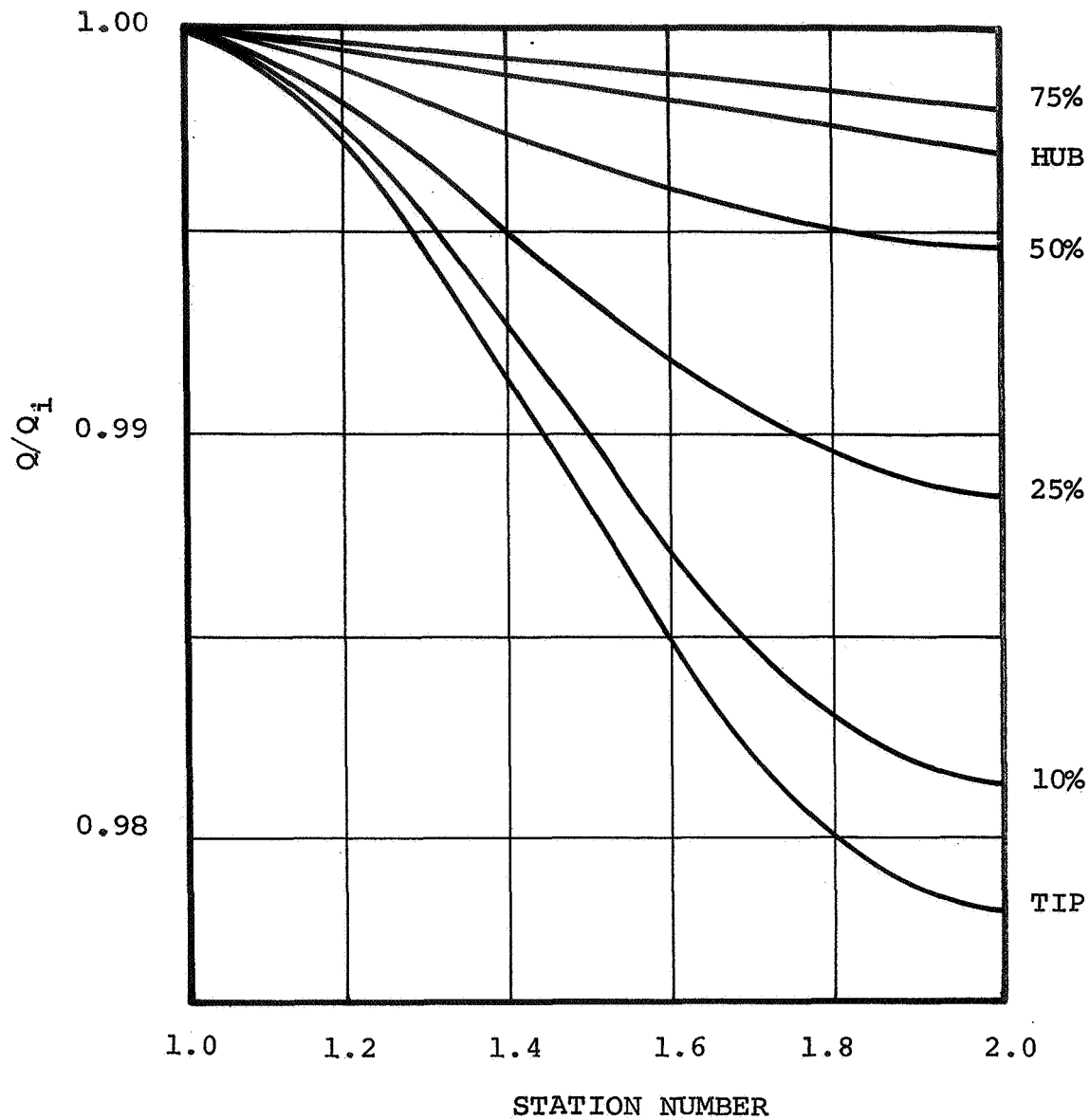

Figure 40. - Loss distribution through the blade.
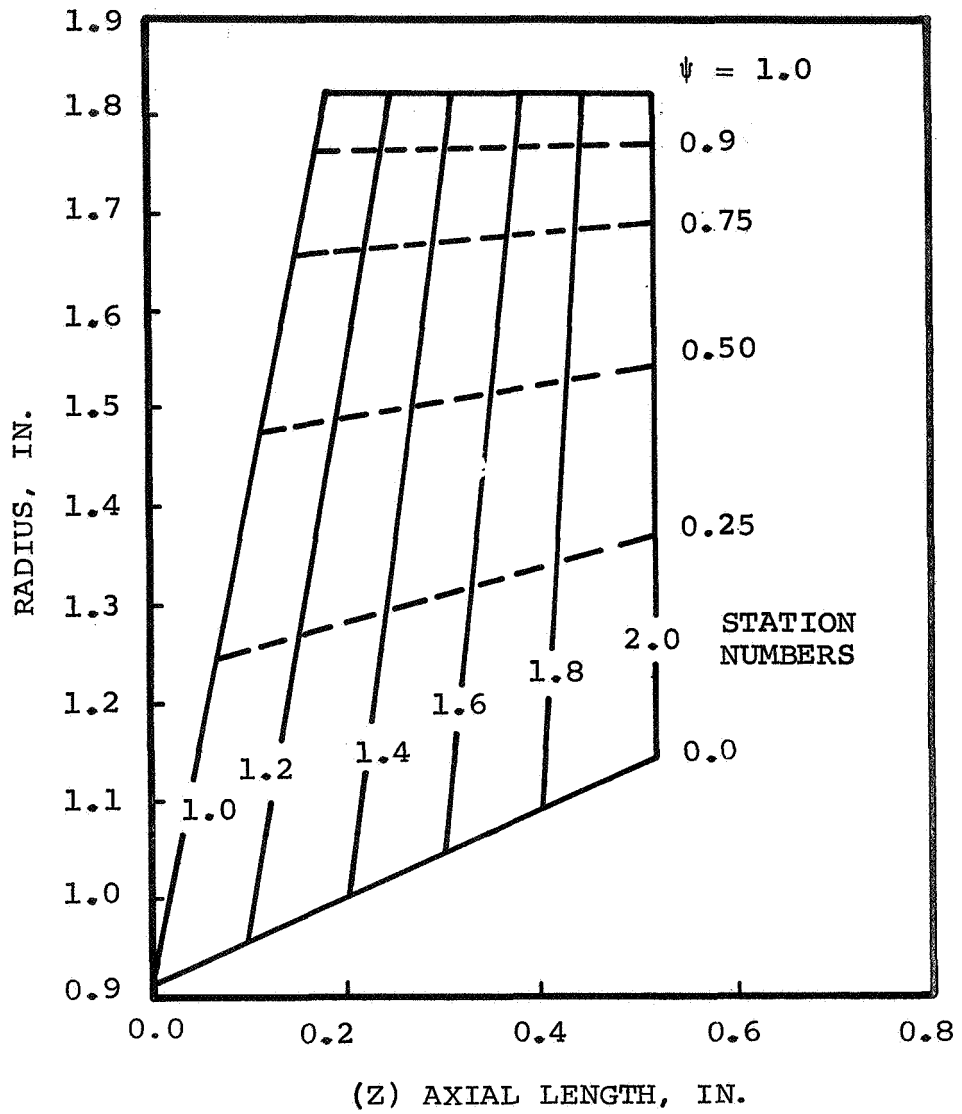
Figure 41. - Meridional view of inducer blade
stations and streamlines.

69
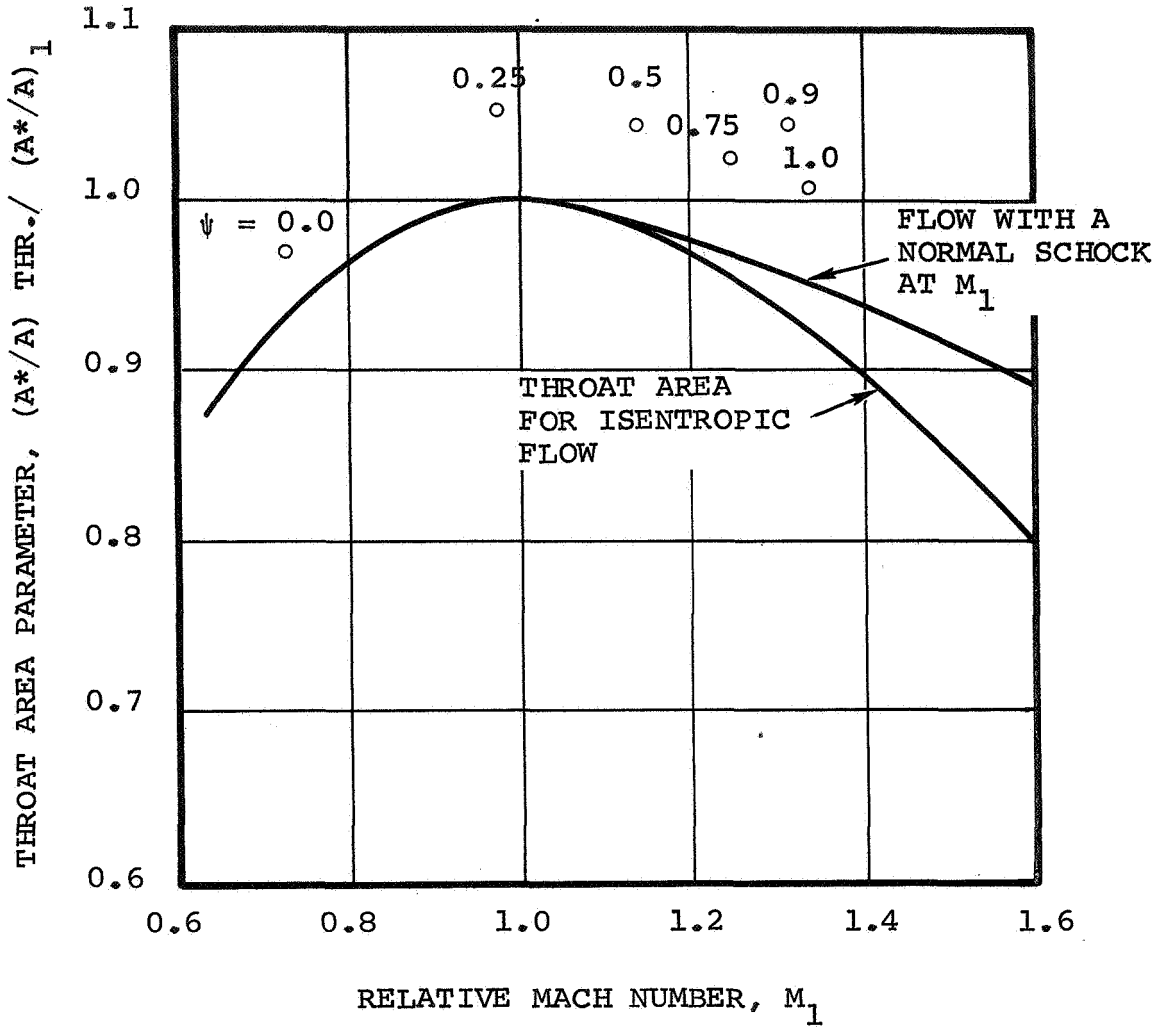
Figure 42. - Throat area check for inducer design.
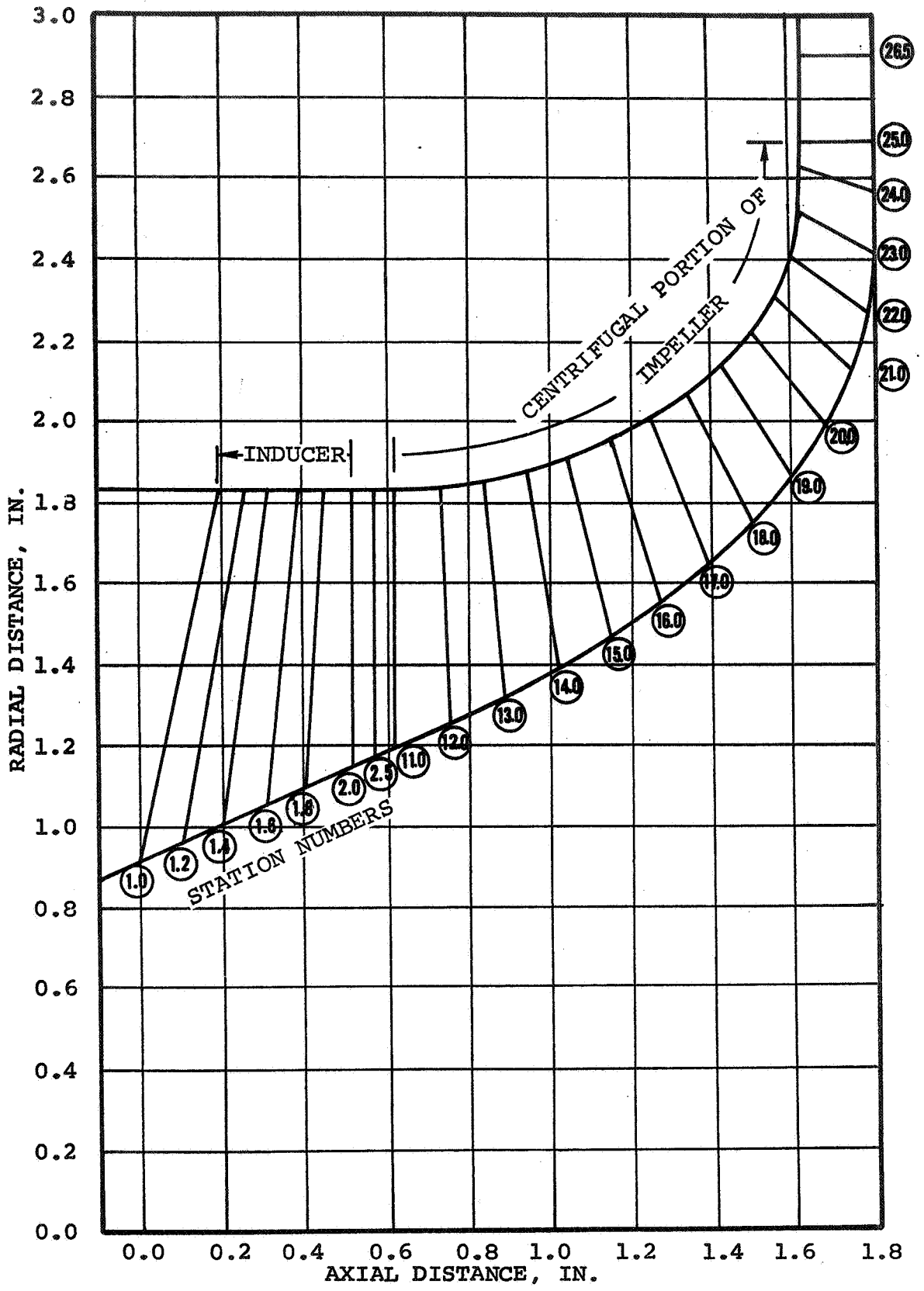
Figure 43. - Tandem impeller calculation stations.

Shroud and hub meridional shapes were defined analytically by a Super-Curve Program that employed the following relation to define the wall coordinates:

$$\frac{R^p}{A} + \frac{L^q}{B} = 1 \qquad (4)$$

where:

R = radius

L = axial length

A, B, p, q are constants, calculated to fit end conditions

Inputs to this program were the coordinates of each end of the curve and either two intermediate points, or one intermediate point and an initial slope. The advantage of using this type of curve for defining the hub and shroud shapes was that the coordinates, slope, and curvature could be calculated exactly at any particular station. This technique has demonstrated that more reliable and consistent results could be obtained from the radial equilibrium flow program because of the sensitivity of the flow solution to nonlinear shifts in slopes and curvatures along the boundary.

For the design of the centrifugal section, the aerodynamic shape of the blades at the hub and shroud was defined by assumed hub and shroud streamlines. Straight line fairing as determined by the cutter angle was used for the intermediate shapes. Impellers were cut on a 5-axis milling machine which required that a variable cutting angle be specified over the entire blade. The Manufacturing Department was consulted regarding which cutter angle distribution was satisfactory from a machining standpoint. With a given shroud and hub geometry and a prescribed cutter angle, the geometry and blade loadings on all other streamlines were fixed. The cutter angle distribution employed in this design is shown in figure 44.

After selecting a starting meridional shape that fit the desired requirements, an initial hub and shroud blade-angle distribution was assumed based on past experience. Initial loadings were then obtained by using the computer program that takes into account radial equilibrium. Meridional shape and blade-angle distribution were adjusted to change loadings. Each time the blade angle and/or the meridional shape was changed, a new set of inputs for the flow program was generated by the 5-axis cutter program using the new geometry and desired cutter-angle distribution as input. The final blade angle distribution used in the impeller design is shown in figure 45.
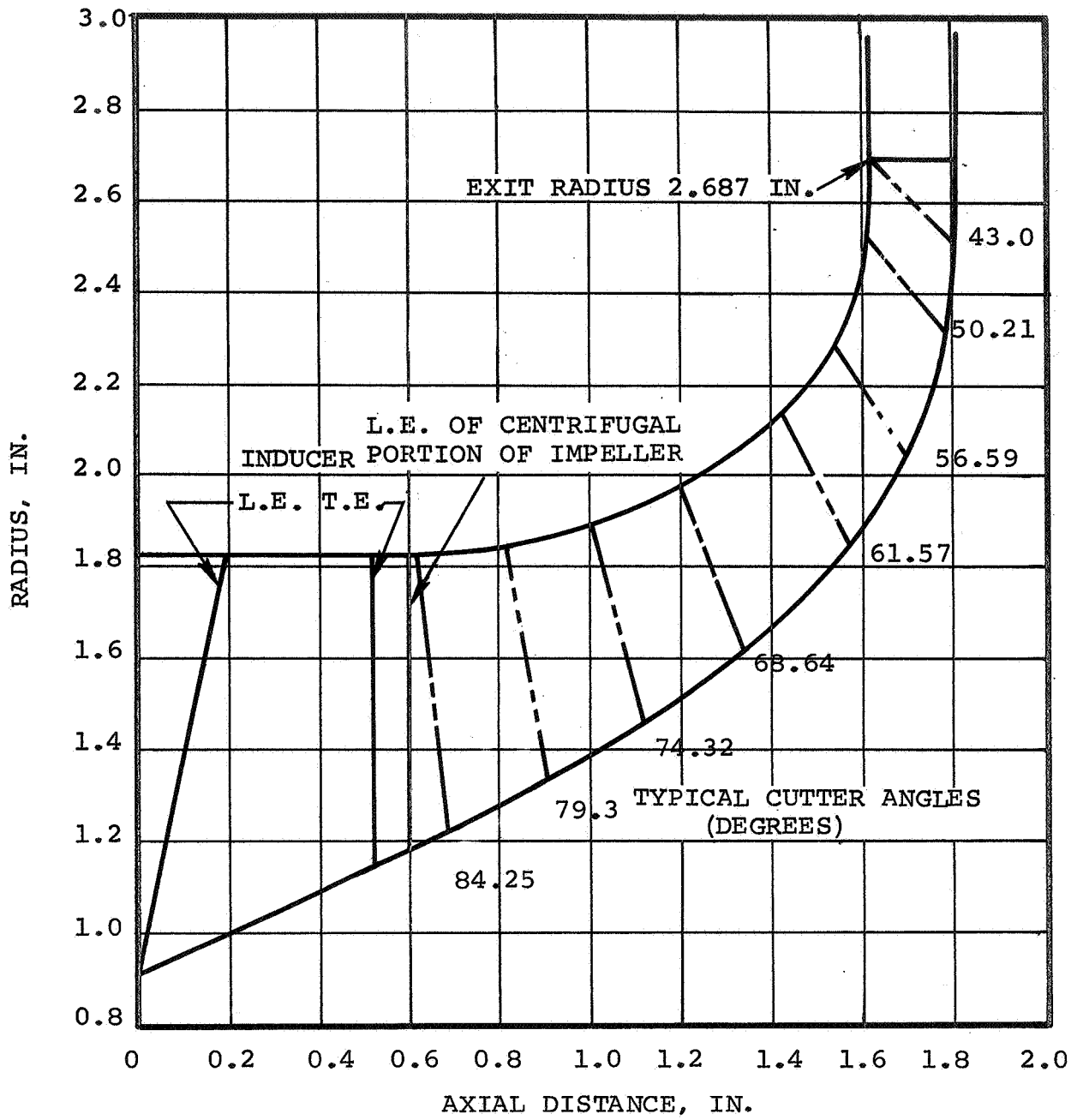
Figure 44. - Five-axis cutter angle distribution.
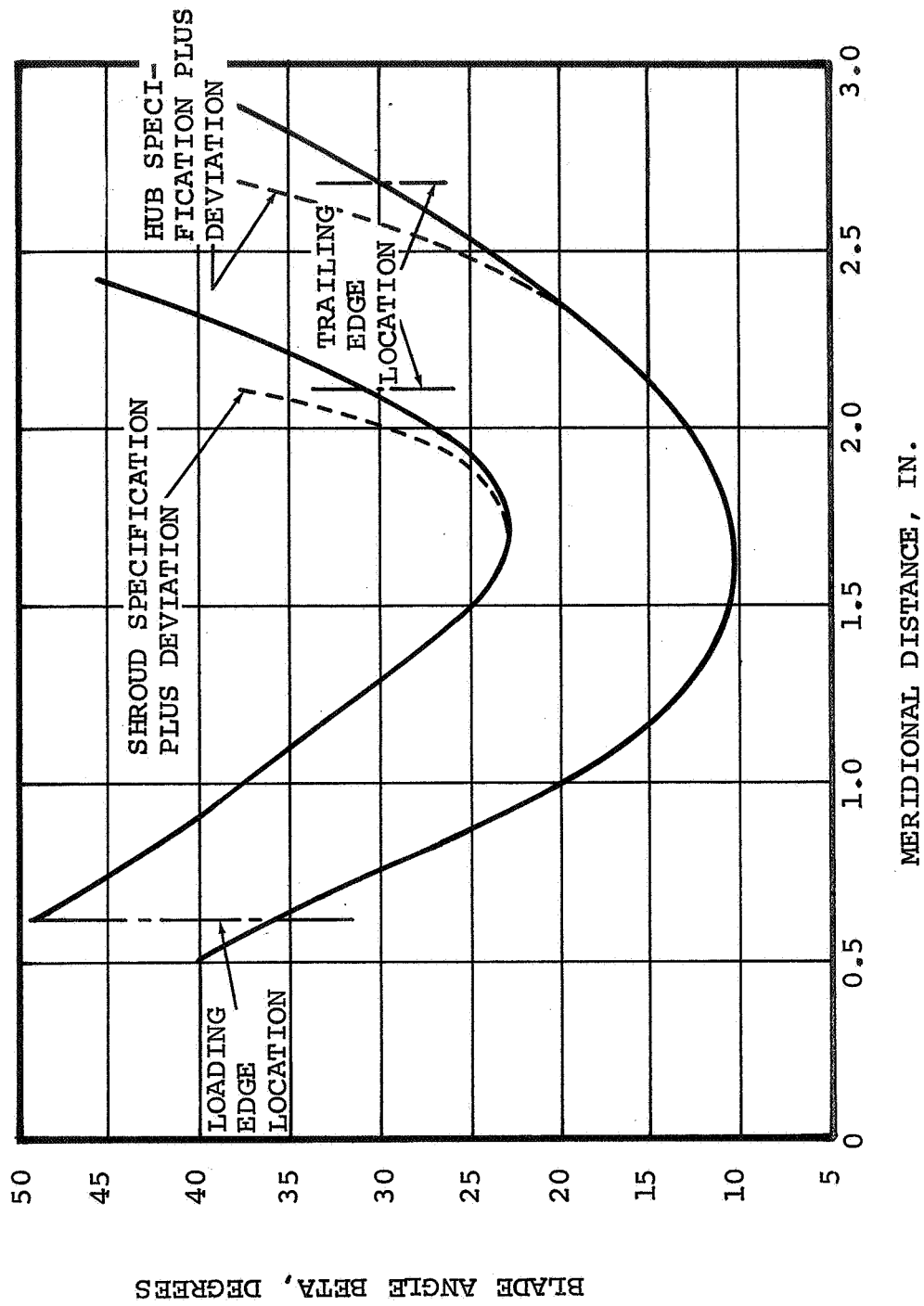
Figure 45. - Blade angle versus meridional distance.

74

Additional Requirements: Applied Mechanics was consulted concerning the requirements for blade thickness, and requested an impeller tip normal thickness of 0.025 inch over the entire length of the blade. To maintain an acceptable taper ratio, the hub tangential thickness was set at approximately 1.5 times the shroud tangential thickness at each calculation station. The required thickness distribution was maintained throughout the blade with the exception of a small region near the inducer tip where the normal thickness was reduced to provide more choke margin in the impeller. The final hub and shroud blade thicknesses employed in the design are shown in figure 46.

Two blockage terms were required for the radial equilibrium flow solution. First, there was an aerodynamic blockage to account for boundary layer build-up and secondary flows. The distribution of aerodynamic blockage both meridionally and across the flow passage was entirely empirical. Past experience had shown that the actual flow area at the impeller exit had to be increased by 10 percent to account for aerodynamic blockage. The assumed distribution of aerodynamic blockage with meridional distance is shown on figure 47. An additional blockage term was needed to account for the blade thicknesses for each station. Either normal or tangential thickness could be input to the flow program and the corresponding blockage term computed internally. The final total blockage as a function of meridional distance is shown in figure 47. Note that an effective wake blockage was assumed for the region between the inducer exit and impeller inlet. This was necessary to avoid unreasonably large changes in the meridional velocity component in the wake region (Station 2.5).

Using the radial equilibrium flow program, it was difficult to calculate loadings at the leading edge station in the impeller. Flow field calculations immediately upstream of the blade leading edge were more easily obtained. To determine the blade setting angles at the leading edge, use was made of the velocities upstream of the leading edge and a theoretical curve of impact-free incidence angles given in NASA Report SP-36 (ref. 8). This curve showed the optimum incidence in terms of solidity, thickness, blade, and flow angles and is reproduced in figure 48. The actual incidence at the leading edge did not match the optimum value across the entire blade. Precise matching of the blade incidence was not possible because of limitations due to the 5-axis cutter. There would also be a choking problem associated with precisely matching the optimum incidence, in that it was desirable to leave at least 7 percent choke margin in the impeller section to assure adequate range. Both blade and air angles at the impeller inlet are shown in figure 49.
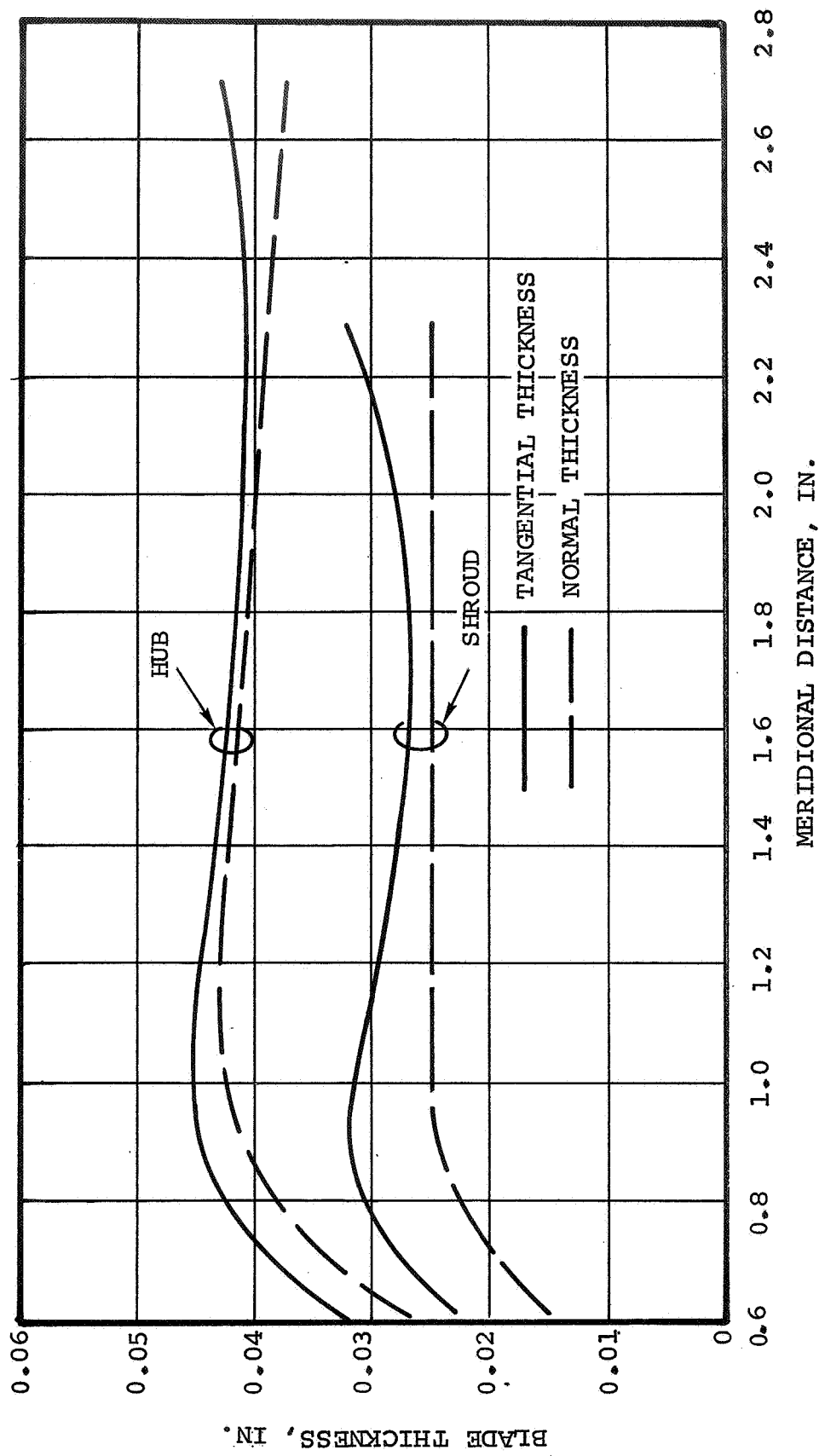
Figure 46. - Impeller blade thickness distribution for centrifugal portion.
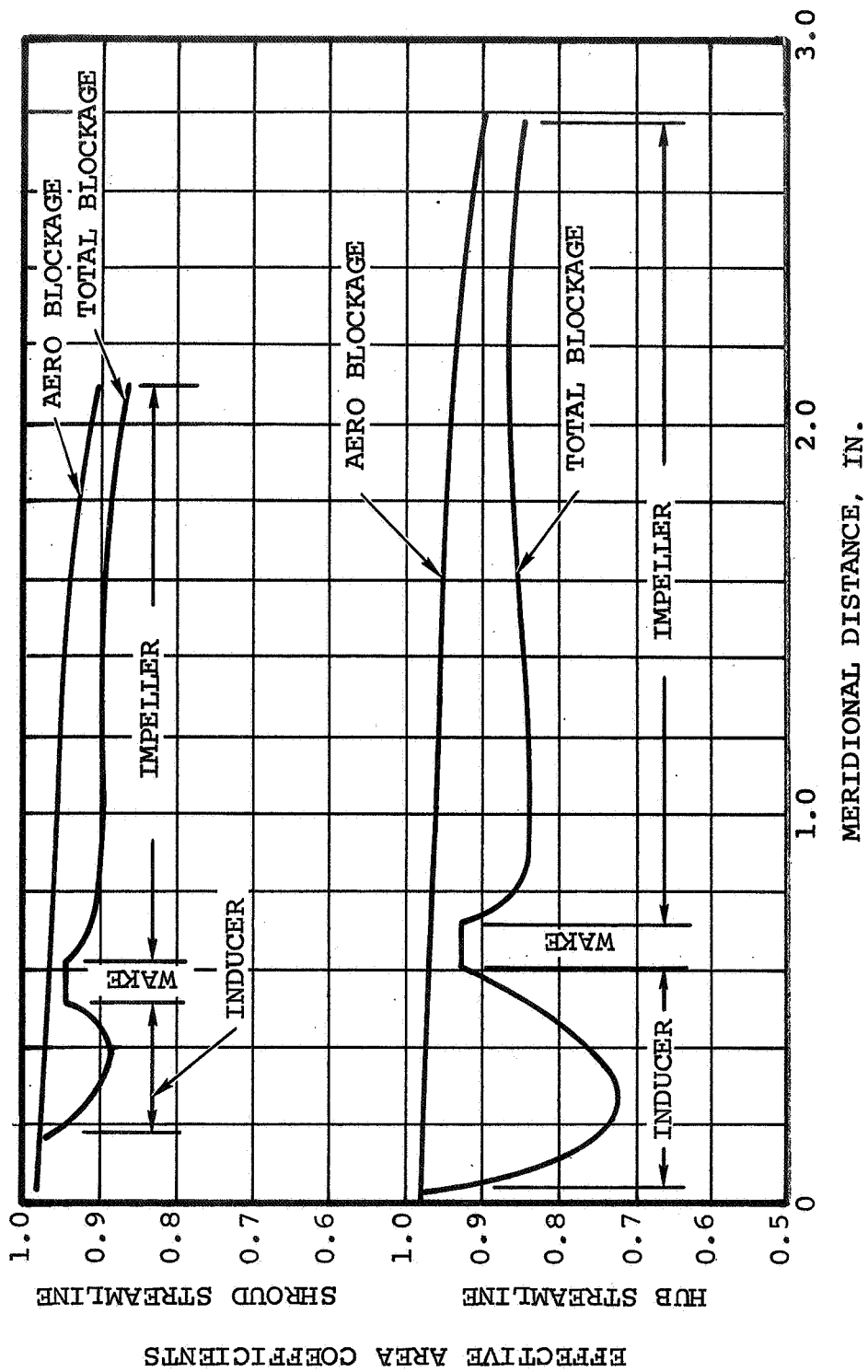
Figure 47. - Blockage distribution for tandem impeller

77
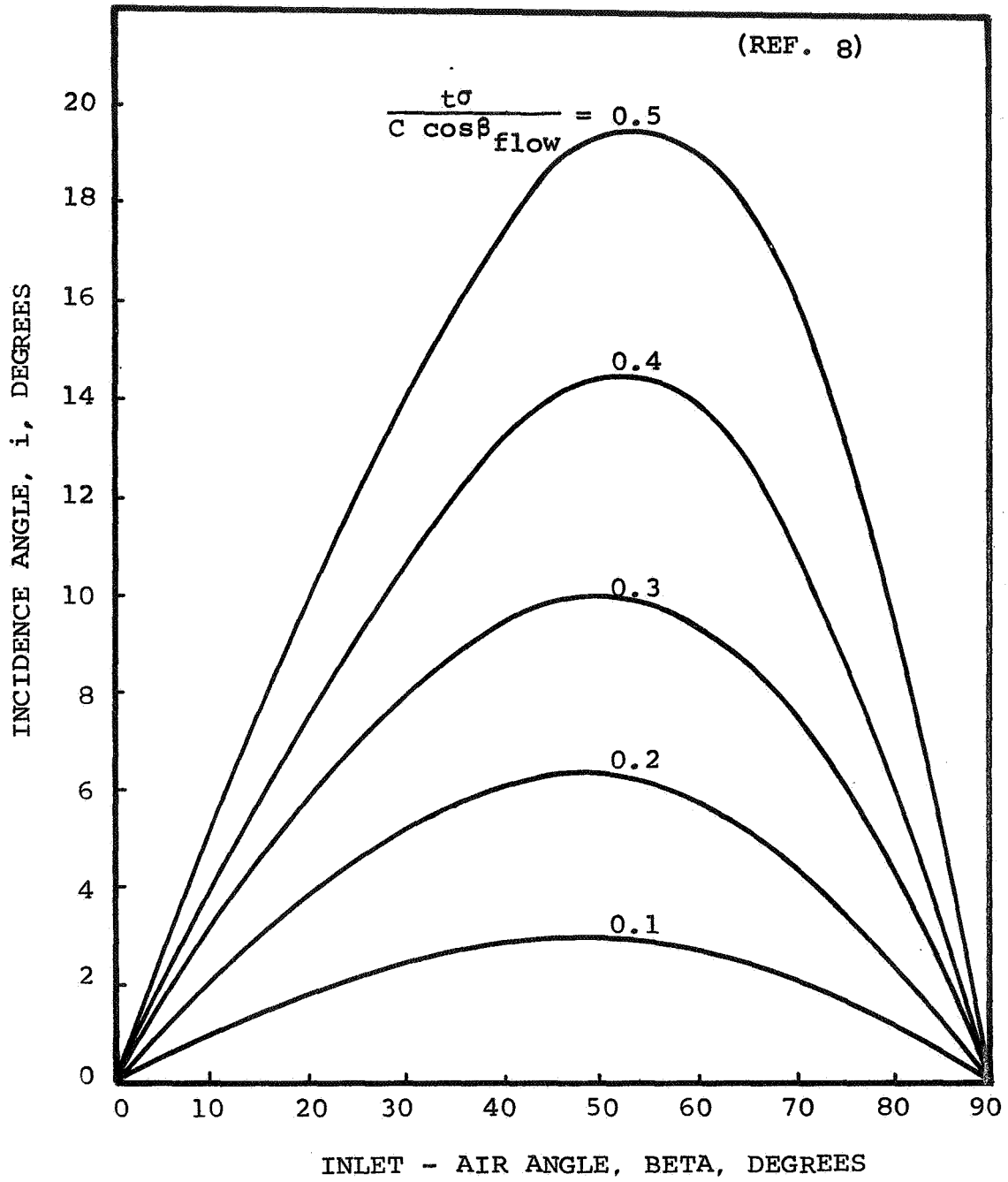
Figure 48. - Design incidence angle relation.
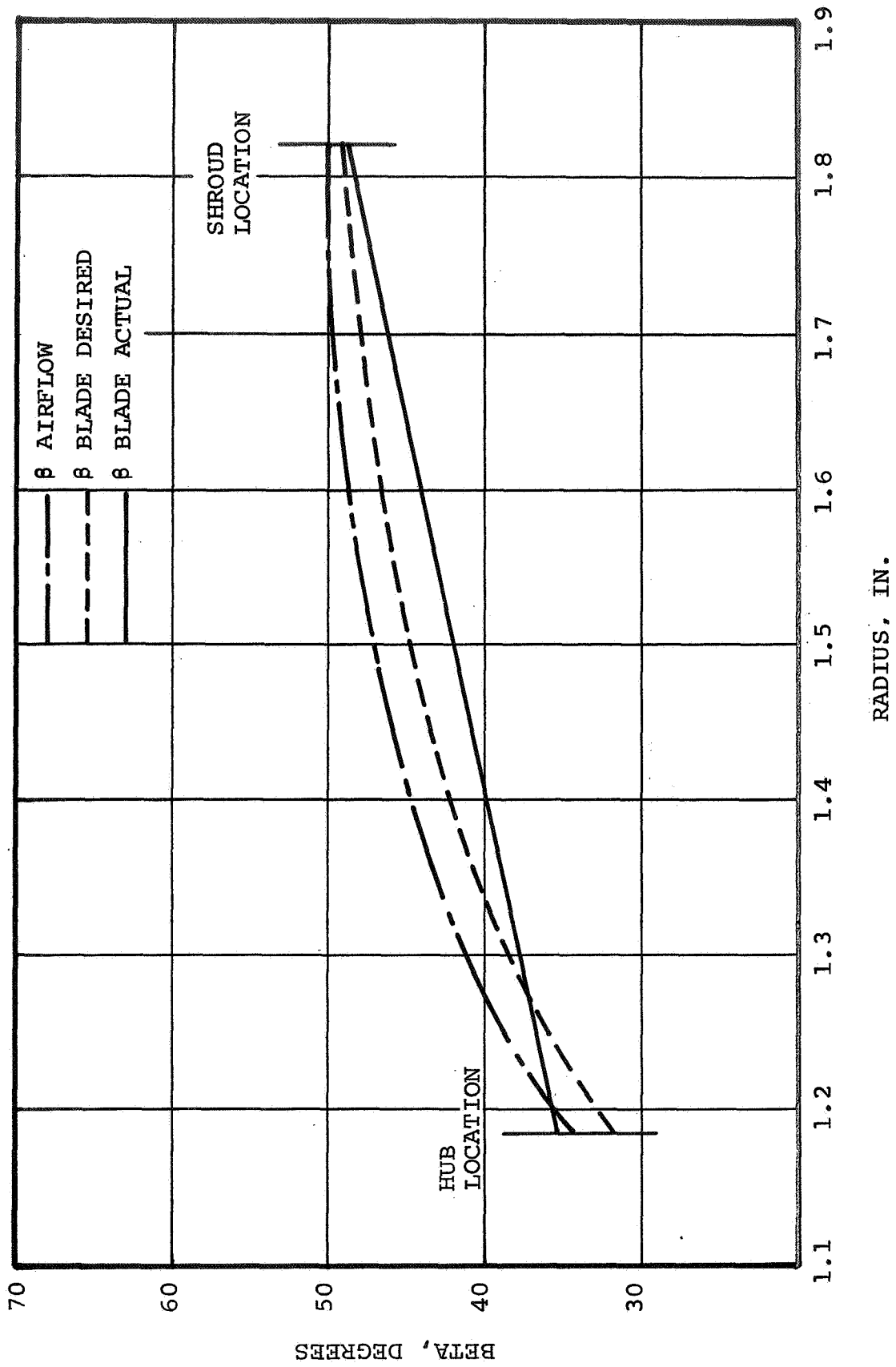
Figure 49. – Impeller inlet angles vs radius.

Final input to the flow program was a specification of the loss distribution through the impeller. Past experience had shown that this was best expressed as an essentially linear drop in the streamline entropy function (inversely proportional to the actual entropy change) for the inlet portion of the impeller. As the flow approached the impeller exit station, the entropy function dropped off more rapidly indicating greater losses in the back end of the compressor where boundary layers and secondary flow effects were accentuated. It was further assumed that the loss level (entropy function) was identical for all streamlines at the impeller exit station. The latter assumption required some qualification. Recent experimental data had shown the loss distribution at the impeller exit to be somewhat skewed with higher losses occurring near the shroud. However, the impeller tested was designed under the assumption of a constant loss level at the impeller exit. If the impeller had been designed for a skewed loss distribution similar to that measured experimentally, the resulting loss profile may have been more asymmetric and overall performance decreased. The fact that the basic compressor performance was quite good despite the skewed loss profile indicated that the original assumption may have been justified.

The assumed loss distribution for the impeller streamlines as a function of meridional distance is shown in figure 50.

Results of Flow Solution: When satisfactory blade loadings were obtained, a check was made of the resulting angular momentum distribution through the impeller. The type of angular momentum distribution found to be most desirable in previous designs was similar to that shown on figure 51. Note particularly the decreasing slope of the angular momentum toward the impeller tip. This is indicative of the flow deviation that takes place near the uncovered tip portion of the impeller. If the resulting distributions were unsatisfactory, a blade angle and/or meridional shape change was necessary.

Blade loadings for the shroud, mean, and hub sections are shown in figures 52, 53, and 54, respectively. These loadings are typical of more recent AiResearch design practice. The corresponding meridional velocity distribution is shown in figure 55.

Final velocity vector triangles at the inlet and exit to the impeller are shown in figures 56 and 57, respectively. Note that the vectors for the true exit blade angle at the impeller exit are shown as dashed lines in figure 57. This difference was representative of the deviation at the impeller exit. It was also indicative of an essentially constant slip factor across the impeller exit width.
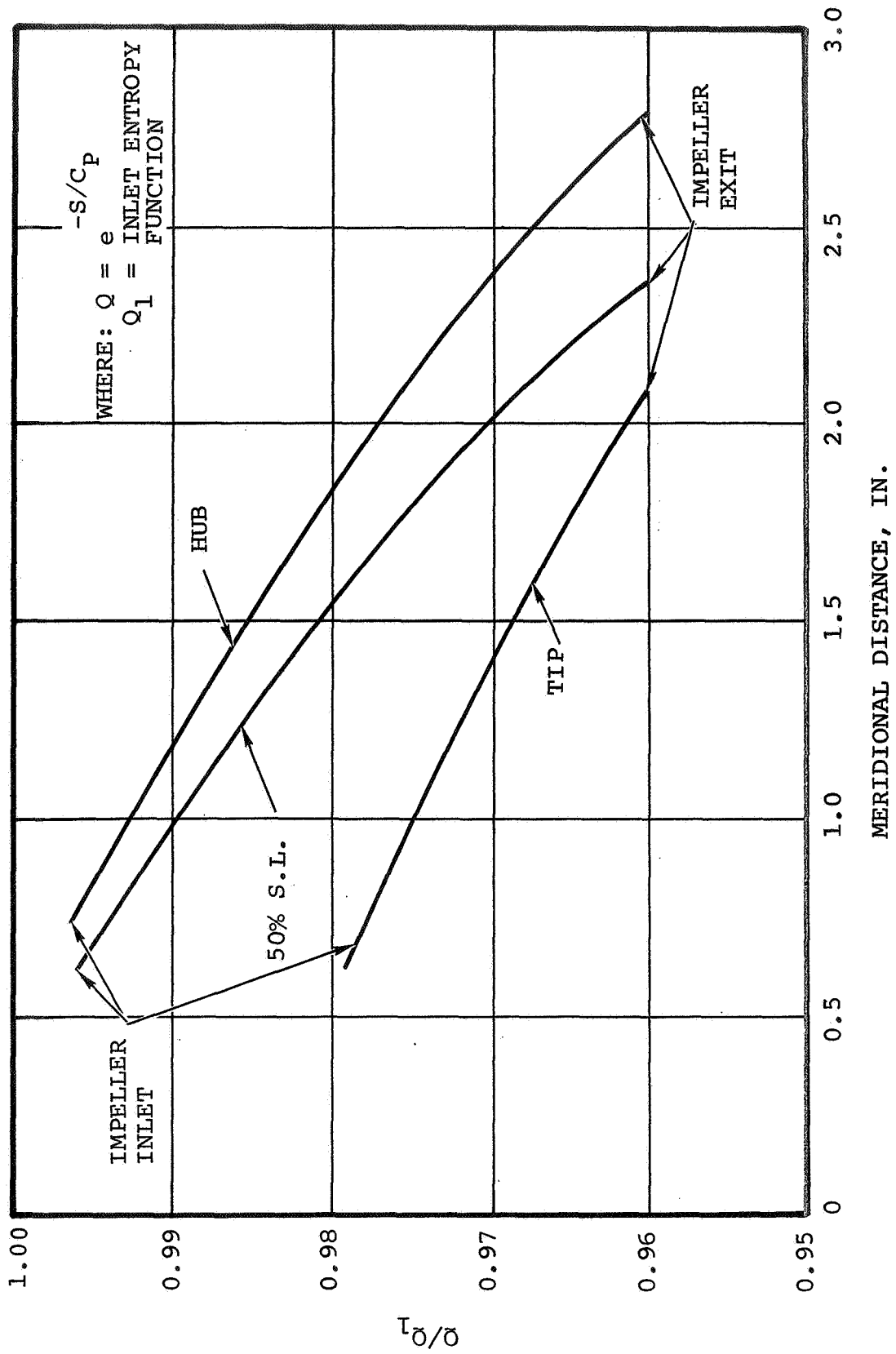
Figure 50. - Streamline entropy relationship through the impeller.
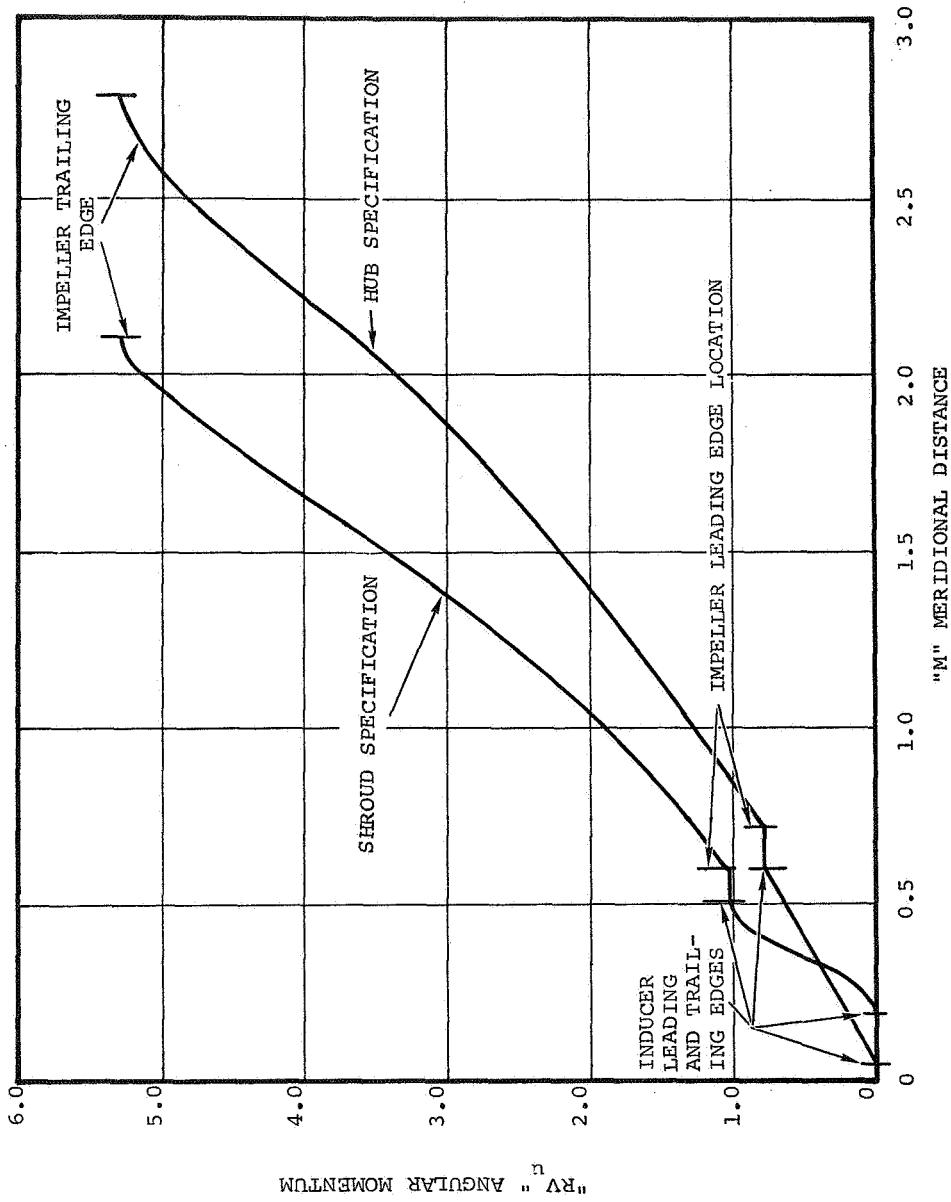
Figure 51. – RV_u vs meridional distance.

82
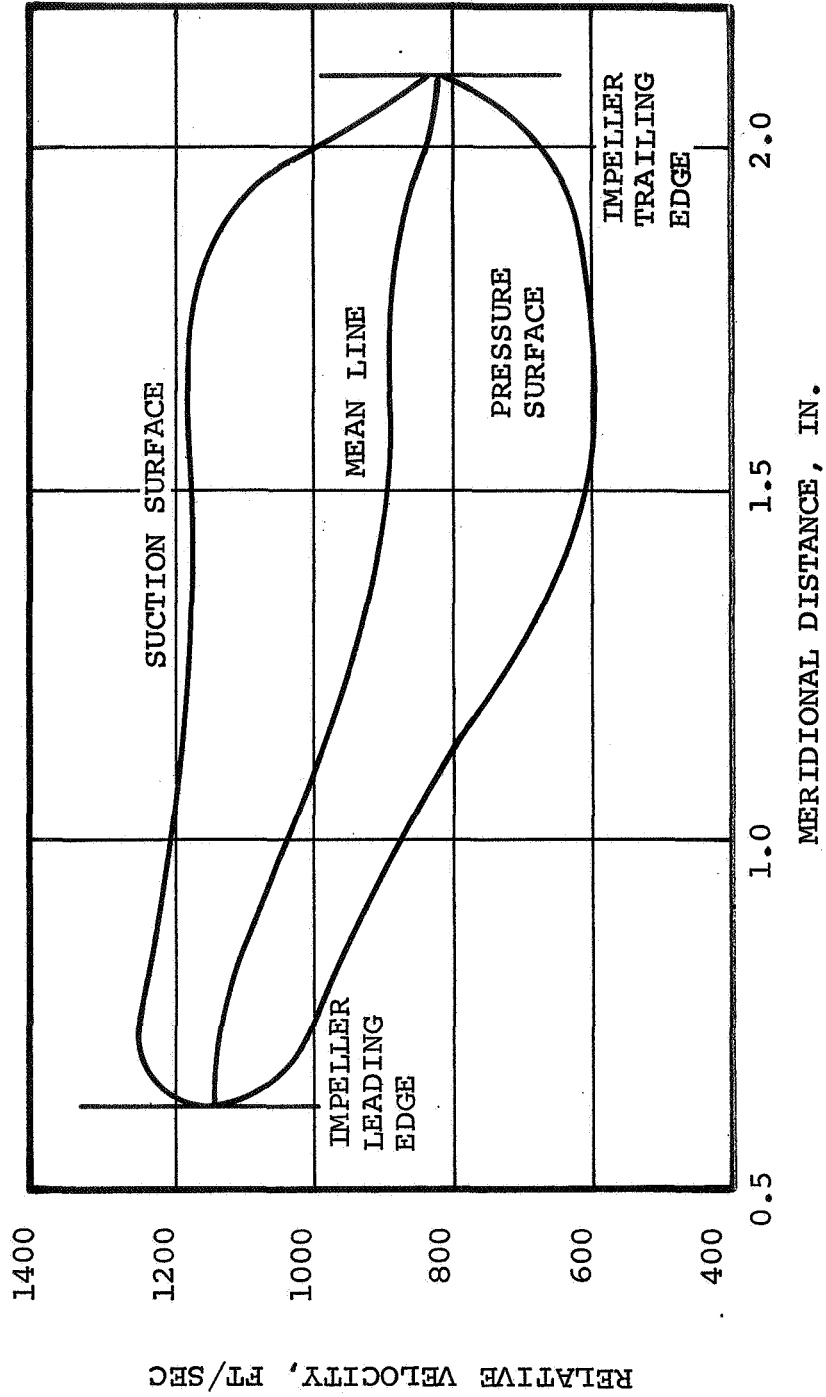
Figure 52. - Blade loading in shroud region.
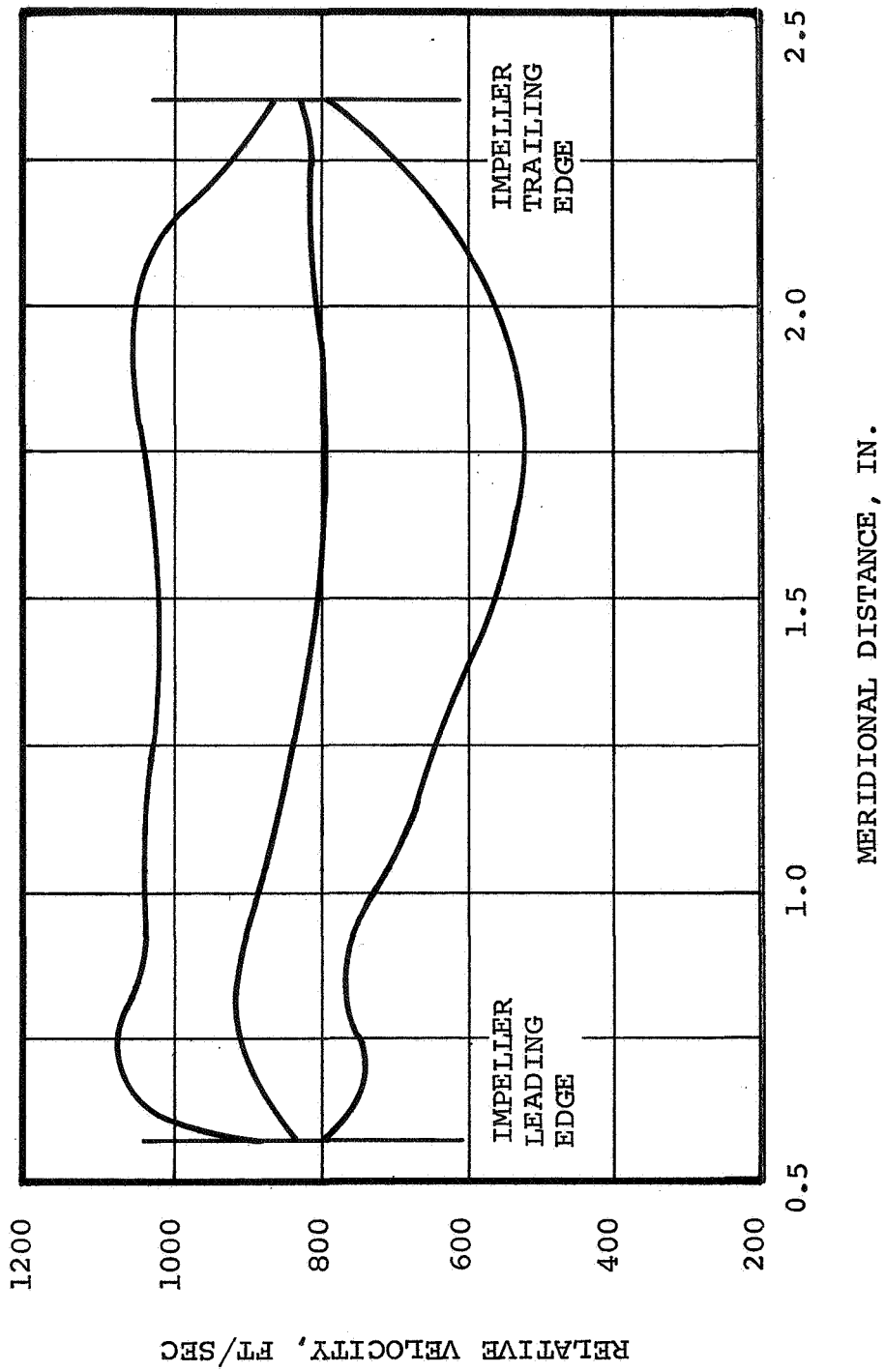
Figure 53. - Blade loading for mean streamline.

84
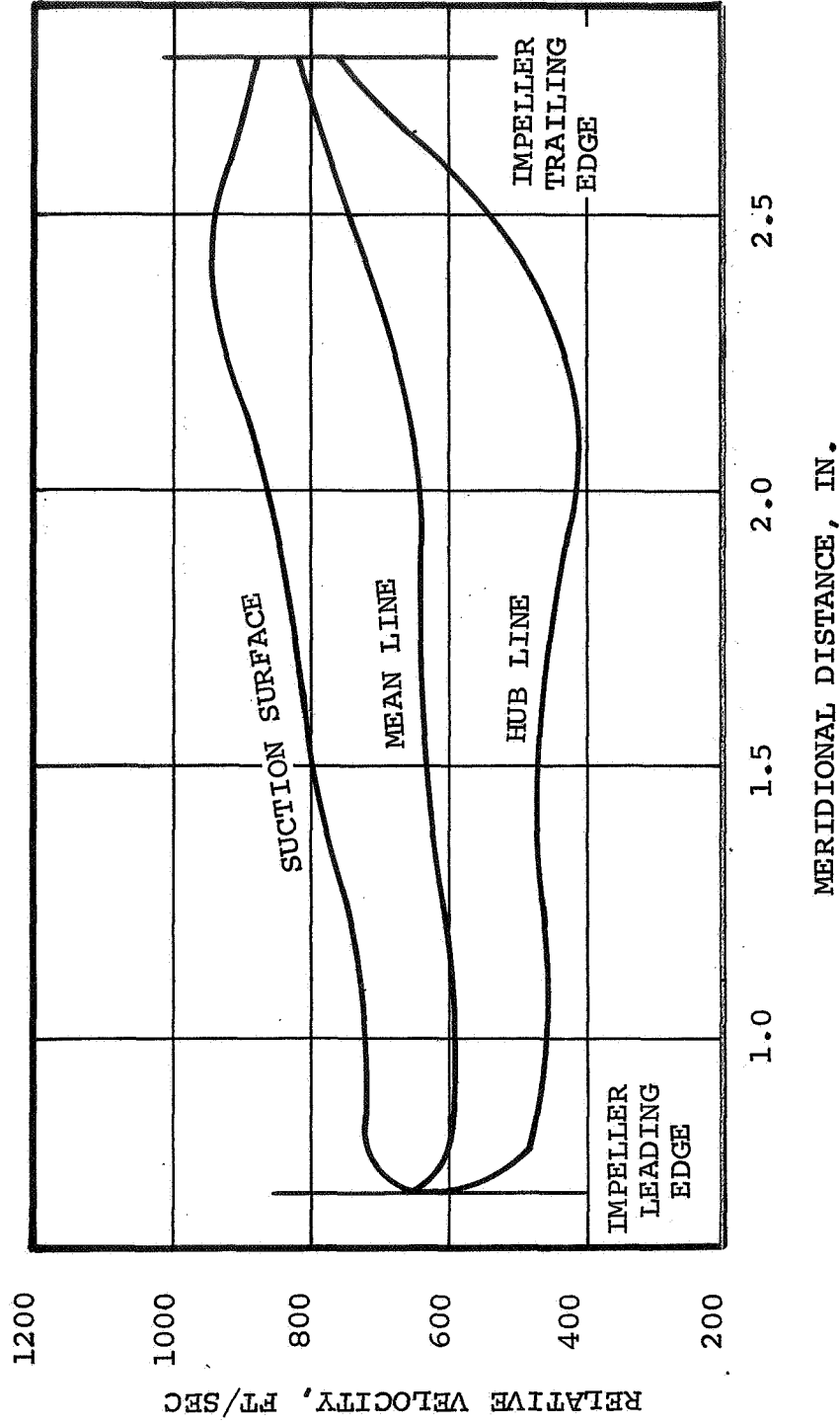
Figure 54. - Blade loading in hub region.
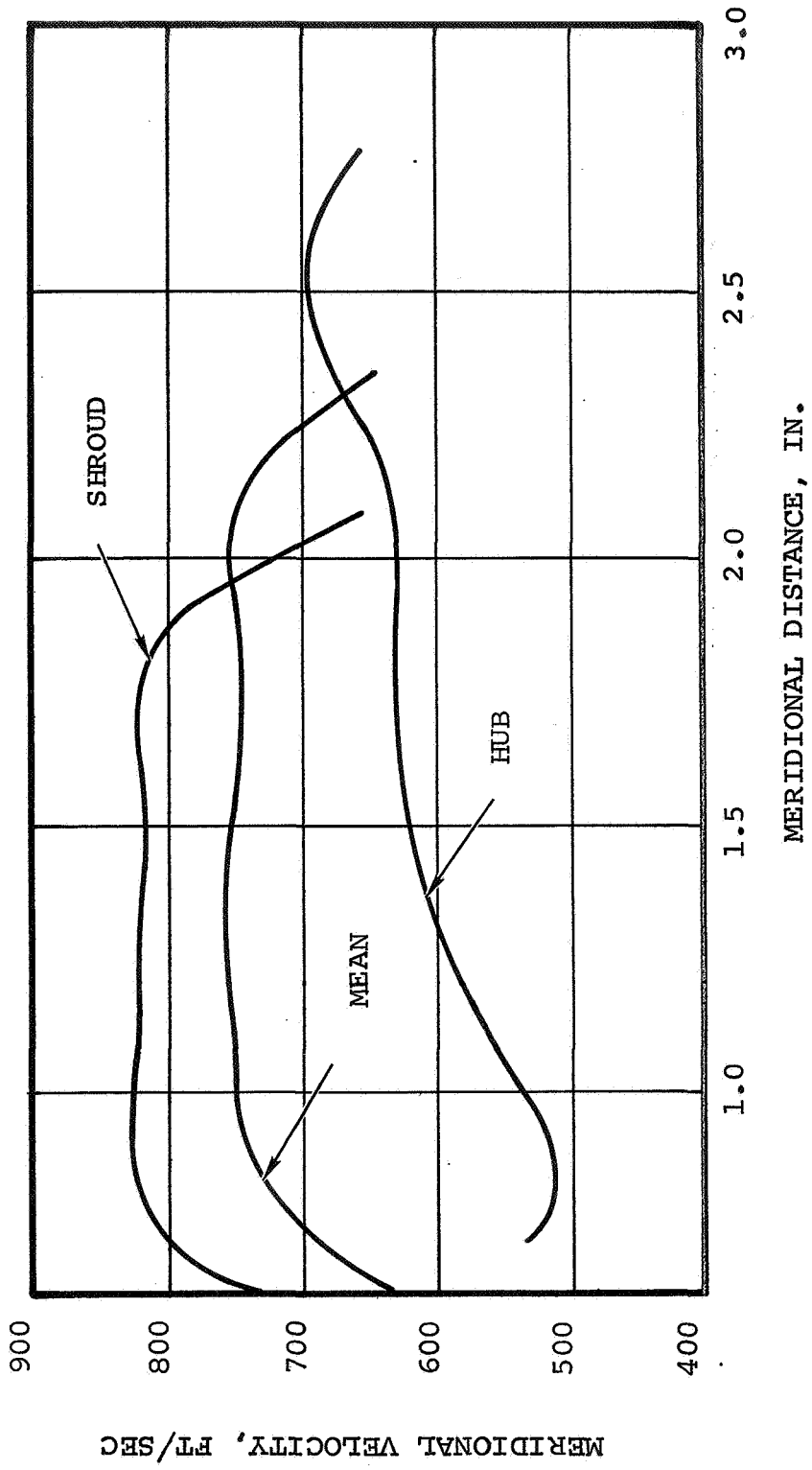
Figure 55. – Meridional velocity through the impeller.

86

IMPELLER INLET

SHROUD

$M_{S_R} = 0.993$

$W_1 = 1136$ $50.6°$ $V_1 = 824$

$V_{M_1} = 721$

877   397

$U_1 = 1274$

MEAN

$M_{M_R} = 0.847$

964    $48.1°$ 746

643

718   378

1096

HUB

$M_{H_R} = 0.571$

650   34.6 706

535

369   460

829
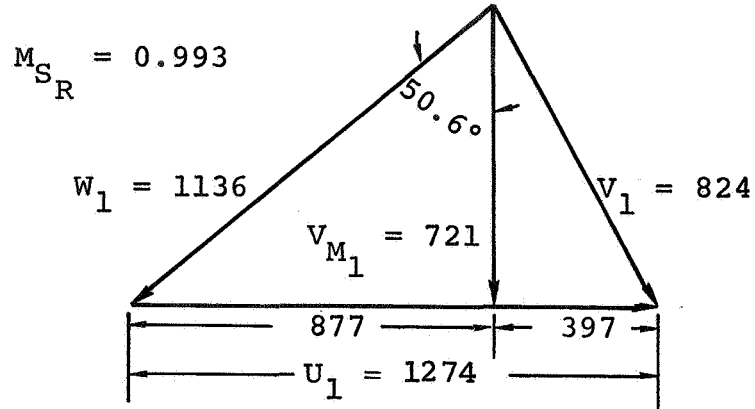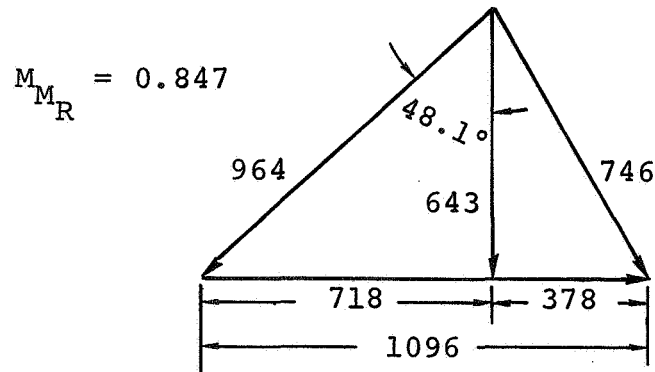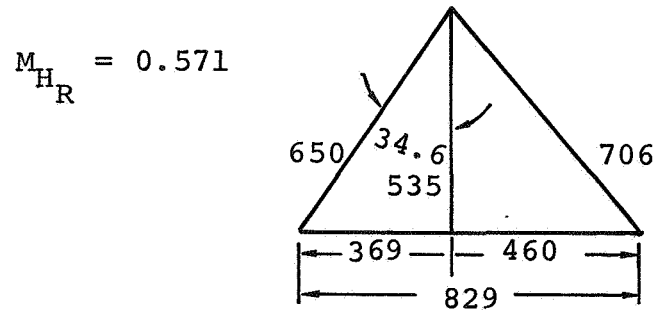
Figure 56. - Final vector triangles - impeller section (immediately upstream of blade).

IMPELLER EXIT

SHROUD

$\beta_{FL} = 38.1°$

$\beta_{BL} = 30.8°$

$V_2 = 1513$

$V_{M_2} = 650$

$M_2 = 826$

510   1366

$U_2 = 1876$

MEAN

$\beta_{FL} = 38.0°$

$\beta_{BL} = 30.8°$

1514

649

824

508   1368

1876

HUB

$\beta_{FL} = 37.6°$

$\beta_{BL} = 30.4°$

1521

653

824

503   1373

1876
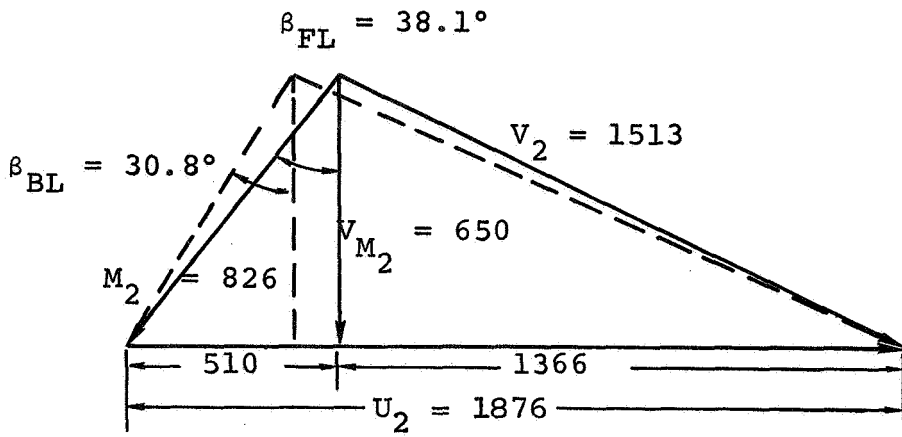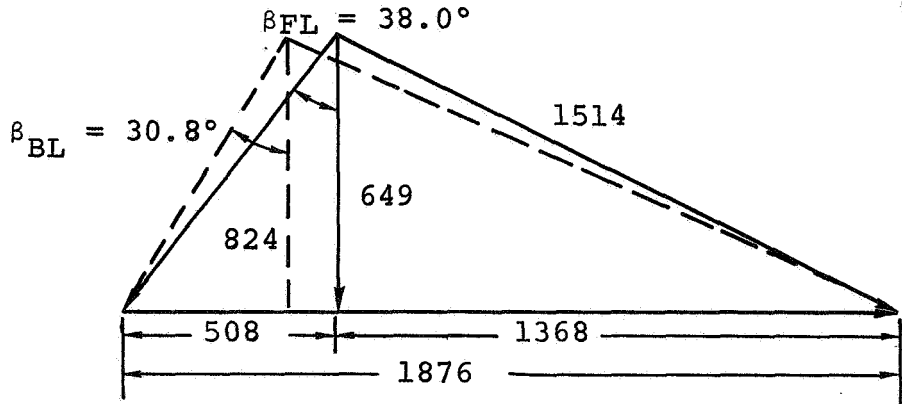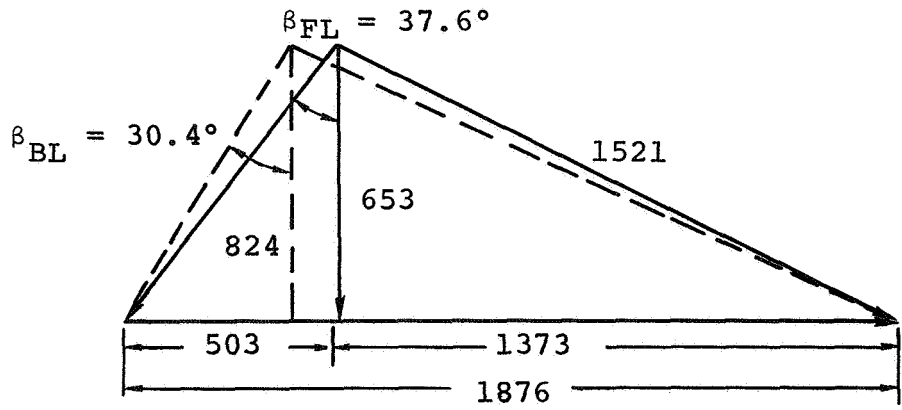
Figure 57. - Final vector triangles - impeller section (inside the blade).

A front view of the design impeller is shown on figure 58.
This impeller had a zero rake angle at the impeller exit. Stress
calculations made by Applied Mechanics showed this design to be
quite satisfactory mechanically despite the leading edge lean
shown here. (Refer to Appendix A.) However, a comparison of the
impeller leading edge with the inducer trailing edge indicated
that there might be problems associated with circumferentially
aligning both sections.

Inducer-Impeller Matching

One potential advantage of the tandem arrangement was that
boundary layer energization might have been accomplished through
proper alignment of the inducer and impeller blades. This was
somewhat debatable in the design since there was no blade overlap
between sections. However, some benefit should have been derived
from the fact that the impeller boundary layer was renewed entire-
ly by the tandem blading. At the same time, an attempt was made
to determine whether blade alignment could produce any boundary
layer energization effects. With this in mind, an investigation
was undertaken to examine the possibilities of matching the flow
from the inducer trailing edge to flow conditions at the impeller
leading edge. Then, since the inducer section could be rotated
with respect to the impeller, a variety of alignment configura-
tions was obtainable for experimental evaluation.

During the inducer-impeller matching effort, two drawbacks
were encountered. First, inducer blade stresses precluded suffi-
cient lean to match with the centrifugal leading edge. Secondly,
because of 5-axis cutter restrictions, the impeller leading edge
could not be curved to mate with the inducer trailing edge. As
a result, an alternate design was developed in which the inducer-
impeller sections were matched in the tip region over all but
the hub region of the blade.

Two problems were quite evident in attempting to line up the
trailing edge inducer and leading edge centrifugal sections. The
inducer section could not be leaned sufficiently to match the
centrifugal leading edge because of excessive blade stresses for
the inducer. At the same time, the impeller leading edge could
not be curved to match the inducer trailing edge because of 5-
axis cutter limitations. Hence, a compromise design was devel-
oped in which the two sections were matched in the tip region
over most of the blade except for the hub region. A front view of
the design inducer-impeller alignment is presented in figure 59.
A top view showing the blade alignment along streamlines is pre-
sented in figures 60 and 61. The latter figures show that the
blades can be matched quite well down to the 75 percent stream-
line, but the hub section does not match at all. However, a mis-
match in the hub region may not be too significant, since the
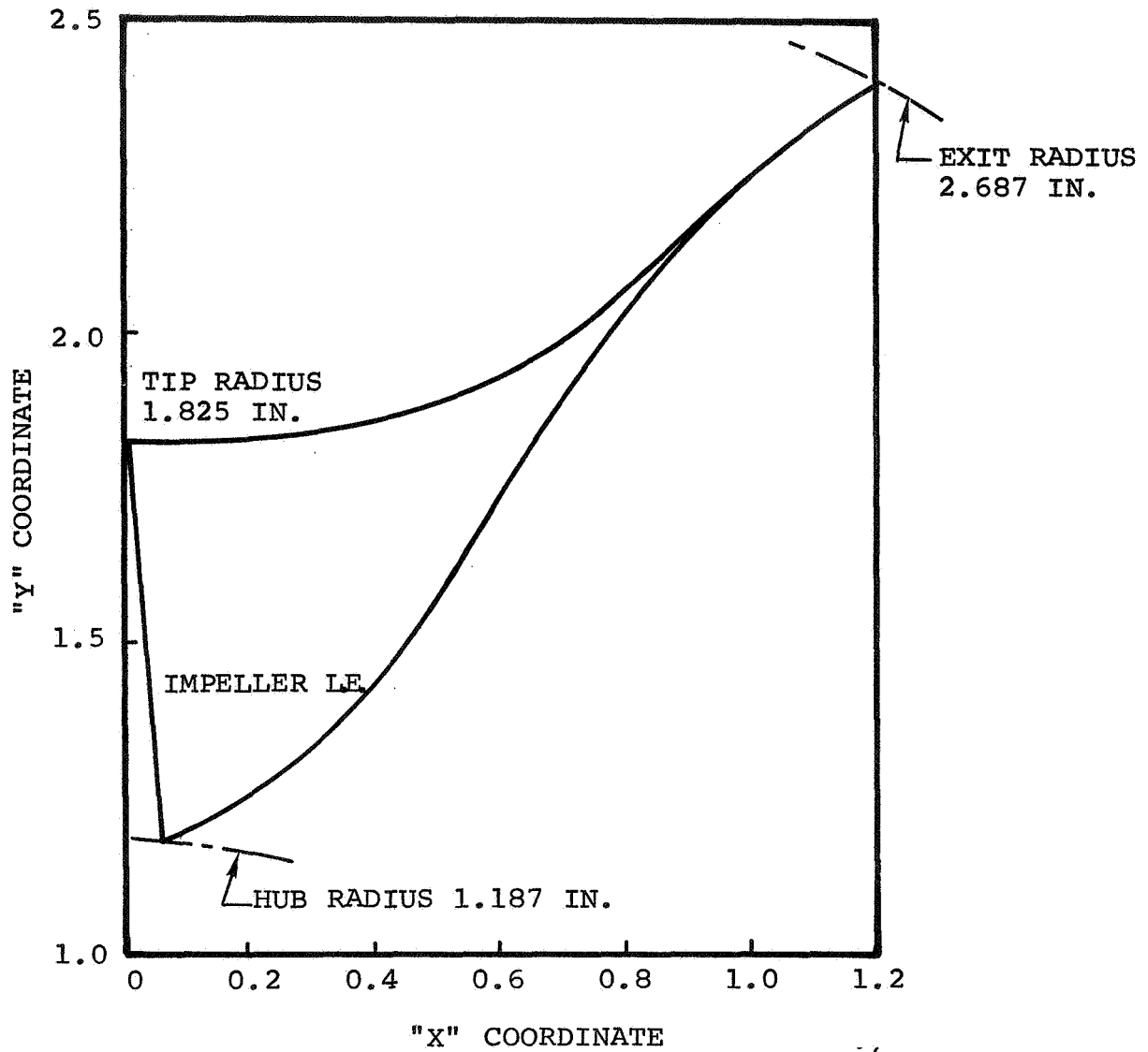
Figure 58. - NASA 6:1 advanced centrifugal compressor
impeller front view.

90
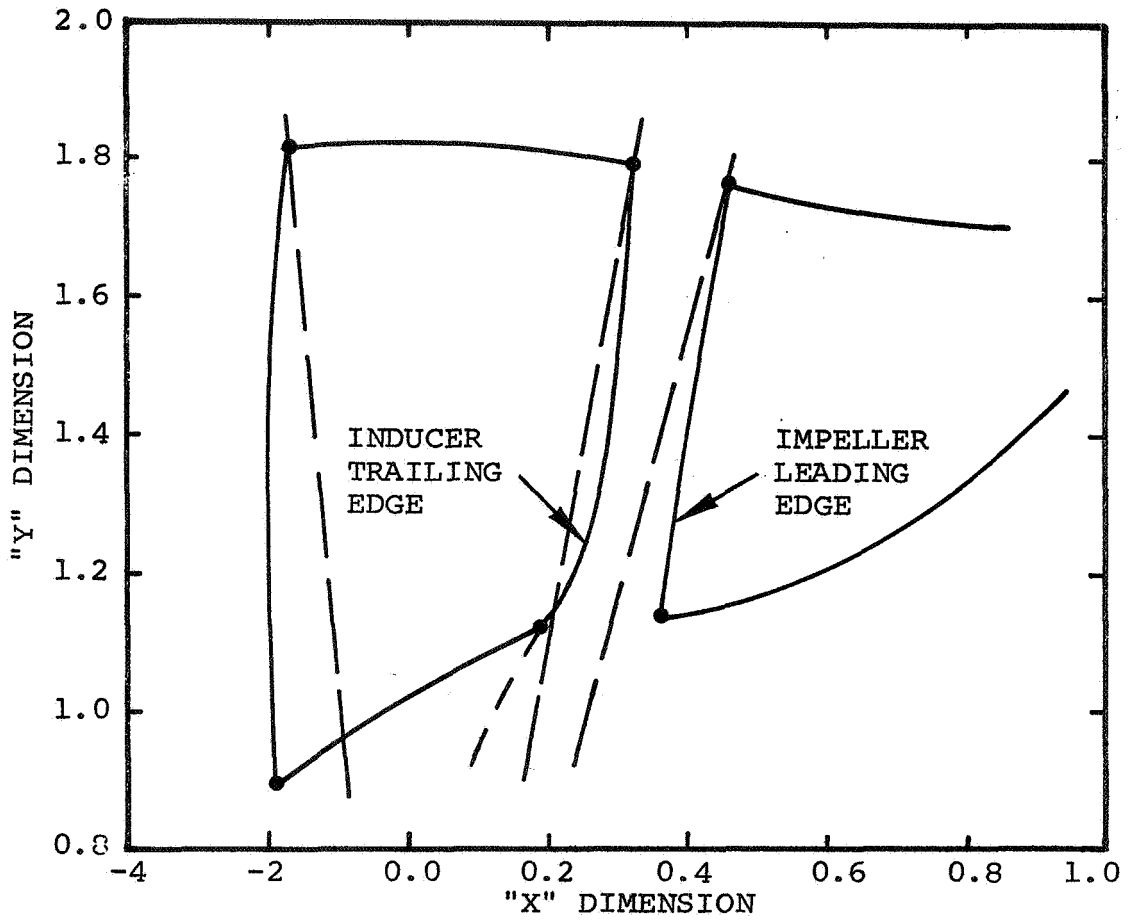
Figure 59. - Front view of inducer-impeller.
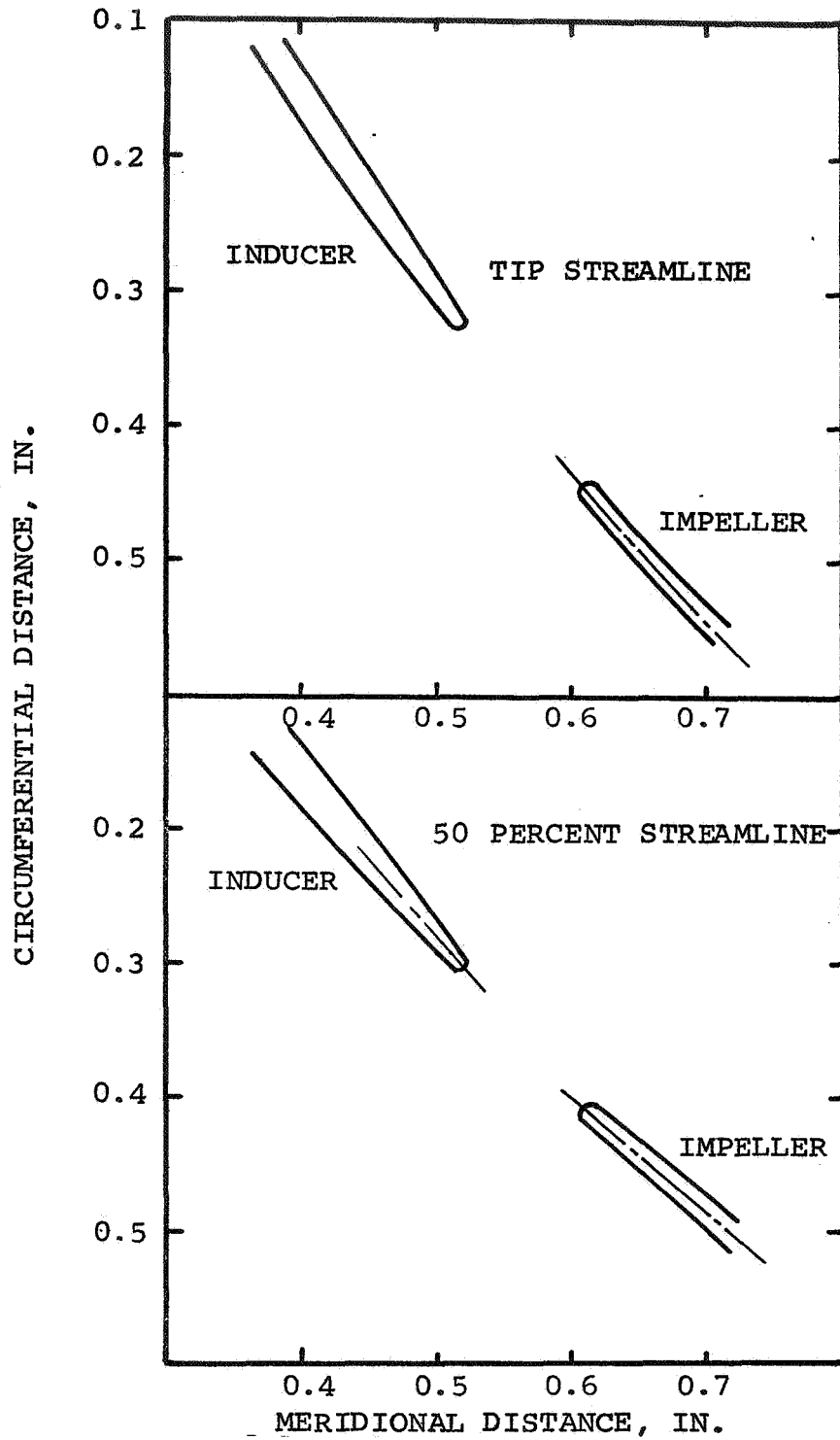
Figure 60. - Cascade projection of inducer-impeller alignment.
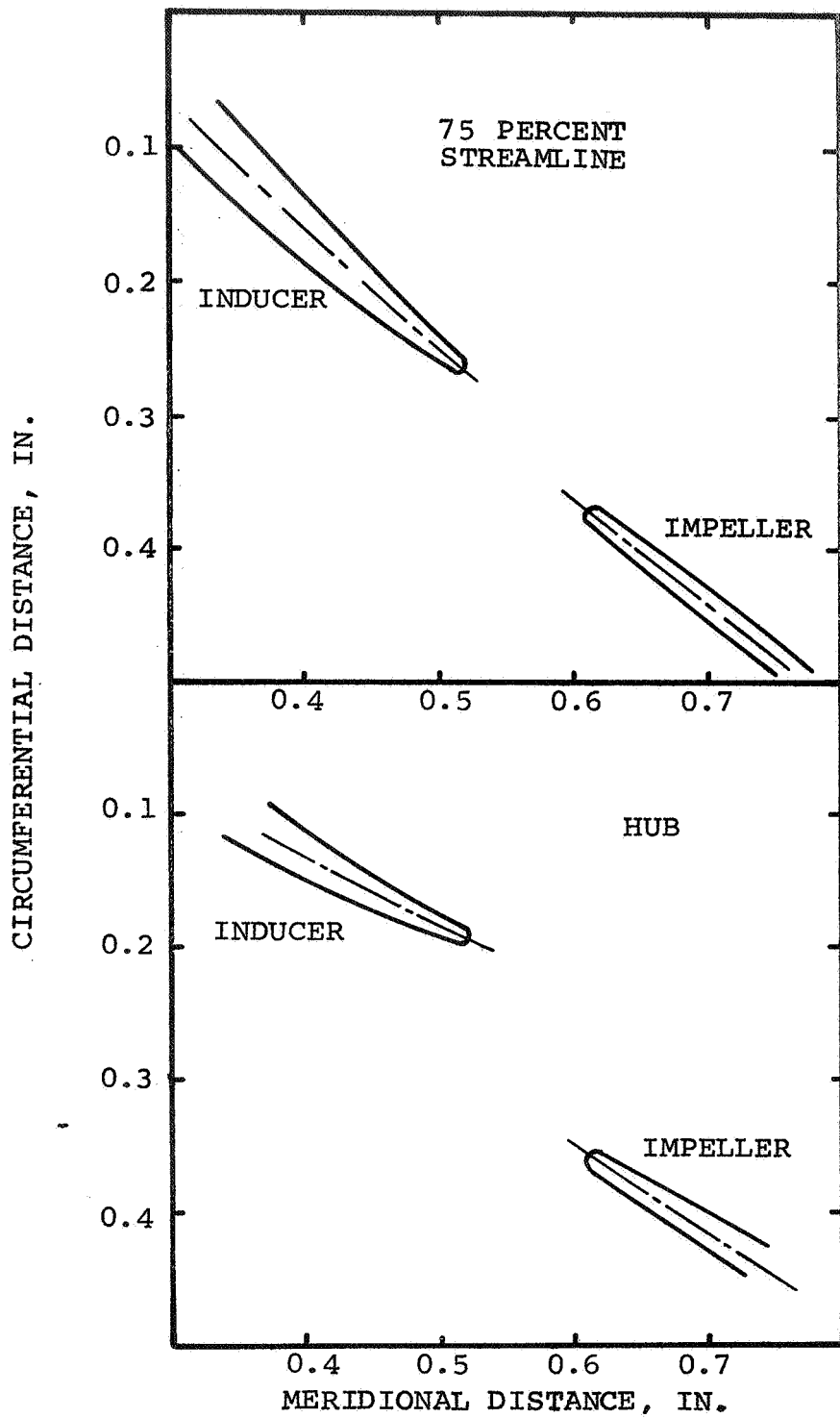
Figure 61. - Cascade projection of inducer-
impeller alignment.

boundary layers in this region are quite thin and boundary-layer energization would have little, if any, effect.

These figures also show the blade sections in line, which would not be the orientation if boundary-layer energization is desired. For a tandem arrangement of two airfoils, the preferred orientation is to let the flow from the pressure surface of the upstream blade pass over the suction surface of the downstream airfoil to impede stall. This may also benefit the existing design as a means of extending the operating range by restricting surge. It is suggested that initial testing be accomplished with the impeller leading edge at the midpoint between the inducer trailing edge. Later tests can then explore the feasibility of boundary-layer energization.

An initial loading check with 24 blades indicated that the front end of the centrifugal portion was lightly loaded with the remaining blade loading quite reasonable. AiResearch practice with centrifugal impellers is to lightly load the inducer section (primarily for range considerations). However, this design has a separate inducer section ahead of the centrifugal section which may negate any advantages for a lightly-loaded impeller inlet. By cutting back every other blade, the loading in the inlet portion of this wheel can be increased. Also, the cut-backs could be made in several steps to determine to optimum splitter location.

A cursory attempt was made to evaluate the blade loadings for a cut-back in every other blade in the centrifugal portion of the tandem impeller. An analysis was made for 12 blades for Stations 11-15 and 24 blades from Stations 16-25 (see figure 24). The resulting blade loadings are presented in figures 62 and 63 for the shroud and hub regions, respectively. These loadings may not be too excessive in light of the fact that the impeller is preceded by a separate inducer. Some concern must be expressed for the high rate of diffusion on the impeller inlet pressure surface in both the shroud and hub region. The adverse pressure gradient along this surface would probably result in boundary-layer separation. However, there is a good chance the separation would be localized and that re-attachment would occur just downstream in a more favorable pressure gradient region. Another factor that could be cause for concern is the low relative velocity along the pressure surface in the hub region (figure 63). AiResearch practice in centrifugal compressors is to avoid too low a minimum velocity in this region because of possible flow reversals. There seems to be little doubt that the splitter configuration would have less range than the final design impeller configuration.

94
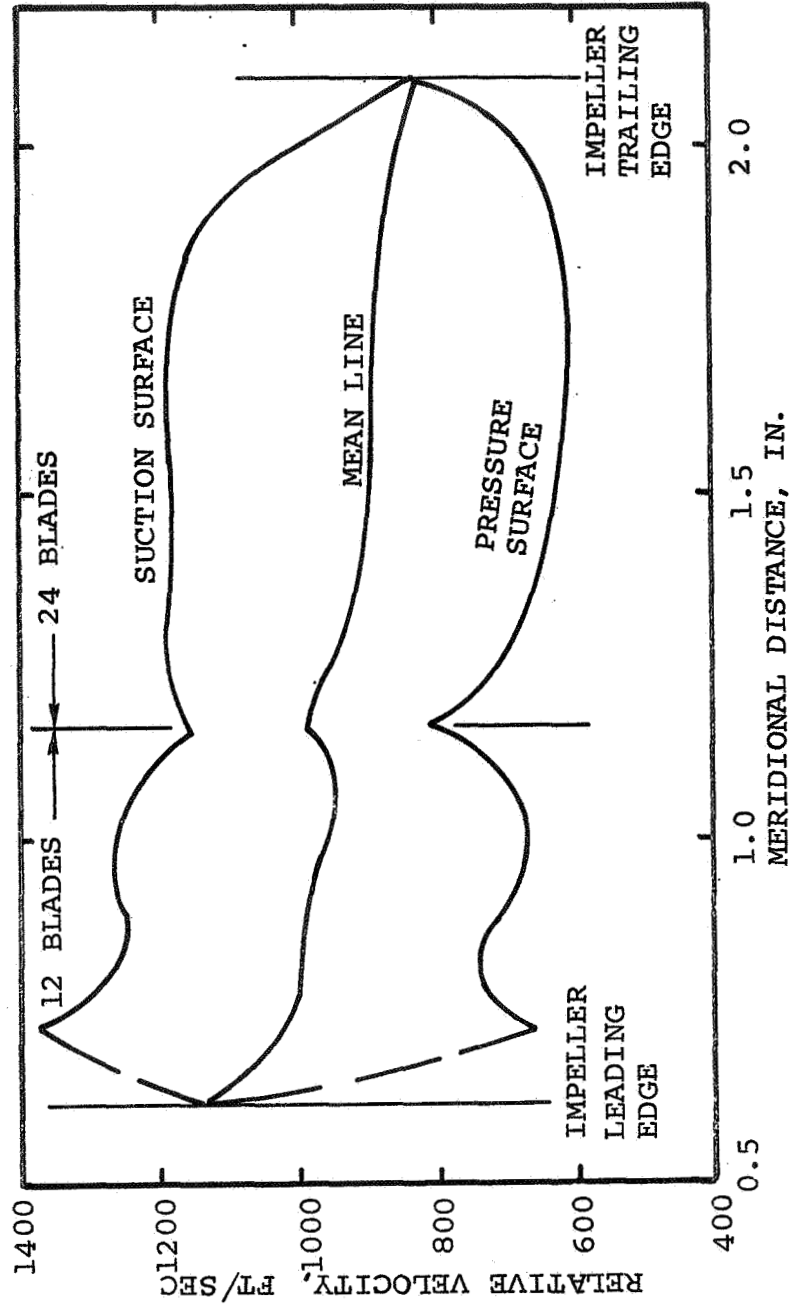
Figure 62. Blade loading in shroud region impeller with 12 blades plus 12 splitters.

95
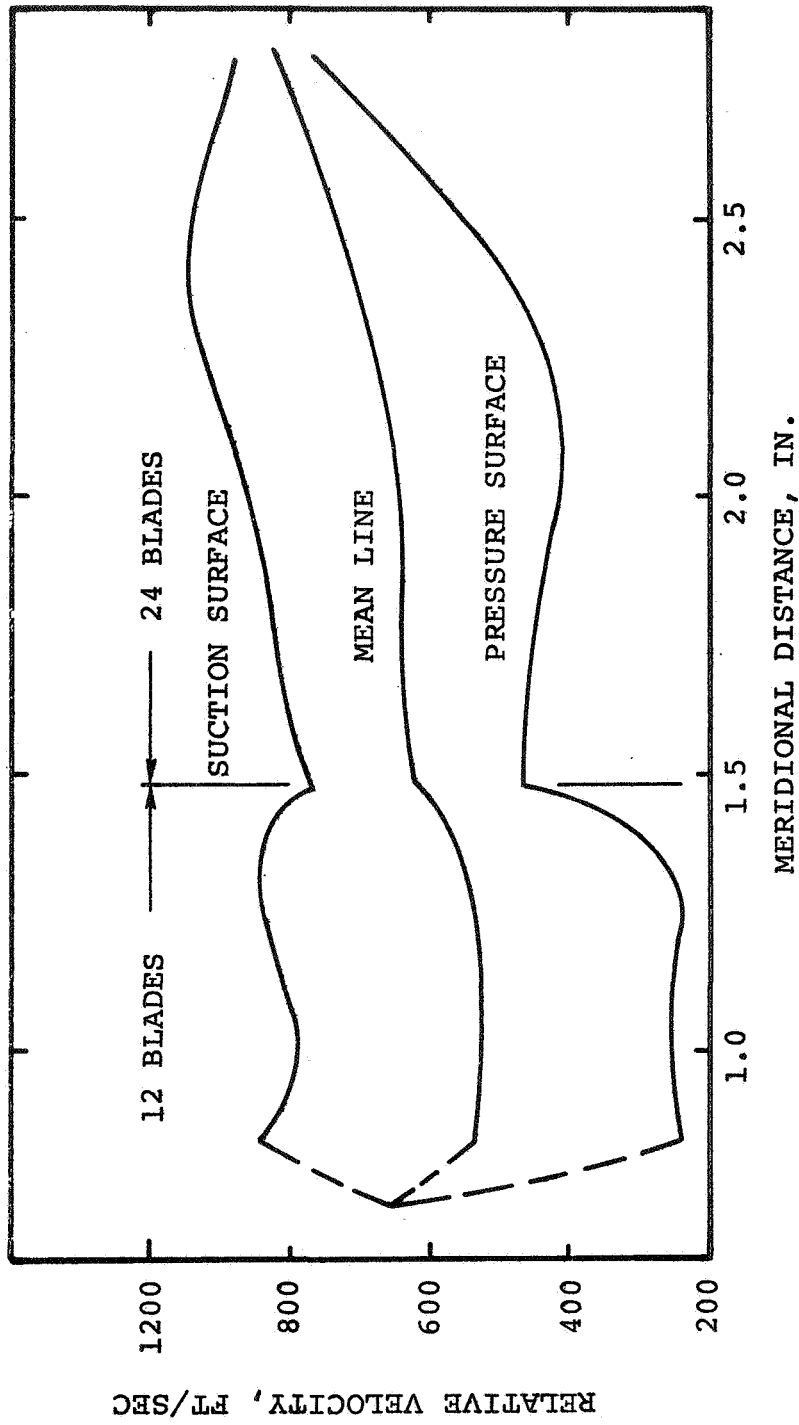
Figure 63. - Blade loading in hub region impeller with 12 blades plus 12 splitters.

Cascade Vane Diffuser Design

The cascade diffuser design utilized two radial cascade blade rows to diffuse and straighten the airflow. The airfoil shapes were NACA 65 series transformed from the axial to the radial plane. Cascade diffuser tests at AiResearch provided data on the loss and turning characteristics of the various sections. Loss trends were similar to those of the NACA two-dimensional cascade data, but the levels had to be increased by a factor of 6.0 to 8.0 to account for low aspect ratio and secondary flow effects. Measured turning characteristics generally indicated some overturning due to the three dimensionality of the flow. Each of these effects was accounted for in the design.

Both two- and three-row cascades were examined for diffusion to the required Mach 0.2 exit condition. It was found that a two-row cascade followed by a vaneless space resulted in a slightly higher pressure recovery than a three-row cascade. The large exit radius for this design was a result of the vaneless space diffusion from a Mach number of 0.306 to 0.20.

The final design was comprised of a tandem configuration shown schematically in figure 64. The first row utilized a NACA 65-4(A10)06 section definition and the second row a NACA 65-10 (A10)06. Based on AiResearch experience, the salient parameters for the two cascade rows were chosen as follows:

	1st Row	2nd Row
Solidity $\dfrac{L}{S_{mean}}$	0.8	1.0
$\dfrac{R_{exit} - R_{inlet}}{R_{imp\ exit}}$	0.15	0.3
Diffusion ratio	0.55	0.55 - 0.60
Min loss angle of attack	3.5 deg	12 deg

These parameters yielded a vane count of 22, a number which implied an acceptable thickness from a stress and a manufacturing viewpoint.

Boundary-Layer Control

The basic purpose of any boundary layer control device is to prevent growth to an unstable condition, thereby prohibiting separation of the flow from the confining walls. As a result of the diffusion inherent in the compressor process, the boundary layer

4.434 IN. RADIUS

3.627 IN. RADIUS

3.224 IN. RADIUS

S_{MEAN}
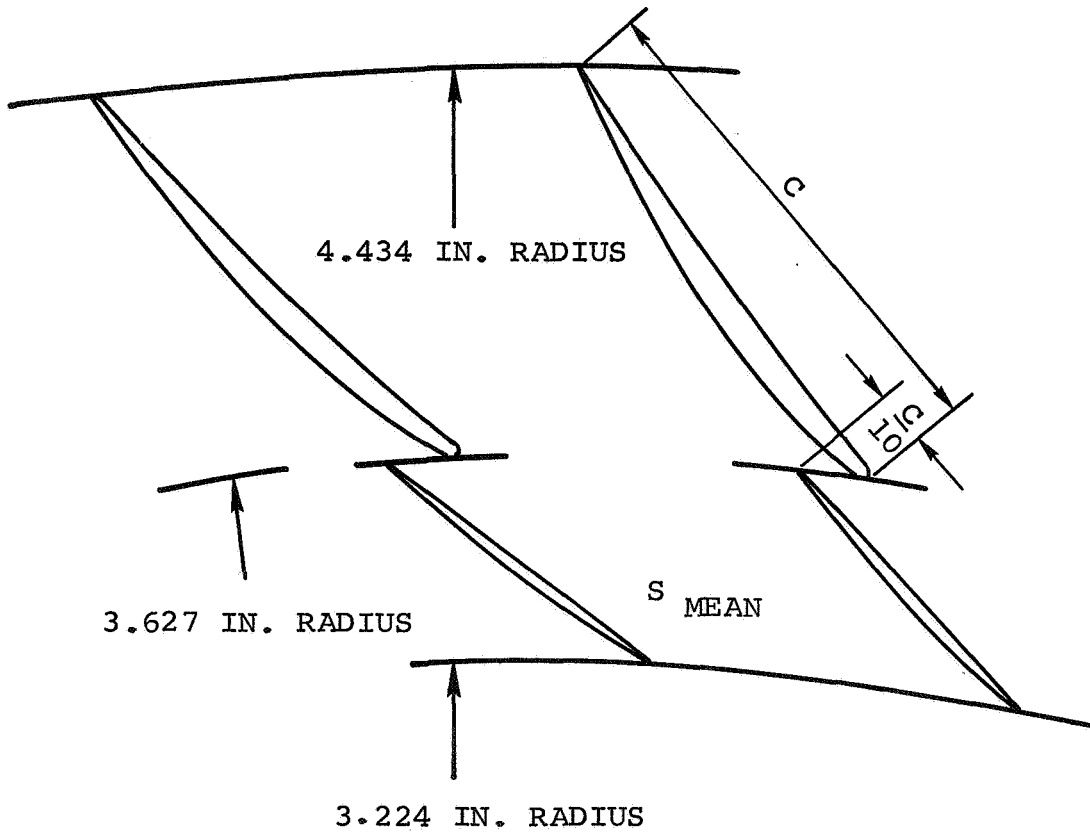
Figure 64. - Cascade diffuser vane alignment
schematic.

is subjected to large adverse pressure gradients and grows rapidly. Judicious design can minimize, but not eliminate, this growth. Because higher stage pressure ratios are required, the problem of eliminating flow separation and the subsequent compressor losses becomes more acute. Where flow separation does occur, boundary-layer control becomes desirable.

Two common methods of control are energization and removal of the boundary layer. In the former, high-energy fluid is introduced parallel to the flow direction in regions where the boundary layer may be weak. In the latter, low-energy fluid is removed from the boundary layer in regions where separation is imminent. In the design of the advanced compressor, a form of boundary-layer energization was employed in both the impeller and diffuser. The tandem impeller and cascade vane diffuser could be considered energization-type, boundary-layer control devices. Boundary-layer removal was also employed as a method of control on the advanced compressor. Control was accomplished by withdrawing the boundary layer through a series of bleed ports on the impeller shroud wall and on the diffuser side wall. The bleed ports are a series of in-line holes effectively spaced around the periphery such that conditions approach withdrawal through a continuous slot. An analysis and description of the boundary layer control schemes used for the advanced compressor is presented in the following paragraphs.

Impeller Boundary Layer Control: Analysis of the impeller boundary layers was accomplished through the use of a calculation program based on Truckenbrodt's method as modified by Scholz. This program computed the characteristic parameters of a two-dimensional boundary layer including compressibility effects and heat transfer to the wall. Both laminar and turbulent flows were handled by the program as well as a prediction of transitions from laminar to turbulent boundary-layer conditions. The basic program required specification of the free-stream velocity as a function of flow path length. Flow separation was predicted by a rapid drop-off in friction coefficient with length. A wide variety of test data was used to check program results and agreement in all cases was excellent.

When examining the impeller, several boundary layer conditions had to be considered. In the neighborhood of the shroud, a shroud boundary layer was calculated based on the mean absolute velocity component and corresponding path length. Relative velocities along the suction and pressure surface at the impeller tip were used to define two additional boundary-layer conditions along the shroud. In the hub region, suction and pressure surfaces as well as the mean relative velocities were employed in the boundary-layer analysis.

Results of boundary layer calculations for the shroud and
hub regions are shown in figures 65 and 66, respectively. These
are plotted as displacement thickness against a nondimensional
distance for flow between the impeller inlet and exit stations.
In the shroud region (figure 66), the boundary layer on the impel-
ler pressure surface grew quite rapidly with flow separation indi-
cated at about 45 percent of the flow length. The boundary layer
on the corresponding suction surface of the impeller indicated a
nominal growth rate over most of the blade with a rapid increase
in displacement thickness toward the trailing edge. In this
case, flow separation was evident over the latter 5 percent of
the blade length. Examination of the shroud boundary layer gener-
ated by the absolute velocity between blades indicated very stable
conditions because the absolute velocity component accelerated
even when operating under an adverse static pressure gradient in
the direction of flow. This indicated that while the impeller
blades themselves might have flow separation problems in the tip
region, the boundary layer along the shroud wall was quite stable.
However, in actual practice, this was not the case since the
boundary layers on the impeller tended to migrate to the tip and
then to the shroud wall as a result of centrifugal forces. There-
fore, flow separation on the pressure surface at the impeller tip
would expand into the shroud region and possibly trigger flow
separation across the entire area between the blades.

Boundary layers in the hub region of the impeller (figure 66)
exhibited more stability than those found in the shroud region.
The impeller pressure-surface boundary layer in the hub region
indicated rapid growth initially, but a diminution further down-
stream as a result of the circumferential area variation. No
flow separation was indicated by computer results; however, a
local separation would have been more realistic because of the
strong adverse pressure gradient at the impeller inlet. The mean-
flow and suction-surface conditions were quite stable and would
cause no problems. These results seemed to indicate that
boundary-layer control was more effective on the upper portion of
the impeller blade and along the shroud wall. Recalling that the
inducer-impeller alignment situation permitted limited matching
of flow conditions between blade sections, a possible mismatch in
the hub region would not have a significant effect on the
boundary-layer energization results.

Lampblack traces from several previous tests of AiResearch
impellers indicated the existence of flow separation along the
shroud wall. A typical case was the AiResearch Model TFE731
Turbofan Engine centrifugal stage which showed a flow separation
region on the shroud wall starting at about 40 percent of the
meridional distance between the impeller inlet and exit stations.
Analysis of the shroud and impeller tip boundary layers showed
that: (1) flow separation occurred on the impeller tip pressure
surface, and (2) the separation location was quite close to that

100
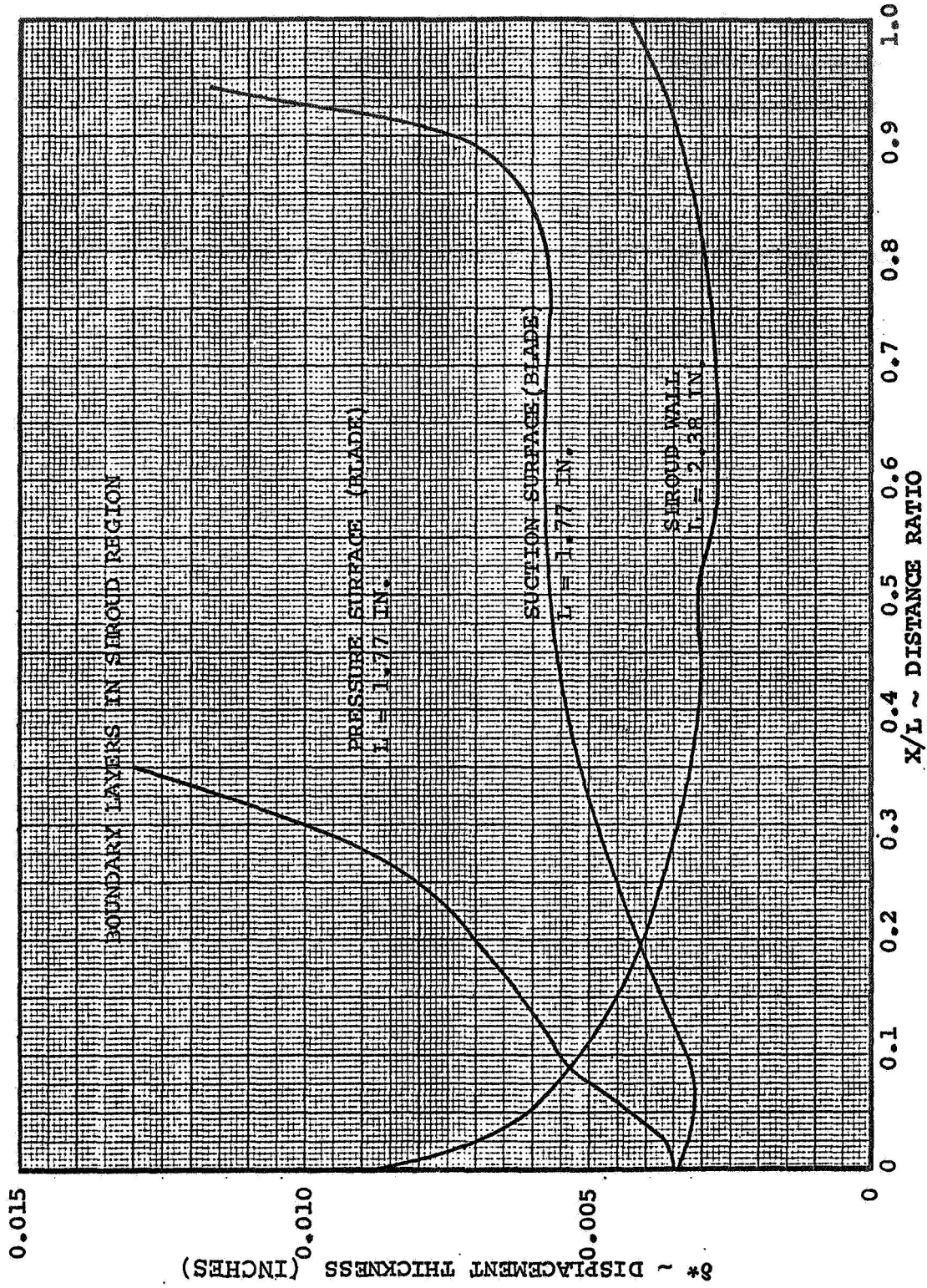
Figure 65. - Boundary layers in shroud region.
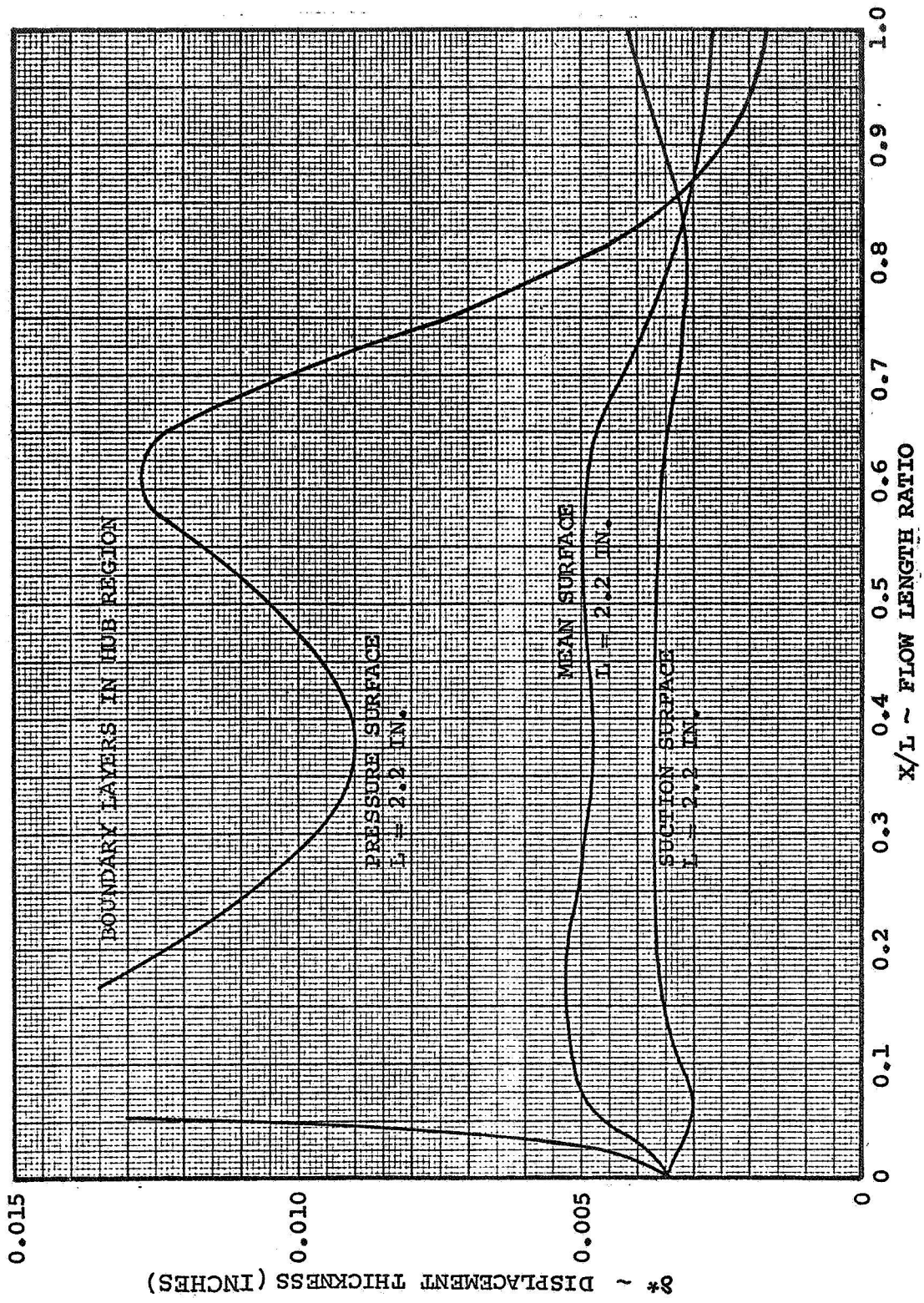
Figure 66. – Boundary layers in hub region.

102

found experimentally in the lampblack tests. The relatively good agreement between analysis and experiment was encouraging, thereby serving as a basis for selecting the bleed locations for the advanced-compressor, boundary-layer control system within the impeller. Resulting bleed port locations for the advanced compressor are shown on figure 67. Location 1 corresponds to a point of the shroud which is just upstream of the calculated separation point for the impeller tip pressure surface. Location 2 corresponds to separation on the impeller tip suction surface. The existance of the latter separation region was not verified experimentally. However, there was a strong possibility that there could have been separation problems in this region. Consequently, a separate boundary-layer bleed system was provided.

An analysis was made to show the effect of bleed on the boundary layer growth for the impeller pressure surface. The resulting displacement thickness distribution with bleed is shown on figure 68. The approach used to make these calculations was to assume that the displacement thickness was reduced by the amount of bleed flow. (Two percent of the total flow was the assumed bleed flow for these calculations.) Results indicated that bleed does stabilize the boundary layer on the impeller pressure surface which would improve impeller performance.

Diffuser Boundary-Layer Control: Analysis of boundary-layer build-up within the diffuser required some revision to the existing boundary-layer program. The computer program was set up to calculate internal flow situations where the core flow was either supersonic or subsonic throughout the flow length. Mixed flows with transition through sonic flow conditions caused the program to blow-up. A change was made to allow the program to compute radial and tangential velocity components in the core flow separately. These were then combined to determine the absolute velocity of the core flow for use in the boundary-layer calculations. A comparison of the revised boundary-layer program results with the conventional vaneless space program based on the Stanitz (ref. 6) method illustrated substantial agreement as shown on figures 69 and 70. Parameters compared in these figures, all plotted as a function of radius ratio, include static pressure, stagnation pressure, flow angle, and Mach number. The largest difference between the boundary-layer and vaneless-space program results occurred in the stagnation pressure calculation. This apparent discrepancy was unexplained at that time. Also, it was really somewhat inconsequential in that the program was to be employed in a more fundamental nature to examine the boundary-layer growth and stability characteristics in the vaneless diffuser region.
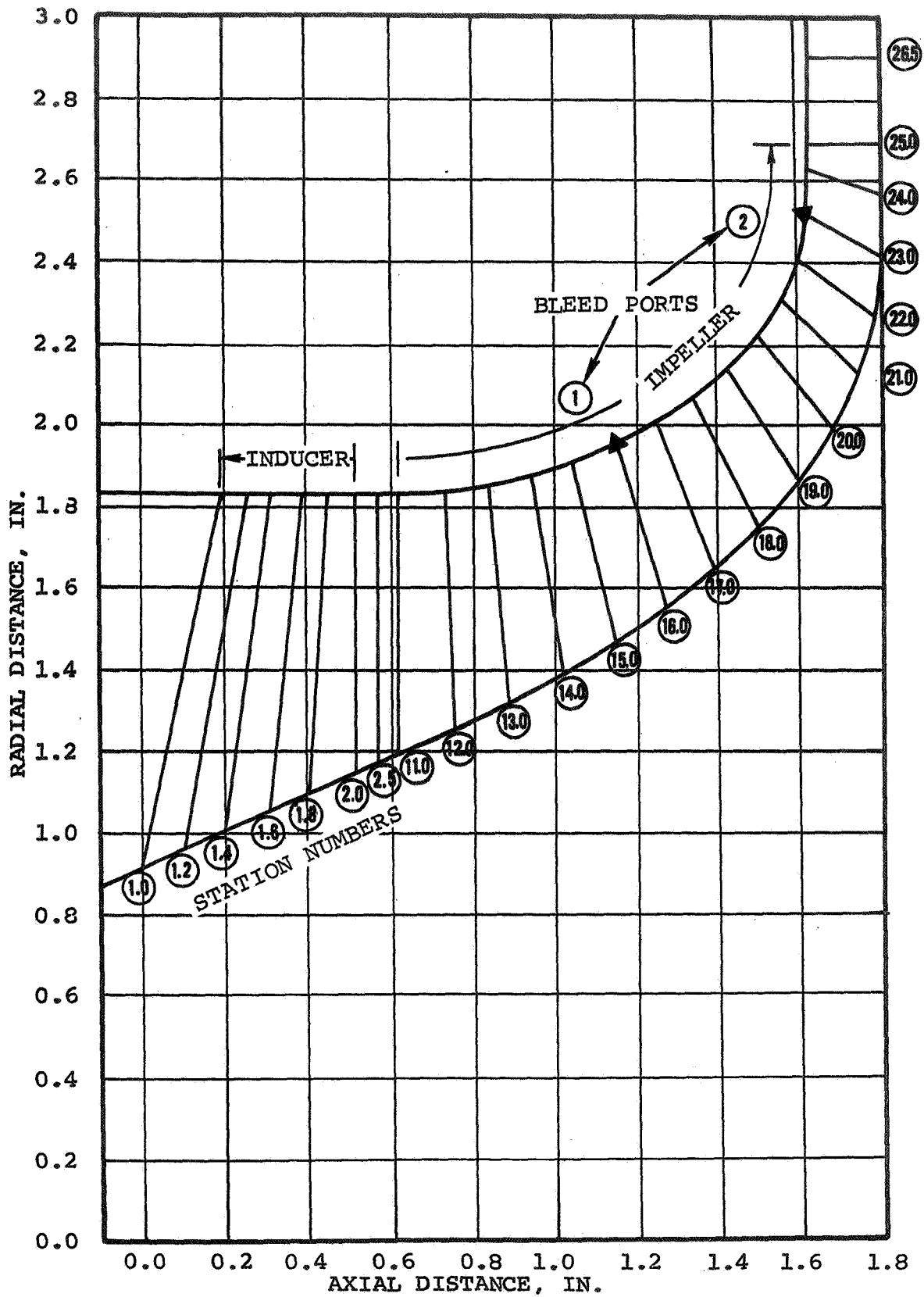
Figure 67. - Boundary layer bleed locations.
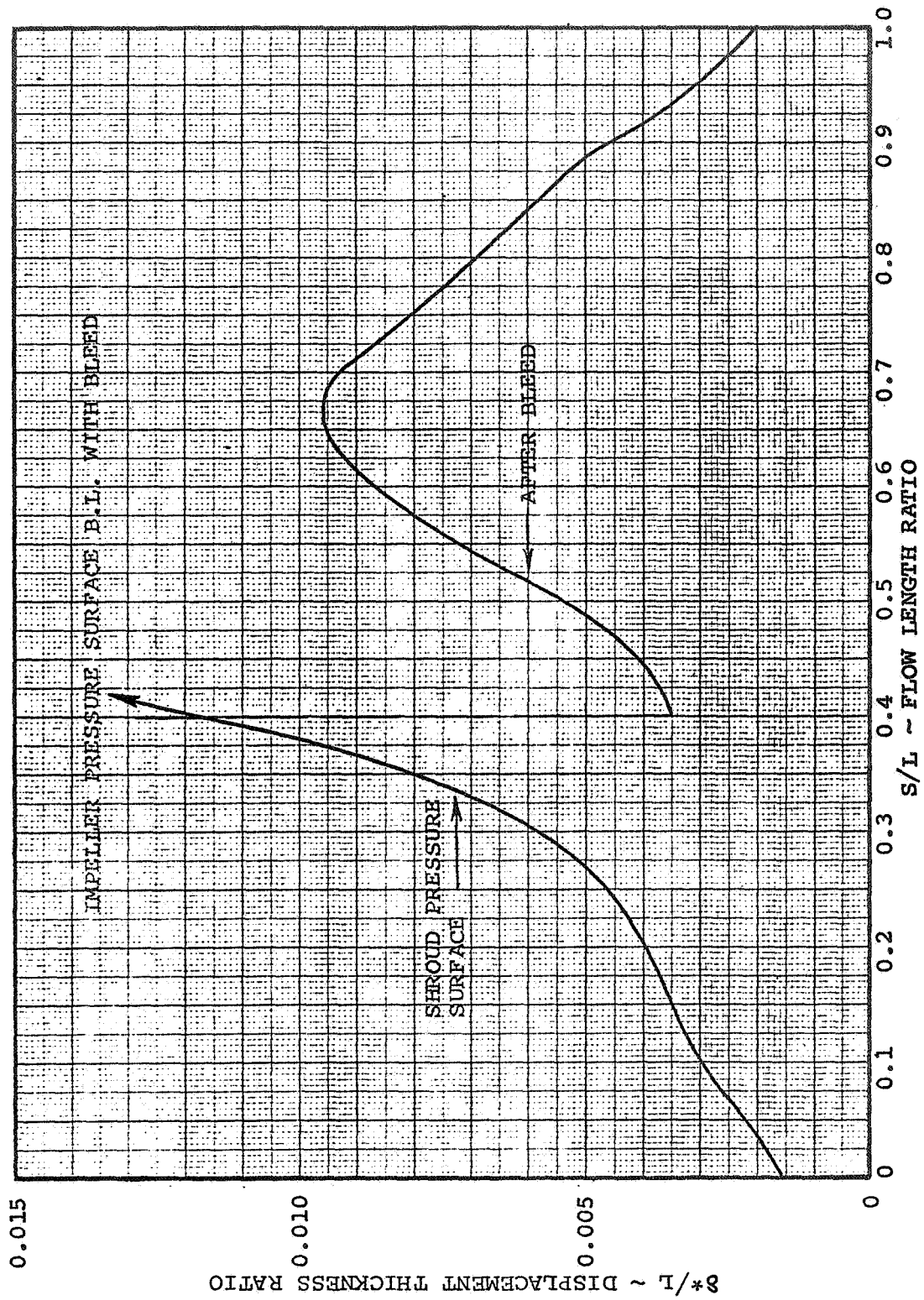
Figure 68. - Impeller pressure surface boundary layer with bleed.
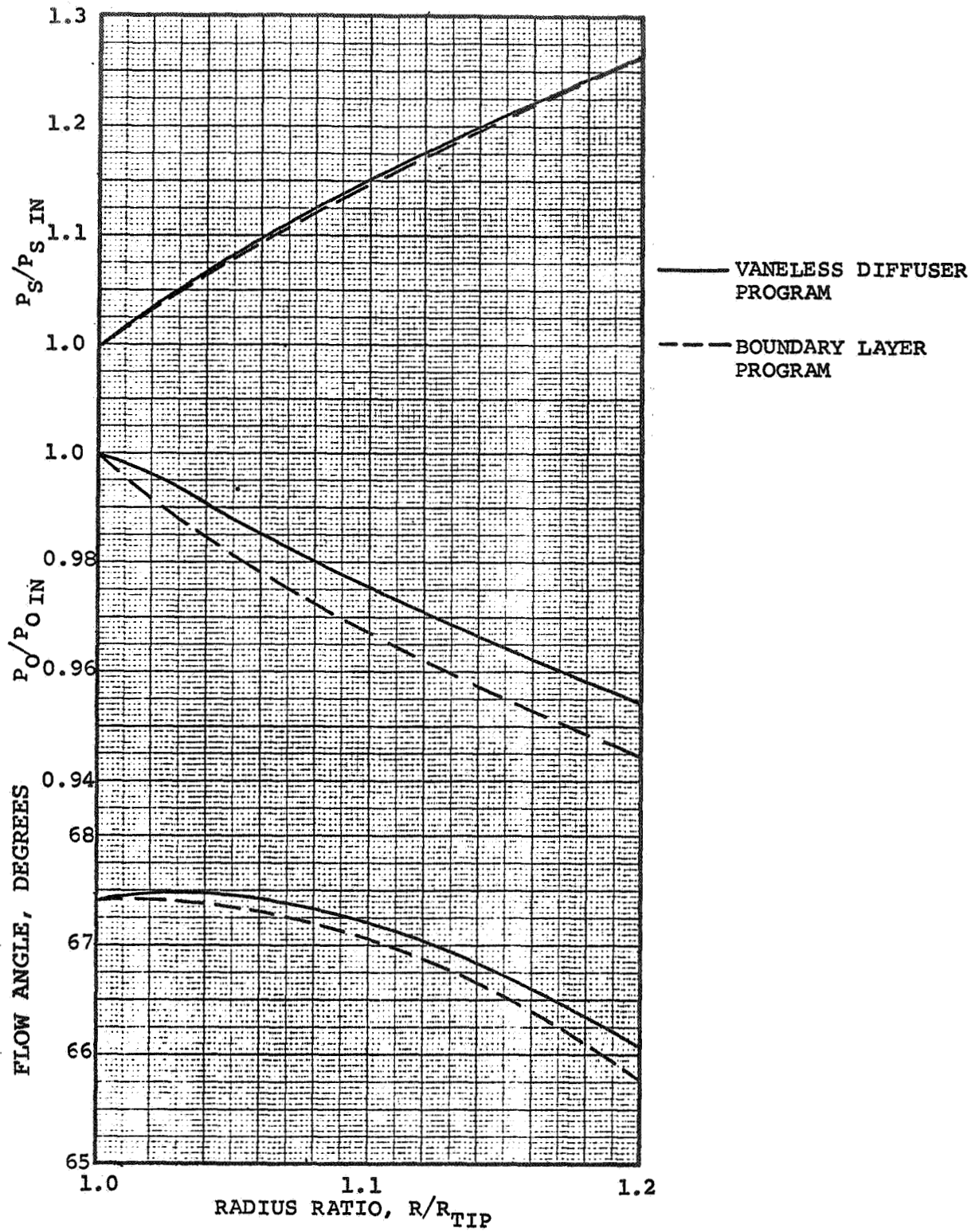
Figure 69. – Boundary layer program results for vaneless diffuser.
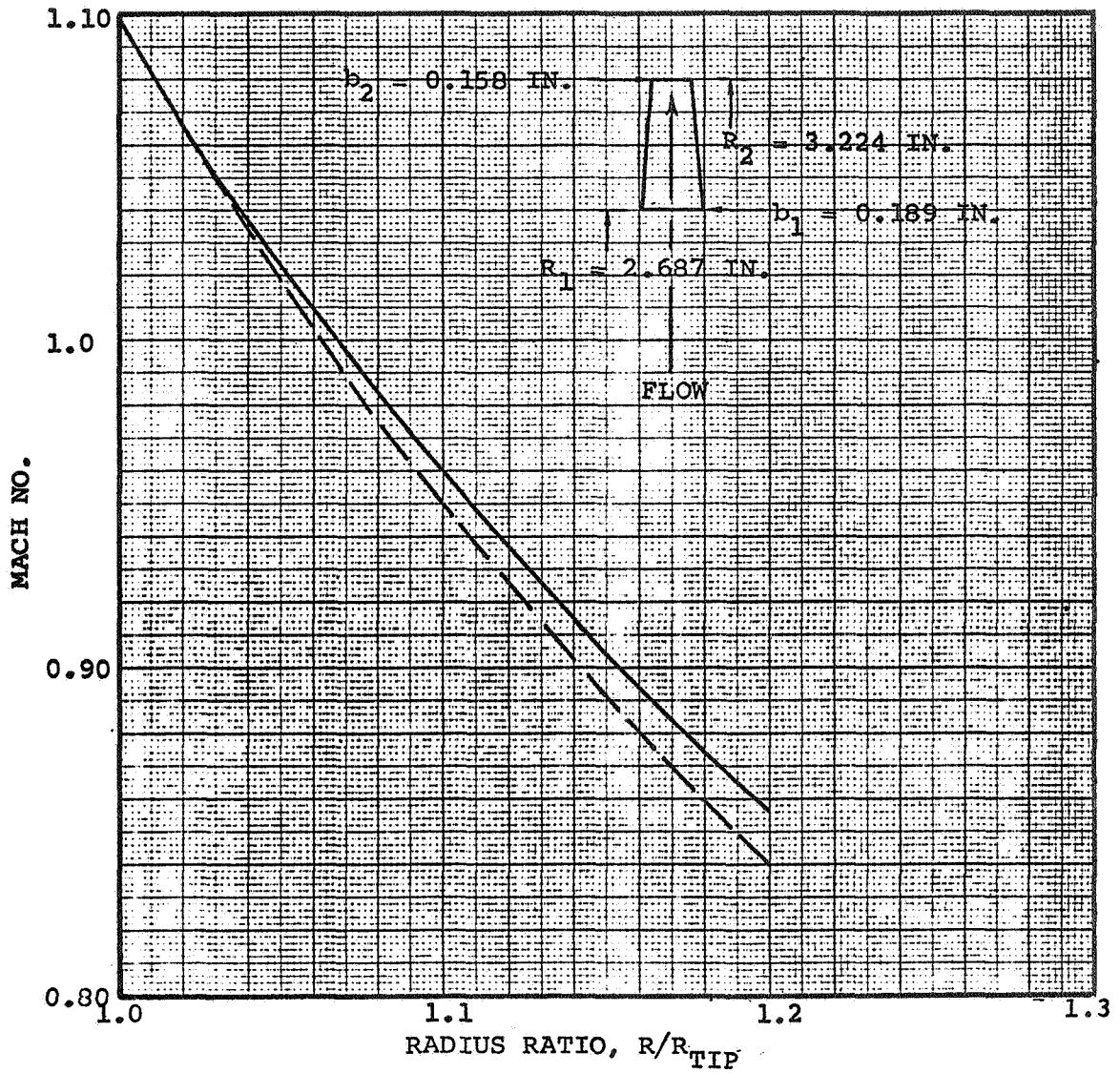
Figure 70. — Boundary layer program results for vaneless
diffuser.

The computed displacement thickness for the boundary layer in the vaneless diffuser is shown on figure 71. This shows the boundary layer to be quite stable over the entire vaneless diffuser region. The relatively smooth development of the boundary layer along the vaneless diffuser wall seemed to make a bleed station at the cascade diffuser inlet unnecessary.

Analysis of boundary-layer growth within the diffuser blade rows was made on the basis of mean-flow conditions through a rectangular diffuser. The assumed equivalent diffuser section for the first cascade row is shown in figure 72. The corresponding boundary-layer growth for the first vane row is shown on figure 73. This indicates a definite change in the rate of boundary-layer growth about midway through the vane row. The decreased slope of the displacement thickness curve was a result of the effect of the lower blade blockage on the area change through the passage. Obviously, the assumption of a mean equivalent diffuser of rectangular cross-section was a gross simplification of actual conditions. However, past experience at AiResearch had shown this to yield a fairly good approximation to actual diffuser performance. In this light, the boundary-layer program predicted a stagnation pressure ratio of 0.969 for the first cascade row, compared to a corresponding value of 0.97 calculated from the cascade diffuser design program based on AiResearch loss data.
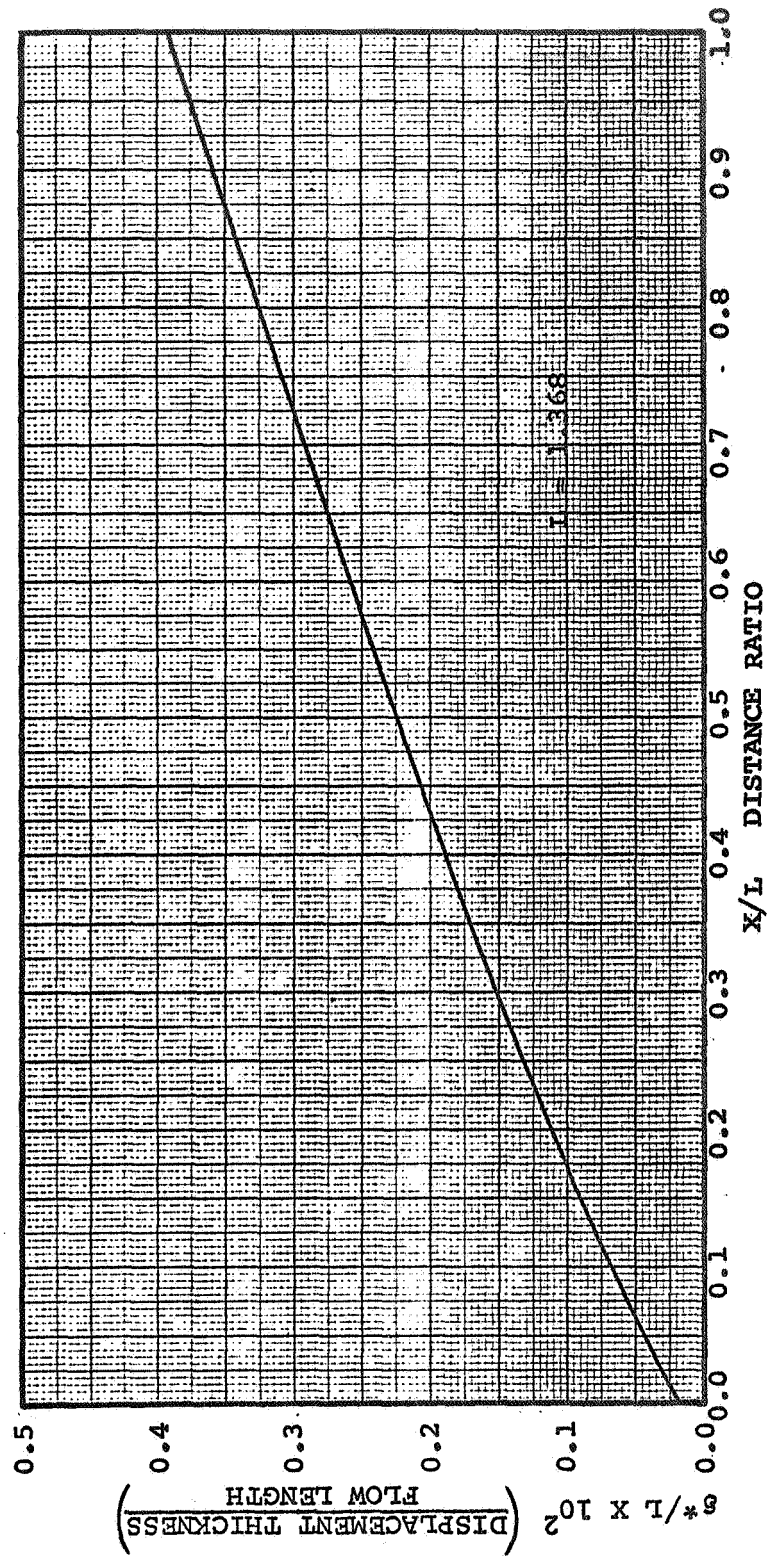
Figure 71. - Displacement thickness in vaneless diffuser.
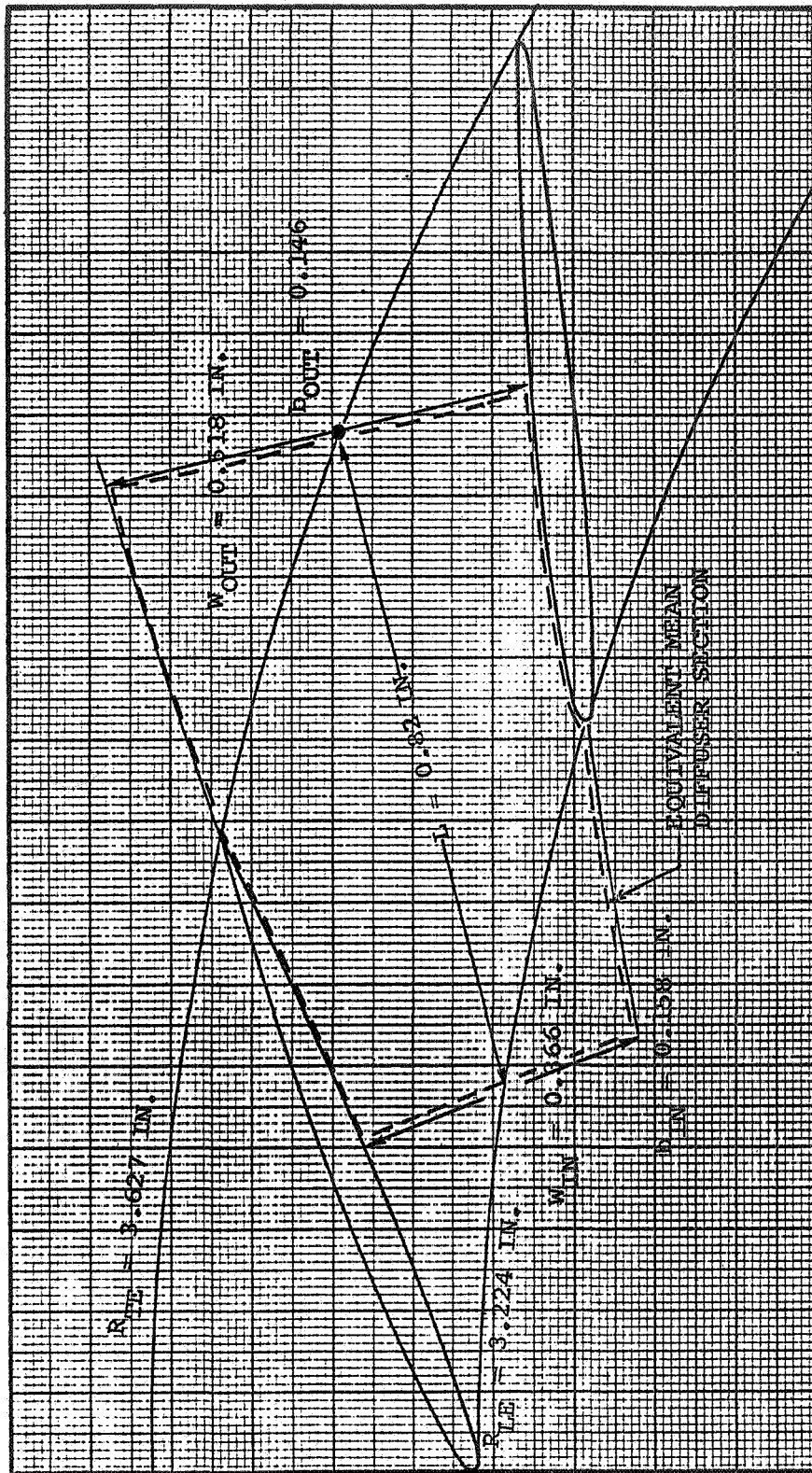
Figure 72. – First row cascade vane diffuser.

110
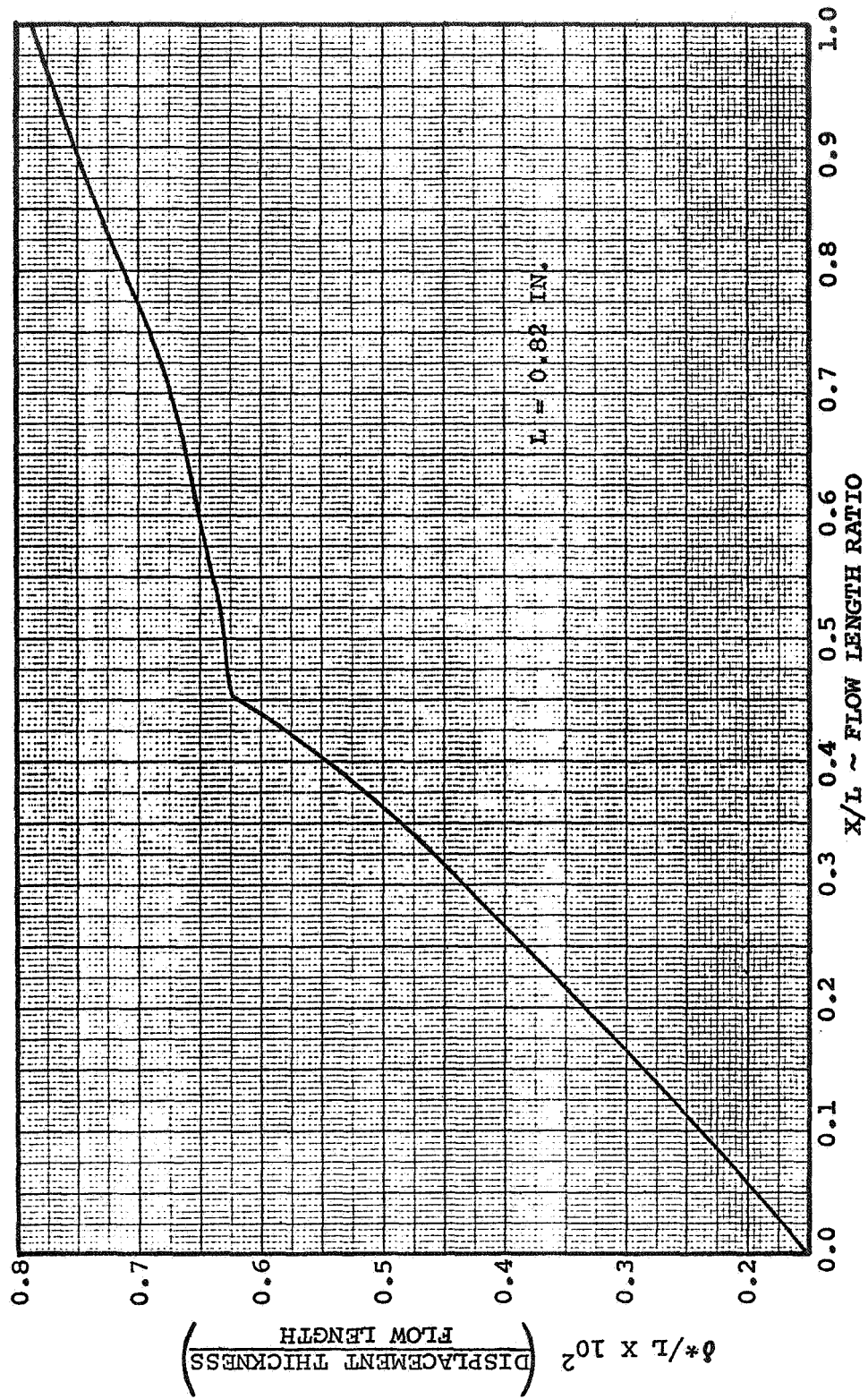
Figure 73. - Displacement thickness for first vane row.

TANDEM IMPELLER DESIGN SUMMARY

Inducer Portion

A list of the pertinent design parameters from the inducer is presented on table IV. Note that multiple-circular-arc blade sections were employed where the inlet flow was supersonic with double-circular-arc sections for subsonic inlet flow. Taper ratio across the blade was 2:1. The distance to the maximum camber rise (a/C) on the blade was at the midpoint of the chord for a double circular arc section, but moved toward the trailing edge as the design inlet Mach number increased. Supersonic camber ratio referred to the amount of turning for the uncovered inlet portion of the blade over the total blade camber. At high inlet Mach numbers, there was very little turning over the supersonic portion of the blade. Therefore, supersonic camber ratio was low at the tip, increasing to 0.49 at the hub.

The final vector triangles for the inducer section are presented on figure 74. These were computed by solving the internal flow-field through the blades with the blade blockage term included. The final flow solution was made with the inducer and impeller coupled together. The effect of the downstream impeller on the inducer air angle was quite significant. Therefore, final blade settings (stagger) for the inducer could not be accomplished until after the impeller was designed and both sections analyzed in series.

A front view of the final inducer blade design is presented in figure 75. Radial lines to the impeller tip section have been included on this figure to illustrate the blade lean at the leading and trailing edge.

Blade stacking for the inducer section did not follow standard axial design practice. Normally, a blade is divided into several radial plane sections and the center-of-mass determined for each section. The blade is next stacked about a radial line passing through the center-of-mass for each plane section. This obviously tends to minimize blade stresses and results in an optimum structural configuration. The straight trailing edge of the inducer design made stacking about the center-of-mass for each section impossible. A desire to match the inducer and impeller flow circumferentially also influenced the final stacking arrangement. However, blade stress considerations were primary so the final stacking arrangement became a best compromise. Additional details concerning the required compromises are discussed in the paragraph entitled Inducer-Impeller Matching. The final stacking arrangement of the inducer section is shown in figure 76.

TABLE IV. - INDUCER DESIGN PARAMETERS

	Tip	50 Percent	Hub
Inlet Diameter, in.	3.65	-	1.825
Exit Diameter, in.	3.65	-	2.28
Airfoil Type	MCA	MCA	DCA
Chord, in.	0.600	0.631	0.634
t_m/C	0.039	0.064	0.080
Camber, degrees	8.44	3.25	17.37
Stagger, degrees	59.6	50.9	35.49
a/C	0.733	0.582	0.5
Supersonic Camber Ratio	0.10	0.35	0.49
Solidity	1.26	1.60	2.35
Inlet Mach No.	1.34	1.11	0.76
Exit Mach No.	0.93	0.78	0.51
"D" Factor	0.359	0.358	0.42
V_{M2}/V_{M1}	0.925	0.905	0.923
Hub-Tip Ratio		0.5	
Aspect Ratio		1.29	
No. of Blades		24.0	
Pressure Ratio		1.525	
Adiabatic Efficiency		0.943	

HUB

$M_{H_R} = 0.756$

824

637

523

50.9°

MEAN

$M_{M_R} = 1.142$

1227

1031

665

57.2°

SHROUD

$M_{S_R} = 1.34$

1441

1274

674

62.1°

A. INDUCER INLET

$M_{H_R} = 0.562$

704

637

731

553

317

479

796

29.9°

$M_{M_R} = 0.799$

914

697

591

1080

383

44.7°

$M_{S_R} = 0.93$

1074

877

736

620

1274

347

54.8°

B. INDUCER EXIT
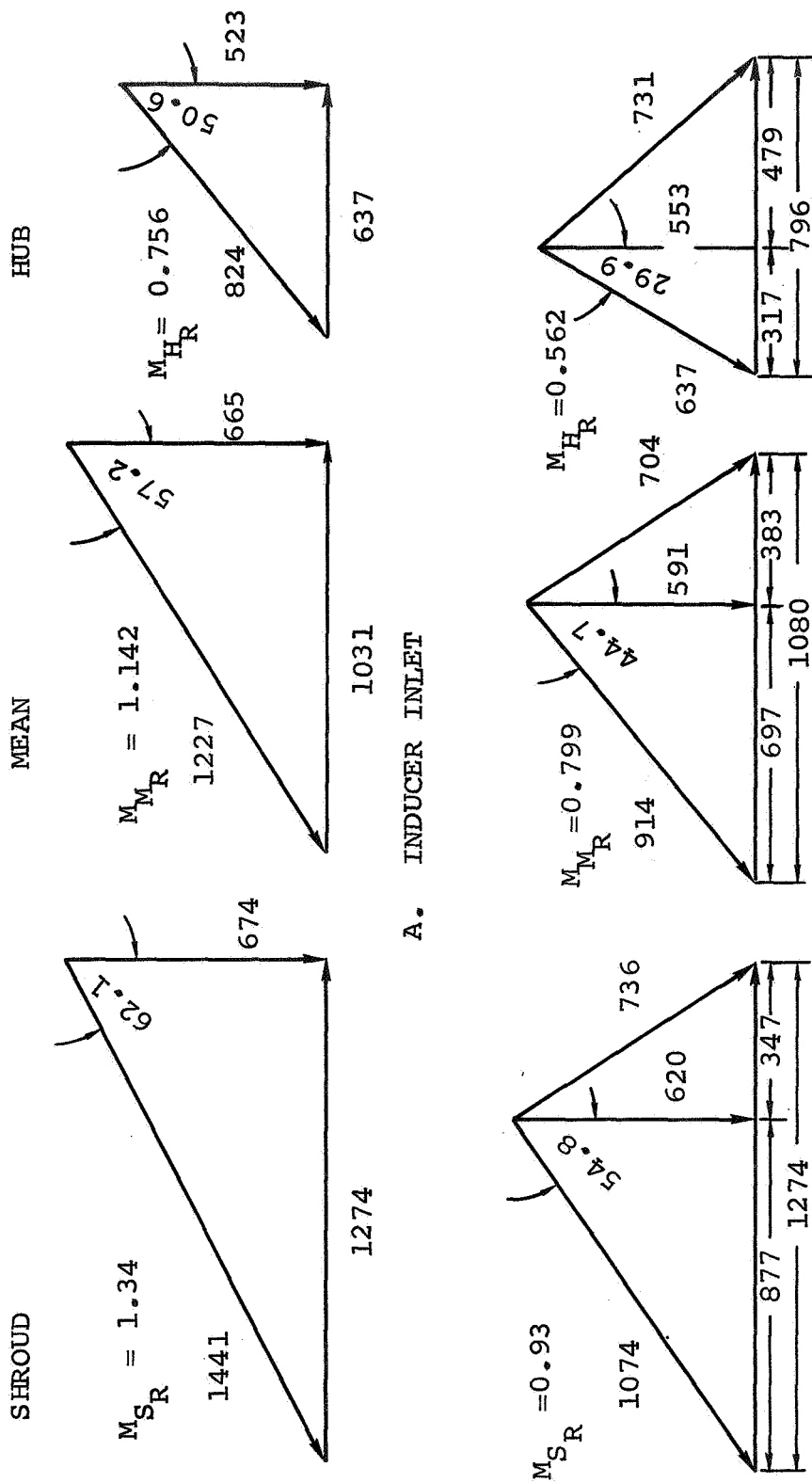
Figure 74. — Final vector triangles — inducer section (through the blade).

115
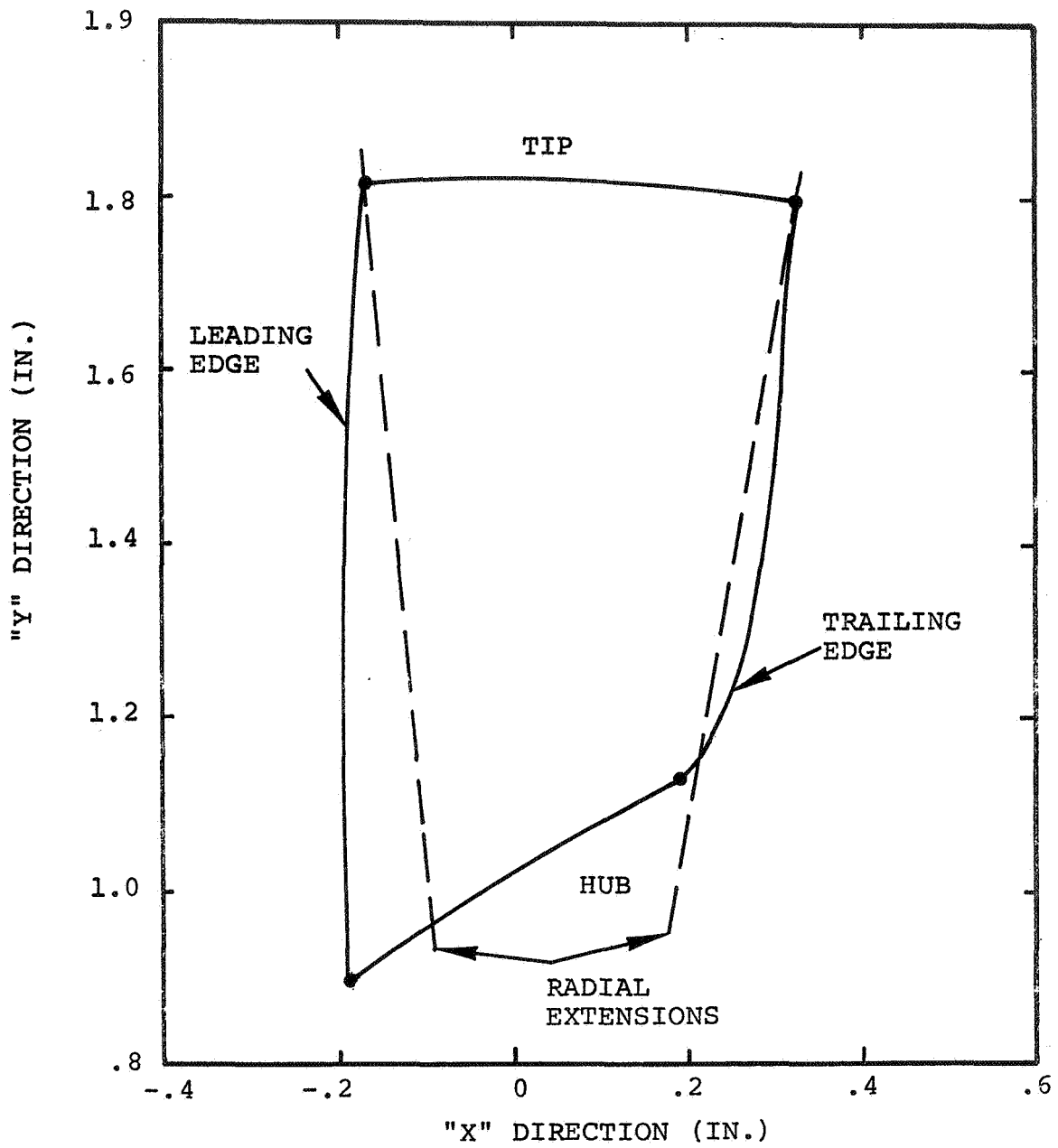
Figure 75. - Front view of inducer blade.
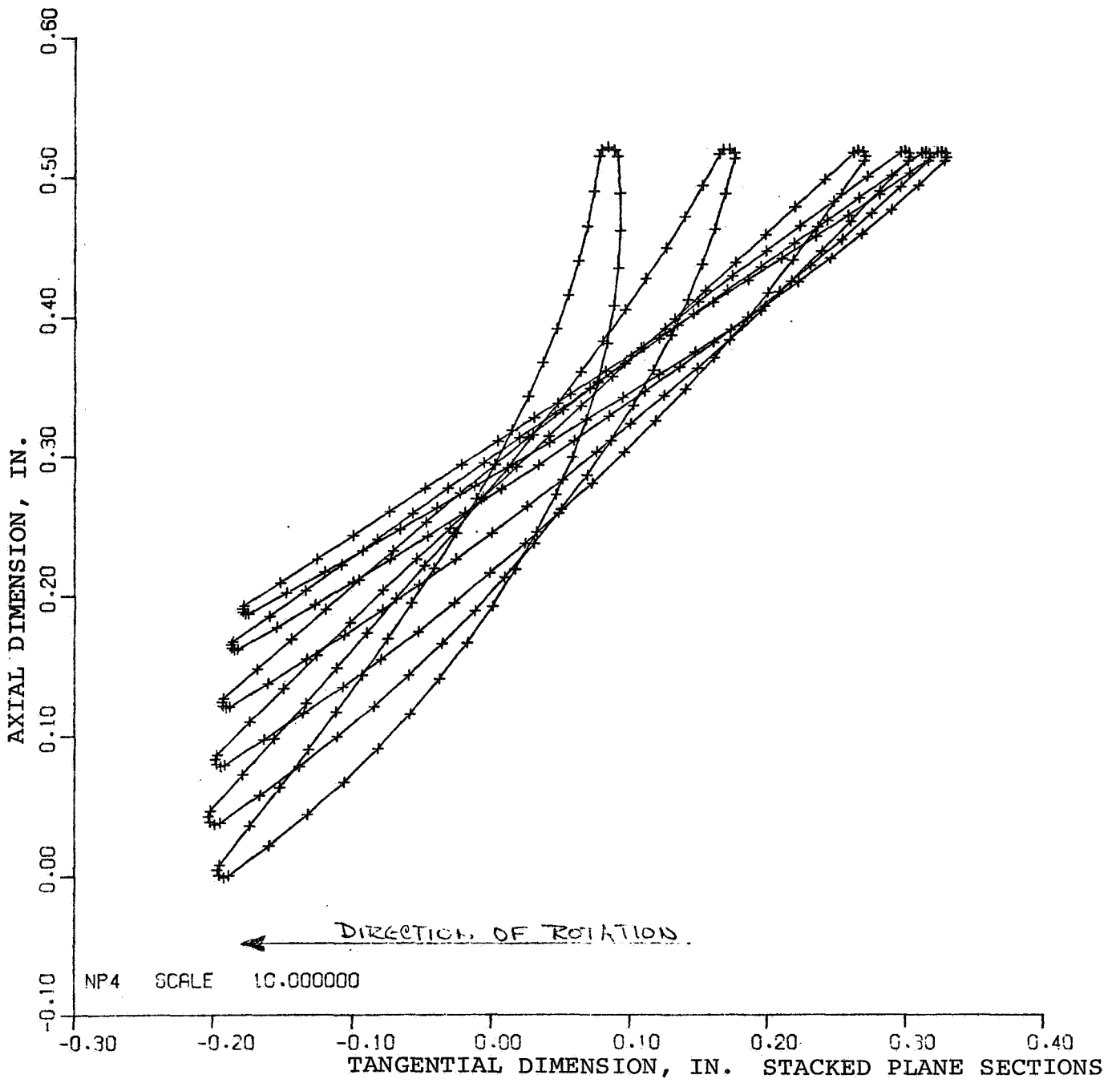
Figure 76. - Final inducer design.

Centrifugal Portion

Accepted AiResearch design procedures were employed in the final design of this portion of the impeller. A summary of the basic design parameters is presented on table V. The design pressure ratio and adiabatic efficiency shown here represent over-all conditions at the impeller exit before any mixing and subsequent diffuser losses. The impeller was designed for 24 blades to match exit flow conditions from the inducer.

Photographs of the inducer hardware and the front view of the impeller section before assembly are presented in figures 77 and 78, respectively. A view of the inducer and impeller assembled is shown in figure 79.

Cascade Vane Diffuser

The performance characteristics for each airfoil shape and a friction coefficient for the vaneless space were input, along with the geometry, to a computer program (ESTOR) which calculated the flow conditions at various points in the radial flow path.

This program produced the data for figure 80 which shows the optimum location of the diffuser leading edge to be at a radius ratio of 1.2, based on the impeller exit radius. A friction coefficient of 0.006 was assumed for both the initial and final vaneless spaces. This friction coefficient value demonstrated good agreement with test data contained in ref. 10. This reference also recommends a constant area vaneless diffuser rather than a parallel wall configuration because it tends to improve the typically poor impeller exit flow profile rapidly. This situation is beneficial to the diffuser operation because it reduces the incidence variation that exists across the passage from hub to shroud.

The meridional layout is shown in figure 81 which also includes the predicted conditions of a number of specific radial locations. A photograph of the cascade diffuser hardware before brazing is presented in figure 82.

Boundary-Layer Control

Impeller Boundary Layer: The basic question of the effect of bleed on overall compressor performance has not been completely resolved. Some conclusions can be made from certain simplified calculations and limited experimental evidence. First, it should be pointed out that the TFE731 radial compressor, which exhibited flow separation in the shroud region based on lampblack tests, exhibited relatively good compressor performance, essentially meeting design specifications. Therefore, any further improvement in compressor performance through the use of boundary layer

TABLE V. - IMPELLER DESIGN PARAMETERS

Centrifugal Portion	
Number of blades	24
Inlet tip diameter, in.	3.650
Inlet hub diameter, in.	2.374
Exit diameter, in.	5.374
Exit blade width, in.	0.184
Exit blade angle, degrees	30.8
Tandem Inducer	
Specific speed	64
Rotational speed, rpm	80,000
Pressure ratio	7:1
Adiabatic efficiency, percent (rotor only)	89

Figure 77. — Front view of inducer before assembly. SKP25657-1

120
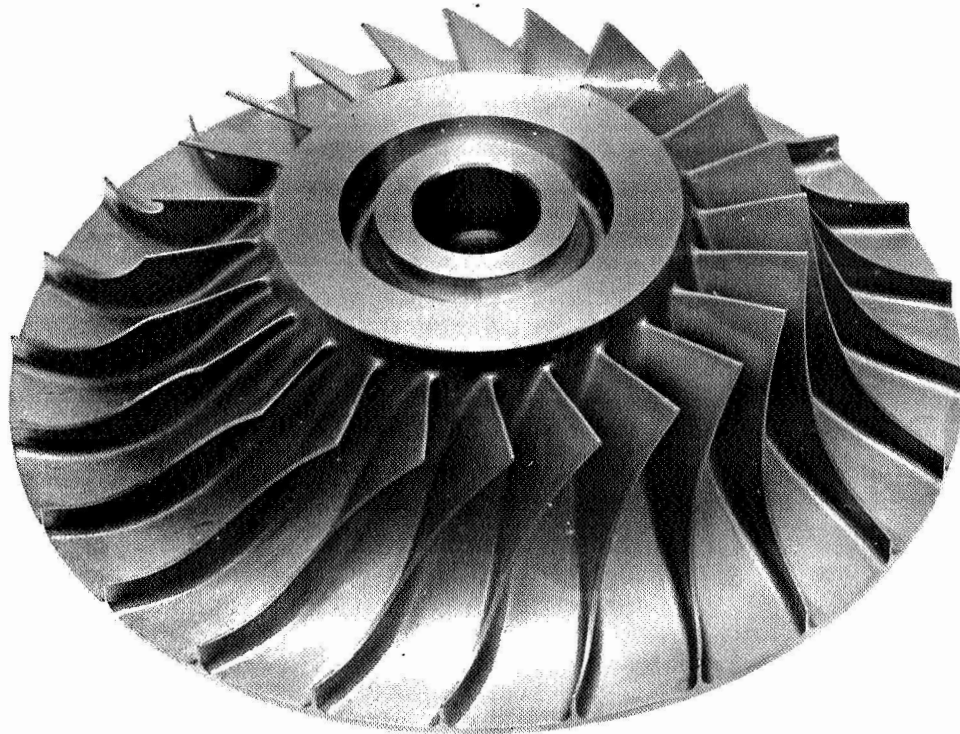
Figure 78. - Front view of impeller before assembly, SKP25658-1.
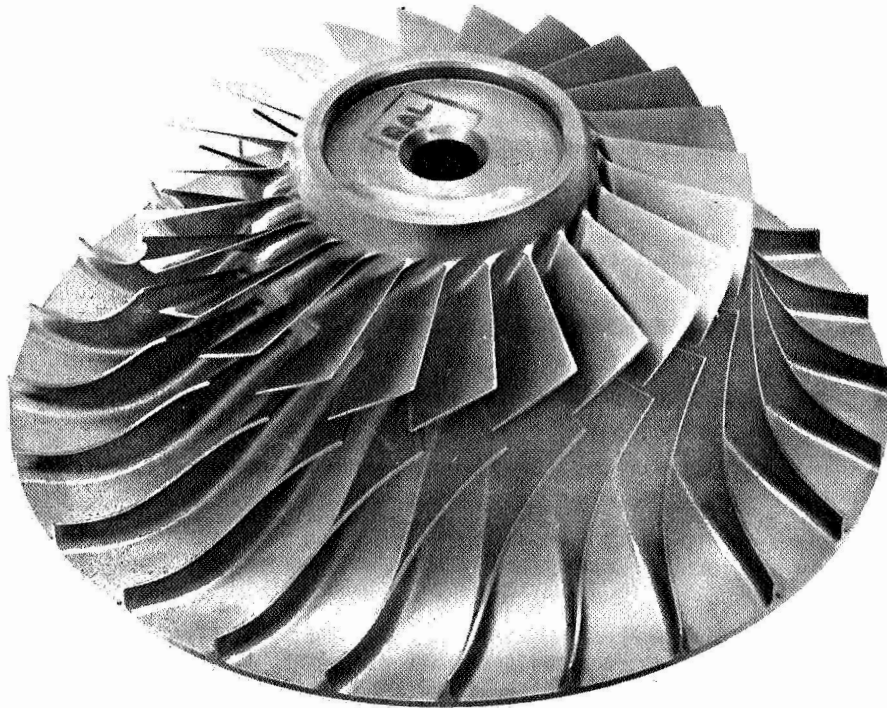
Figure 79. - Inducer and impeller assembly.
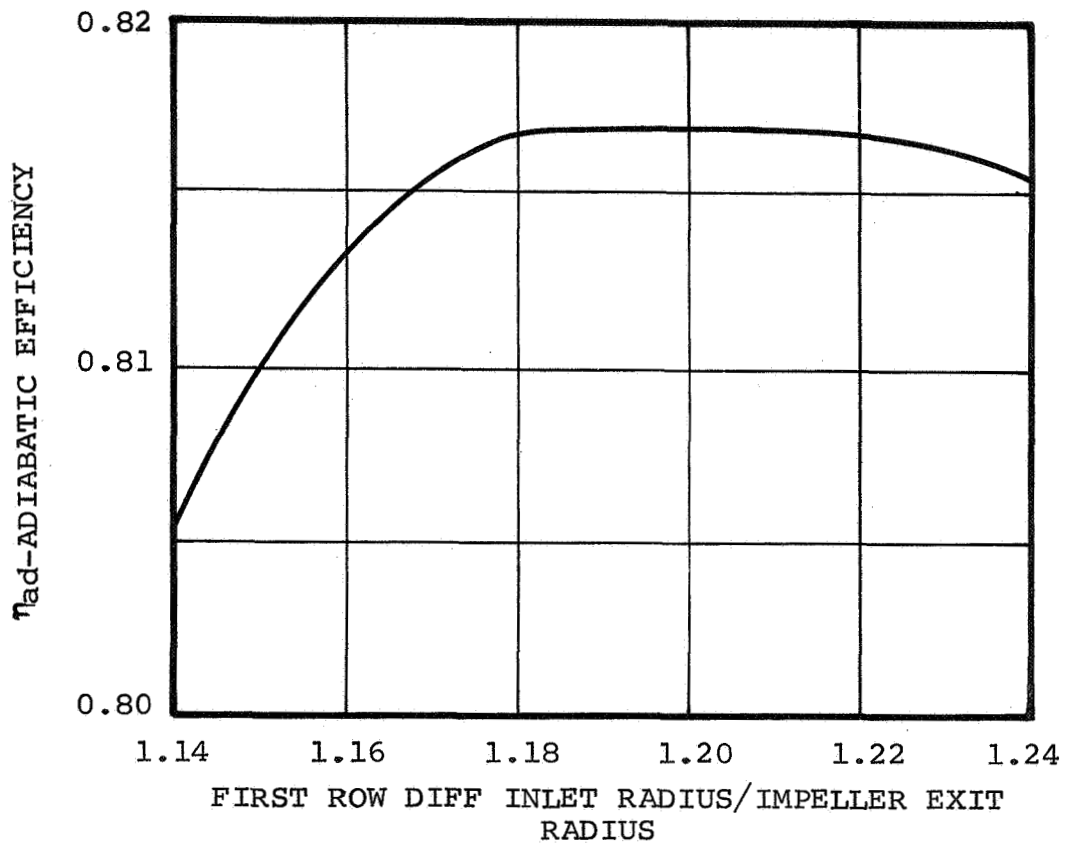
Figure 80. - Overall compressor efficiency versus
diffuser inlet radius ratio.

NOTES:

1. NUMBER OF TANDEM BLADES = 22
2. FIRST BLADE ROW IS NACA 65-4(A10)06
3. SECOND BLADE ROW IS NACA 65-10(A10)06

0.146 IN.

COLLECTOR

0.146 IN.

DIFFUSER
ROW
2

0.146 IN.

DIFFUSER
ROW
1

0.158 IN.

VANELESS
SPACE

0.189 IN.

RADIAL
IMPELLER

STATION	RADIUS, IN.	TOTAL PRESSURE RATIO	MACH NUMBER	EFFICIENCY
6	6.29	6.186	0.203	0.817
5	4.434	6.247	0.306	0.823
4	3.627	6.385	0.518	0.835
3	3.224	6.583	0.851	0.853
2	2.687	6.9985	1.099	0.890
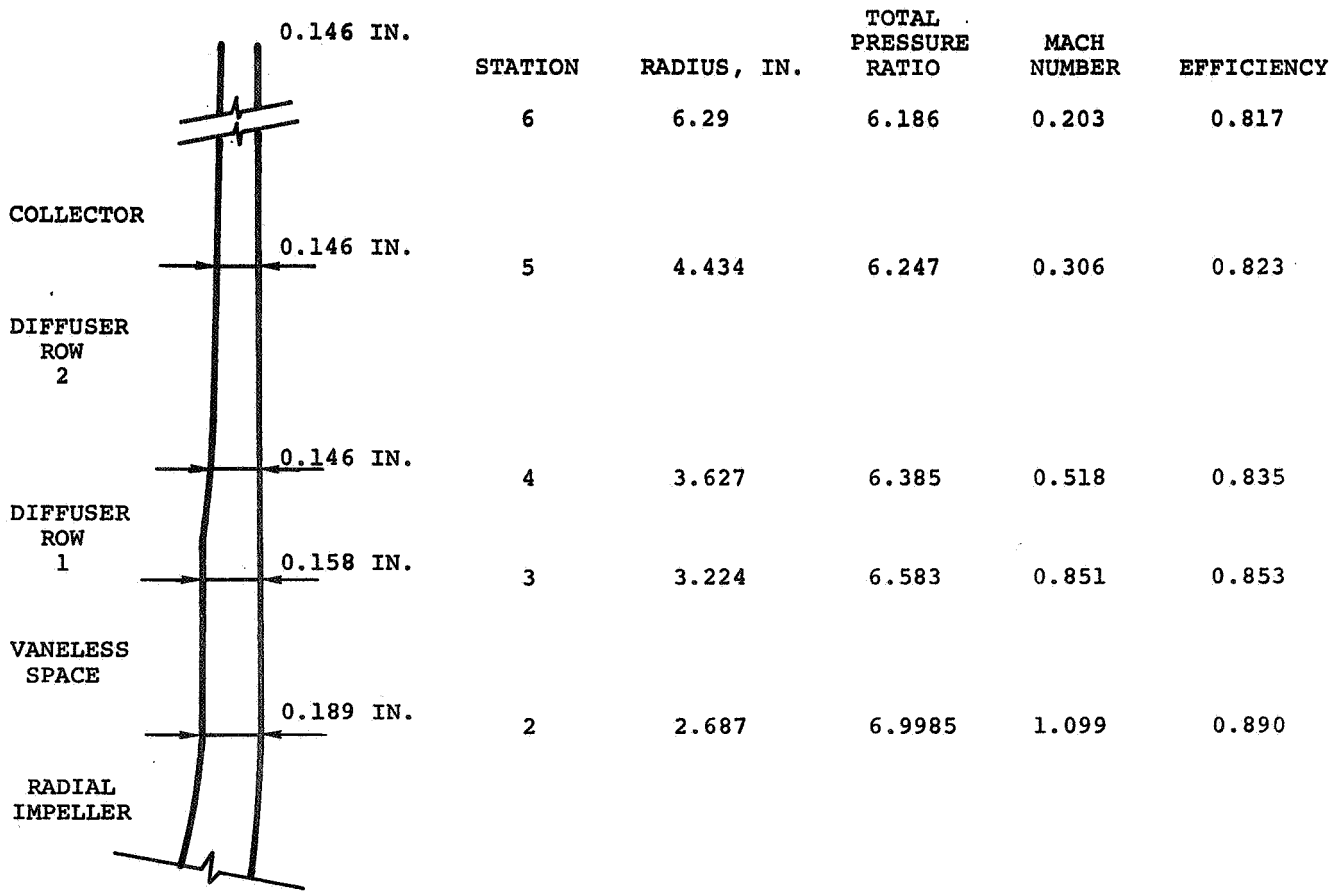
Figure 81. - Cascade diffuser design parameters.

Figure 82. - Inside view of diffuser halves before brazing.

125

control would necessarily be small ($\sim$ 1 to 2 percent). A computation was made of the work required to compress the bleed air to bleed port conditions at Location 1 shown in figure 67. Results indicated that 2 percent bleed flow was equivalent to about 0.9 points of compressor efficiency. In other words, the resulting gain in compressor efficiency from boundary-layer control would have to be greater than 0.9 points (with 2 percent bleed flow) to show an overall performance advantage. Obviously, bleed air taken from a location further downstream would require an even greater gain for a favorable performance tradeoff.

Experimental data showing the effects of boundary-layer bleed on overall compressor performance is quite limited. AiResearch has designed a radial compressor stage for Rolls-Royce in which a small amount of cooling air ($\sim$ 1 percent) is bled through holes in the shroud. They have informally reported that compressor performance is increased about 1-1/2 to 2 points with the bleed system operating. This bleed system was not designed for efficient removal of the boundary layer and it is probable that further gains are possible through the use of a more efficient system. However, even the demonstrated gains are sufficient to trade off favorably with the work required to initially compress the bleed air. Consequently, it appears likely that an overall performance gain with boundary-layer control can be demonstrated for the advanced compressor.

Diffuser Boundary Layer: Boundary layer blockage at the exit of the first cascade row is beginning to form a significant portion of the passage. This, plus the fact that past experience has indicated that most problems related to cascade diffusers can be traced to the later stages, led to the selection of a boundary-layer control system to be located at the inlet of the second row of vanes for the cascade diffuser. However, the advanced compressor will have provision for boundary-layer control on the shroud wall within the impeller, which should provide stable flow along the diffuser shroud wall. This being the case, it may be more advantageous to apply boundary-layer control to the hub wall of the diffuser while the impeller control system is operating. Without any bondary-layer control in the impeller region, shroud side control should be used in the diffuser. The flexibility of the dual control system for the diffuser looks very favorable for this application.

A boundary-layer analysis of conditions in the second vane row indicates that an inlet bleed system will result in a decrease in overall compressor performance. This means that the work

126

required to compress the boundary-layer control fluid to bleed conditions does not tradeoff favorably with the increased adiabatic efficiency for the remaining fluid. Of course, in engines where cooling flows are required, overall cycle benefits may result if these flows are used to improve diffuser performance.

There are other factors which cannot be assessed by boundary-layer calculations. One is the effect of the low-energy, boundary-layer fluid on the angle of attack and loss bucket limits of the vane row. The actual three-dimensional nature of the diffuser flow may result in a significant performance improvement that cannot be predicted analytically. It definitely seems logical that small bleed flows in the diffuser would increase the operating range with very little effect on performance.

In general, boundary-layer control within the diffuser does not seem to offer the same potential advantage for increased overall performance as boundary-layer control in the impeller. However, there are sound reasons for exploring diffuser boundary-layer control experimentally, and provision for this will be incorporated into the delivered hardware.

Overall Component Design Parameters

A summary of the design parameters pertaining to each component and the entire stage is presented in table VI.

TABLE VI. - DESIGN SUMMARY

Overall Design

Corrected Weight Flow, lb/sec	2
Total Pressure Ratio	6.19:1
Rotational Speed, rpm	80,000
Adiabatic Efficiency	0.817

Inducer

No. of Blades	24
Total Pressure Ratio, $P_1/P_o)$	1.525:1
Inlet Tip Diameter, in.	3.65
Hub/Tip Ratio	0.5
Adiabatic Efficiency	0.943
Flow/Frontal Area, lb/ft^2 sec	27.52

Impeller

No. of Blades	24
Total Pressure Ratio, P_2/P_o	7:1
Inlet Tip Diameter, in.	3.65
Inlet Hub/Tip Ratio	0.65
Exit Tip Diameter, in.	5.374
Adiabatic Efficiency	0.89

128

TABLE VI. - DESIGN SUMMARY (Contd)

Vaneless Space #1

Inlet Mach No.	1.099
Exit Mach No.	0.853
Radius Ratio, R_3/R_2	1.2
Total Pressure Ratio, P_3/P_0	6.58:1
Adiabatic Efficiency	0.853

Cascade Vane Diffuser

Exit Mach No.	0.306
Radius Ratio, R_4/R_3	1.375
Total Pressure Ratio, P_4/P_0	6.25:1
Adiabatic Efficiency	0.823

Vaneless Space #2

Exit Mach No.	0.203
Radius Ratio, R_5/R_4	1.42
Total Pressure Ratio, P_5/P_0	6.19:1
Adiabatic Efficiency	0.817

4. CONCLUDING REMARKS

All pertinent assumptions and fundamental design procedures used to define the aerodynamic shape of the NASA Advanced Compressor components have been described in detail in this report. For the most part, design of the tandem inducer/impeller followed proven industrial design practice. Axial flow design techniques were employed in the inducer section design and centrifugal design methods used in the centrifugal portion. Both sections were analyzed in a tandem arrangement to incorporate mutual interference effects between the inducer and impeller regions.

Design of the cascade vane diffuser uses a combination analytical/empirical approach developed by AiResearch. Overall, the cascade diffuser design procedures have proven quite successful when evaluated experimentally. However, some problems have been experienced with defining the optimum blade angle at the leading edge of the first stage because of the high Mach number and the three-dimensional nature of the flow from the impeller discharge. Usually two or three blade settings are required to establish an optimum first-row blade stagger. The diffuser design described here has included past experience and a consistent flow analysis for setting the cascade vane inlet angles. However, there is still a distinct possibility of a diffuser mismatch, and it is recommended that some provision be made to provide a backup configuration for early test evaluation.

APPENDIX A

MECHANICAL DESIGN ANALYSES
OF NASA ADVANCED
COMPRESSOR TEST RIG
SA-9163-MR
(13 pages)

AIRESEARCH MANUFACTURING COMPANY OF ARIZONA
A DIVISION OF THE GARRETT CORPORATION

MECHANICAL DESIGN ANALYSES
OF NASA ADVANCED
COMPRESSOR TEST RIG

SA-9163-MR   April 5, 1971

I. INTRODUCTION

This report summarizes the mechanical design analyses completed to date on the NASA Advanced Compressor Test Rig.

Included in this report are the results of:

(1) Centrifugal and thermal stress analyses of the following parts:

   (a) Impeller disk

   (b) Inducer disk

   (c) Tandem inducer blades

   (d) Tandem impeller blades

   (e) Labyrinth seal

(2) Critical speed and bearing load analyses of the compressor rig rotating assembly

(3) Tie-bolt design and preload determination

II. ANALYSES AND RESULTS

A. Tandem Inducer and Impeller Disk Stress Analyses

This analysis, based on the finite element approach, was performed to determine an impeller design capable of withstanding the

thermal and centrifugal stress environment present in the subject rig.
The estimated temperature distribution is presented in Figure B16058.
Distribution of the impeller disk stresses are presented in Figure
B16059 and the inducer stresses are presented in Figure B16060. The
analyses are based on the operating speed of 80,000 rpm. The material
is Titanium (Ti-6Al-4V). The centrifugal and thermal deflections at
the rim and the bore are presented in Figure B16061. The axial tip
deflection at the exit is 0.0081 inch and the radial tip deflection
is also 0.0081 inch. All the radial deflections are with respect to
centerline and all the axial deflections are with respect to compressor
bearing.

The other pertinent information is summarized in a table below:

	Inducer Disk	Impeller Disk
Bore maximum stress, psi	31,000	102,000
Hub average tangential stress, psi	15,372	37,549
Minimum hub burst speed, rpm	220,000	120,800
I_p, lb-in.-sec^2	0.00069	0.00886
I_D, lb-in.-sec^2	0.00038	0.00544
Mass, lb-sec^2/in.	0.00095	0.00531

B. **Tandem Inducer and Impeller Blades Stress and Natural Frequency Analyses**

This analysis, based on the finite element approach, computes the
centrifugal stress for the blades. The inducer blade equivalent
stresses are presented in Figure B16063 and the impeller equivalent
stresses are presented in Figure B16062. The results show that the
maximum inducer equivalent stress is 59,000 psi and the maximum
impeller equivalent stress is 68,000 psi. Therefore, the maximum

centrifugal stress is 67.0 percent of the yield strength of the titanium blades at temperatures of 450°F.

The natural frequency analyses results are presented in the impeller interference diagram, Figure B16064, in which the natural frequencies are plotted vs rotational speed. Also shown is the 22 diffuser vanes excitation line. The points of intersection of the lines are possible resonant points. The results show that no excitation of lower mode would occur at the operating speed.

C. Critical Speed and Bearing Loads of the Rotating Assembly

The critical speeds are computed for the rotating assembly with the two bearings hydraulic resilient mounted. Figure B16065 shows bearing load vs rotating speed for the assumed mass eccentricity of 0.00035 inch. Bearing loads of 55 lb are estimated for both bearings at the operating speed of 80,000 rpm.

D. Tie-bolt Design and Preload Determination

The ability of tie-bolt load in maintaining rotor integrity depends to a large extent on the magnitude of rotor bending moments imposed on the rotating group as the assembly passes through its critical speed points.

This criterion establishes an initial tie-bolt load of 12,000 lb. A diameter of 0.324 inch bolt and 4340 steel RC (42-46) material is recommended for the tie-bolt design.

E. **Labyrinth Seal Stress Analysis**

The centrifugal and thermal stress analysis of the labyrinth seal ring has been completed. Distribution of equivalent stresses of the seal is presented in Figure B16066. The radial growth of the seal at the operating speed exceeds the radial growth of the impeller disk by 0.0003 inch radially. Therefore, a 0.001-inch press fit of the seal on the impeller disk is required.
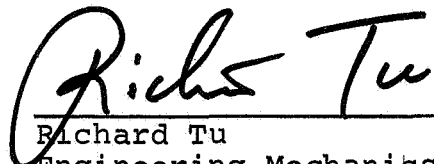
Richard Tu
Engineering Mechanics

Approved: E. Nelson
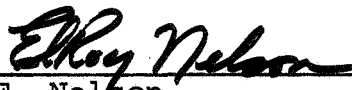
Attachments: Figures B16058 through B16066

RT:jlh
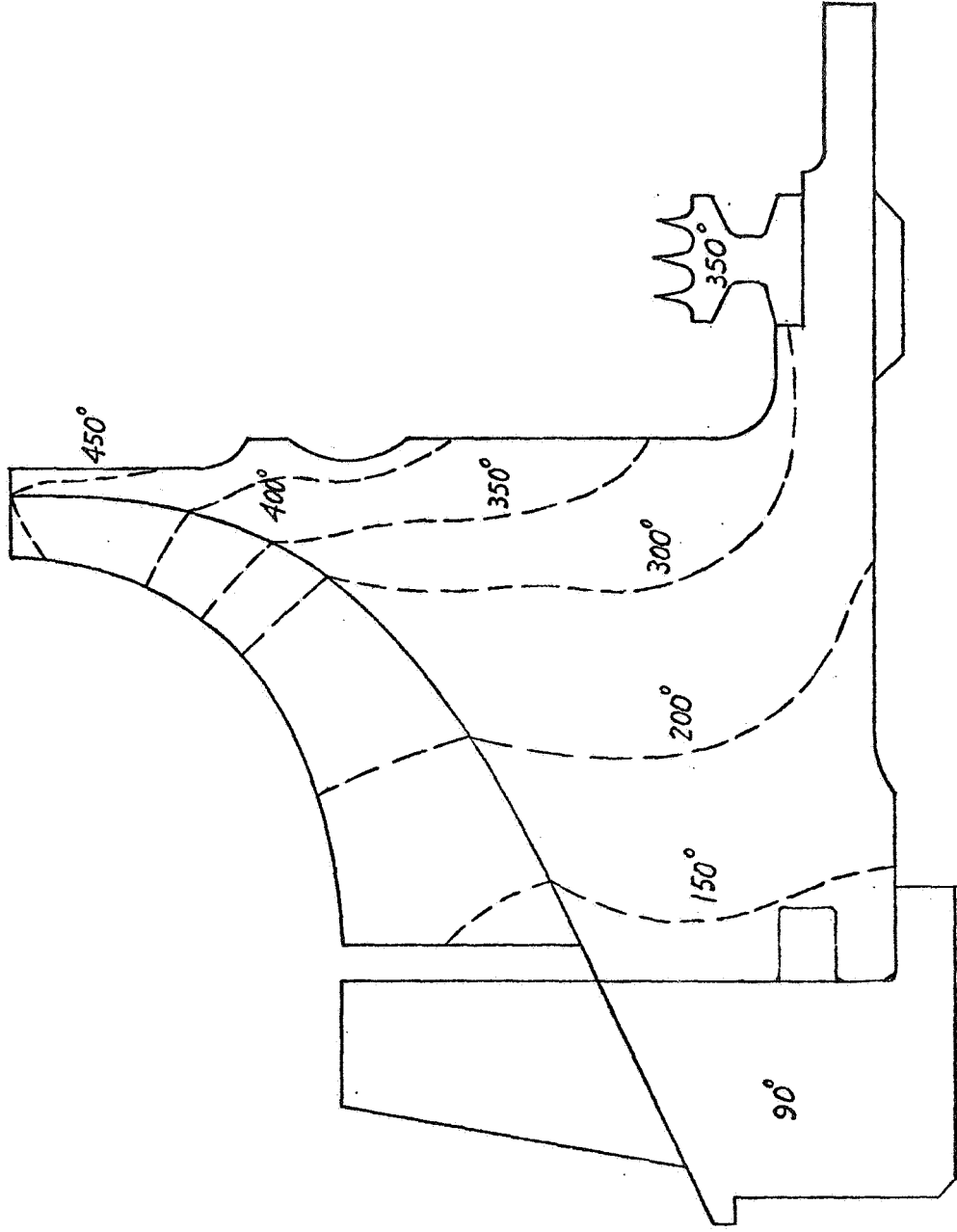
AXIS OF ROTATION

ESTIMATED TEMPERATURE DISTRIBUTION, °F
FIGURE B16058

NOTES:
(1) N = 80,000 RPM
(2) MATERIAL = Ti-6Al-4V
(3) N_{BURST} = 120,800 RPM OR 151% of 80,000 RPM
(4) σt_{AVE} = 37,549 PSI

EQUIVALENT STRESS (KSI)

TANGENTIAL STRESS (KSI)

RADIAL STRESS (KSI)

AXIS OF ROTATION

RADIUS, INCHES
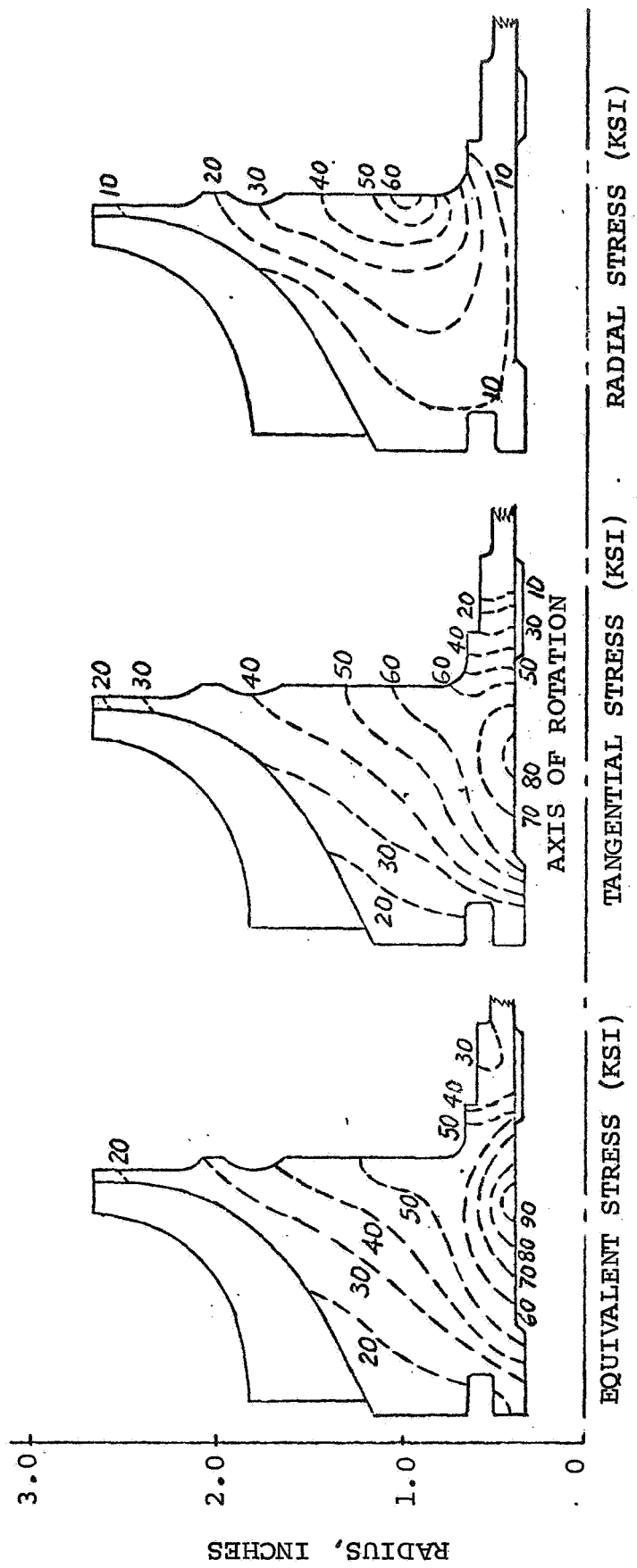
IMPELLER DISK STRESSES
FIGURE B16059

NOTES:

(1) N = 80,000 RPM

(2) MATERIAL = T_i-6Al-4V

(3) N_{BURST} = 220,000 RPM

(4) $\sigma_{t_{AVE}}$ = 15,400

TANGENTIAL STRESS (KSI)

RADIAL STRESS (KSI)

EQUIVALENT STRESS (KSI)

AXIS OF ROTATION
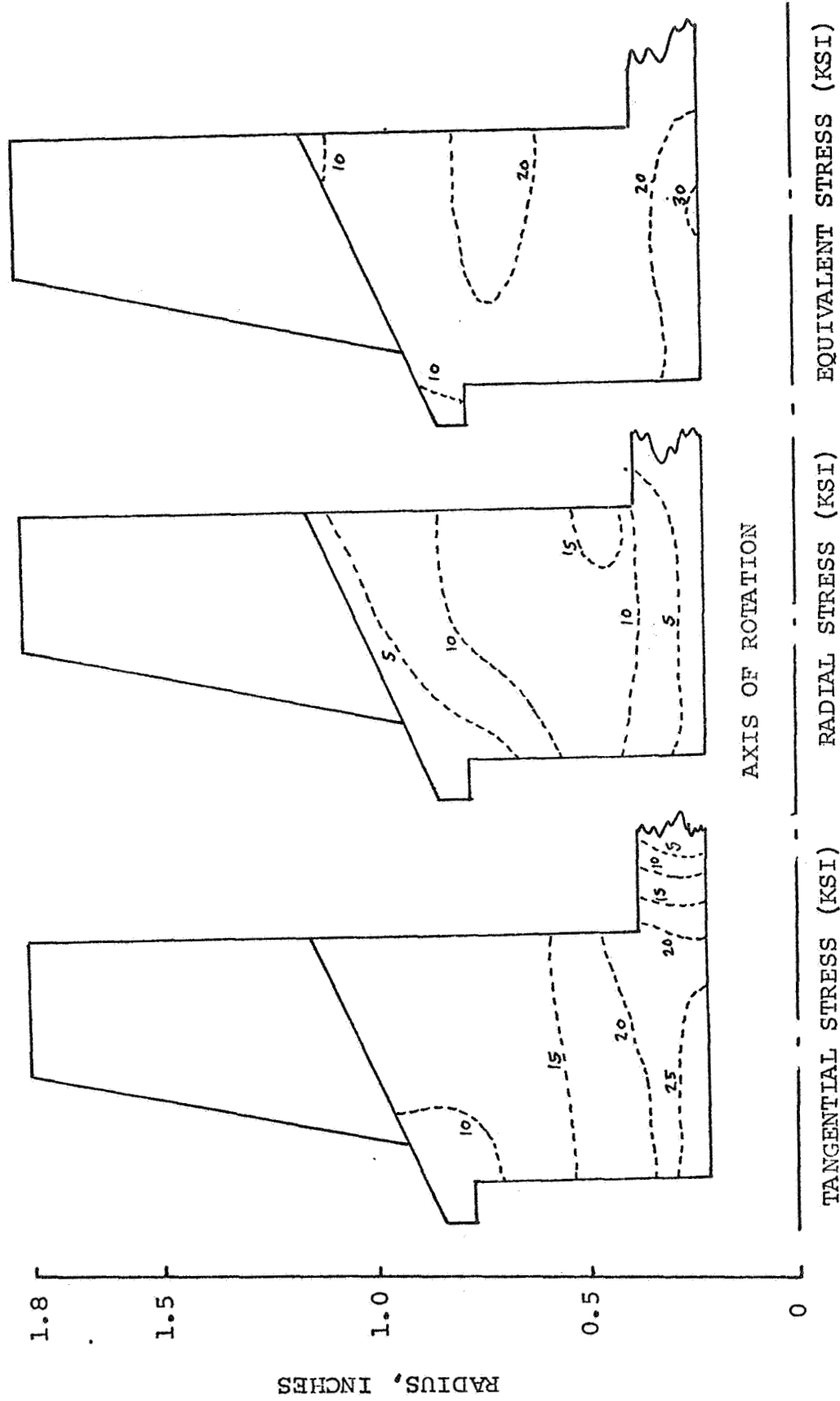
INDUCER DISK STRESSES

FIGURE B16060

RADIUS, INCHES

CENTRIFUGAL AND THERMAL DEFLECTIONS

FIGURE B16061

NOTES:

(1) DEFLECTION IN INCHES

(2) RADIAL DEFLECTIONS WITH RESPECT TO CENTERLINE

(3) AXIAL DEFLECTION WITH RESPECT TO COMPRESSOR BEARING

(4) 80,000 RPM

NOTES:

(1) N = 80,000 RPM

(2) MATERIAL = T_i-6Al-4V
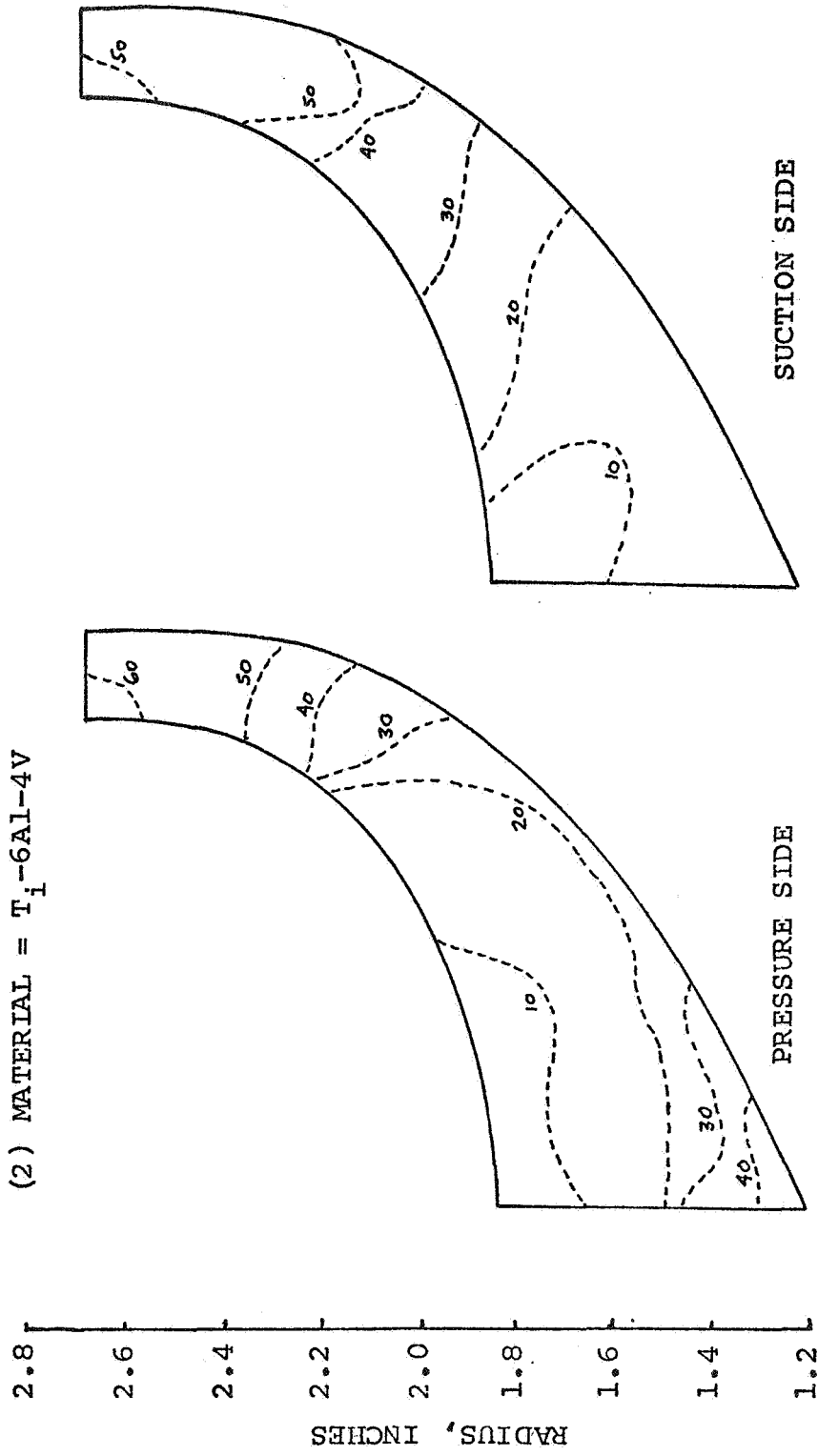
IMPELLER EQUIVALENT STRESSES — KSI

FIGURE B16062

NOTES:
(1) N = 80,000 RPM
(2) ρ = 0.16
(3) STRESSES IN KSI

PRESSURE SIDE

SUCTION SIDE
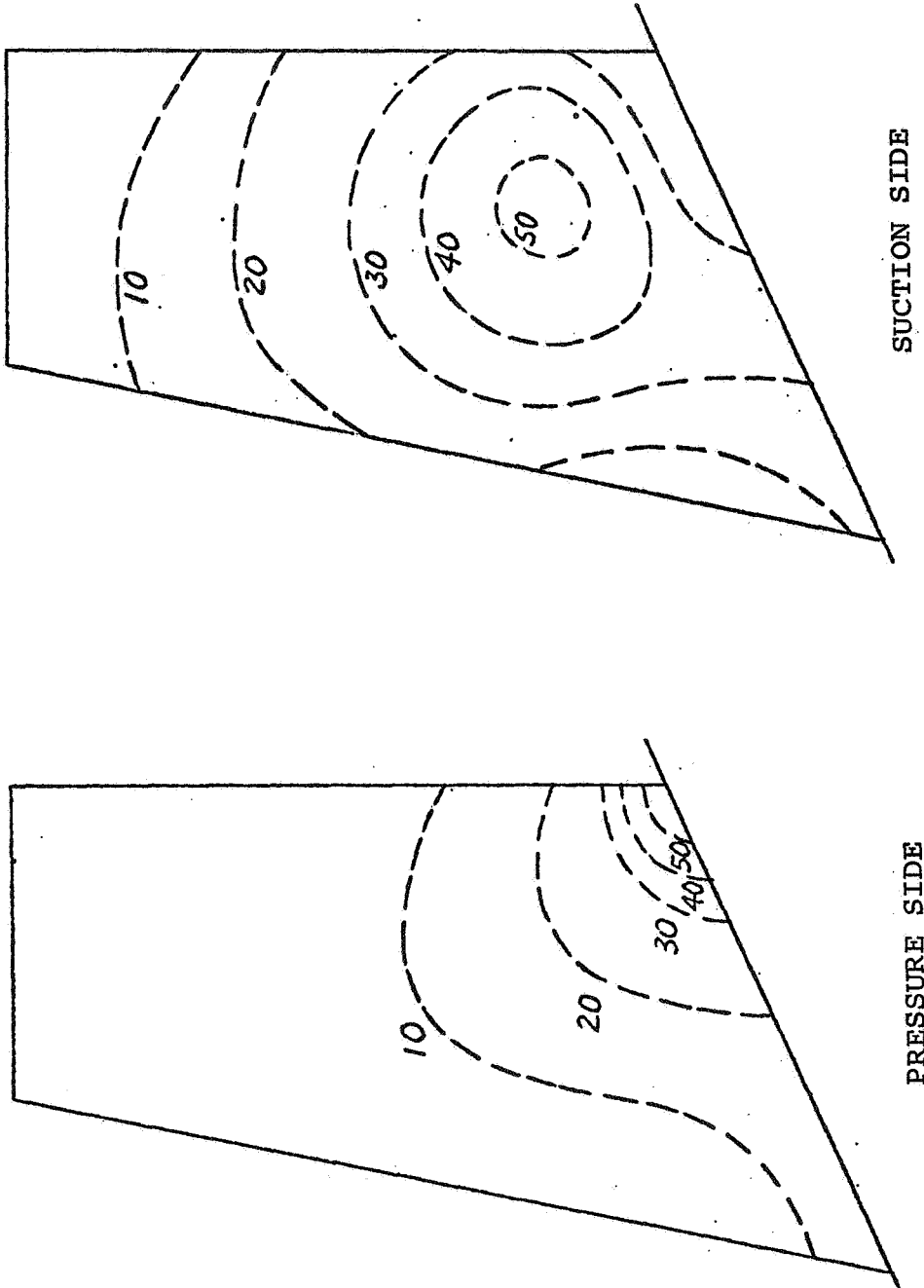
INDUCER BLADE QUIVALENT STRESSES

FIGURE B16063
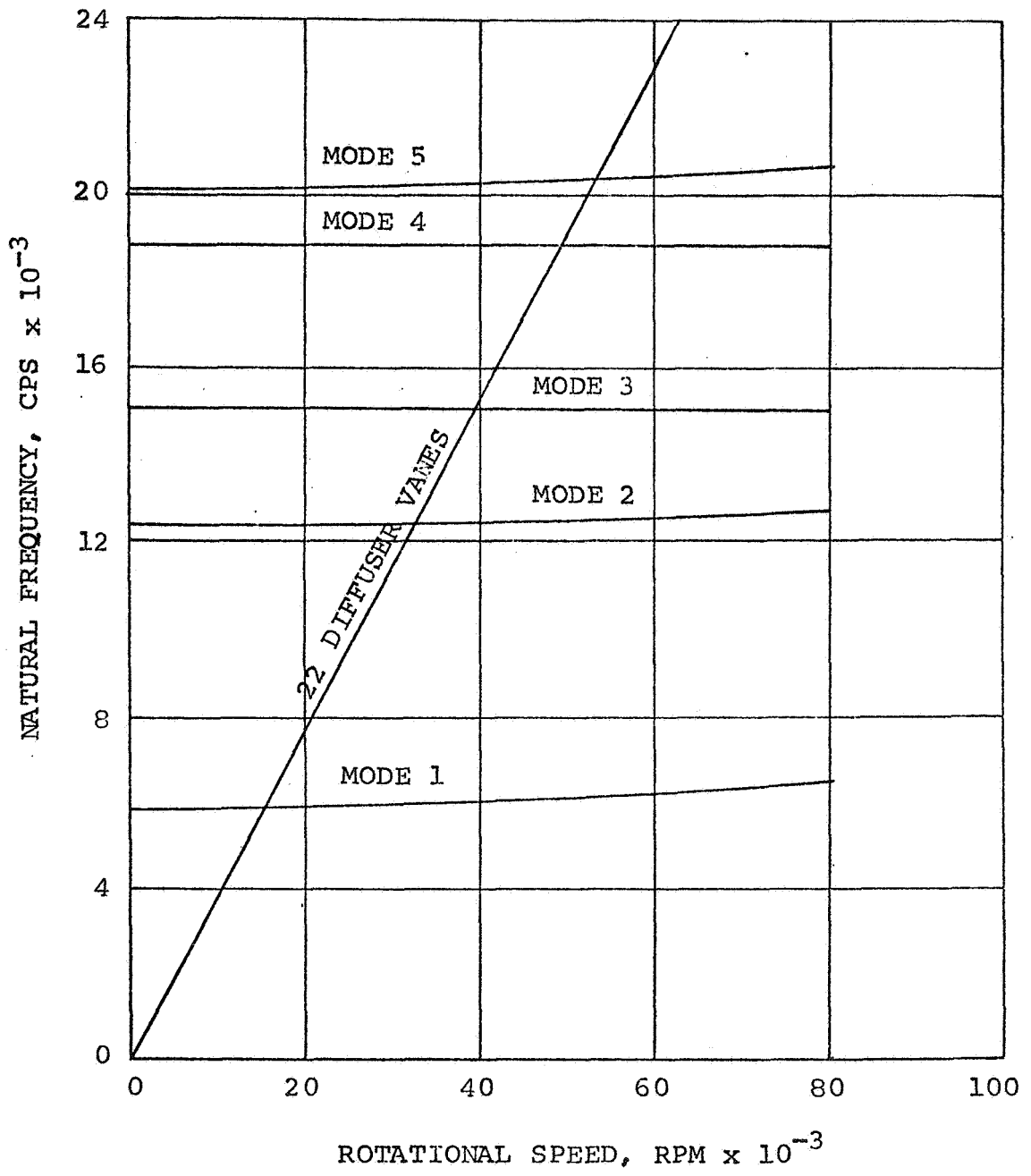
IMPELLER INTERFERENCE DIAGRAM

FIGURE B16064

NOTES:
(1) $K_1 = K_2$
(2) BEARINGS ARE
     HYDRAULICALLY MOUNTED

COMPRESSOR   TURBINE
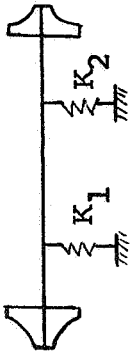
SCHEMATIC VIEW
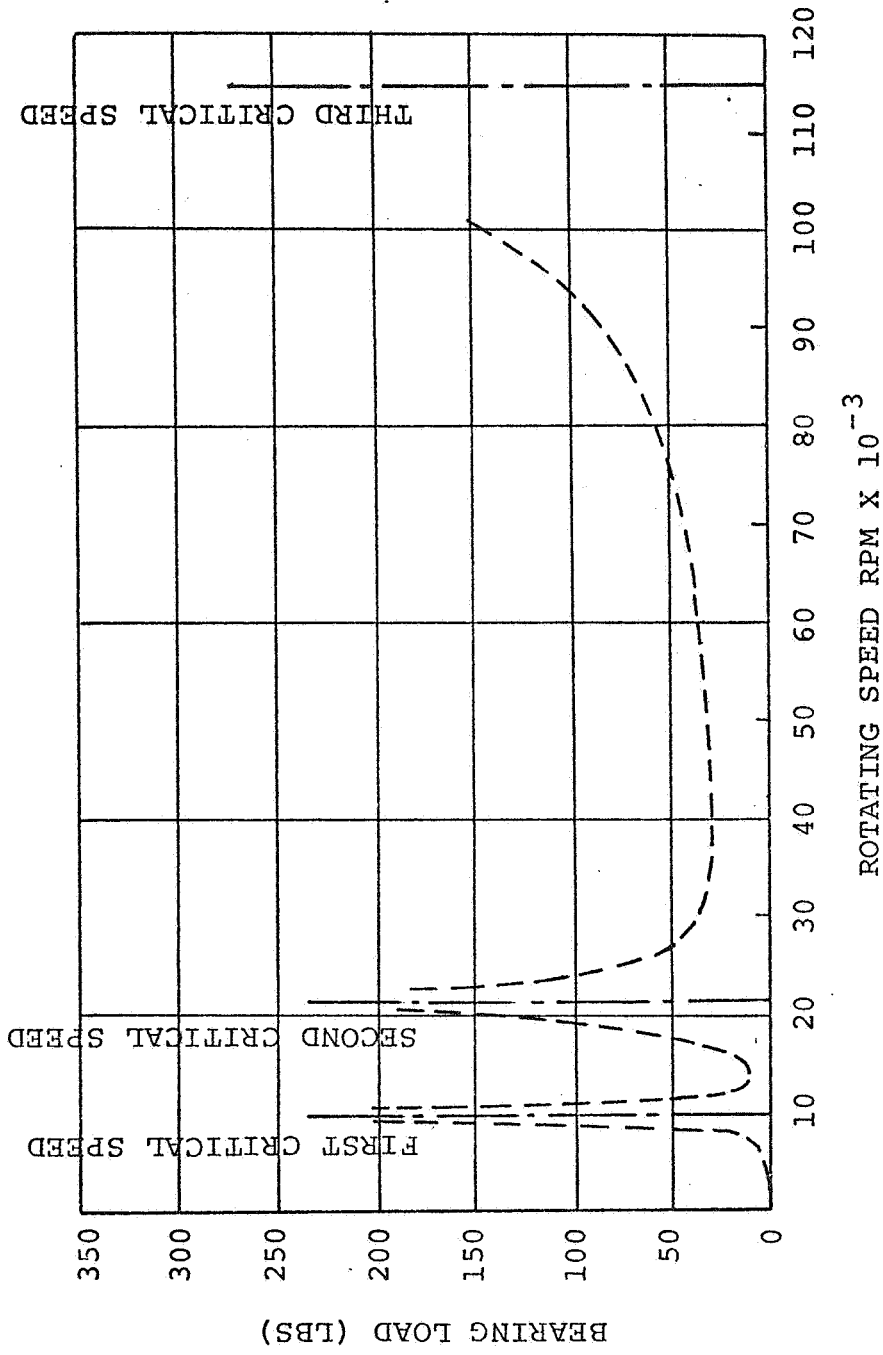
BEARING LOADS OF NASA COMPRESSOR TEST RIG

FIGURE B16065

NOTES:
(1) N = 80,000 RPM
(2) MATERIAL = T_i - 6Al-4V

RADIAL STRESS (KSI)

TANGENTIAL STRESS (KSI)

EQUIVALENT STRESS (KSI)
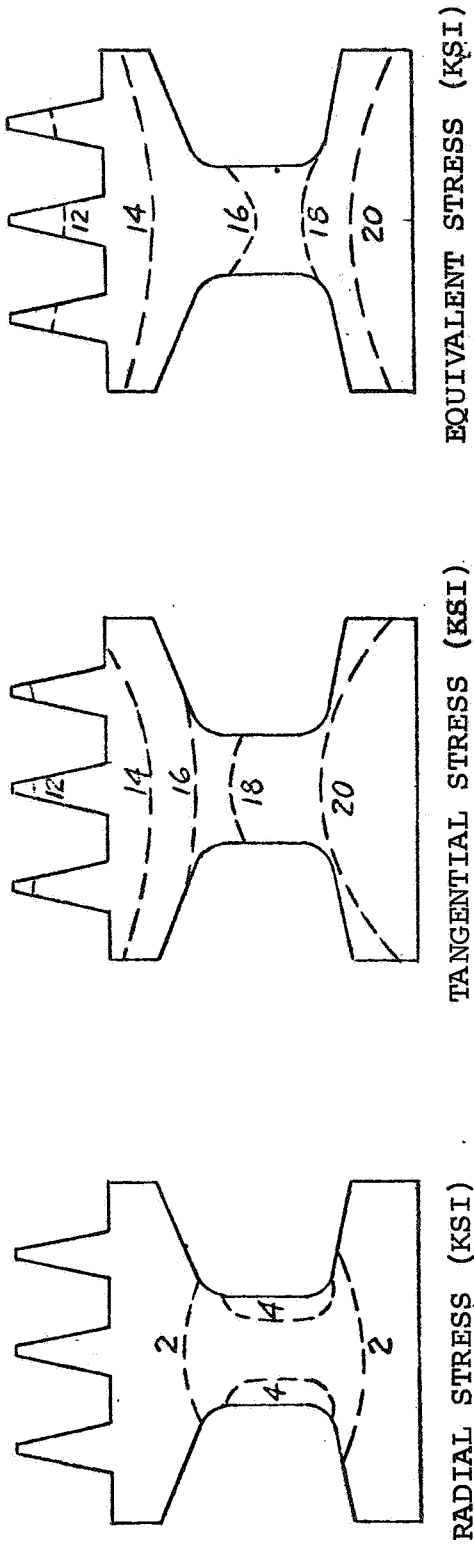
LABYRINTH SEAL STRESSES

FIGURE B16066

APPENDIX B

AIR BEARING FOR NASA
COMPRESSOR TEST RIG
SA-9158-MR
(13 pages)

AIRESEARCH MANUFACTURING COMPANY OF ARIZONA
A DIVISION OF THE GARRETT CORPORATION

AIR BEARINGS FOR NASA
COMPRESSOR TEST RIG

SA-9158-MR Rev 1   March 23, 1971

I.   DESIGN REQUIREMENT

Design externally pressurized gas bearings for radial and axial support of the diffuser housing to permit aerodynamic torque measurements with virtually zero frictional drag on the air cushion. The design requirements specify:

(a)   Axial loading will be nominally 450 lbs due to 1-G load plus aerodynamic thrust reaction.

(b)   The radial loads will be practically negligible in view of the method of suspension.*

II. BEARING TYPE

The bearings are static, orifice compensated air pads requiring external pressurization.

The model used for analysis is shown in Figure SA-9158-C1. This applies to the thrust as well as radial support pads. Total load is obtained by integration of the pad forces at various clearances. Stiffness is obtained by measuring the slope of the load-gap curve.

---

*The unit is suspended with axis vertical. The aerodynamic thrust load is 385 lbs, and allowance for 1-G load is 65 lbs.

III. PERFORMANCE

A. Main Thrust Bearing (G-Pad)

Load and air flow versus film thickness is shown in Figure
SA-9158-C1 for air at a supply pressure of 117.1 psia and 100°F.

The air gap shown for the optimum film stiffness is 0.001 inch,
requiring an entry orifice size of 0.032 inch for the performance
given (air flow = 0.01 lb/sec, pad stiffness = 800,000 lb/in., 6 pads
acting together).

Operation with larger gaps may be effected, if required, by
changing the orifice size as indicated (dotted lines give performance
for the case dn = 0.091, h = 0.002). The flow will increase by a
factor of 8. However, intermediate settings may be made by following
the rule $dn \sim h^{3/2}$, flow $\sim h^3$.

B. Journal Bearing

Similar methods result in performance curves for the journal
bearings. Figure SA-9158-C2 shows the basic performance characteris-
tics. The only loading that will be applied in the radial direction
will result from uneven mass distribution with respect to the vertical
axis. Instrumentation can be balanced with appropriate counterweights
to prevent loading beyond the capacity shown. Aerodynamic loading is
expected to remain symmetric about the vertical axis. The loss flow
design will be tried first.

IV. PERFORMANCE ANALYSIS (see APPENDIX)

A. Bosco
Engineering Mechanics
Preliminary Design

APPROVED:
E. Nelson

Attachments: Figures SA-9158-C1, and C-2
              Appendix

AIRESEARCH MANUFACTURING COMPANY

DATE 4/71
PREPARED BY AB
CHECKED BY

CALC. NO.
MODEL
PART NO.

CASE I LOW FLOW DESIGN   dn = 0.032 IN. ———
CASE II HIGH FLOW DESIGN dn = 0.091 IN. —— —

AIR FLOW LB/SEC

LOAD (LBS)

POCKET PRESSURE (PSIG)

CHOKED FLOW

LOAD

RUNNER
PAD
BEARING

r_2
r_1
GAP
POCKET ORIFICE
SUPPLY PRESSURE

LOAD

POCKET PRESSURE

PRESSURE DISTRIBUTION

FLOW

AIR GAP h, INCHES
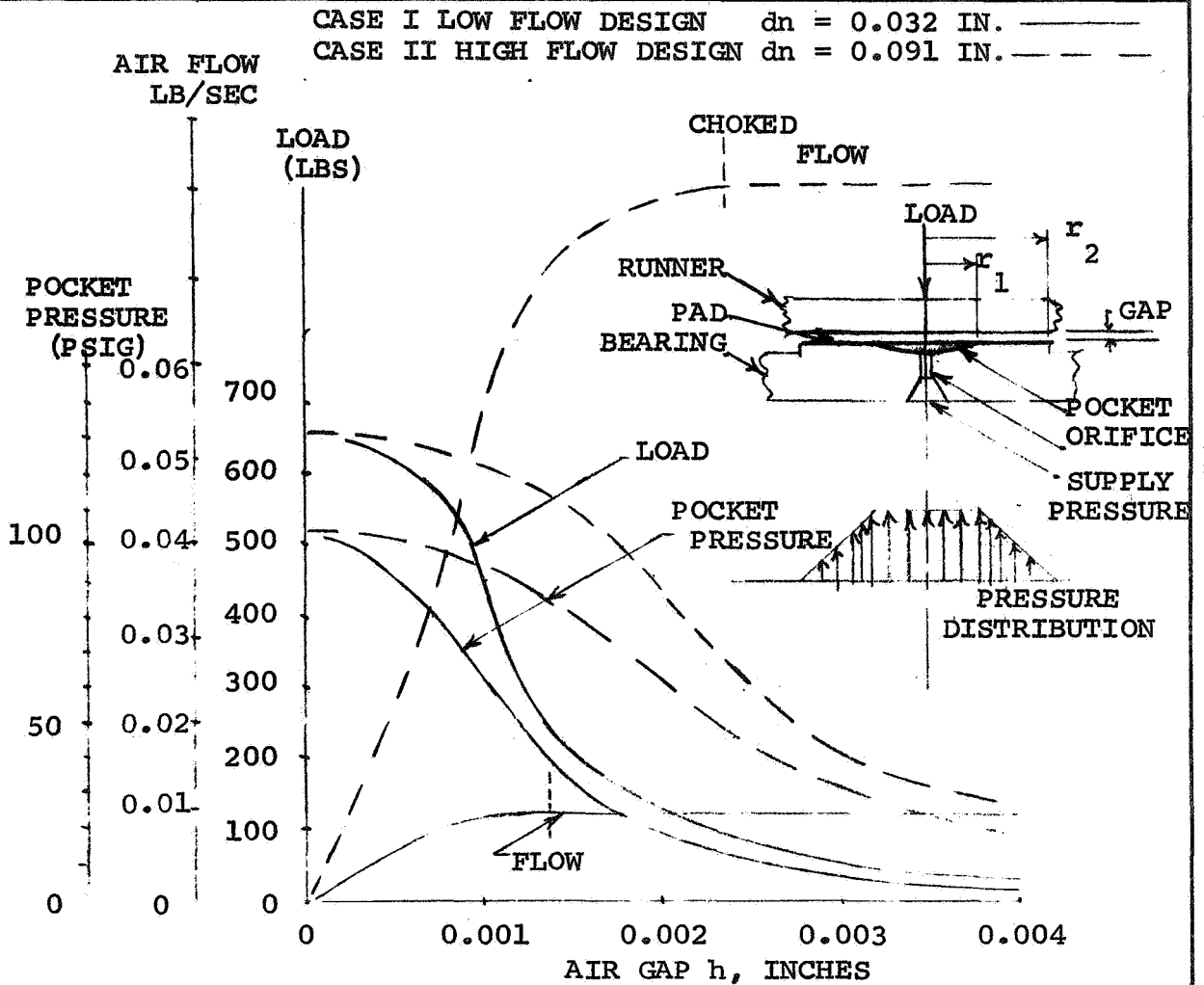
EXTERNALLY PRESSURIZED, ORIFICE
COMPENSATED, AIR THRUST BEARING

NOTES:
SUPPLY PRESSURE	P_s = 117.1 PSIA	
VISCOSITY	μ = 2.60 x 10^{-9} REYNS	AIR AT 100°F
GAS CONSTANT	R = 640 IN./°R	
NO. OF PADS	= 6	
PAD SIZE	2.36 IN.^{2}	
POCKET SIZE	0.26 IN.^{2}	
ORIFICE SIZE	0.032 IN. LOW FLOW DESIGN (CASE I)	
	0.091 IN. HIGH FLOW DESIGN (CASE II)	

STIFFNESS = 800,000 LB/IN. AT 450 LB LOAD CASE I
          = 400,000 LB/IN. AT 450 LB LOAD CASE II
AIR FLOW = 0.0102 LB/SEC AT 450 LB LOAD CASE I
          = 0.0808 LB/SEC AT 450 LB LOAD CASE II

SA-9158-C1

FORM P2427
LOFTIN'S

REPORT
PAGE 3 OF

SA-9158-MR

DATE_____4/71_____

PREPARED BY_____AB_____

CHECKED BY_____

CALC. NO._____

MODEL _____

PART NO._____

CASE I OPTIMIZED FOR 0.002 IN. DIA CLEARANCE ————————

CASE II OPTIMIZED FOR 0.004 IN. DIA CLEARANCE ——— — —

FLOW   LOAD   CASE I LOW FLOW DESIGN dn = 0.011 IN.
(LB/SEC) (LBS)   CASE II HIGH FLOW DESIGN dn = 0.032 IN.

GAP h, INCHES (LOADED SIDE)
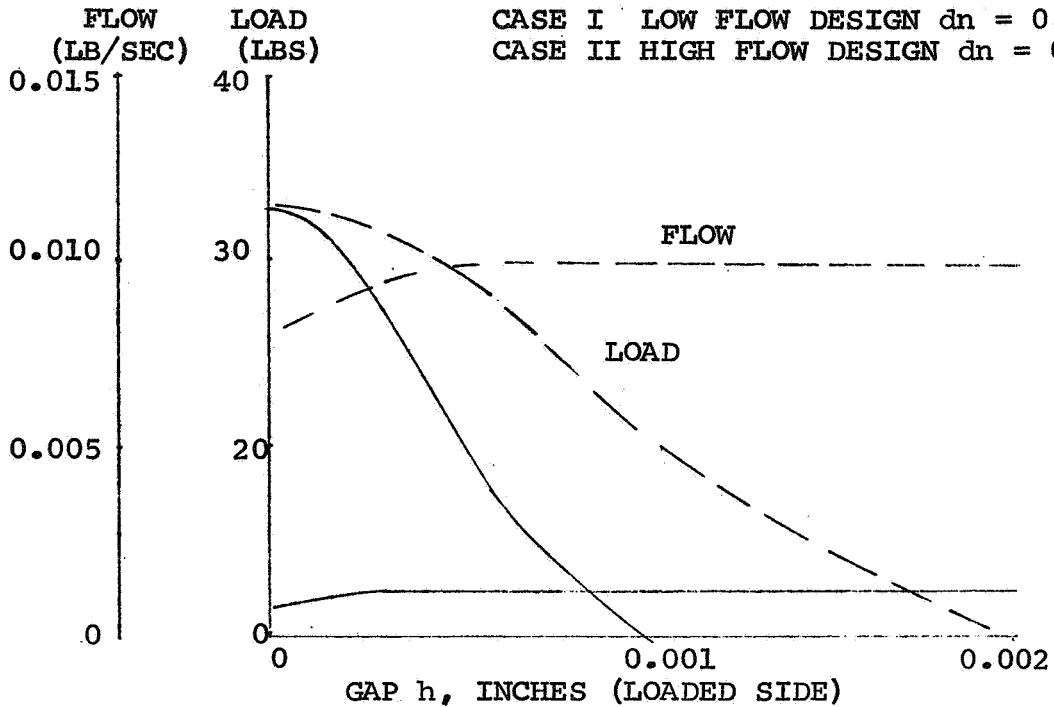
EXTERNALLY PRESSURIZED AIR JOURNAL BEARING PERFORMANCES

NOTES: SUPPLY PRESSURE P_s = 117.1 PSI
         VISCOSITY μ = 2.6 x 10^{-9} REYNS } AIR AT 100°F
         GAS CONSTANT   R = 640 IN./°R
         NO. OF PADS   = 6
         PAD AREA   = 0.36 IN.^{2}
         POCKET AREA   = 0.04 IN.^{2}

MAXIMUM LOW FLOW DESIGN: dn = 0.011 IN., FLOW = 0.0013 LB/SEC
  FLOW   HIGH FLOW DESIGN: dn = 0.032 IN., FLOW = 0.0102 LB/SEC

AVERAGE STIFFNESS = 34,000 LB/IN. LOW FLOW DESIGN
                  = 17,000 LB/IN. HIGH FLOW DESIGN

SA-9158-C2

APPENDIX

NASA COMPRESSOR AIR BEARING
PERFORMANCE ANALYSIS

A. LOAD CAPACITY

Laminar one-dimensional flow in a narrow slot is obtained by applying Newton's viscosity law $\tau = \mu(du/dy)$ to an element of fluid in static equilibrium (Reference 1, page 152). The resulting equation for the velocity gradient is (see list of symbols at end of appendix):

$$\frac{\partial^2 u}{\partial y^2} = -\frac{1}{\mu}\frac{dp}{dx} \tag{1}$$

Integration for the case where velocities are zero at the walls and velocity gradients are zero at the center of the thin film yields the velocity function:

$$\frac{\partial^2 u}{\partial y^2} = -\frac{1}{\mu}\frac{dp}{dx}\left[\frac{h^2}{4} - y^2\right] \tag{2}$$

Volumetric flow out of a radial slot is:

$$Q = 2\int_{0}^{h/2} 2\pi r\; u\; dy \tag{3}$$

Letting $W = \rho g Q$ for weight flow and $g = \dfrac{p}{RT_s}$ for a perfect gas, and substituting (2) in (3) the weight flow becomes:

$$W_c = \frac{\pi h^3}{12 \mu R T_s} \cdot \frac{p_o^2 - p_a^2}{\ell n \left(\frac{r_2}{r_1}\right)} \tag{4}$$

Since the weight flow is constant, Equation (4) is valid for any value of $r = r_2$, $p = p_a$, and Equation (4) now yields the pressure at any radius:

$$p = p_o \left[1 - \frac{1 - \left(\frac{p_a}{p_o}\right)^2}{\ell n \left(\frac{r_2}{r_1}\right)} \ell n \left(\frac{r}{r_1}\right) \right]^{1/2} \tag{5}$$

Now the load is obtained by integrating the function:

$$F = \pi p_o r_1^2 + 2\pi \int_{r_1}^{r_2} p\, r\, dr - \pi p_a r_2^2 \tag{6}$$

Solutions have been obtained (Ref. 2) for the exact pressure functions, Equation (5), and for linearized pressure. These are shown in Figure SA-9158-C3.

The linearized solution is simple and seems adaptable for the case $0.1 \leqq r_1/r_2 \leqq 0.7$

DATE_____

PREPARED BY_____

CHECKED BY_____

CALC. NO._____

MODEL NASA COMP.

PART NO. AIR BRG.
DESIGN

$\frac{F}{\pi p_o' r_2^2}$

SOLUTION BASED
ON LINEAR
PRESSURE DROP
EQUATION (7)

EXACT SOLUTION
(From Ref. 2)

$\frac{r_1}{r_2} = 1/3$ SELECTED FOR
EXISTING DESIGN

1.0

0.5

0

NON-DIMENSIONAL LOAD

0   0.50   1.00

RATIO, RECESS RADIUS TO OUTSIDE RADIUS, $\frac{r_1}{r_2}$
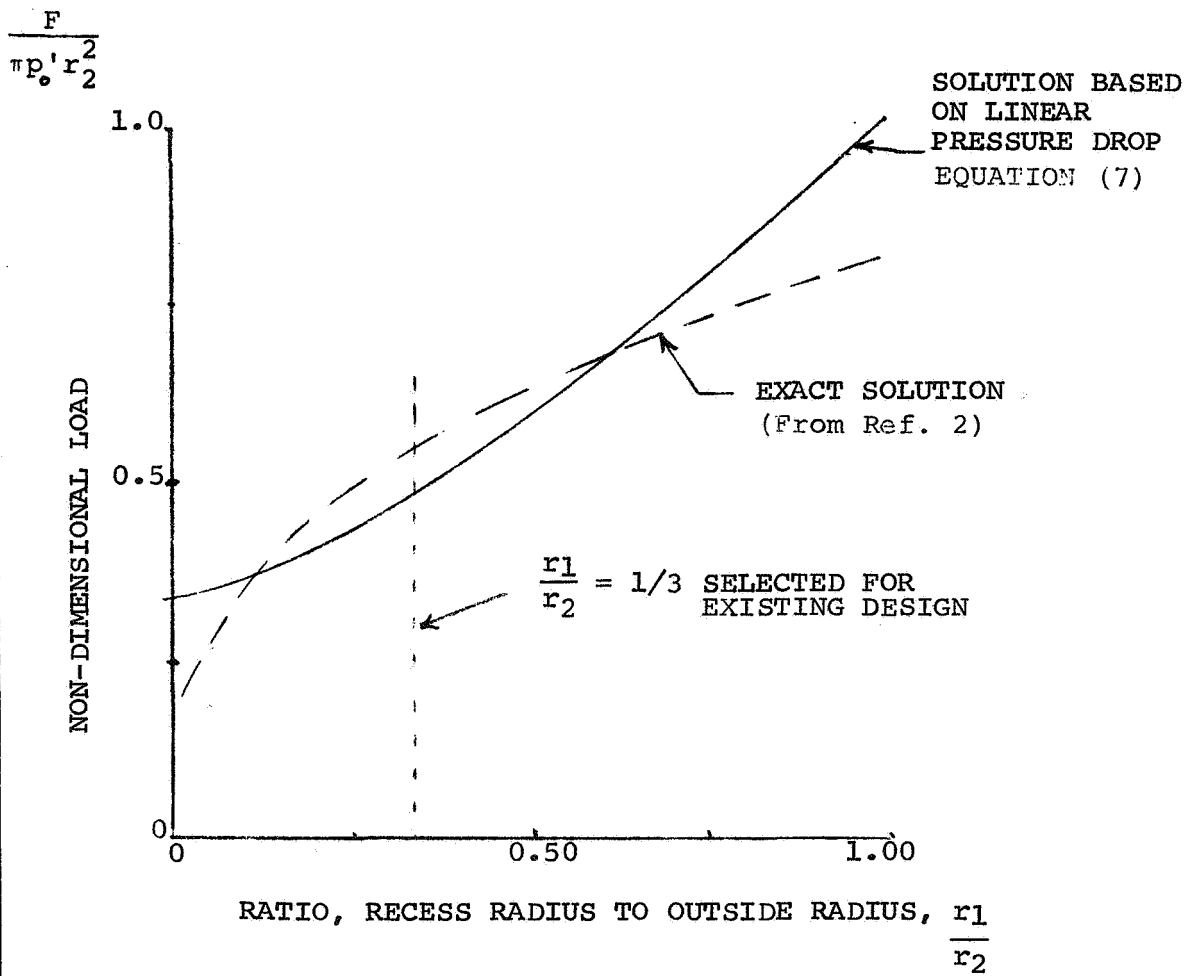
SA-9158-C3

LOAD CAPACITY FOR EXTERNALLY
PRESSURIZED GAS BEARING CIRCULAR
PAD. (ISOTHERMAL EXPANSION ASSUMED)

FORM P2427

LOFTIN'S

REPORT _____

PAGE   F

The non-dimensionalized linear solution for load is:

$$\frac{F}{\pi p_o' r_2^2} = \frac{1}{3}\left[1 + \left(\frac{r_1}{r_2}\right) + \left(\frac{r_1}{r_2}\right)^2\right] \qquad (7)$$

where

$$p_o' = (p_o - p_a) = \text{gage pressure}$$

B. STIFFNESS

Estimation of the flow and stiffness requires that continuity be satisfied for the flow passing through the supply orifice and then through the seat (capillary).

Ideal nozzle flow (isothermal) is given by:

$$W_n = \frac{C_d \; A_n \; P_s \; \Psi}{\sqrt{R \, T_s}}$$

$$A_n = \frac{\pi d_n^2}{4} \qquad (8)$$

$$\Psi = \left[2g \; \frac{k}{k-1}\left(\left(\frac{p_o}{p_s}\right)^{\frac{2}{k}} - \left(\frac{p_o}{p_s}\right)^{\frac{k+1}{k}}\right)\right]^{1/2}$$

$$W_n = W_c$$

Since $W_n = W_c$ we obtain the film thickness:

$$h = \left[\frac{C_d \, A_n \, p_s}{\sqrt{R \, T_s}} \, \psi \, \frac{12\mu \, R \, T_s \, \ell n\left(\frac{r_2}{r_1}\right)}{\pi (p_o^2 - p_a^2)} \right]^{1/3} \qquad (9)$$

Now for the near-choked conditions the function ψ becomes nearly constant and the gas film stiffness can be estimated by finding:

$$\frac{dF}{dh} = \frac{\frac{\partial F}{\partial p_o}}{\frac{\partial h}{\partial p_o}} \qquad (10)$$

The foregoing assumptions yield the gas film stiffness near the choked condition:

$$\frac{dF}{dh} = - \frac{3}{2} \frac{F}{h} \left[1 + \frac{p_a}{p_o} \right] \qquad (11)$$

Optimum stiffness of the air film is secured by maximizing the function df/dh. This is done by evaluating (p_s/p_o) when

$$\frac{d(K)}{d\left(p_s/p_o\right)} = \frac{d}{d\left(p_s/p_o\right)} \frac{\frac{\partial F}{\partial \left(p_s/p_o\right)}}{\frac{\partial h}{\partial \left(p_s/p_o\right)}}$$

where

$$K = \frac{dF}{dh}$$

For the geometry assumed it was found that $\left(p_o/p_s\right)$ approaches the ratio of 0.69 for optimum stiffness.

C.   ORIFICE SIZING AND "AIR HAMMER"

"Air Hammer" tendency is reduced by restricting the trapped air volume in the pocket to a minimum value compatible with orifice requirements. This means that δ and r_1 are selected to just satisfy the following inequalities:

$$\pi d_n \, \delta \; > \; \frac{\pi d_n^2}{4} = \text{orifice area}$$

$$2\pi r_1 \, h \, > \; \frac{\pi d_n^2}{4} = \text{orifice area}$$

When $\pi d_n \, \delta$ approaches the orifice area it begins to act as a secondary restrictor. Now the performance can be met by simply increasing the supply pressure p_s. This is what will happen when and if it is necessary to further reduce the pocket depth δ for stability.

AIRESEARCH MANUFACTURING COMPANY OF ARIZONA
A DIVISION OF THE GARRETT CORPORATION

LIST OF SYMBOLS

g = acceleration of gravith, inches per $\sec^2$

h = film thickness (or clearanches), inches

A_n = orifice area, square inches

d_n = orifice diameter, inches

D_m = mean pad diameter, inches

r = radial dimension, inches

r_1 = pad recess radius, inches

r_2 = outside pad radius, inches

n = number of pads

p_s = supply pressure, psia

p_o = recess pressure, psia (p_o' is gauge pressure)

p_a = ambient pressure, psia

k = ratio of specific heats, c_p/c_v

R = gas constant, inches per °F

T_s = gas supply temperature, °F

F = thrust load per pad, pounds

W_n = flow per orifice, pounds per second (per pad)

W_c = radial flow through bearing clearance space, pounds per second (per pad)

L = equivalent pad length (radially), inches

B = equivalent pad length (along circumference), inches

u = flow velocity, inc./sec

y = film height dimension, inches

x = flow dimension, inches

Q = flow volume, $in.^3/sec$

LIST OF SYMBOLS (Contd)

δ = recess depth, inches

μ = viscosity (absolute), $\dfrac{\text{lb sec}}{\text{in.}^2}$

ρ = mass density, $\dfrac{\text{lb sec}}{\text{in.}^4}$

Ψ = adiabatic orifice flow function = $\left[2g\ \dfrac{k}{k-1}\left(\left(\dfrac{p_o}{p_s}\right)^{\frac{1}{k}} - \left(\dfrac{p_o}{p_s}\right)^{\frac{k+1}{k}}\right)\right]^{1/2}$

c_d = orifice coefficient of flow

REFERENCES

1. Fuller, D., "Theory and Practice of Lubrication for Engineers."

2. Gross, W. A., "Gas Film Lubrication."

SYMBOLS

a   Distance to point of maximum camber rise projected onto chord, inches

b   Diffuser width, inches

C   Chord, inches

C_p Specific heat

C_{pr} Static pressure coefficient, $\dfrac{P_2 - P_1}{P_{T_1} - P_1}$

d*   Throat diameter for pipe diffuser, inches

D   Diffusion factor

H_{ACT} Actual stage enthalpy rise

i   Incidence angle, degrees

L   Axial length, inches

m   Deviation coefficient

M   Mach number

N   Rotational speed, rpm

N_b Number of blades

N_s Specific speed

P   Static pressure

P_T Total pressure

PR   Pressure Ratio

Q   Streamline entropy function

Q_{av} Volumetric flow rate, cu ft/sec

R   Radius, inches

S   Entropy

t   Blade thickness, inches

SYMBOLS (Contd)

T_T Total temperature, °R

U   Tangential velocity, ft/sec

V   Absolute velocity, ft/sec

V_M Axial velocity, ft/sec

W   Relative velocity, ft/sec

X   Length, inches

$\overline{X}$ Empirical adder for deviation angle, degrees

X Cartesian coordinate system perpendicular to compressor
Y axis with origin at the axis of symmetry, inches

α Absolute air angle, degrees

β Relative air angle or blade angle, degrees

δ Deviation angle, degrees

δ^* Displacement thickness

η_{ad} Adiabatic efficiency

λ Blockage

σ Solidity, chord/spacing

$\emptyset$ Expansion angle for pipe diffuser

$\overline{\omega}$ Total pressure loss coefficient

SUBSCRIPTS

h   Hub

s   Shroud

1   Upstream

2   Downstream

REFERENCES

[1] Seyler, D.R. and L.H. Smith, "Single-Stage Experimental Evaluation of High Mach Number Compressor Rotor Blading, Part 1 - Design of Rotor Blading," NASA CR-54881, April 1967.

[2] Runstadler, P.W. and R.C. Dean, "Straight Channel Diffuser Performance at High Inlet Mach Numbers," ASME Paper No. 68-WA/FE-19.

[3] Kenny, D.P., "A Novel Low Cost Diffuser for High Performance Centrifugal Compressors," ASME Paper No. 68-GT-38.

[4] Groh, F.G., G.M. Wood, R.S. Kulp, and D.P. Kenny, "Evaluation of a High Hub/Tip Ratio Centrifugal Compressor," ASME Paper No. 69-WF/FE-28.

[5] Truckenbrodt, E., "A Method of Quadrature for Calculation of the Laminar and Turbulent Boundary Layer in the Case of Plane and Rotationally Symmetrical Flow," NACA TM 1379, 1955.

[6] Stanitz, J.D., "One-Dimensional Compressible Flow In Vaneless Diffusers of Radial and Mixed-Flow Centrifugal Compressors Including Effects of Friction, Heat Transfer, and Area Change", NACT IN 2610.

[7] Scholz, N., "Supplements to the Procedure of Boundary-Layer Quadrature by E. Truckenbrodt", AiResearch Report No. AD-5090-MR.

[8] NASA SP-36, "Aerodynamic Design of Axial-Flow Compressors".

[9] Seyler, D.R. and J.P. Gostelow, "Single-Stage Experimental Evaluation of High Mach Number Compressor Rotor Blading, Part 2 - Performance of Rotor 1B," NASA CR-54582, September 1967.

[10] Pampreen, R.C., "Vaneless Radial Diffuser Study," AiResearch Report AD-5131-R, 10 June 1959.